Numerical models of the early stages of planet formation

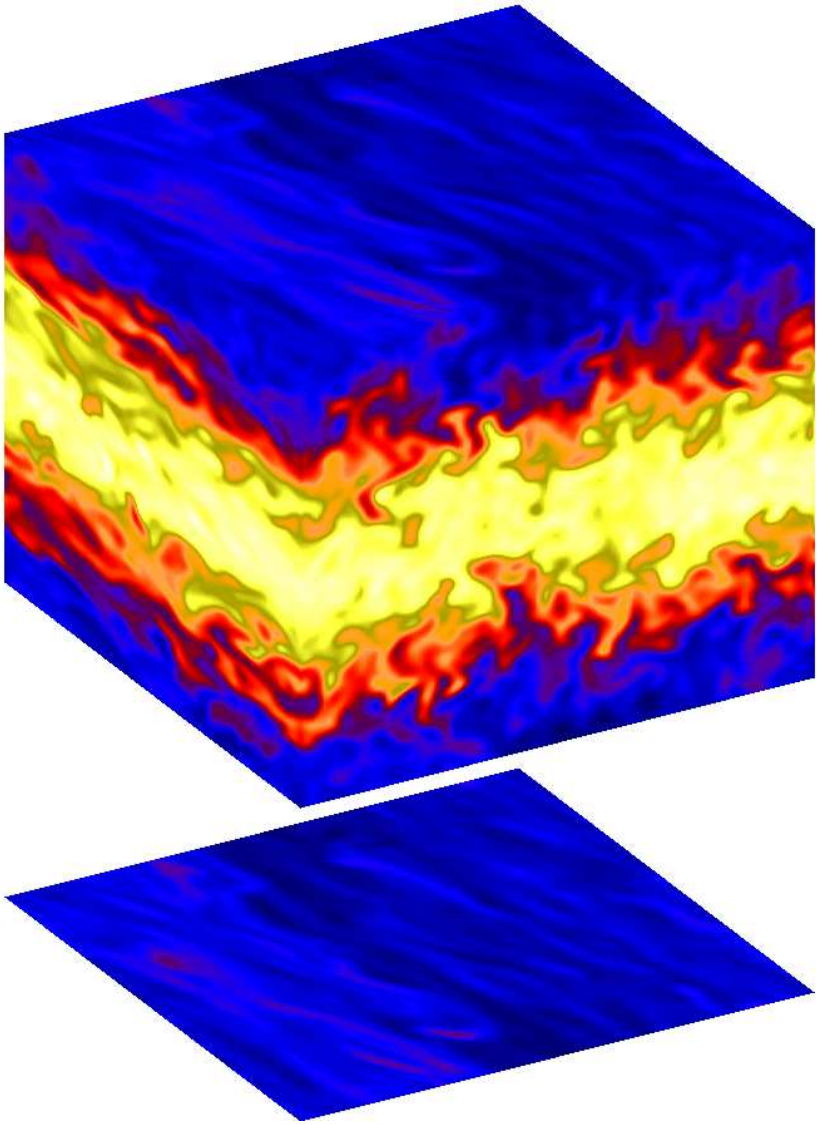

Anders Johansen

Dissertation

submitted to the
Combined Faculties for the Natural Sciences and for Mathematics
of the Ruperto-Carola University of Heidelberg (Germany)
for the degree of

Doctor of Natural Sciences

presented by

cand.scient.

Anders Johansen

born in Gentofte (Denmark)

Oral examination: July 18, 2007

Numerical models of the early stages of planet formation

Referees: **Prof. Dr. Thomas Henning**

Prof. Dr. Ralf S. Klessen

Abstract

This PhD thesis deals with the early stages of planet formation and the growth from μm dust grains to kilometer-sized planetesimals. Dust grains are diffused by the turbulence in the protoplanetary disc. We measure the diffusion coefficient of magnetorotational turbulence and relate it to the turbulent viscosity. Diffusion is surprisingly as strong as viscosity, even though most of the viscosity comes from magnetic stresses that do not directly affect diffusion. The ratio between turbulent viscosity and turbulent diffusion (the Schmidt number) is found to depend strongly on the strength of an imposed vertical magnetic field. Large field strengths yield a Schmidt number that is much larger than unity. Larger solid particles, i.e. rocks and boulders, are not only diffused by magnetorotational turbulence, but also experience concentrations in transient high pressure regions of the turbulent gas, reaching local densities two orders of magnitude higher than the average. Discs that are not susceptible to the magnetorotational instability can develop turbulence due to the sedimentation of solids. The radial pressure gradient of the gas, together with a vertical gradient in the solids-to-gas ratio, leads to a vertical shear in the orbital velocity of the gas, unstable to the Kelvin-Helmholtz instability. The turbulent state is characterised by a number of dense clumps of solids that form due to the dependence of the orbital velocity on the local solids-to-gas ratio, making denser regions plough through less dense regions and scoop up the material at the full Keplerian speed. Isolating the effect of this streaming instability, by ignoring vertical stratification, we find that the turbulent state depends strongly on the background solids-to-gas ratio and on the friction time of the particles. Marginally coupled solids display huge overdensities and a diffusion coefficient that approaches that of the magnetorotational turbulence, more tightly coupled solids develop only a very weak non-linear state.

Zusammenfassung

Diese Doktorarbeit behandelt die ersten Stufen der Planetenentstehung und des Wachstums von μm-grossen Staubkörnern zu km-grossen Planetesimalen. Staubkörner werden von der Turbulenz durch die protoplanetare Scheibe diffundiert. Wir bestimmen den Diffusionskoeffizienten von magnetorotationeller Turbulenz und seinen Zusammenhang mit der turbulenten Viskosität. Die Diffusion ist überraschenderweise so stark wie die Viskosität, obwohl der Grossteil der Viskosität aus der magnetischen Spannung entsteht, die die Diffusion nicht direkt beeinflußt. Das Verhältnis von turbulenter Viskosität und turbulenter Diffusion (die Schmidt-Zahl) hängt empfindlich von der Stärke des überlagerten vertikalen Magnetfeldes ab. Große Feldstärken ergeben Schmidt-Zahlen, die viel größer als eins sind. Größere Festkörperteilchen wie etwa Steine und Brocken werden nicht nur durch die magnetorotationelle Turbulenz diffundiert, sondern auch in kurzlebigen Hochdruckgebieten des turbulenten Gases konzentriert und erreichen lokale Überdichten von zwei Größenordnungen über dem Mittelwert. Scheiben, in denen die magnetorotationelle Instabilität nicht auftritt, entwickeln Turbulenz aufgrund der Sedimentation von Festkörpern. Der radiale Druckgradient des Gases führt zusammen mit einem vertikalen Gradienten im Massenverhältnis Gas-zu-Festkörper zu einer vertikalen Scherung in der Kreisgeschwindigkeit des Gases, und dadurch zu einer Kelvin-Helmholtz-Instabilität. Der turbulente Zustand ist durch eine Anzahl dichter Partikelklumpen gekennzeichnet, die durch die Abhängigkeit der Kreisgeschwindkeit vom lokalen Staub-zu-Gas-Verhältnis entstehen, wodurch sich dichtere Klumpen mit Kepler-Geschwindigkeit durch weniger dichte Gebiete pflügen. Bei Isolation dieses Strömungsinstabilitätseffektes durch Vernachlässigung der vertikalen Schichtung zeigt sich, dass der turbulente Zustand stark vom globalen Staub-zu-Gas-Verhältnis und von der Reibungszeit der feste Partikel abhängt. Marginal gekoppelte Partikel zeigen große Überdichten und einen Diffusionskoeffizienten vergleichbar dem bei magnetorotationeller Turbulenz. Kleinere Partikel entwickeln nur einen sehr schwach nicht-linearen Zustand.

Preface

This thesis work was performed at the Max-Planck-Institut für Astronomie in the period between August 2004 and May 2007 under the supervision of Dr. Hubert Klahr and Prof. Dr. Thomas Henning.

The thesis itself consists of six papers published in refereed journals:

- "Dust diffusion in protoplanetary discs by magnetorotational turbulence" (2005)[1]
  Johansen A., & Klahr H.
  The Astrophysical Journal, vol. 634, p. 1353-1371

- "Gravoturbulent formation of planetesimals" (2006)
  Johansen A., Klahr H., & Henning Th.
  The Astrophysical Journal, vol. 636, p. 1121-1134

- "Dust sedimentation and self-sustained Kelvin-Helmholtz turbulence in protoplanetary disc mid-planes" (2006)
  Johansen A., Henning Th., & Klahr H.
  The Astrophysical Journal, vol. 643, p. 1219-1232

- "Turbulent diffusion in protoplanetary discs: The effect of an imposed magnetic field" (2006)
  Johansen A., Klahr H., & Mee A. J.
  Monthly Notices of the Royal Astronomical Society, vol. 370, p. L71-L75

- "Protoplanetary disc turbulence driven by the streaming instability: Linear evolution and numerical methods" (2007)
  Youdin A., & **Johansen A.**
  The Astrophysical Journal, in press

- "Protoplanetary disc turbulence driven by the streaming instability: Non-linear saturation and particle concentration" (2007)
  Johansen A., & Youdin A.
  The Astrophysical Journal, in press

[1] This paper was awarded the "Patzer Prize" for best refereed paper by a PhD student at the MPIA in 2005.

I was not the first author of Youdin & Johansen (2007), but this paper came about as a split of a longer paper, so I was heavily involved with the writing, and all code improvements and computer simulations for the paper were done by me.

I have devoted a chapter of the thesis to each of the abovementioned projects (Chapters 2–7), in order by which they were finished, so that the evolution of theoretical concepts and computational methods appears in its natural sequence. Thus the two chapters on the diffusion properties of magnetorotational turbulence (Chapters 2 and 5) are not consecutive. The scientific chapters are meant to be self-contained each with an individual introduction and conclusion. Chapters are cross referenced internally either by chapter number or (more commonly) by author (year) publication id.

All computer simulations in this thesis were done with the Pencil Code. The code, including improvements done for the thesis work, is publicly available under a GNU open source license and can be downloaded at `http://www.nordita.dk/data/brandenb/pencil-code/`.

Notation and terminology

The individual papers have been edited for fitting together in the thesis. Certain repetitions have been deleted and language has been made uniform, especially on terminology of solids: I decided to use the word "solids" rather than "dust" to generally describe condensed material in discs. Thus the terminology in the first four chapters has been changed from what appears in print elsewhere.

Mathematical notation is fairly standard throughout, except for a few exceptions. Both Ω_0 and Ω are used for the Keplerian frequency at the centre of the shearing box. The subscript for solids is either d or p, referring to dust and to particles. I decided not to standardise mathematical notation because of the risk of introducing subtle errors in the text.

Acknowledgements

A number of people helped me during my thesis work. My supervisors, Hubert and Thomas, were always there for me with ideas, suggestions and support. They also encouraged me to develop my own science, which I am deeply grateful for. I was paid one month by NORDITA in Copenhagen in the time between finishing the master's thesis and beginning the PhD in Heidelberg. I am grateful to Axel Brandenburg and Anja Andersen for arranging this. Anja and Axel are also thanked for their continuous support and many recommendation letters. In this connection I am grateful to "Christian & Ottilia Brorsons Rejselegat" for paying part of the moving expenses when coming to Heidelberg. I am also thankful for several rounds of support from "Det Johansenske Familielegat".

I have throughout my thesis work had the opportunity to interact with a number of brilliant astrophysicists both at the MPIA and at other places in Germany and around the globe. At the MPIA the collaboration with Kees Dullemond and Frithjof Brauer was especially fruitful because our topics are so close and yet so different. I would generally like to thank Christian

Fendt, Dima Semenov, Patrick Glaschke and Jürgen Steinacker for inspiring discussions and for helping me understanding their different topics of expertise. Coryn Bailer-Jones is thanked for being the "local native speaker" in issues with the English language (in this connection I would like to thank Jürgen Steinacker for translating the thesis abstract into proper German). Sascha P. Quanz is thanked for always being overbearing with my many questions regarding the formal requirements for the PhD work.

The Annette Kade Student Fellowship Program at the American Museum of Natural History allowed me to spend 6 weeks working with Mordecai-Mark Mac Low and Jeff Oishi at the American Museum of Natural History in New York (May–June 2006). This was a very inspiring stay where we managed to develop together a self-gravity solver for superparticles (the paper is still in preparation and not part of the thesis). Thank you, Jeff and Mordecai, for your warm hospitality during my stay in New York. In this connection I would like to thank Andrew Youdin for a very fruitful intercontinental collaboration (and for finding the odd amount of inconsistencies in my disc parameters). Jim Stone and Jeremy Goodman are thanked for much input (mostly through Andrew, but also for the couple of days that I spent at Princeton) to the project on the streaming instability.

Scientifically I am also grateful to a number of anonymous referees who greatly improved the science and presentation of the papers through their detailed referee reports.

Computer simulations for this thesis were initially performed at Danish Center for Scientific Computing in Odense. For the last two years I used first the RIO cluster and then the PIA cluster at the Rechenzentrum Garching, a 256 processor computer belonging to the two theory groups at the MPIA. The acquisition of PIA was an enormous help for my science. I must have used close to a million processor hours on PIA since then. I would like to thank Christian Guggenberger, the systems administrator at PIA, for lots of help with setting up the Pencil Code to begin with and also with the day-to-day problems and challenges.

Not least I would like to thank my parents for their support in many difficult decisions, such as moving to another country. Odin is thanked for company in the countless dark mornings in front of the laptop. My wife, Ane, is thanked for letting all this make sense and for generally not finding astronomy very interesting.

Chihiro: Haku, listen, I just remembered something from a long time ago, I think it may help you. Once, when I was little, I dropped my shoe into a river. When I tried to get it back I fell in, I thought I'd drown, but the water carried me to shore. It finally came back to me, the river's name was the Kahaku river, I think that was you, and your real name is Kahaku river.
Haku: You did it, Chihiro, I remember, I was the spirit of the Kahaku river.
Chihiro: A river spirit?
Haku: My name is the Kahaku river.
Chihiro: They filled in that river, it's all apartments now.
Haku: That must be why I can't find my way home Chihiro, I remember you falling into the river, and I remember your little pink shoe.
Chihiro: So, you're the one who carried me back to shallow water, you saved me... I knew you were good!

– From Hayao Miyazaki's "Spirited Away"

Contents

Introduction

The diversity of the planets and moons in the solar system is breathtaking: icy methane plains on Pluto, the majestic rings of Saturn, a sub-surface ocean on Europa, scorching hot Venus, and not least our water-rich Earth, teeming with life. How did all these amazing bodies form? To answer this question we need to look back 4.6 billion years (4567.2 ± 0.6 million years to be more precise, see Amelin et al. 2002) and dive into a swirling nebula of gas and dust that orbited the young Sun.

In the earliest stages of planet formation micrometer-sized dust grains collide and gradually build up kilometer-sized *planetesimals*, bodies that are so large that they can attract each other directly by gravity. This is an important landmark on the way to real planets because of the change to gravity-dominated growth.

A crucial factor in the evolution of dust grains into planetesimals is the presence of gas in the disc. The motion of solid bodies is coupled to that of the gas through drag forces. Small dust grains are so strongly affected by drag that an almost constant solids-to-gas ratio is forced by the turbulent motion of the gas. As the solid bodies grow to meter-sizes, these boulders take a whole Keplerian orbit to react to the motion of the gas. This allows some freedom in their motion, e.g. to form a dense sedimentary layer around the mid-plane of the disc, while gas drag is still not insignificant, as it will be once planetesimal sizes are reached.

The road from boulders to planetesimal is poorly known. One danger in being marginally coupled (i.e. at an orbital time-scale) to the gas is that gas orbits slightly slower than the Keplerian speed, due to the radial pressure gradient in the disc, whereas boulders do not feel this pressure gradient and want to orbit at the Keplerian speed. The consequent gaseous head wind drains the boulders of angular momentum and cause them to spiral into the inner disc on a time-scale of a few hundred local orbits (Whipple 1972; Weidenschilling 1977a). Thus growth beyond marginal coupling (to perhaps 10 m objects) must happen faster than the radial drift time-scale. Another problem with the growth from boulders to planetesimals is that boulders stick together poorly (Benz 2000), leaving serious doubt about whether growth by simple sticking alone is a viable road to planetesimals. It was proposed already by Safronov (1969) and by Goldreich and Ward (1973) that a sedimented mid-plane layer of solids will become gravitationally unstable and contract under its own weight, forming planetesimals on a short time-scale and without the necessity for efficient sticking. This has nevertheless remained a controversial theory, mostly because even relatively low levels of turbulence in the disc will stir up the sedimentary layer and keep it from obtaining critical density (Weidenschilling and Cuzzi 1993).

Thus turbulence plays a crucial role in planetesimal formation scenarios by setting the width of the sedimentary layer of solids and determining whether gravitational instability is allowed. Turbulent motions also transport small dust grains around, affecting observational properties of protoplanetary discs and possibly explaining the presence of crystalline silicates in solar system comets that formed at several tens of AU from the Sun where silicates are otherwise supposed to be amorphous (Gail 2001).

In this thesis I address a number of issues related to the early stages of planet formation from 2-D and 3-D computer simulations of solids (dust grains, pebbles, rocks and boulders) moving in turbulent protoplanetary discs. I consider both turbulence from a global view point, as given by the magnetorotational instability, and mid-plane turbulence caused by the sedimentation of solids itself. The fundamental questions of interest are:

- What are the diffusion properties of magnetorational turbulence?
- Does turbulence only diffuse or can it also locally concentrate solids?
- Does turbulence slow down the radial drift of solids?
- What are the properties of sedimentation-induced mid-plane turbulence?
- What happens to the free energy in the relative drift of solids and gas?

Here is a brief overview of the contents of the individual chapters:

Chapter 1
The first chapter of the thesis consists of a brief review of planet formation to serve as reference for the scientific chapters. Constraints on the planet formation process from observations of exoplanets and protoplanetary discs and from meteoritics are presented. Standard scenarios of planet formation – the planetesimal hypothesis for the first stages of planet formation and the core accretion model for giant planet formation – are introduced.

Chapter 2
The second chapter considers the turbulent transport of small dust grains in magnetorotational turbulence. Although seemingly random the motion displays one very predictable feature: any local overdensity of solids is diffused out by the turbulence. Measuring the turbulent diffusion coefficient tells something fundamental about the turbulence and gives important knowledge about the ability of the solids to sediment out of the gas. The Schmidt number, i.e. the ratio of turbulent viscosity to turbulent diffusion, is found to be around unity, surprisingly high when considering that most of the turbulent viscosity comes from magnetic stresses that do not directly influence diffusion. Some indications are found that pebble-sized solids are concentrated in anticyclonic eddies of the turbulent flow.

Chapter 3
In the third chapter larger solids, i.e. rocks and boulders, are considered. Boulders have the tendency to end up in any rotating or overdense region of the gas. High pressure regions in the magnetorotationally turbulent flow come and go, just like in the Earth atmosphere, but stay together long enough, a few Keplerian orbits, that the boulders concentrate there. The local bulk density of solids is found to reach up to two orders of magnitude higher than the average.

The radial drift of the solids is also temporarily slowed down by the high pressures, leading to an overall reduction of the drift speed by approximately 40%. The overdensities can be important for planetesimal formation: it is shown that the densest regions are gravitationally unstable and should contract under their own weight if the self-gravity of the boulders was considered.

Chapter 4
The fourth chapter explores the sedimentation of solids in discs with no magnetic turbulence. A different kind of turbulent state, caused by a Kelvin-Helmholtz instability in the orbital velocity profile of the gas, sets in due to the sedimentation of solids. The width of the sedimentary layer is found to be in good agreement with an analytical model of Sekiya (1998) for tightly coupled solids (rocks and pebbles). The non-linear turbulent state consists of a number of interacting, highly overdense particle clumps. This is explained by the dependence of the drift velocity on the local solids-to-gas ratio, causing overdense clumps to plough through less dense regions, thus gaining more and more mass, while losing particles downstream to the sub-Keplerian flow.

Chapter 5
We briefly return to magnetorotational turbulence in the fifth chapter to see the effect of a vertical magnetic field on the Schmidt number. The imposed field increases the turbulent viscosity dramatically, but the turbulent diffusion does not rise as quickly, leading to an increased value of the Schmidt number.

Chapter 6
Finally in the sixth and seventh chapters the streaming instability, found in Chapter 4 to be the source of particle clumping in the mid-plane, is considered in isolation by turning off vertical gravity from the star in order to untangle the streaming instability from the related Kelvin-Helmholtz instability. Chapter 6 considers the linear evolution of the streaming instability. An improved particle-mesh drag force scheme is presented.

Chapter 7
In Chapter 7 the non-linear evolution of the streaming instability is considered. The energy present in the relative drift of gas and solids is converted to turbulence and leads to huge local overdensities in the boulders. The turbulent state is found to depend strongly on the background solids-to-gas ratio and on the friction time of the solids. Marginally coupled solids display huge overdensities and strong turbulent motion at large scales, where tightly coupled solids develop weaker overdensities with shorter lifetimes on smaller scales.

Chapter 8
The results of the entire thesis work are summarised in Chapter 8. Some outlook is given to possible future extensions of the presented models.

Appendix A
Appendix A contains a number of appendices from the individual chapters.

Chapter 1

Planet formation

This chapter contains a general introduction to the field of protoplanetary discs and planet formation and is meant as a reference and background for many of the concepts treated in the scientific chapters. The reader is referred to Viktor Safronov's classical book on planet formation (there should be an English translation available at any well-equipped science library), but also to the recent Protostars and Planets V review on the early stages of planet formation by Dominik et al. (2007) and to the book on planet formation that was the result of the December 2004 meeting at Ringberg Castle (Klahr and Brandner 2006).

The bodies in the solar system tell us something very important about their birth. Meteorites are direct leftovers from the planet formation epoch. Radiometric dating of meteorites reveals to us the age of the planets. A special class of meteorites, carbonaceous chondrites, contain the most pristine material in the solar system, from which the fundamental connection that the Sun and the planets formed at the same time and from the same material is inferred. The current mass of heavy elements in the planets can be used to reconstruct the density structure of the solar nebula from which the planets formed.

Young stars show an excess of infrared radiation which is not in accordance with the black body spectrum of the central object. This is the echo of stellar light, absorbed by microscopic dust grains in vast circumstellar discs and reemitted as infrared radiation. Observations of protoplanetary discs around young stars tell us something extremely important, namely that a variety of masses, sizes and environments exist. They also tell us that stars accrete mass through the disc, which is interpreted by theorists to be a consequence of Keplerian shear instabilities and turbulent gas motion in the disc. Turbulence in turn has a huge influence on the first stages of planet formation.

1.1 The planets and the Sun were born together

Direct evidence of the planet formation process comes from meteorites. Isotope ratios of radiactive decay products allow very precise dating, giving the solar system an age of roughly

4.55 billion years (as originally measured by Patterson 1956). More modern measurements of calcium-aluminium-rich inclusions (CAIs), possibly representing the first condensations in the solar nebula, yield ages of 4.5672 ± 0.0001 billion years (Amelin et al. 2002). Dating of iron meteorites is largely in agreement with these numbers (4.5662 billion years, see Baker et al. 2005).

The carbonaceous chondrites meteorite class contains the most pristine bodies in the solar system, having not been significantly heated since their formation (Trieloff et al. 2003). Isotopic abundances of refractory elements in carbonaceous chondrites show great similarity with the Sun's atmosphere (e.g. Norton 2002). This is a strong indication that the planets and the Sun formed out of the same material, since abundances of molecular clouds in the Milky Way vary both spatially and temporally. There are, however, notable differences in the composition of meteorites and the Sun: there is an overabundance of Lithium in the meteorites relative to the Solar atmosphere. This disproves the hypothesis that planets formed out of material extracted from the Sun, because Li is destroyed by thermal protons as it is mixed by convection down into layers of temperature $T \gtrsim 2 \times 10^6\,\mathrm{K}$ (Iben 1967). Element abundances in meteorites thus give us hard proof that the planets and the Sun formed out of the same material, but that one part of the material went into the Sun and another part into meteorite parent bodies.

The next piece of evidence comes from the orbits of the planets. All the planets, dwarf planets and asteroids orbit the same way around the Sun. That is another indication that the planets were not caught by the Sun from interstellar space. These simple considerations lead us to accept a primordial cloud of gas and dust, the solar nebula, as the birthplace of the planets. The different ages of CAIs and chondrules (Amelin et al. 2002) are an indication that the processes leading to planet formation, i.e. the gradual agglomoration of dust particles into larger structures, took place over millions of years.

1.2 Minimum mass solar nebula

One can make an estimate of the structure of the solar nebula by looking at the contents of heavy (i.e. condensable) elements in the current planets (Kusaka et al. 1970; Weidenschilling 1977b; Hayashi 1981). The rationale is that gas was dispersed by radiation from the young Sun, whereas the original contents of solids had already been incorporated in large solid bodies when the luminosity of the Sun grew high enough to evaporate the disc. This can only be partially true since radial drift can seriously affect the distribution of solids in the nebula (Stepinski and Valageas 1996; Youdin and Shu 2002; Youdin and Chiang 2004). But accepting the premise of the investigation leads to an estimate of around $\Sigma_\mathrm{g} = 150\,\mathrm{g\,cm^{-2}}$ at Jupiter's location ($r = 5\,\mathrm{AU}$) in the solar nebula. This comes from smoothing out Jupiter's mass of heavy elements (being approximately 5% of the planet's total mass) over an annulus between $r = 2.5$ AU and $r = 7.5$ AU. The overall column density of the minimum mass solar nebula (MMSN) is inferred to be (Weidenschilling 1977b; Hayashi 1981)

$$\Sigma_\mathrm{g}(r) = 1700\,\mathrm{g\,cm^{-2}} \left(\frac{r}{\mathrm{AU}}\right)^{-1.5} \tag{1.1}$$

as a function of orbital distance r. This gives a total mass of $0.013 M_\odot$ when integrating from $r_1 = 0.35\,\mathrm{AU}$ to $r_2 = 35\,\mathrm{AU}$. The temperature of a passively irradiated disc is (Kusaka et al. 1970; Hayashi 1981)

$$T(r) = 280\,\mathrm{K}\,\left(\frac{r}{\mathrm{AU}}\right)^{-0.5} \tag{1.2}$$

Viscous heating may heat the inner disc if the α-value is significant (Lynden-Bell and Pringle 1974), but this contribution can generally be ignored for $r > 5\,\mathrm{AU}$ as long as the turbulent viscosity is not too high ($\alpha_\mathrm{t} < 0.01$, Dullemond and Dominik 2004).

1.3 Protoplanetary disc observations

The dust in protoplanetary discs shows up as a long wavelength excess in the combined spectrum of star and disc – the thermal emission of dust grains at a few 100 K reprocessed from the original visible radiation from the central T Tauri star (Mendoza 1968; Chiang and Goldreich 1997). This infrared excess allows the determination of disc masses (by assuming a canonical dust-to-gas ratio). Beckwith et al. (1990) considered 86 pre-main-sequence stars and detected discs around 42% of them, with disc masses varying from $0.001 M_\odot$ to $1 M_\odot$. This would put the minimum mass solar nebula in the low end of the range, with disc masses one to two orders of magnitude higher occurring in nature.

Sicilia-Aguilar et al. (2006) find that the near infrared excess decreases with the age of the young stars, an indication that small grains in the inner disc have sedimented towards the midplane and/or been incorporated into larger bodies. Coagulation of small grains is in fact expected from theoretical grounds to be very fast (Dullemond and Dominik 2005), so the mere presence of small dust grains in discs of millions of years age is best interpreted as products of collisional fragmentation of larger bodies, possibly already in a sedimented mid-plane layer.

Radiation of mm and cm wavelengths was detected in circumstellar discs by Wilner et al. (2000). Testi et al. (2003) conclude that this radiation is not due to an exotic disc geometry, but rather that it traces large solid particles (with radii in the mm or cm range) at several 100 AU from the star. The longer wavelength emission from larger grains is polluted with free-free radiation. It was pointed out by Brauer et al. (2007) that mm grains are marginally coupled to the tenuous, cold gas at a $r = 100\,\mathrm{AU}$, so that radial drift should be at its highest possible value for those particles. Thus the (for planet formation theorists) fantastic discovery of large solid particles in protoplanetary discs comes with a huge mystery: how do those grains stay at high orbital radii without drifting? Brauer et al. (2007) explored theoretical ways to keep marginally coupled particles from drifting, including decreased drift in a dense sedimentary mid-plane layer, but found no obvious explanation except for photoevaporation of the outer disc, which would make the gas thin enough to not affect the pebbles significantly.

1.3.1 Accretion

Turbulence in protoplanetary discs drives accretion onto the central star by acting as an effective viscosity that is orders of magnitude higher than the molecular viscosity. Accretion

also leads to a heating of the gas in the disc, especially in the mid-plane where the density is highest. Radiation from the central star is nevertheless often a more important heat source than accretion. Accretion manifests itself more clearly in ultraviolet radiation originating when disc material lands on the stellar surface (Bertout et al. 1988). Gullbring et al. (1998) measured the accretion luminosities of T Tauri stars and translated the measurements into mass accretion rate $\dot{M}$. They find values in the interval $\dot{M} = 10^{-9\ldots-7} M_\odot\,\mathrm{yr}^{-1}$. Coupling the mass accretion rate with a disc model yields the turbulent viscosity of the disc ν_t through the relation (Shakura and Sunyaev 1973; Pringle 1981)

$$\nu_\mathrm{t} = (3\pi)^{-1} \frac{\dot{M}}{\Sigma}\,, \tag{1.3}$$

where Σ is the column density of gas and solids. Making use of the famous non-dimensionalisation with sound speed c_s and orbital frequency Ω_K of Shakura and Sunyaev (1973), $\nu_\mathrm{t} = \alpha_\mathrm{t} c_\mathrm{s}^2 \Omega_\mathrm{K}^{-1}$, yields the α-value of the disc as

$$\alpha_\mathrm{t} = (3\pi)^{-1} \frac{\dot{M}}{\Sigma} \frac{\Omega_\mathrm{K}}{c_\mathrm{s}^2}\,. \tag{1.4}$$

For the minimum mass solar nebula we get $\alpha_\mathrm{t} = 10^{-4\ldots-2}$ from typical mass accretion rates.

Sources of turbulence

Observations tell us that discs accrete. This must be coupled to a sufficiently strong theory for the source of the turbulence that drives accretion. The Keplerian shear flow is inherently hydrodynamically stable (see e.g. Chandrasekhar 1961), i.e. infinitely small perturbations to the pure Kepler flow die out quickly with time. If the gas couples sufficiently with magnetic fields, then the flow is linearly unstable to the magnetorotational instability (Balbus and Hawley 1991; Hawley and Balbus 1991), the only linear shear instability known to operate in Keplerian discs (Balbus and Hawley 1998). A number of non-magnetic instabilities may develop turbulence under different disc conditions – gravitational instability in massive discs (Toomre 1964), convective instability leading to convective heat transport from a hot mid-plane to the surface layers (Lin and Papaloizou 1980), Rossby wave instability in local pressure maxima (Li et al. 2000), baroclinic instability (Klahr and Bodenheimer 2003) that leads to the formation of vortices, just to name a few – but none of those instabilities get their energy directly from the Keplerian shear the way the magnetorotational instability does. There is actually at least two more instabilities associated with the coupled motion of gas and solids: the Kelvin-Helmholtz instability operating on the vertical shear profile of the gas (Goldreich and Ward 1973; Weidenschilling 1977a) and the streaming instability (Youdin and Goodman 2005) deriving its energy from the relative flow of solids and gas. Both these instabilities gain their energy from the radial pressure support of the disc and are not Keplerian shear instabilities either. They are also confined to a small region around the mid-plane of the disc where the solids-to-gas ratio is around unity or higher, but both instabilities have an importance for planet formation (see Chapters 4, 6 and 7 of this thesis).

The magnetorotational instability is only present if a certain minimum ionisation fraction is obtained (with the number density ratio of electrons to neutrals of order $x \equiv n_\mathrm{e}/n_\mathrm{H} \sim 10^{-13}$, see Gammie 1996). Ionisation is thought to be given by a combination of cosmic rays (with

a penetration depth of around $\Sigma_{\rm g} \approx 100\,{\rm g\,cm^{-2}}$), high energy radiation from the star and/or the environment and decay of radioactive elements (Gammie 1996; Sano et al. 2000; Fromang et al. 2002; Semenov et al. 2004; Ilgner and Nelson 2006a). The equilibrium ionisation fraction comes from a balance between ionisation and recombination, the latter is given by chemical reactions and by gas-grain reactions. The inability of the magnetorotational instability to operate in parts of the disc where the column density distance to the surface is too high has lead to the concept of a "dead zone" in protoplanetary discs (Gammie 1996). The dead zone is generally thought to have the shape of a wedge that goes from a few AU to a few 10 AU in orbital distance and have an opening angle comparable to the scale-height-to-radius ratio H/r. This zone covers a large fraction of the volume where planets are thought to form, so the presence of dead zones in protoplanetary discs potentially has a big influence on planet formation. Our picture of the relation between dead and active regions is nevertheless still in the making. Small grains (submicron-sized) are particularly efficient reducers of the ionisation fraction. Sano et al. (2000) show that if the peak grain size grows by just an order of magnitude over the interstellar value, then the dead zone should vanish altogether at 5 AU in low mass discs. Since planet formation intrinsically puts mass from microscopic grains into gradually larger bodies, this could point to a decrease in the size of the dead zone with time. The radiation field from the star is also not static. Ilgner and Nelson (2006b) show that dead zones may disappear regularly when flares on the young star sends ionising X-rays through the disc. Perhaps most intriguing is the effect of the active surface layers on the mid-plane. The simulations by Fleming and Stone (2003) showed that the turbulent layers affect the dead zone dynamically, causing motion and even accretion there. More recently Turner et al. (2007) found that free charges are mixed from the active regions into the dead zone, allowing for magnetic fields to diffuse to the mid-plane. All in all the dead zone is likely a time-dependent phenomenon that exists at certain times during the evolution of protoplanetary discs, but may vanish entirely at other times (presumably later in the life of discs when the column density decreases due to accretion and more dust mass is bound up in larger solid bodies).

1.4 The planetesimal hypothesis

The modern view of planet formation was developed during the 1960s, especially by Viktor Safronov in his book "Evolution of the protoplanetary cloud and formation of the Earth and the planets". I refer generally to the introduction of Safronov (1969) for a review of older theories of planet formation. At the time of Safronov's monumental work there was a beginning realisation that the planets formed in a circumstellar disc of gas and dust, but the details of the process were far from well-known.

Dust grains, and solid bodies in general, experience a friction force from the gas. The friction is directed against the relative velocity between a solid particle and the surrounding gas $\boldsymbol{v}-\boldsymbol{u}$,

$$\frac{\partial \boldsymbol{v}}{\partial t} = \ldots - \frac{1}{\tau_{\rm f}}(\boldsymbol{v}-\boldsymbol{u})\,, \tag{1.5}$$

and works on a time-scale $\tau_{\rm f}$ called the friction time. This equation, together with a corresponding equation for the back-reaction friction force from the solids on the gas, form the

basics of the field of *dust dynamics* which this thesis focuses on.

The Epstein drag force regime is valid when the mean free path of the gas molecules λ is longer than the size of the solid. Here the friction time is given as

$$\tau_{\rm f} = \frac{R_\bullet \rho_\bullet}{c_{\rm s} \rho_{\rm g}} \,, \tag{1.6}$$

where $R_\bullet$ is the radius of the solid body, $\rho_\bullet$ is its internal density, $c_{\rm s}$ is the sound speed of the gas and $\rho_{\rm g}$ is the density of the gas. Considering the mid-plane of the disc one can express the radius of the solid body as a function of the friction time as

$$R_\bullet = (2\pi)^{-1/2} \Omega_{\rm K} \tau_{\rm f} \frac{\Sigma_{\rm g}}{\rho_\bullet} \,, \tag{1.7}$$

by using the relations $\rho_{\rm g,mid} = \Sigma_{\rm g}/(\sqrt{2\pi}H)$ and $c_{\rm s} = H\Omega_{\rm K}$ where H is the gas scale height. Thus marginally coupled solids with $\Omega_{\rm K}\tau_{\rm f} = 1$ are approximately 50 cm in diameter at $r = 5$ AU (where $\Sigma_{\rm g} = 150\,{\rm g\,cm^{-2}}$ in the minimum mass solar nebula, see equation 1.1).

Initially dust grains are well-mixed with the gas. The scale height of the solids-to-gas ratio H_ϵ is (Dubrulle et al. 1995)

$$\frac{H_\epsilon}{H} = \sqrt{\frac{\delta_{\rm t}}{\Omega_{\rm K}\tau_{\rm f}}} \,, \tag{1.8}$$

where $H = c_{\rm s}\Omega_{\rm K}^{-1}$ is the scale height of the gas and $\delta_{\rm t}$ is a dimensionless turbulent diffusion coefficient, similar to the α-value that is used for viscosity. As long as the grains are small, with $\Omega_{\rm K}\tau_{\rm f} \ll \delta_{\rm t}$ and thus $H_\epsilon \gg H$, they will stay suspended throughout the vertical extent of the disc. These grains collide due to brownian motion, forming larger and larger dust agglomorates (Dominik and Tielens 1997) that will eventually decouple from the turbulence and fall towards the mid-plane. A run-away growth occurs, leading the largest particles to reach sizes of approximately 1 cm at the mid-plane (Safronov 1969).

As the solids grow, their tendency to move independently of the gas increases. The gas rotates with a speed that is slighter lower than the Keplerian value due to the radial pressure gradient of the gas. The sub-Keplerian gaseous head wind is a constant sink of angular momentum for the solids. One can by simple algebra derive the radial velocity v_r of the solids as (Nakagawa et al. 1986)

$$v_r = \frac{\Omega_{\rm K}\tau_{\rm f}}{(1+\epsilon)^2 + (\Omega_{\rm K}\tau_{\rm f})^2} \frac{H}{r} \left(\frac{\partial \ln P}{\partial \ln r} \right) c_{\rm s} \,, \tag{1.9}$$

where $\epsilon \equiv \rho_{\rm p}/\rho_{\rm g}$ is the local solids-to-gas ratio, H/r is the disc aspect ratio and $\partial \ln P/\partial \ln r < 0$ is the radial pressure support of the gas. The radial drift speed peaks for marginally coupled solids with $\Omega_{\rm K}\tau_{\rm f} = 1$, corresponding to approximately m-sized boulders for the physical conditions at 5 AU in the solar nebula (equation 1.7). The time-scale for the radial drift can be estimated as $t_{\rm drift} \sim r/v_r$, giving for isolated marginally coupled solids

$$\Omega_{\rm K} t_{\rm drift} = \frac{1}{\frac{1}{2}\left(\frac{H}{r}\right)^2 \left(-\frac{\partial \ln P}{\partial \ln r}\right)} \equiv \frac{1}{\eta} \,. \tag{1.10}$$

This crude estimate ignores any kind of change in friction time due to the radially dependent density and temperature of the disc or due to coagulation. Typical values of η range from $\eta = 10^{-3}$ to $\eta = 10^{-1}$, yielding radial drift times of anywhere between a few and a few hundred local orbits (Adachi et al. 1976; Cuzzi et al. 1993).

If one can somehow jump past the radial drift barrier (e.g. by efficient coagulation in a disc with no global turbulence, see Weidenschilling 1997), the next important step is the formation of planetesimals. These bodies can be defined as being big enough that their gravitational cross sections are significantly larger than their physical cross sections. This definition is very useful because it is based on physics that can plausibly lead to improved agglomoration. The collisional cross section of two self-gravitating bodies of radii R_1 and R_2 is

$$A_{\rm coll} = \pi(R_1 + R_2)^2 \left(1 + 2\theta_{\rm S}\right) , \tag{1.11}$$

where

$$\theta_{\rm S} = \frac{1}{2}\left(\frac{v_{\rm esc}}{v}\right)^2 \tag{1.12}$$

is the ratio of the mutual escape velocity of the bodies to their relative speed (it is sometimes called the Safronov factor). The corresponding radius where $\theta_{\rm S} = 1$ can be written as

$$R \approx 1\,{\rm km} \left(\frac{\rho_\bullet}{1000\,{\rm kg\,m^{-3}}}\right)^{-1/2} \left(\frac{v}{\rm m\,s^{-1}}\right) , \tag{1.13}$$

where $\rho_\bullet$ is the material density of the bodies. Depending on collisional speed and material density gravitational focusing becomes important for bodies of approximately 1-10 km in size. This can be used as a definition of planetesimals. Since the escape velocity of the largest body is proportional to its radius, the gravitational cross section increases as $A \propto R^4$ in the gravity regime. The number density of the bodies decreases as $n \propto R^{-3}$ as they collide and merge. This leads to decreased growth times with increasing particle radii (Stewart and Wetherill 1988). As a few bodies detach from the continuous size distribution, run away growth from planetesimals into 1000 km protoplanets occurs.

1.4.1 Formation of planetesimals by self-gravity

The linear stability analysis of Goldreich and Ward (1973) gives the largest wavelength $\lambda_{\rm GW}$ that is unstable to radial self-gravity modes as

$$\lambda_{\rm GW} = \frac{4\pi^2 G \Sigma_{\rm p}}{\Omega_{\rm K}^2} , \tag{1.14}$$

where G is the gravity constant, $\Sigma_{\rm p}$ is the column density of solids and $\Omega_{\rm K}$ is the Keplerian orbital frequency[1]. This expression is formally valid in the limit of vanishing particle pressure and ignores the potentially important effect of drag forces on the collapse (Youdin 2005a,b). Inserting nominal values at $r = 5\,{\rm AU}$ gives

$$\lambda_{\rm GW} \approx 1.4 \times 10^{10}\,{\rm cm} \left(\frac{M_\star}{M_\odot}\right)^{-1} \left(\frac{\Sigma_{\rm p}}{1.5\,{\rm g\,cm^{-2}}}\right) \left(\frac{r}{5\,{\rm AU}}\right)^3 . \tag{1.15}$$

[1]Safronov (1969) describes this result and its relevance to planetesimal formation as well; the critical wavelength is also derived in Toomre (1964) for the formation of giant molecular clouds.

Assuming that all the solid mass within a single unstable wavelength collapses to a single gravitationally bound solid object, the radius of the object is

$$R \approx \left(\frac{\Sigma_\mathrm{p}\xi^2\lambda_\mathrm{GW}^2}{\rho_\bullet}\right)^{1/3} \approx 50\,\mathrm{km}\,\xi^{2/3}\left(\frac{M_\star}{M_\odot}\right)^{-2/3}\left(\frac{\Sigma_\mathrm{p}}{1.5\,\mathrm{g\,cm^{-2}}}\right)\left(\frac{r}{5\,\mathrm{AU}}\right)^2\left(\frac{\rho_\bullet}{2\,\mathrm{g\,cm^{-3}}}\right)^{-1/3}, \tag{1.16}$$

where $\xi < 1$ is a parameterisation of the most unstable wavelength relative to the largest unstable wavelength. A reasonable value is $\xi = 1/2$. At $r = 1\,\mathrm{AU}$ with $\Sigma_\mathrm{p} \sim 15\,\mathrm{g\,cm^{-2}}$ one recovers the "classical" 10-km planetesimals of the Goldreich-Ward analysis. Applying on the other hand to $r = 5\,\mathrm{AU}$ with $\Sigma_\mathrm{p} \sim 1.5\,\mathrm{g\,cm^{-2}}$, planetesimals are more like 50 km, because the unstable wavelengths contain way more mass.

Formation of planetesimals by self-gravity is attractive because of the poor sticking properties of m-sized boulders (Chokshi et al. 1993; Benz 2000) and because their fast radial drift puts a severe time-scale constraint on the growth to sizes unaffected by friction. It is nevertheless a controversial theory because of its dependence on a low velocity dispersion of solids and a high local bulk density of solids (Weidenschilling 1980; Weidenschilling and Cuzzi 1993; Weidenschilling 1995). Global turbulence keeps the bulk density of solids from reaching very high values in the mid-plane. Even in a completely non-turbulent disc, which is hardly realistic since even dead zones have random gas motion and angular momentum transport (Fleming and Stone 2003), turbulence will arise due to the sedimentation of solids. The generally sub-Keplerian gas is forced by the solids in the mid-plane to move Keplerian. This vertical shear is unstable to Kelvin-Helmholtz instabilities, whose consequent turbulence stirs up the mid-plane layer and prevents sedimentation of solids. This picture nevertheless does not take into account local concentration by the streaming instability (see Chapters 6–7) which can potentially lead to a collapse of overdense particle clumps in the sedimentary layer.

1.5 Further evolution into planets

However planetesimals form, by coagulation or self-gravity or a combination of both, their gravitational focusing property helps greatly in the further progress towards protoplanets and planet cores. In the core accretion scenario for gas giant planet formation an icy/rocky core forms by accreting planetesimals and then proceeds to attract gas when the core mass reaches 10 Earth masses after approximately 500,000 years at $r = 5$ AU (Pollack et al. 1996). The next phase is a slower accretion of gas and planetesimals that lasts a few million years before the planet becomes massive enough for a run away accumulation of gas to occur (Mizuno 1980).

Pollack et al. (1996) and Hubickyj et al. (2005) find that formation times of gas giant planets can be in agreement with the life-time of the solar nebula ($\approx 10^7$yr) for a nebula with an increase in solids of 4 over the nominal minimum mass solar nebula. That is an important theoretical constraint for planetesimal formation that the column density of solids in the minimum mass solar nebula is not high enough to explain the formation of Jupiter within the life-time of the disc. A similar enhancement in solids is necessary to explain formation times of Saturn and Uranus.

The models by Pollack et al. (1996) did not include the effect of orbital migration of the planet cores. The gravitational interaction between the growing core and the disc is slightly asymmetric and the resulting torque from the disc on the planet leads to a net inward migration (Goldreich and Tremaine 1980; Ward 1997). If this type I migration is efficient, then the existence of any gas giant planets in the outer solar system is unexplained because planet embryos are lost into the central star before being able to grow large enough to open a gap. But assuming that migration is far less efficient than expected from the purely analytical approach Alibert et al. (2005) show that Jupiter and Saturn can form in a few million years, much faster than in models with no migration because the growing core keeps migrating into pristine regions where the planetesimals have not been depleted yet. Alibert et al. (2005) nevertheless still require disc masses that are 3-4 times higher than the minimum mass solar nebula. Possible physical mechanisms to stall type I migration are random torques exerted by a turbulent disc (Nelson and Papaloizou 2004) and a change in the structure of the planet wakes when treating heating and radiation transfer (Paardekooper and Mellema 2006).

1.6 Alternative formation of giant planets

Not only the solid subdisc can be gravitationally unstable – if the surface density of gas is high enough, then even the gas can contract under its own gravity (Cameron 1978). The major difference is that gas has strong pressure support that counteracts the collapse. The dispersion relation in a thin disc reads (Goldreich and Ward 1973)

$$\omega^2 = k^2 c_\mathrm{s}^2 + \Omega_\mathrm{K}^2 - 2\pi G \Sigma_\mathrm{g} k \,, \tag{1.17}$$

where ω is the complex frequency of a hydrogravity eigenmode and k is the scale of an infinitely small perturbation. Gravitational instability occurs when $\omega^2 < 0$. The first term on the right hand side is due to pressure, which stabilises the small scales, and the second due to rotation, which stabilises all scales. The destabilisation comes solely from gravity.

Solving equation (1.17) for $\omega^2 < 0$ yields the Toomre criterion (Toomre 1964) for axisymmetric instability

$$\Sigma_\mathrm{g} > \frac{c_\mathrm{s} \Omega_\mathrm{K}}{\pi G} \,. \tag{1.18}$$

For typical values of $c_\mathrm{s} = 5 \times 10^4 \,\mathrm{cm\,s^{-1}}$ and $\Omega_\mathrm{K} = 1.7 \times 10^{-8} \,\mathrm{s^{-1}}$ at $r = 5 \,\mathrm{AU}$ the limiting column density is $\Sigma_\mathrm{g} \approx 4000 \,\mathrm{g\,cm^{-2}}$, a more than 20 times higher value than at the same location in the minimum mass solar nebula. Gravitational instability in the gas and contraction into discrete planets is obtained in the models by Boss (1997) by putting 10 Jupiter masses of gas within a disc of radius 10 AU, giving a total disc mass of 10% of the mass of the Sun.

Another issue with the gravitational formation of giant planets is that contracting gas clumps heat up rapidly and need a way to cool down in order for the collapse to continue. Gammie (2001) and Rice et al. (2003) show that marginally unstable discs must cool down faster than approximately an orbital period for collapse to continue. This cooling is envisioned to take place via efficient convection in the models presented in Boss (2002). It was nevertheless

shown by Cai et al. (2006) using radiative transfer models that the cooling time of gravito-turbulence is too long to allow for condensations to occur. Also gravitational collapse does not benefit from increased amounts of solids, in opposition to the very clear trend of finding more planets around metal-rich stars (Santos et al. 2001). This statement is nevertheless challenged by Mayer et al. (2006) [see also Rice et al. (2005) and Boley et al. (2007)] who find that an increased metallicity leads to a decrease in the adiabatic index γ and thus to increased susceptibility for gravitational collapse.

Chapter 2

Dust diffusion by magnetorotational turbulence

From Johansen & Klahr (2005): The Astrophysical Journal, vol. 634, p. 1353–1371

2.1 Abstract

We measure the turbulent diffusion coefficient of dust grains embedded in magnetorotational turbulence in a protoplanetary disc directly from numerical simulations and compare it to the turbulent viscosity of the flow. The simulations are done in a local coordinate frame comoving with the gas in Keplerian rotation. Periodic boundary conditions are used in all directions, and vertical gravity is not applied to the gas. Using a two-fluid approach, small dust grains of various sizes (with friction times up to $\Omega_0\tau_{\rm f} = 0.02$) are allowed to move under the influence of friction with the turbulent gas. We measure the turbulent diffusion coefficient of the dust grains by applying an external sinusoidal force field acting in the vertical direction on the dust component only. This concentrates the dust around the mid-plane of the disc, and an equilibrium distribution of the dust density is achieved when the vertical settling is counteracted by the turbulent diffusion away from the mid-plane. Comparing with analytical expressions for the equilibrium concentration we deduce the vertical turbulent diffusion coefficient. The vertical diffusion coefficient is found to be lower than the turbulent viscosity and to have an associated vertical Schmidt number of about 1.5. A similar radial force field also allows us to measure the radial turbulent diffusion coefficient. We find a radial Schmidt number of about 0.85 and also find that the radial turbulent diffusion coefficient is around 70% higher than the vertical. As most angular momentum transport happens through magnetic Maxwell stresses, both the vertical and the radial diffusion coefficients are found to be significantly higher than suggested by the angular momentum transport by Reynolds stresses alone. We also find evidence for trapping of dust grains of intermediate friction time in turbulent eddies.

2.2 Introduction

Knowledge of the transport properties of particles embedded in a turbulent gas medium is important in many aspects of protoplanetary disc modelling. If the spatial number density distribution of dust grains in a disc is required for the model, one must know the effect of turbulent diffusion on the dust grains.

Vertical diffusion — The distribution of tiny dust grains, with radii smaller than around 100 μm, determines the observability of protoplanetary discs around young stellar objects through their contribution to the infrared parts of the spectrum. An interesting observational effect of turbulent diffusion is its influence on the vertical settling of dust grains. The settling affects the spectral energy distribution of protoplanetary discs, since flaring discs, i.e. where the scale height of the gas density increases with radial distance, have a much stronger mid- to far-infrared excess than self-shadowing discs, where the scale height after a certain distance from the protostar begins to fall with radial distance (e.g. Dullemond 2002). Recent model calculations by Dullemond and Dominik (2004) show that the vertical settling of dust grains towards the mid-plane of the disc can change an initially flaring disc into a partially self-shadowing disc, thus effecting the observability of the disc. These calculations depend – among other things – on the strength of the turbulence in the disc (the turbulent viscosity) and on the turbulent diffusion coefficient of dust grains in the direction perpendicular to the disc mid-plane. Also, Ilgner et al. (2004) recently considered the effect of vertical mixing in protoplanetary discs on the distribution of various chemical species and found the distribution to be influenced greatly by mass transport processes, again underlining the importance of vertical turbulent diffusion in the modelling of protoplanetary discs.

Radial diffusion — Crystalline silicate dust grain features observed in comet spectra are often attributed to radial mixing in the solar nebula (e.g. Hanner 1999). Silicate dust grains are formed primarily in amorphous form, but they can become crystalline if exposed to temperatures above ~ 1000 K. Such a heating can obviously have occurred in the hot inner parts of the solar nebula, whereas comets are expected to have formed in the cold outer regions of the nebula, so in this picture some radial mixing must take place between the inner and outer nebula. Gail (2001) and Bockelée-Morvan et al. (2002) consider disc models where crystallization of silicates happens in the inner, hot parts of the disc. It is found that in a few times 10^4 years the crystalline silicate fraction reaches a uniform value outside the crystallization region due to radial turbulent diffusion, and that the value can approach unity for realistic disc parameters. From high resolution observations of three protoplanetary discs, van Boekel et al. (2004) find that the inner 1-2 AU of these discs contain a higher crystalline silicate fraction than the outer 2-20 AU. This supports the theory that crystalline dust grains form in the hot inner disc and are subsequently transported to the outer disc by turbulent gas motion.

The existence of chondrules (millimeter-sized solid inclusions found in primitive meteorites, see e.g. Norton 2002) is believed to be the result of collisions and coagulation of small dust grains (Blum and Wurm 2000). The size distribution of chondrules may be explained by selective sorting in the turbulent solar nebula (Cuzzi et al. 2001). The first step in planet formation is the build-up of kilometer-sized rocky and icy planetesimals (in the planetesimal hypothesis of Safronov 1969), either from sticking or due to a gravitational instability in

the vertically settled dust layer. In the latter case, the equilibrium scale height of the dust layer is determined by the turbulent diffusion coefficient of the dust grains in the vertical direction (Cuzzi et al. 1993). An alternative planet formation hypothesis, the gravitational instability hypothesis (see Boss 2003, and references therein), states that planets form as a direct gravitational instability in the gas of a protoplanetary disc. The ability of a disc to undergo gravitational instability depends on its density and temperature structure, which is again dependent on the distribution and thus the turbulent transport of tiny dust grains.

It is a modern paradigm of protoplanetary discs that shear instabilities in the gas flow lead to turbulence, which is again responsible for such diverse effects as heating, angular momentum transport and diffusion. The actual turbulence is often parametrized in a single parameter, the turbulent viscosity (which can be non-dimensionalized into the α-value of Shakura and Sunyaev 1973). This single parameter determines both heating, angular momentum transport and diffusion. Candidates for protoplanetary disc turbulence are many. Most pronounced linear instabilities are vertical convective instability (Lin and Papaloizou 1980) and the magnetorotational instability (Balbus and Hawley 1991), although the former has proved to lead to inward rather than outward transport of angular momentum (Ryu and Goodman 1992). Other instabilities have been proposed, such as the baroclinic instability of Klahr and Bodenheimer (2003) which must be non-linear according to Klahr (2004), a linear Rossby wave instability (Li et al. 2000) and a linear stratorotational instability (Dubrulle et al. 2005; Shalybkov and Rüdiger 2005).

Today's most accepted source of turbulence is magnetorotational turbulence (MRI). For completely ionized discs, the emergence of self-sustained turbulence through the linear magnetorotational shear instability seems inevitable, both in local shearing box simulations (Brandenburg et al. 1995; Hawley et al. 1995) and in global accretion disc simulations (Armitage 1998; Arlt and Rüdiger 2001). The application of the ideal MHD equations to protoplanetary discs is only justified where the ionization fraction is relatively high (e.g. Fromang et al. 2002; Semenov et al. 2004). This may be given in the hot and dust-free inner parts of the disc, as well as away from the mid-plane of the disc and at large radial distances where the ionization is determined by cosmic ray and high energy photon penetration. In protoplanetary discs this had lead to the concept of a magnetically dead zone near the mid-plane of the disc where the ionization fraction is too low to sustain MRI. Fleming and Stone (2003) consider local shearing box simulations with a vertically dependent ionization fraction and find that some turbulent stresses are induced in the dead zone by the surrounding MRI turbulence. Thus angular momentum can be transported even in regions of the disc that are not magnetorotationally unstable.

It is often assumed that turbulent transport takes place as diffusion. For dust grains, the turbulent flux is assumed proportional to the gradient of the dust-to-gas ratio (Dubrulle et al. 1995). Such a prescription does not per se determine a certain value for the turbulent diffusion coefficient. Hence it is often parametrized to be a scalar that is equal to the turbulent viscosity of the gas for tiny grains but falls gradually for larger and larger grain sizes (Cuzzi et al. 1993; Schräpler and Henning 2004). One argument for setting the turbulent diffusion coefficient equal to the turbulent viscosity is that the radial velocity fluctuations are the base of both (non-magnetic) angular momentum transport and diffusion (Tennekes and Lumley 1972 p. 143). Such an approach is simple to use, but caution should be taken regarding its

validity, both regarding the numerical value of the turbulent diffusion coefficient and regarding the isotropy that is implicitly assumed when making it a scalar.

The validity of the whole diffusion description must also be addressed An obvious cause of concern is the presence of dust-trapping mechanisms in the turbulent gas flow. Gas turbulence and global pressure gradients, e.g. from vertical and radial stratification, are the cause of two important trapping mechanisms. Whenever the gas is pressure-supported and in force balance, the embedded dust grains feel an excess force in the opposite direction to the gas pressure gradient, since they can never be in the same force equilibrium without pressure support. The dust grains thus feel an acceleration relative to the gas. This has various effects, e.g. vertical settling of the dust layer towards the mid-plane of protoplanetary discs or inward radial drift of dust grains if there is an outwards decreasing gas pressure in the disc, a notorious problem in planet formation (Weidenschilling 1977a). The dust grains reach a terminal velocity when the friction with the gas balances out the acceleration due to the missing pressure gradient. The terminal velocity of very small dust grains is proportional to the friction time. In non-turbulent disc models only global pressure gradients are present, but in a turbulent disc local, fluctuating regions of high and low pressure are expected to occur. Then dust grains continuously move up the local pressure gradient, and this contributes to the random motion of the grains, which is responsible for turbulent diffusion. Magnetic pressure gradients actually give the same effect, as we will show analytically in Sect. 2.3.3. A local concentration of dust grains can not be described as diffusion, so one of the goals of this chapter is to test the validity of the global diffusion picture in the presence of turbulent pressure gradient trapping.

For larger dust grains, where the friction time becomes comparable to the orbital period of the disc, another important dust-trapping mechanism sets in. Stationary rotational structures in the gas (e.g. anticyclones) are given by an equilibrium between the global Coriolis force from the rotating disc and the centrifugal force of the rotating structure. As they enter such a structure, large dust grains experience a slow acceleration, due to drag forces with the gas. Rotating initially with the gas, but much slower, the Coriolis force dominates over the centrifugal force, and the dust grains are sucked into the eddy. This vortex trapping was proposed by Barge and Sommeria (1995), and has since then been subject of much theoretical investigation (e.g. Chavanis 2000; Johansen et al. 2004). The conclusions are that vortices are extremely efficient at trapping dust grains, and this efficiency may even explain how gas planets are formed before the dispersion of the gas disc (Klahr and Bodenheimer 2006). Vortex trapping would seem to be potentially even more threatening to the global diffusion description than pressure gradient trapping.

In this chapter we measure the turbulent diffusion coefficient of dust grains directly from numerical simulations of three-dimensional magnetorotational turbulence. We treat the physics of protoplanetary discs in the shearing sheet approximation, in which a local coordinate frame corotating with the disc is considered. Dust is added as an extra fluid that interacts with the gas through a drag force. The turbulent diffusion coefficient is measured by exposing the dust fluid to an external force field and then comparing the resulting dust density with analytical expressions derived with a parametrized diffusion term. By comparing the measured value to the turbulent viscosity we examine whether the two are indeed equal as is often assumed. We specifically address the question of whether the diffusion coefficient is isotropic by mea-

suring diffusion in both the vertical and the radial direction. Finally we quantify the effect of dust-trapping mechanisms on the whole diffusion picture by examining correlations between turbulent gas features and the dust-to-gas ratio.

The chapter is built up as follows. In Sect. 2.3 we describe the dynamical equations for the motion of gas and dust and the computer code that we use to solve them numerically. Then we go into details in Sect. 2.4 about how we deduce the turbulent diffusion coefficient from computer simulations by comparing the equilibrium dust density with analytical expressions. In Sect. 2.5 we describe the units and the boundary conditions of the simulations. The results are described in the following two sections; Sect. 2.6 describes the turbulent evolution of the gas while Sect. 2.7 describes the evolution of the dust, especially the measured turbulent diffusion coefficients and Schmidt numbers and the presence of dust-trapping mechanisms in the gas. Finally conclusions, discussions and some outlook to potential further investigations into the subject of turbulent diffusion of dust grains appear in Sect. 2.8.

2.3 Dynamical equations

In this section we present the dynamical equations we use for gas velocity, gas density, magnetic vector potential, dust velocity and dust density. We integrate the dynamical equations using the Pencil Code. This is a finite difference code that uses sixth order centred spatial derivatives and a third order Runge-Kutta time-stepping scheme. See Brandenburg (2003) for details on the numerical schemes and test runs. The Pencil Code solves the dynamical equations in their non-conservative form and gives very similar results to the ZEUS code for the statistical properties of MRI turbulence (see Balbus and Hawley 1998 and references therein).

The Pencil Code requires artificial diffusivity terms in the dynamical equations to stabilise the finite difference numerical scheme. For the purpose of calculating turbulent diffusion coefficients it is vital that we can reduce the artificial mass diffusion as much as possible in order to distinguish the measured turbulent diffusion from the imposed artificial diffusion. The biggest contribution to the turbulent transport of dust grains is expected to come from the fast and far moving large scales, so keeping the large scales unaffected by diffusion is important. To achieve this we use hyperdiffusivity terms in all the dynamical equations. Hyperdiffusivity involves replacing the regular diffusivity terms (involving second order derivatives) with differential operators that use higher order derivatives. This quenches unstable modes at the smallest scales of the simulation, while at the same time the large scales are kept unaffected by diffusivity. We have checked, by varying the value of the artificial diffusion coefficient, that hyperdiffusion does not have any effect on the turbulent diffusion coefficients that we measure. The use of hyperdiffusivity is discussed further in Appendix A.1. There the hyperversions that we adopt for viscosity, mass diffusion and resistivity are also presented.

In this section we also develop a method for being able to treat numerically the motion of very tiny dust grains with friction times much shorter than the computational time-step of the gas. This so-called short friction time approximation is presented and discussed in the last part of the section.

2.3.1 Gas dynamics

We consider the motion of gas and dust in the shearing sheet approximation (e.g. Goldreich and Tremaine 1978; Brandenburg et al. 1995). Here a local coordinate frame corotating with the disc at a distance r_0 from the central source of gravity is considered. The coordinate axes are defined as following. The x-axis points always away from the central gravity source, and the y-axis points in the direction of the Keplerian flow (as seen from a non-comoving frame). The z-axis points perpendicular to the disc along the direction of the angular velocity vector $\boldsymbol{\Omega}_0$ of the orbital motion. In this frame, the Keplerian flow velocity field has the linearised form $\boldsymbol{u}_0 = -\frac{3}{2}\Omega_0 x\hat{\boldsymbol{y}} \equiv u_y^{(0)}\hat{\boldsymbol{y}}$. We choose to measure velocities relative to the Keplerian flow, $\boldsymbol{u} - \boldsymbol{u}_0 \rightarrow \boldsymbol{u}$. Such a transformation introduces new shear terms in the equation of motion, but it has the advantage that the Keplerian velocity is zero everywhere. The equation of motion relative to the main shear flow in the shearing sheet approximation is

$$\frac{\partial \boldsymbol{u}}{\partial t} = -(\boldsymbol{u}\cdot\boldsymbol{\nabla})\boldsymbol{u} - u_y^{(0)}\frac{\partial \boldsymbol{u}}{\partial y} + \boldsymbol{f}(\boldsymbol{u}) - \frac{1}{\rho}\boldsymbol{\nabla}P + \frac{1}{\rho}\boldsymbol{J}\times\boldsymbol{B} + \boldsymbol{f}_\nu(\boldsymbol{u},\rho)\,. \tag{2.1}$$

The first term on the right hand side of equation (2.1) is the advection due to any velocity relative to the main shear flow, while the second term covers the advection due to the shear flow. The function $\boldsymbol{f}(\boldsymbol{u})$ is defined as

$$\boldsymbol{f}(\boldsymbol{u}) = \begin{pmatrix} 2\Omega_0 u_y \\ -\frac{1}{2}\Omega_0 u_x \\ 0 \end{pmatrix} \tag{2.2}$$

and is an effect of Coriolis force. The last three terms in equation (2.1) are the pressure gradient force, the magnetic Lorentz force (where the volume current density $\boldsymbol{J}$ is defined through Ampère's law $\boldsymbol{\nabla}\times\boldsymbol{B} = \mu_0\boldsymbol{J}$), and a hyperviscosity term based on the function $\boldsymbol{f}_\nu$ defined in equation (A.4). We ignore the effect of vertical gravity on the gas, because we are interested in the ideal case to measure the isotropy/non-isotropy of magnetorotational turbulence and the local transport properties of the gas without introducing additional isotropy-breaking effects. Ignoring the stratification effectively means that we are considering the disc close to the mid-plane where the vertical gravity is vanishing. Future work on the properties of dust diffusion in local shearing box simulations should take the vertical stratification of the disc into account.

The evolution of the gas density ρ is determined by the continuity equation

$$\frac{\partial \rho}{\partial t} = -u_y^{(0)}\frac{\partial \rho}{\partial y} - \rho\boldsymbol{\nabla}\cdot\boldsymbol{u} - \boldsymbol{u}\cdot\boldsymbol{\nabla}\rho + f_{\mathrm{D}}(\rho)\,, \tag{2.3}$$

where the first term on the right hand side is again an effect of advection due to the main shear flow. The two next terms come from the standard term $\boldsymbol{\nabla}\cdot(\rho\boldsymbol{u})$ from the continuity equation. In the last term we include artificial mass diffusion through the function f_{D} defined in equation (A.6). An isothermal equation of state is used where the pressure depends on the density as $P = c_{\mathrm{s}}^2\rho$. Here c_{s} is the constant sound speed.

The induction equation determines the evolution of the magnetic vector potential $\boldsymbol{A}$. Evolving the vector potential has the advantage over evolving the magnetic field $\boldsymbol{B} = \boldsymbol{\nabla}\times\boldsymbol{A}$ in that

it maintains a solenoidal magnetic field (i.e. $\boldsymbol{\nabla} \cdot \boldsymbol{B} = 0$) at all times. The induction equation in the shearing sheet approximation is

$$\frac{\partial \boldsymbol{A}}{\partial t} = -u_y^{(0)} \frac{\partial \boldsymbol{A}}{\partial y} + \frac{3}{2} \Omega_0 A_y \hat{\boldsymbol{x}} + \boldsymbol{u} \times \boldsymbol{B} + \boldsymbol{f}_\eta(\boldsymbol{A}) \,. \tag{2.4}$$

The first term on the right hand side of equation (2.4) is the advection due to the main shear flow, while the second is the so-called magnetic stretching term, another effect of shear (Brandenburg et al. 1995). The two last terms are the standard electromotive force and a resistivity term based on the function $\boldsymbol{f}_\eta$ defined in equation (A.8).

2.3.2 Dust dynamics

The dust grains are considered as a fluid without any pressure support. Any pressure gradient force on the dust due to collisions between dust grains and gas molecules can also be ignored since the solid density of dust grains is so large that the resulting acceleration is negligibly small.

In the fluid approach, the equation of motion for the dust velocity relative to the Keplerian flow is

$$\frac{\partial \boldsymbol{w}}{\partial t} = -(\boldsymbol{w} \cdot \boldsymbol{\nabla})\boldsymbol{w} - u_y^{(0)} \frac{\partial \boldsymbol{w}}{\partial y} + \boldsymbol{f}(\boldsymbol{w}) + \boldsymbol{f}_\nu(\boldsymbol{w}, n) - \frac{1}{\tau_\mathrm{f}}(\boldsymbol{w} - \boldsymbol{u}) + \boldsymbol{g}(x, y, z) \,. \tag{2.5}$$

The first four terms on the right hand side appear similar here as in the gas momentum equation. The last two terms in equation (2.5) are the drag force and an externally imposed force field $\boldsymbol{g}$ that we use to drive a non-zero diffusion equilibrium in the dust density. This is explained in more detail in Sect. 2.4.

We let the dust and the gas couple through a drag force proportional to, but in the opposite direction of, the velocity difference between the dust and the gas. The strength of the drag force is characterised by the friction time τ_f. Any relative motion between dust and gas is damped by the drag force with an e-folding time of τ_f. The physics of the dust grain and the gas enters in the expression of the friction time. When the mean free path of the gas molecules is larger than the dust grain radius, the dust grain is in the Epstein regime (e.g. Weidenschilling 1977a). Here the friction time of a spherical dust grain with radius $a_\bullet$ and solid density $\rho_\bullet$ can be expressed as

$$\tau_\mathrm{f} = \frac{a_\bullet \rho_\bullet}{c_\mathrm{s} \rho} \,, \tag{2.6}$$

where c_s is the sound speed in the surrounding gas and ρ is the gas density. The sound speed and the gas density are approximately constant in the unstratified and isothermal case, so we can treat τ_f as constant that depends only on the given particle radius and solid density.

Treating dust as a fluid is justified as long as the mean free path of the fluid constituents is smaller than the typical dimensions of the system. In the case of the gas, one compares the mean free path of the molecules with the thickness of the disc H_0. For the dust grains the collisions among the grains themselves are unimportant for determining a mean free path. Here the collisions with the gas molecules are the important effect. The mean free path for the

dust grains can be defined as the distance one grain has to float with respect to the gas before it has lost a significant fraction of its momentum. For a spherical grain moving with a speed w relative to the gas, this value can be determined as $\ell = w\tau_{\rm f}$. The condition for treating dust as a fluid is then that $\ell \ll H_0$. Because all motions are subsonic, we can replace w by $c_{\rm s}$ as an upper limit and get the expression $\Omega_0\tau_{\rm f} \ll 1$ for the validity of the fluid approach.

In a typical solar nebula type protoplanetary disc, the scale height is of the order of $H_0 \sim 10^{12}$ cm at $r_0 = 5\,\mathrm{AU}$, while the gas density can be taken to $\rho_0 \sim 10^{-10}\,\mathrm{g\,cm^{-3}}$ at the same radial distance. Then the connection between grain radius and dimensionless friction time is

$$a_\bullet = \Omega_0\tau_{\rm f} H_0 \frac{\rho_0}{\rho_\bullet} \sim 10^2 \Omega_0\tau_{\rm f}\,\mathrm{cm}\,. \tag{2.7}$$

This means that, as a rule of thumb, the value of the dimensionless friction time corresponds to the radius of the dust grain measured in meters.

To preserve momentum the gas should be affected by a drag force $\boldsymbol{f}_{\rm drag} = -\tau_{\rm f}^{-1}\rho_{\rm d}/\rho(\boldsymbol{u}-\boldsymbol{w})$ from the dust. Here $\rho_{\rm d}/\rho$ is the dust-to-gas ratio. We shall ignore the back-reaction drag force from the dust on the gas, because the dust-to-gas ratio is small in the early stages of a protoplanetary disc.

We represent dust mass density by the number density n of dust grains. The continuity equation for the dust number density n is

$$\frac{\partial n}{\partial t} = -u_y^{(0)}\frac{\partial n}{\partial y} - n\boldsymbol{\nabla}\cdot\boldsymbol{w} - \boldsymbol{w}\cdot\boldsymbol{\nabla}n + f_{\rm D}(n)\,, \tag{2.8}$$

where we use artificial diffusion, through the function $f_{\rm D}(n)$ defined in equation (A.6), only to stabilise the numerical scheme. By varying the value of the artificial diffusion coefficient D_3, which is defined in Appendix A.1, we have made sure that adding artificial diffusion has no effect on the measured turbulent diffusion coefficients. The value of D_3 needed to stabilise the runs are for all runs several orders of magnitude below the measured turbulent diffusion coefficient.

We now have two possibilities to solve the dust equation of motion (eq. [2.5]): For large particles, with friction times larger than the Courant time-step ($\Omega_0\tau_{\rm f} > 0.001$, see Table 2.1), we can use the explicit integration scheme from the Pencil Code. But for the smaller particle cases ($\Omega_0\tau_{\rm f} \ll 0.001$), where the friction time is much shorter than the Courant time-step, we will use the short friction time approximation, a semianalytical time integration that is presented below.

2.3.3 Short friction time approximation

The radii of dust grains observed in protoplanetary discs are often on the order of micrometers or even nanometers. The friction time of microscopic dust grains in a protoplanetary disc is very short compared to the orbital period, around a few minutes for the location of Jupiter in a typical solar nebula. That is of course not a problem for nature, but the smallest scales of computer simulations are many orders of magnitude larger than in nature, and thus the computational time-step for an explicit code such as the Pencil Code is much larger than

Table 2.1. Run parameters

Run (1)	Res (2)	$g_z^{(0)}$ (3)	$g_x^{(0)}$ (4)	$\Omega_0\tau_{\rm f}$ (5)	$a_\bullet/{\rm m}$ (6)	SFTA (7)	$\mu_3=\eta_3=D_3$ (8)
64a_z	64^3	1000	0	2×10^{-7}	2×10^{-7}	Yes	1.3×10^{-11}
64b_z	64^3	10	0	2×10^{-5}	2×10^{-5}	Yes	1.3×10^{-11}
64c_z	64^3	0.01	0	0.02	0.02	No	1.3×10^{-11}
128a_z	128^3	1000	0	2×10^{-7}	2×10^{-7}	Yes	1.3×10^{-12}
128c_z	128^3	0.01	0	0.01	0.01	No	1.3×10^{-12}
64a_x	64^3	0	1000	2×10^{-7}	2×10^{-7}	Yes	1.3×10^{-11}
64b_x	64^3	0	10	2×10^{-5}	2×10^{-5}	Yes	1.3×10^{-11}
64c_x	64^3	0	0.01	0.02	0.02	No	1.3×10^{-11}
128a_x	128^3	0	1000	2×10^{-7}	2×10^{-7}	Yes	1.3×10^{-12}
128c_x	128^3	0	0.01	0.01	0.01	No	1.3×10^{-12}
64a_ng	64^3	0	0	2×10^{-7}	2×10^{-7}	Yes	1.3×10^{-11}
64c_ng	64^3	0	0	0.02	0.02	No	1.3×10^{-11}

Note. — The first column gives the name of the run, the second the resolution, the third and fourth the vertical and radial gravity strength, the fifth column the friction time, the sixth column the corresponding grain radius in a typical solar nebula at $r_0 = 5\,{\rm AU}$, the seventh column whether we used the short friction time approximation or not, and the eighth column the value of the artificial viscosity μ_3, magnetic diffusivity η_3 and mass diffusion D_3.

the friction time of tiny dust grains. This causes a potential problem in resolving both timescales at the same time. To follow the motion of the tiniest dust grains, applying the explicit integration scheme as used in the Pencil Code, a time-step must be chosen that is at least an order of magnitude shorter than the friction time. Thus the computation time for simultaneously following the evolution of gas and dust becomes prohibitively long. One can now either use an implicit integration scheme, which would introduce further problems, and also make major changes in the code necessary, or one can use a kind of semianalytical integration scheme that works as follows.

For very short friction times, the dust is able to settle to an equilibrium velocity, where the drag force is exactly balanced by the other force terms that are present in the dust equation of motion (eq. [2.5]), on a timescale that is much shorter than the computational time-step of the gas. Thus it is possible, under a few reasonable assumptions, to solve algebraically for the terminal dust velocity as a function of gas velocity and density. To do this, we first subtract the gas equation of motion (eq. [2.1]) from the dust equation of motion (eq. [2.5]). This results in an equation for the evolution of relative velocity $\boldsymbol{w}-\boldsymbol{u}$,

$$\frac{\partial(\boldsymbol{w}-\boldsymbol{u})}{\partial t}+(\boldsymbol{w}\cdot\boldsymbol{\nabla})\boldsymbol{w}-(\boldsymbol{u}\cdot\boldsymbol{\nabla})\boldsymbol{u}+u_y^{(0)}\frac{\partial(\boldsymbol{w}-\boldsymbol{u})}{\partial y}=\boldsymbol{f}(\boldsymbol{w}-\boldsymbol{u})-\frac{1}{\tau_{\rm f}}(\boldsymbol{w}-\boldsymbol{u})+\boldsymbol{g}+\frac{1}{\rho}(\boldsymbol{\nabla}P-\boldsymbol{J}\times\boldsymbol{B})\,, \tag{2.9}$$

where the viscosity terms have been ignored since any real physical viscosity is expected to be orders of magnitude weaker than the other force terms. We now assume that the computational time-step of the gas is much longer than the friction time, $\delta t \gg \tau_{\rm f}$. Here δt will be given by the Courant criterion. This criterion determines the maximum time-step that can be taken by an explicit numerical scheme without becoming unstable. The allowed time-step gets shorter with increasing grid resolution. With the condition $\delta t \gg \tau_{\rm f}$, all terms from the gas equation of motion can be considered to be constant for the duration of the acceleration of the dust grain to its terminal velocity. This specifically also applies to the pressure gradient force and the Lorentz force that are present also in equation (2.9). Then we can search for a time-independent equilibrium solution for $\boldsymbol{w}-\boldsymbol{u}$. We expect any time-independent solution of equation (2.9) to have a dust velocity that is very close to the gas velocity, because the short friction time couples the dust velocity strongly to the gas velocity. Setting therefore $\boldsymbol{w}=\boldsymbol{u}$ in all other terms than the drag force term (this is legitimised below) leaves the algebraic equilibrium equation

$$0=-\frac{1}{\tau_{\rm f}}(\boldsymbol{w}-\boldsymbol{u})+\boldsymbol{g}+\frac{1}{\rho}(\boldsymbol{\nabla}P-\boldsymbol{J}\times\boldsymbol{B})\,. \tag{2.10}$$

Solving for $\boldsymbol{w}$ then yields

$$\boldsymbol{w}=\boldsymbol{u}+\tau_{\rm f}\left[\boldsymbol{g}+\frac{1}{\rho}(\boldsymbol{\nabla}P-\boldsymbol{J}\times\boldsymbol{B})\right]\,. \tag{2.11}$$

Reinserting this solution into equation (2.9) shows that it was reasonable to ignore all advection, shear and Coriolis terms, while keeping the friction, gravity, pressure gradient and Lorentz terms, as long as the friction time is sufficiently short.

This is the short friction time approximation. The specific form of the short friction time dust velocity approximation depends on the forces that are assumed to work on the gas and on the

dust, so equation (2.11) is only valid for the specific choice of force terms that are considered in this work. The presence of gravity in the dust velocity approximation comes from only considering gravity to work on the dust. This is is good for the purpose of measuring the turbulent diffusion coefficient, whereas in nature gravity of course affects both dust and gas. The gravity term would then drop out of the short friction time approximation, but it would reappear in the form of the vertical pressure gradient of the stratified gas. One must also take into consideration that the dust velocity in equation (2.11) is expressed as a function of the resolved part of the gas velocity only. All unresolved small scales would also contribute to the random motion of the tiny dust grains (as would Brownian motion), but the important scales for turbulent transport are the largest scales in the box, since they contribute most to the total gas velocity field.

The equilibrium dust velocity given by the short friction time approximation ensures that the relative velocity between dust and gas does not change on timescales shorter than the computational time-step. That means that if the gas is being accelerated, then the same amount of acceleration must be working on the dust, and so the relative velocity between the dust and the gas stays constant until sufficient time has passed for the pressure gradient force and the Lorentz force to change at the computational timescale.

The ith component of the Lorentz force appearing in equation (2.11) can be rewritten as

$$(\boldsymbol{J} \times \boldsymbol{B})_i = \nabla_j \left(\frac{B_i B_j}{\mu_0} - \frac{B^2}{2\mu_0} \delta_{ij} \right) , \tag{2.12}$$

where the first term in the parenthesis on the right hand side is due to magnetic pressure and the second to magnetic tension. This allows the ith component of the short friction time approximation dust velocity to be rewritten as

$$w_i = u_i + \tau_{\mathrm{f}} \left[g_i + \frac{1}{\rho} \nabla_j \left(P \delta_{ij} + \frac{B^2}{2\mu_0} \delta_{ij} - \frac{B_i B_j}{\mu_0} \right) \right] . \tag{2.13}$$

Thus dust grains move relative to the gas not only because of (additional) gravity and (missing) pressure gradient force, but also due to (missing) magnetic pressure gradient force and (missing) magnetic tension. We shall still refer to the effect as pressure gradient trapping, even though the magnetic tension term in equation (2.13) does not mimic a pressure gradient.

We must stress again that the short friction time approximation is only valid for small particles. If one considers larger bodies (e.g. > 1 mm at $r_0 = 5\,\mathrm{AU}$ in a typical solar nebula), first the Coriolis forces and then the advective transport terms can no longer be ignored. For these particles we directly integrate the dust equation of motion (eq. [2.5]) together with the other dynamical equations. With even larger objects finally the fluid approach fails as soon as $\ell > H_0$. In this case one has to apply a particle algorithm to follow the dust evolution (e.g. Klahr and Henning 1997).

2.4 Diffusion coefficient

In this section we describe how we calculate the diffusion coefficient of dust grains embedded in a turbulent gas. We do this by comparing the results of numerical simulations with analytical

solutions to the non-turbulent flow equations that include a parametrized diffusion.

If the turbulent motion of the gas and the dust has not been resolved, the continuity equation of the dust would have to incorporate an explicit diffusion term,

$$\frac{\partial n}{\partial t} = -\boldsymbol{\nabla} \cdot \left[(\boldsymbol{w} + u_y^{(0)} \hat{\boldsymbol{y}}) n - D_{\mathrm{t}} \rho \boldsymbol{\nabla} \left(\frac{n}{\rho} \right) \right] . \tag{2.14}$$

The gas flow is here assumed to be completely stationary, and the only effect of the non-resolved turbulence is through the parametrized diffusion term. The continuity equation is written in a conservative form where the diffusion flux is proportional to and in the opposite direction of the gradient of the dust-to-gas ratio. This is the way turbulent diffusion is normally assumed to act (see e.g. Dubrulle et al. 1995).

The task now is to find a way to extract D_{t} from the non-stationary turbulent motion found in computer simulations. This is only possible if $\boldsymbol{\nabla} n$ is not zero everywhere, as otherwise the diffusion coefficient does not enter equation (2.14) at all for a constant ρ. One can now either follow the time dependent diffusion of an initial dust concentration somewhere in the centre of the box or look for a time independent equilibrium solution. The first approach has the disadvantage that it is difficult to obtain good statistics, as one has always a very special distribution with a distinct wavelength, whereas the turbulence could act on all scales. Therefore we use the latter possibility and search for an equilibrium solution where we can achieve much better statistics.

We force an equilibrium solution with a non-zero dust density gradient by exposing the grains to an external force field $\boldsymbol{g}$. Depending on its specific form, this force field will eventually result in an equilibrium where the pile-up of dust grains imposed by $\boldsymbol{g}$ is balanced completely by mass diffusion in the opposite direction. By comparing the analytical expression for the equilibrium dust number density, whose only free parameter is D_{t}, to the equilibrium density obtained when the turbulence is resolved in computer simulations, we can derive the turbulent diffusion coefficient. We will often refer to the external force field simply as gravity because of the qualitative similarities to real gravity.

First the diffusion in the z-direction is considered. Here we define a vertical gravity field

$$g_z = -g_0 \sin(k_z z) , \tag{2.15}$$

where $k_z = 2\pi/L_z$ in order to have periodic boundaries in the vertical direction. Here L_z is the vertical extent of the box, and z is defined to lie in the interval between $-\frac{1}{2}L_z$ and $\frac{1}{2}L_z$. Using periodic boundary conditions demands that we use a periodic force field in order to have a periodic equilibrium solution. The gravity field defined in equation (2.15) is linear around the mid-plane, as the gravity field normally considered for thin discs also is, but away from the mid-plane it becomes zero again on the top and bottom boundaries of the box. Such a force gives a periodic dust distribution to determine the turbulent viscosity coefficient from (we will show below that the equilibrium logarithmic dust density becomes cosinusoidal with z). For a normal thin disc vertical gravity field, $g_z = -\Omega_0^2 z$, the equilibrium logarithmic dust density becomes quadratic with z, which is obviously not periodic.

To find the equilibrium dust number density, we solve now equations (2.5) and (2.14) for $\partial \boldsymbol{w}/\partial t = \partial n/\partial t = \boldsymbol{u} = w_x = w_y = 0$, $w_z = w_z(z)$ and $n = n(z)$. This yields the differential

equation system

$$0 = -w_z \frac{\partial w_z}{\partial z} - \frac{1}{\tau_\mathrm{f}} w_z - g_0 \sin(k_z z)\,, \tag{2.16}$$

$$0 = -\frac{\partial}{\partial z}\left(w_z n - D_z^{(\mathrm{t})} \frac{\partial n}{\partial z} \right)\,, \tag{2.17}$$

where we neglect the ρ-dependence in the diffusion term, because the turbulent gas density fluctuations are very small, as expected in subsonic turbulence. For any sufficiently short friction time, the advection term in equation (2.16) can be safely ignored, leaving only the algebraic equation

$$0 = -\frac{1}{\tau_\mathrm{f}} w_z - g_0 \sin(k_z z) \tag{2.18}$$

with the solution

$$w_z = -\tau_\mathrm{f} g_0 \sin(k_z z)\,. \tag{2.19}$$

Inserting equation (2.19) into equation (2.16) shows that the advection term is fully negligible for $\tau_\mathrm{f}^2 g_0 k_z \ll 1$.

The equilibrium solution to the continuity equation must now be able to continuously replace material that is being transported towards the mid-plane by new material transported away from the mid-plane by diffusion. It is seen that equation (2.17) has the general solution

$$\ln n = \frac{1}{D_z^{(\mathrm{t})}} \int w_z(z) \mathrm{d}z \tag{2.20}$$

for any integrable function $w_z(z)$. Here we have assumed that there is no net flux of dust grains $\overline{w_z} = 0$ by setting the contents of the parenthesis on the right hand side of equation (2.17) equal to zero. Inserting the equilibrium dust velocity from equation (2.19) into the integral in equation (2.20) gives the equilibrium logarithmic dust number density as

$$\ln n = \ln n_1 + \frac{\tau_\mathrm{f} g_0}{k_z D_z^{(\mathrm{t})}} \cos(k_z z)\,, \tag{2.21}$$

where $\ln n_1$ is an integration constant that corresponds physically to the logarithmic number density at $z = \pm\frac{1}{4} L_z$. The amplitude of the cosine distribution depends only on friction time, gravity strength and gravity wave number, which are all known input parameters, and the unknown value of the turbulent diffusion coefficient in the vertical direction. Thus the value of the turbulent diffusion coefficient can be determined uniquely from this amplitude.

The number density distribution in equation (2.21) is not normalized. The connection between n_1 and the column density Σ_0 is

$$\Sigma_0 = \int_{-1/2\,L_z}^{1/2\,L_z} n_1 \exp\left[\frac{\tau_\mathrm{f} g_0}{k_z D_z^{(\mathrm{t})}} \cos(k_z z) \right] \mathrm{d}z = \frac{2\pi n_1}{k_z} \frac{1}{\pi} \int_0^\pi \exp\left[\frac{\tau_\mathrm{f} g_0}{k_z D_z^{(\mathrm{t})}} \cos(k_z z) \right] \mathrm{d}(k_z z)\,, \tag{2.22}$$

where the last equality holds because the cosine function is symmetric in z. The modified Bessel function of the first kind of order m is defined as

$$I_m(x) = \frac{1}{\pi} \int_0^\pi \mathrm{e}^{x \cos\theta} \cos(m\theta) \mathrm{d}\theta\,, \tag{2.23}$$

so the connection between Σ_0 and n_1 becomes simply

$$\Sigma_0 = \frac{2\pi n_1}{k_z} I_0 \left(\frac{\tau_\mathrm{f} g_0}{k_z D_z^{(\mathrm{t})}} \right) . \tag{2.24}$$

Isolating n_1 finally yields

$$n_1 = \frac{k_z \Sigma_0}{2\pi I_0 \left(\frac{\tau_\mathrm{f} g_0}{k_z D_z^{(\mathrm{t})}} \right)} . \tag{2.25}$$

For infinite diffusion $D_z^{(\mathrm{t})} \to \infty$, the argument of the Bessel function in equation (2.25) is zero, and using $I_0(0) = 1$ from equation (2.23), we get $\Sigma_0 = n_1 L_z$. Thus $n_1 = n_0$, where n_0 is the average dust number density in the box, as expected for the special case of infinite diffusion. In the case of a finite diffusion coefficient, $n_1 \neq n_0$.

For the radial x-direction, a similar sinusoidal gravity field can be defined to give the equilibrium dust density as

$$\ln n = \ln n_1 + \frac{\tau_\mathrm{f} g_0}{k_x D_x^{(\mathrm{t})}} \cos(k_x x) , \tag{2.26}$$

formally identical to the vertical case. The derivations are given in Appendix A.2. With equations (2.21) and (2.26) we are armed with two powerful analytical expressions for the number density distribution of dust grains in diffusion equilibrium with an externally imposed force field. By comparing computer simulations of magnetorotational turbulence with these analytical results, we can extract the turbulent diffusion coefficient of the dust grains in both the vertical and the radial directions independently. The next sections describe the setup of the simulations and the results that we get.

2.5 Units and boundary conditions

We adopt non-dimensional variables by measuring velocities relative to the isothermal sound speed, $[\boldsymbol{u}] = [\boldsymbol{w}] = c_\mathrm{s}$, and densities relative to the initial density in the box, $[\rho] = \rho_0$; $[n] = n_0$. The unit of dust-to-gas ratio ϵ_d is $[\epsilon_\mathrm{d}] = \epsilon_0 = m_0 n_0 / \rho_0$, where m_0 is the mass of the individual dust grains. Time is measured in units of inverse Keplerian angular speed, $[t] = \Omega_0^{-1}$, although often stated in orbits $T = 2\pi\Omega_0^{-1}$. The unit of magnetic field is $[\boldsymbol{B}] = c_\mathrm{s}\sqrt{\mu_0 \rho_0}$. Derived from these basic units are the unit of distance $[\boldsymbol{x}] = c_\mathrm{s}\Omega_0^{-1}$ and the unit of magnetic vector potential $[\boldsymbol{A}] = c_\mathrm{s}^2 \Omega_0^{-1} \sqrt{\mu_0 \rho_0}$. The unit of turbulent viscosity and turbulent diffusion coefficient can also be derived from the basic units to be $[\nu_\mathrm{t}] = [D_\mathrm{t}] = c_\mathrm{s}^2 \Omega_0^{-1}$. In these units the turbulent viscosity and the turbulent α-value take the same numerical value.

We choose a box length of 2π in all directions. In order to keep the background shear flow subsonic at all points we choose the arbitrary normalization $\Omega_0 = 0.2$. We have checked by setting Ω_0 to unity that the evolution of the simulations indeed scale with the value of Ω_0, and thus that the scale-free diffusion coefficients and α-values are independent of the choice of Ω_0.

Periodic boundary conditions are applied in all directions. Connected points at the periodic x-boundary have a time-dependent shift as is appropriate in the shearing sheet approximation.

2.6 Evolution of gas

As an initial condition, we perturb the gas velocity components with random fluctuations of amplitude $\delta \boldsymbol{u} \sim 10^{-3}$. The toroidal component of the magnetic vector potential is perturbed by a standing cosine wave $A_y = A_0 \cos(k_x x) \cos(k_y y) \cos(k_z z)$ of amplitude $A_0 = 0.2$ and wave numbers $k_x = k_y = k_z = 1$. The resulting vertical component of the magnetic field is $B_z = -A_0 k_x \sin(k_x x) \cos(k_y y) \cos(k_z z) = B_0(x, y) \cos(k_z z)$. Such a wave is unstable to shear if k_z is sufficiently small (i.e. at sufficiently large scales). As shown by Balbus and Hawley (1991), the wave number interval for instability of the vertical magnetic field component is $0 < k_z < \sqrt{3}\Omega_0 / v_{\rm A}$, where the Alfvén speed is defined as $v_{\rm A}^2 = B_0^2/(\mu_0 \rho_0)$. For $0 < |B_0| < 0.2$, the upper limit wave number is always larger than around $k_z = \sqrt{3}$, so $k_z = 1$, the largest scale present in the simulation, is well within the unstable regime.

We run simulations in two different resolutions, 64^3 and 128^3. In Table 2.1 the parameters that are used in the different runs are listed. As there is no back-coupling from the dust on the gas, the gas evolution depends mainly on resolution, since the high resolution runs require less artificial diffusivity. The dust only affects the gas through its contribution to the computational time-step.

2.6.1 Self-sustained turbulence

Initially the magnetic and kinetic energies in the box increase, but the increase stops after around half an orbit, and then the magnetic and kinetic energies fall slowly to an equilibrium state during a transition time of around ten orbits. In the equilibrium state the turbulence is self-sustained, in the sense that energy is pumped from the gravitational field primarily into magnetic energy (via the magnetorotational instability). The Lorentz force transfers some of this magnetic energy into turbulent kinetic energy which again transfers energy back into the magnetic field in a dynamo process. Finally the energy is dissipated through resistivity and viscosity. The whole process is sketched in Brandenburg et al. (1995). Because we assume an isothermal equation of state, there is no heating of the gas due to dissipative processes.

The time evolution of kinetic energy components, magnetic energy components, and Reynolds and Maxwell stresses is shown in Fig. 2.1 for a time span of 100 orbits. All turbulence parameters are approximately constant in time, within a certain fluctuation interval, and show no sign of decaying after the steady state has set in after around ten orbits. Most of the kinetic energy (top panels) is present in the horizontal components of the velocity field, which is always measured relative to the Keplerian flow, whereas the vertical component contains a factor of two lower kinetic energy (this anisotropic trend is normal to MRI simulations, see e.g. Hawley et al. 1995). For the magnetic energy (middle panels), almost the entire energy is kept in the toroidal component of the magnetic field. The ratio between kinetic and magnetic energies stays approximately constant in time with the magnetic energy being a factor of around two higher than the kinetic energy. The Reynolds and Maxwell stresses (shown in the two bottom panels) can be converted into a turbulent viscosity and normalized to a turbulent α-value of Shakura and Sunyaev (1973). These values are shown for the different runs in the second and third columns of Table 2.2. The magnetic α-value is around a factor of four times

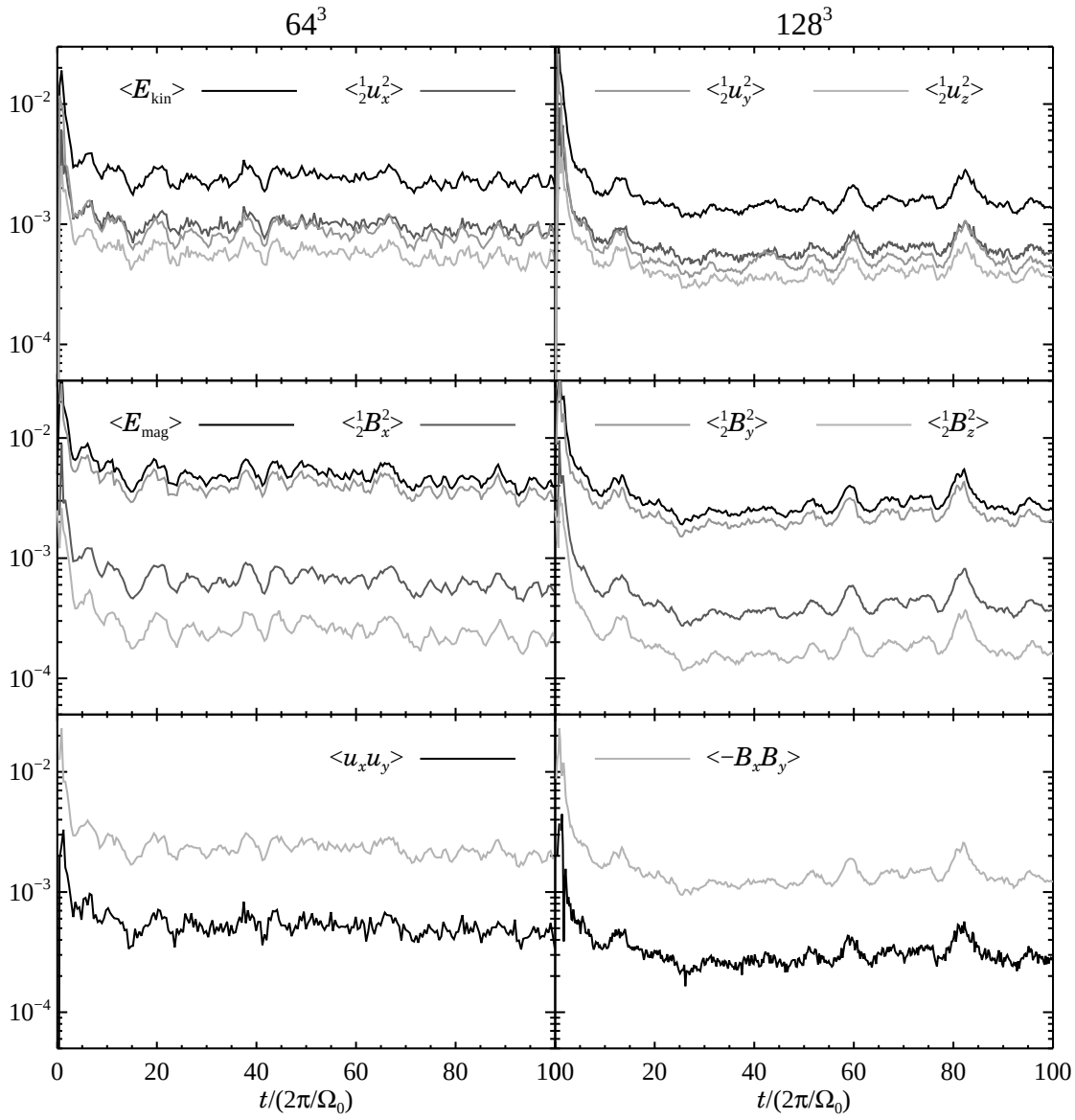

Fig. 2.1 Evolution of various turbulence parameters for a 64^3 run (left panels) and a 128^3 run (right panels). The top panels show the evolution of total kinetic energy and its directional components. The radial and toroidal directions have comparable values of kinetic energy, whereas the vertical direction has around a factor of two less. The magnetic energy (middle panels) is completely dominated by the toroidal magnetic field. The *uy* component of the Reynolds and Maxwell stresses (lower panels) is effectively a measure of the turbulent viscosity. The magnetic stresses are around four times higher than the kinetic stresses.

the non-magnetic, so most angular momentum transport happens because of magnetic fields. In the shearing sheet approximation the Keplerian background velocity is linear in space, so there is no pile-up of angular momentum anywhere in the box.

Table 2.2. Turbulent viscosities and turbulent diffusion coefficients

Run (1)	$\alpha_{\rm t}/10^{-3}$ (2)	$\alpha_{\rm t}^{\rm (mag)}/10^{-3}$ (3)	$D_z^{\rm (t)}/10^{-3}$ (4)	$D_x^{\rm (t)}/10^{-3}$ (5)	Sc_z (6)	Sc_x (7)
64a_z	0.34 ± 0.07	1.52 ± 0.27	1.18 ± 0.11	—	1.58	—
64b_z	0.34 ± 0.07	1.52 ± 0.27	1.18 ± 0.11	—	1.58	—
64c_z	0.33 ± 0.08	1.47 ± 0.29	1.12 ± 0.14	—	1.60	—
64a_x	0.34 ± 0.07	1.52 ± 0.27	—	2.07 ± 0.28	—	0.90
64b_x	0.34 ± 0.07	1.52 ± 0.27	—	2.07 ± 0.28	—	0.90
64c_x	0.33 ± 0.08	1.47 ± 0.29	—	2.12 ± 0.75	—	0.85
128a_z	0.19 ± 0.03	0.85 ± 0.12	0.82 ± 0.10	—	1.27	—
128c_z	0.19 ± 0.04	0.85 ± 0.19	0.79 ± 0.13	—	1.31	—
128a_x	0.16 ± 0.02	0.75 ± 0.10	—	1.15 ± 0.14	—	0.79
128c_x	0.18 ± 0.03	0.83 ± 0.12	—	1.27 ± 0.30	—	0.79

Note. — The first column gives the name of the run. The second and third columns show the turbulent α-values based on Reynolds and Maxwell stresses, respectively. Since there is no back-reaction from the dust on the gas, these values are only affected by the dust through the dust's contribution to the time-step. The next two columns show the measured turbulent diffusion coefficients, and in the last two columns we write the vertical and radial turbulent Schmidt numbers.

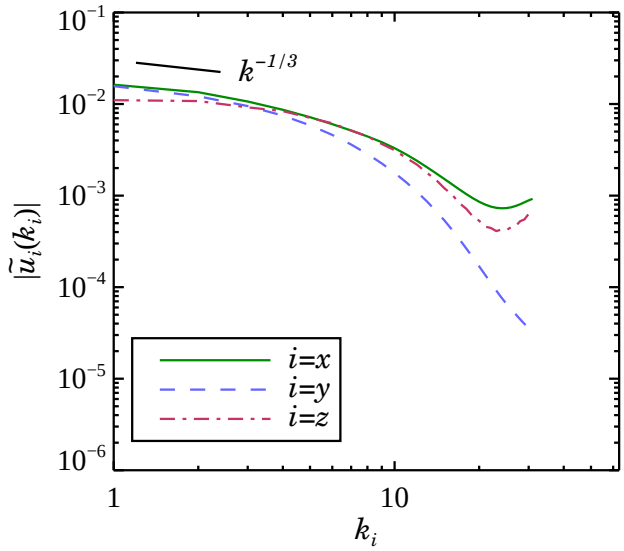

Fig. 2.2 Fourier spectrum of the velocity components of the gas for a 64^3 resolution run, averaged from 10 to 100 orbits. A Kolmogorov $k^{-1/3}$ line is shown for reference. Both the radial and the toroidal components show a Kolmogorov-like behaviour on large scales, whereas the vertical component is flatter. At small scales dissipation becomes important. The radial and vertical directions show a rise in power on the very smallest scales.

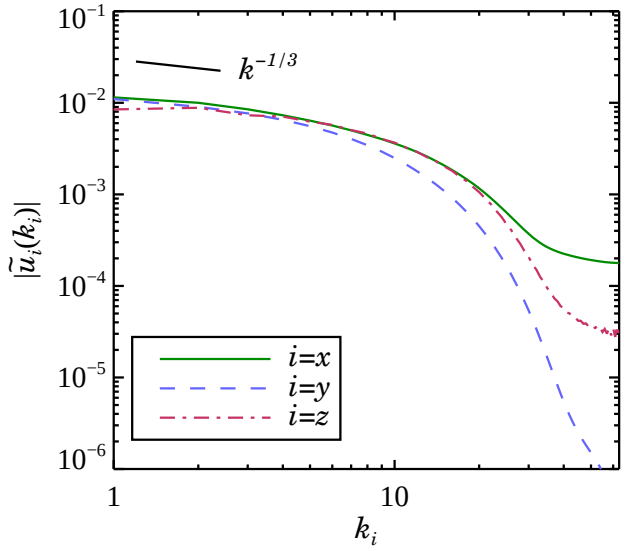

Fig. 2.3 Same as Fig. 2.2, but for a 128^3 resolution run. The vertical velocity component still has a flatter slope in the inertial range than the two other components, but the surplus power at the very smallest scale is greatly diminished compared to the 64^3 run.

The magnetorotational instability injects energy at the largest scales of the box. The smaller scales are then set in motion as the large scale motion cascades down to smaller and smaller scales. Under the assumption that there is no pile-up of kinetic energy at any scales, the Fourier spectrum should obey a Kolmogorov-law $\tilde{u}(k) \sim k^{-1/3}$. The Fourier spectra of all velocity components for 64^3 and 128^3 runs are shown in Figs. 2.2 and 2.3. For reference a $k^{-1/3}$ line is shown. The spectra are averages taken from 10 to 100 orbits. At large scales, the power spectra approximately obey a Kolmogorov law, but at smaller scales, where dissipation becomes important, the slope becomes steeper. There is some excess power at the very smallest scales, especially for the 64^3 run. This is due to unstable modes at the smallest scales of the box. Curiously the excess power is only present in the radial and vertical directions and not in the toroidal direction, but this may be an effect of the shearing out of all variables along y. The power in the small scale modes is still negligible compared to the large scales, so the rise in power does not influence the diffusion of the dust. These rises in power are typical for simulations with a low diffusivity, see e.g. Haugen et al. (2004a). According to mixing length theory, the contribution from the different length scales to the total turbulent diffusion coefficient scales as $D_k \sim \tilde{u}_k/k \sim k^{-4/3}$, so the largest scales of the box are expected to give the dominating contribution to the total turbulent diffusion coefficient.

One also sees from Figs. 2.2 and 2.3 that in both cases the vertical velocity amplitude on the large scales is smaller than the radial and toroidal velocity amplitude at large scales. This gives already a hint that vertical turbulent diffusion might be weaker than radial turbulent diffusion.

2.7 Evolution of dust

The dust is initially at rest and has a constant number density $n(x, y, z) = n_0$. It is then set free to evolve under the influence of friction with the gas and the imposed gravity field. The dust begins to concentrate near the centre of gravity (horizontal mid-plane, with $z = 0$, for vertical gravity, vertical mid-plane, with $x = 0$, for radial gravity), but eventually an equilibrium configuration is reached where the turbulent diffusion prevents further concentration. This situation is shown in Fig. 2.4 for a 128^3 run with $\Omega_0 \tau_{\rm f} = 2 \times 10^{-7}$ and vertical gravity. The run is labelled 128a_z in Table 2.1, and the friction time corresponds to tiny dust grains or molecules with radii of 0.2 micrometers in a typical solar nebula. The plot shows dust density contours at the sides of the simulation box. The turbulent motion is clearly visible, and the resulting turbulent diffusion is the only reason why there is no further settling of the dust layer towards the mid-plane. The amplitude of the concentration around the mid-plane is maintained approximately constant for the entire duration of the simulation (one hundred orbits).

2.7.1 Diffusion timescale

Before proceeding with measuring diffusion coefficients, we will first make an estimate of the time it takes to get from a constant dust density to the equilibrium where sedimentation is balanced by turbulent diffusion. We consider the case of vertical gravity. The logarithmic

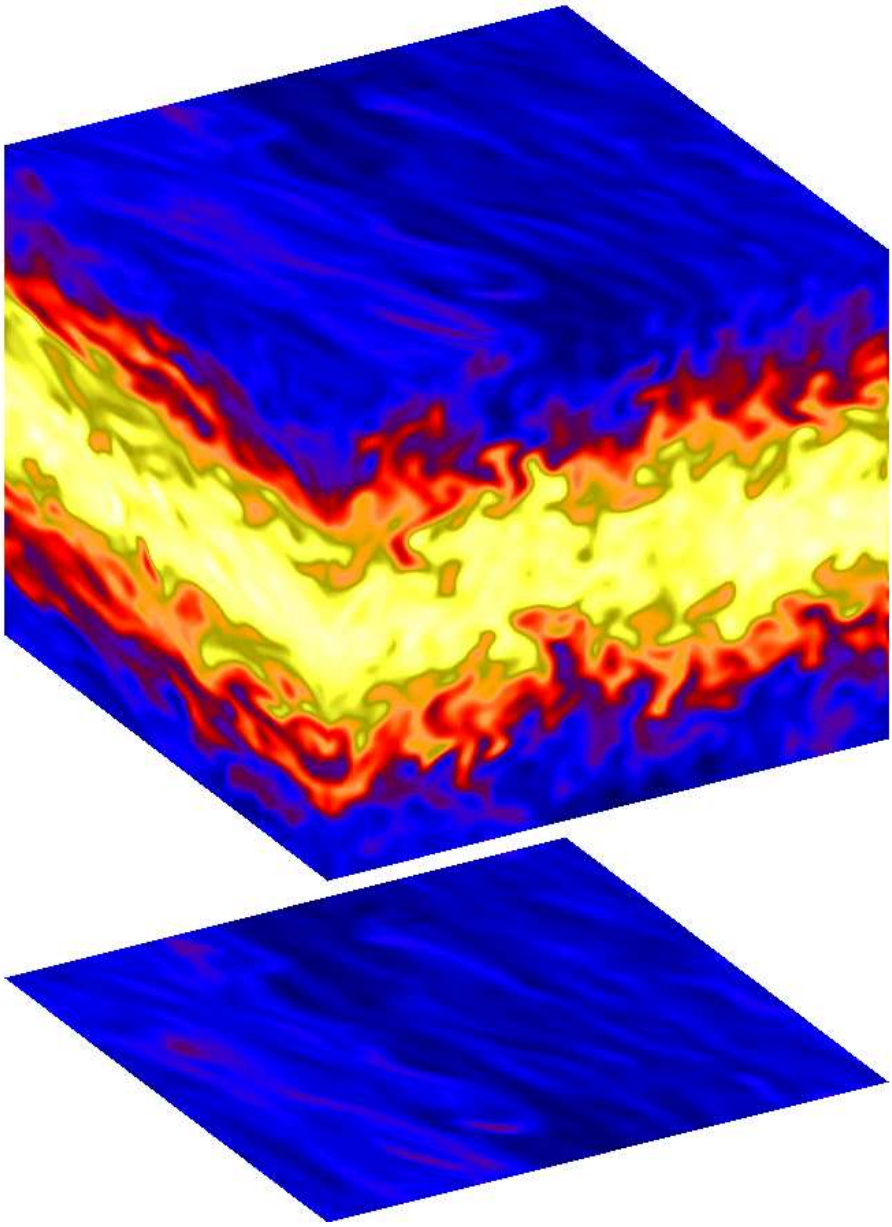

Fig. 2.4 Dust density contours at the sides of the simulation box for the short friction time run 128a_z. The radial direction is towards the right while the shearing direction is towards left. The dust is concentrated around the mid-plane due to a vertical gravity acting only on the dust. Turbulent transport alone prevents the further vertical settling of the dust layer. This configuration is statistically unchanged for at least one hundred orbits.

dust density must rise from an initial value $\ln n_0$ to the equilibrium value given by equation (2.21). When the amplitude of the equilibrium cosine function is small, $A_{\ln n} \ll 1$, then we can assume that $n_1 \approx n_0$. The increase in logarithmic dust density is then simply

$$\Delta \ln n = \frac{\tau_{\rm f} g_0}{k_z D_z^{(\rm t)}} \cos(k_z z) \,. \tag{2.27}$$

This increase is caused by the vertical sedimentation. In the short friction time approximation the dust velocity can be written as $w_z = -\tau_{\rm f} g_0 \sin(k_z z)$. The change in logarithmic dust density due to vertical settling can be approximated with the expression

$$\frac{\partial \ln n}{\partial t} = -\frac{\partial w_z}{\partial z} = k_z \tau_{\rm f} g_0 \cos(k_z z) \,. \tag{2.28}$$

Here we have ignored the advection of mass for simplicity. The diffusion timescale $t_{\rm D}$ can now be estimated by dividing equation (2.27) with equation (2.28). This yields

$$t_{\rm D} = \frac{1}{k_z^2 D_z^{(\rm t)}} \,. \tag{2.29}$$

Rewriting the diffusion coefficient in dimensionless units as $D_z^{(\rm t)} = \delta_z^{(\rm t)} c_{\rm s}^2 \Omega_0^{-1}$, the diffusion timescale can be written as $\Omega_0 t_{\rm D} = [(c_{\rm s}\Omega_0^{-1} k_z)^2 \delta_z^{(\rm t)}]^{-1}$. With $\Omega_0 = 0.2$, $k_z = 1$ and $\delta_z^{(\rm t)} = 0.002$, the diffusion timescale is around three orbits. The diffusion timescale for radial diffusion is completely equivalent to equation (2.29).

For a linear gravity field, Dullemond and Dominik (2004) derive a diffusion timescale similar to equation (2.29). On the other hand, Dubrulle et al. (1995) state a diffusion timescale of $1/(\Omega_0^2 \tau_{\rm f})$. This expression is actually a gravitational settling timescale that determines the amount of time it takes to increase the dust density in the mid-plane significantly due to gravity. Since the diffusion equilibrium sets in at very modest mid-plane overdensities for small dust grains, the timescale for such grains to reach diffusion equilibrium is much shorter than the gravitational settling timescale.

In Fig. 2.5 we plot the evolution of the logarithmic dust density averaged over the x- and y-directions for the run 64a_z. Starting at a time of zero orbits, curves are shown at two orbits time separation up to a time of ten orbits. The timescale to reach diffusion equilibrium is evidently around a few orbits (the saturated state is shown in Fig. 2.6). This is in good agreement with the analytical estimates given above.

2.7.2 Measured turbulent diffusion coefficients

We now turn to measuring the turbulent diffusion coefficient from the equilibrium configuration that is illustrated in Fig. 2.4. According to equations (2.21) and (2.26), the equilibrium logarithmic dust density should be a cosine function if diffusion is the proper description of the turbulent transport. As an example of how the vertical diffusion coefficient is measured, we show in Fig. 2.6 the logarithmic dust density averaged over the radial and toroidal directions for the run 64a_z at a time of $t = 38$ orbits. Also shown is the minimum χ^2 cosine fit (dotted line). The fit is excellent, and this shows that here the turbulent transport of the

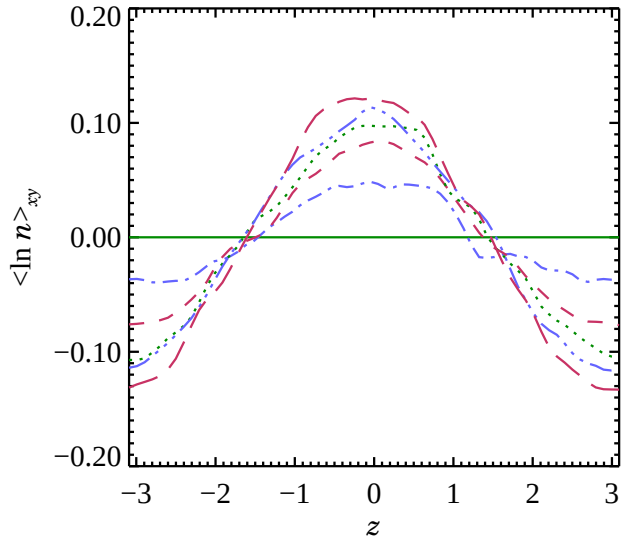

Fig. 2.5 The logarithmic dust density of the run 64a_z, averaged over x and y, at different times. The curves are each separated by two orbits going from $t = 0$ (full line) to $t = 10$ orbits (long-dashed line). The approach to equilibrium happens on a timescale of a few orbits, in good agreement with the analytical estimate of the diffusion timescale that is presented in the text.

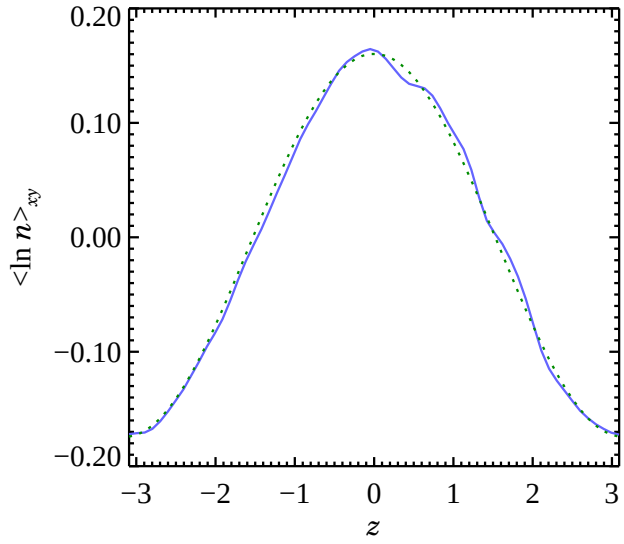

Fig. 2.6 The logarithmic dust density averaged over x and y as function of vertical height z (full line) and a cosine fit (dotted line). The cosine fit is in excellent agreement with the data. This shows that the turbulent transport is indeed well described as diffusion. Shown here is for the short friction time run 64a_z at a time of 26 orbits. The fit quality (defined in the text) is $Q \approx 0.005$.

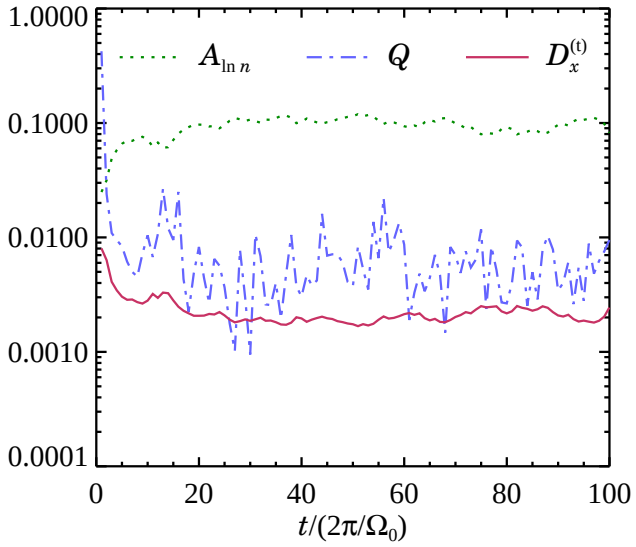

Fig. 2.7 Time evolution of the fitted cosine amplitude (dotted line), the fit quality (dash-dotted line) and the derived radial turbulent diffusion coefficient (full line) for the short friction time run 64a_x with radial gravity. Both the fit amplitude, and hence the turbulent diffusion coefficient, are approximately constant in time, although small variations are seen. The fit quality is generally excellent, but it fluctuates with around an order of magnitude during the 100 orbits shown here. Compare with Fig. 2.8 which shows the evolution of the same variables for an intermediate friction time run.

dust grains is well-described as diffusion. In Fig. 2.7 we plot, for the same run, the full time evolution of the amplitude of the best-fit cosine function and the quality of the fit, Q. The fit quality is defined as

$$Q \equiv \frac{\sum_i [\langle \ln n \rangle_{xy}(z_i) - (\ln n)_{\rm fit}(z_i)]^2}{\sum_i [\langle \ln n \rangle_{xy}(z_i)]^2} \,. \tag{2.30}$$

Here the sum is taken over the entire vertical direction and $\langle \ldots \rangle_{xy}$ is used to denote the average taken over the x- and y-directions. In Fig. 2.7 we also plot the turbulent diffusion coefficient derived from the amplitude using equation (2.21). Both the amplitude and the turbulent diffusion coefficient stay approximately constant in time. The fit quality fluctuates by more than an order of magnitude, but is generally very good (Q is less than 0.02 at all times). A similar behavior is found for all runs with short friction times, both for vertical and for radial gravity.

We have also run simulations without the short friction time approximation. Here the friction time must be at least a few times longer than the computational time-step of the gas in order to resolve the frictional acceleration in our explicit numerical scheme, but shorter than an orbital period for the fluid approach to be valid. We shall refer to such values of the friction time as intermediate friction times. Simulations with a freely evolving dust velocity serve both the purpose of showing in how far the short friction time approximation is valid, and also how the turbulent diffusion coefficient behaves when the friction time becomes larger and acceleration effects come into play. Remember that the short friction time approximation

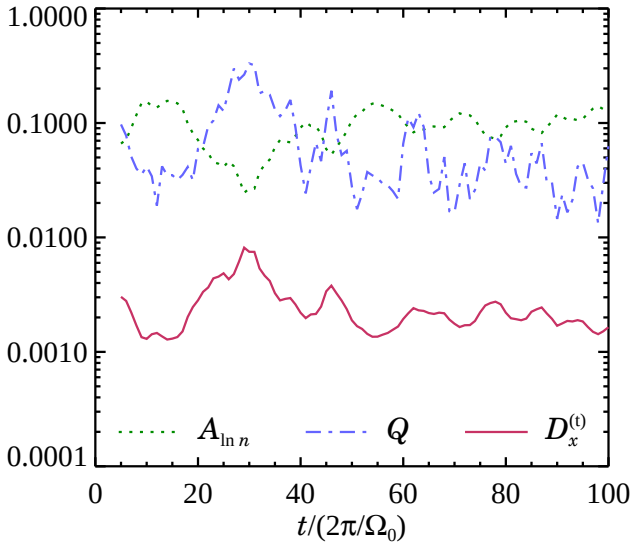

Fig. 2.8 Same as Fig. 2.7, but for the intermediate friction time run 64c_x. Obviously the cosine amplitude and the derived turbulent diffusion coefficient change much more violently with time. The fit quality is also a lot worse. The average diffusion coefficient is actually the same as for the short friction time run shown in Fig. 2.7, but the poor fit quality here means that the diffusion description of turbulent transport is not as good as it is in the short friction time runs.

assumes that the dust grains can always reach an equilibrium velocity in one computational time-step. Hence effects such as vortex trapping in turbulent eddies are not possible in the short friction time approximation. The time evolution of cosine amplitude, fit quality and turbulent diffusion coefficient for the intermediate friction time run 64c_x (with radial gravity and a friction time of $\Omega_0\tau_{\rm f} = 0.02$ corresponding to dust grains with radii of a few centimeters) is shown in Fig. 2.8. Here the amplitude changes a lot with time, and the fit quality Q rises above 0.1 on several occasions. Apparently diffusion is not at all times a good description of the turbulent transport in this run, even though the grains are still relatively well-coupled to the gas. Nevertheless, the time averaged diffusion coefficient in Fig. 2.7 and Fig. 2.8 is approximately the same as for the small grains.

The measured turbulent diffusion coefficients in the vertical and radial directions are shown in Table 2.2. In Fig. 2.9 we plot the diffusion coefficients together with the α-value based on the Reynolds stress, $\alpha_{\rm t}$, and the α-value based on the Maxwell stress, $\alpha_{\rm t}^{(\rm mag)}$. We include 1-$\sigma$ fluctuation intervals on all measurements. The radial diffusion is seen to be much stronger (around 70%) than the vertical diffusion. This is also to be expected from Fig. 2.1, since the root-mean-square of the vertical velocity component is smaller than for the horizontal components, so the velocity fluctuations in the radial direction are stronger than in the vertical direction.

From the length of the fluctuation bars in Fig. 2.9, it is clear that the fluctuations in the turbulent diffusion coefficient are very small for the short friction time limit. Combined with

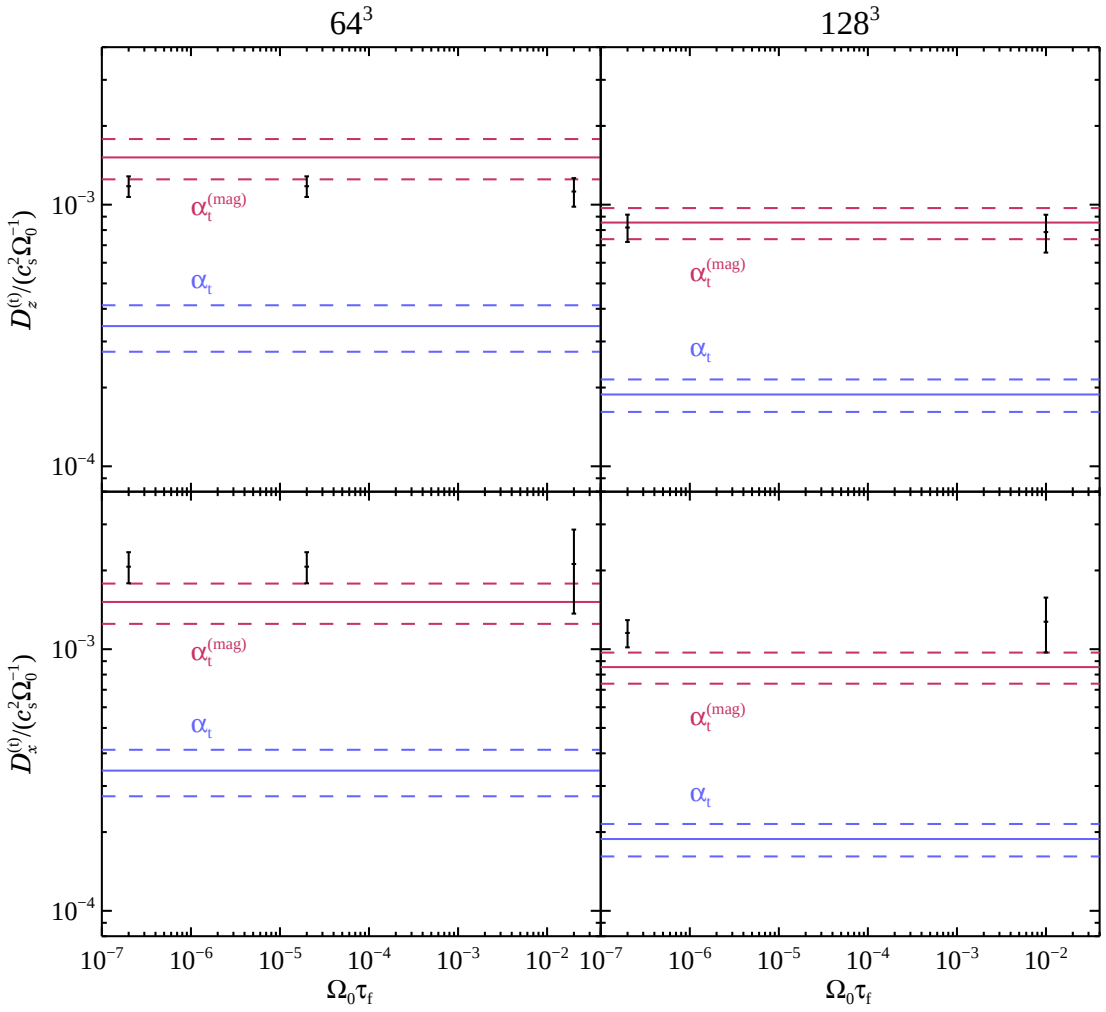

Fig. 2.9 The measured turbulent diffusion coefficient as a function of $\Omega_0\tau_f$ for a resolution of 64^3 (left panels) and 128^3 (right panels). The vertical diffusion coefficient is shown in the top panels, while the radial diffusion coefficient is shown in the bottom panels. For reference the turbulent α-values based on both the Reynolds stress and the Maxwell stress are shown including their 1-σ fluctuation intervals. The radial diffusion coefficient is comparable to the sum of the turbulent α-values and is around 70% higher than the vertical diffusion coefficient.

the fact that the quality of the cosine fit is excellent, this means that the turbulent transport in that case is well-described as diffusion. For intermediate friction times, with a freely evolving dust velocity, the fluctuation in the turbulent diffusion coefficient becomes larger, especially in the radial direction. The average values of the diffusion coefficients nevertheless stay approximately constant both for short and intermediate friction times. This gives confidence in that the short friction time approximation is indeed valid for very small dust grains.

Schmidt number

It is of great interest to compare the measured diffusion coefficients with the turbulent viscosity, since a popular parametrization of turbulent diffusion is to set the diffusion coefficient equal to the turbulent viscosity coefficient. It is seen from Table 2.2 that the vertical diffusion coefficient is generally around a factor of three to four times the non-magnetic α-value, but the value is comparable to the magnetic α-value. The radial diffusion coefficient is slightly higher than the total turbulent α-value.

We quantify the difference between the measured turbulent diffusion coefficients and the turbulent viscosity through the Schmidt number Sc. This is defined as the ratio between the turbulent viscosity and the turbulent diffusion coefficient as

$$\mathrm{Sc} = \frac{\nu_\mathrm{t}}{D_\mathrm{t}} \,. \tag{2.31}$$

For anisotropic turbulence, the Schmidt depends on the direction. Unfortunately there is no way to estimate the turbulent viscosity in the vertical direction, as there is no background shear and thus no flux of angular momentum vertically, so we shall use the value for the radial turbulent viscosity even for the vertical Schmidt .

The measured Schmidt numbers are shown in the last two columns of Table 2.2. The vertical Schmidt number is found to be above unity in the range $\mathrm{Sc}_z = 1.27 \ldots 1.60$, while the radial Schmidt number is below unity in the range $\mathrm{Sc}_x = 0.79 \ldots 0.90$ and falling with increasing resolution. This is quite surprising as Schmidt numbers smaller than one could not be expected from standard diffusion theory. It is not possible to say whether the vertical Schmidt number would be similarly low if we had scaled with the proper vertical turbulent viscosity, because this quantity is, as mentioned above, not known.

Dependence on particle size

Much analytical work has been devoted to parametrizing the dependence of the diffusion coefficient on dust particle radius (Safronov 1969; Voelk et al. 1980; Cuzzi et al. 1993; Dubrulle et al. 1995; Schräpler and Henning 2004; Reeks 2005). According to Schräpler and Henning (2004), ignoring the effect of the mean motion of the dust grains, the diffusion coefficient can be written as

$$D_\mathrm{t} = \frac{D_0}{1 + \mathrm{St}} \,. \tag{2.32}$$

Here St is the Stokes number, and the factor $1/(1 + \mathrm{St})$ determines the variation of diffusion coefficient with particle radius. The Stokes number is defined as the ratio of the friction time to the turn-over time τ_c of the largest eddies. Assuming that the rotation speed of the largest eddies as $v_\mathrm{e} = \alpha_\mathrm{t}^q c_\mathrm{s}$ and choosing $q = 0.5$, one can (following Schräpler and Henning 2004) derive the expression

$$D_\mathrm{t} = \frac{D_0}{1 + 4^{-1}\pi\Omega_0\tau_\mathrm{f}} \,. \tag{2.33}$$

Thus for the largest grains considered in this work, with $\Omega_0\tau_\mathrm{f} = 0.02$, the expected change in diffusion coefficient due to particle size is around 1.5%. This is well below the fluctuation intervals in the measurements. Our results indeed confirm that there is no apparent

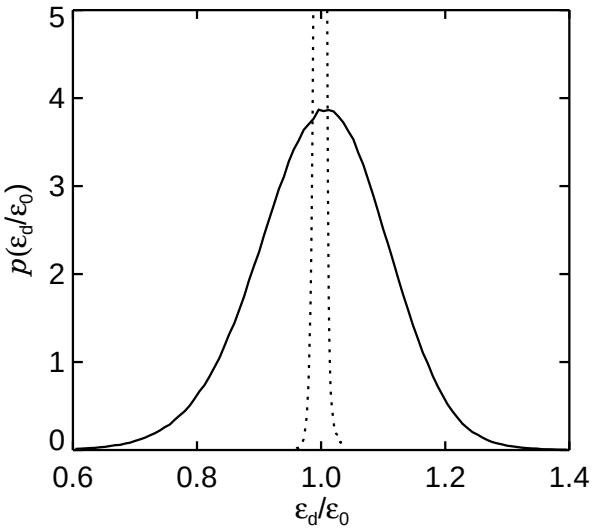

Fig. 2.10 Dust-to-gas ratio probability distribution function for runs with $\Omega_0\tau_f = 0.02$ (full line) and $\Omega_0\tau_f = 2 \times 10^{-7}$ (dotted line) without gravity on the dust. For the intermediate friction run, there is a much higher probability for very low or very high dust-to-gas ratios, compared to the short friction time run where the dust-to-gas ratio is sharply peaked around $\epsilon_d = \epsilon_0$. The full probability curve for the short friction time run is shown in Fig. 2.11.

size-dependence on the measured diffusion coefficient for our chosen grain size range. This also confirms the interpretation that the variation in the observed disc thickness at various wavelengths is due to differential settling between particles of different sizes (e.g. Dullemond and Dominik 2004) and not due to a variation in the diffusion coefficient with particle size.

2.7.3 Local dust density enhancement

To explore why the diffusion coefficient fluctuates so much in the intermediate friction time runs, we plot in Fig. 2.10 the dust-to-gas ratio probability function for an intermediate friction time run with $\Omega_0\tau_f = 0.02$ (full line) and a short friction time run with $\Omega_0\tau_f = 2\times10^{-7}$ (dotted line) for a resolution of 64^3 and no gravity. These two gravity-free runs are named 64c_ng and 64a_ng, respectively. The probability of a grid point having a dust-to-gas ratio between ϵ_d and $\epsilon_d + \Delta\epsilon_d$ is

$$p(\epsilon_d) = \frac{\Delta f(\epsilon_d)}{\Delta\epsilon_d}\,, \tag{2.34}$$

where $\Delta f(\epsilon_d)$ is the fraction of all grid points in the simulation box having a dust-to-gas ratio between ϵ_d and $\epsilon_d + \Delta\epsilon_d$. We average over 10 orbits taken equidistantly between orbits 10 and 100. According to Fig. 2.10 the probability of finding grid points with very high or very low dust-to-gas ratios is much higher in the intermediate friction time run than in the short friction time run. The dust-to-gas ratio in the short friction time run is extremely peaked around $\epsilon_d = \epsilon_0$, thus only the bottom part of the curve could be shown in Fig. 2.10. The full curve is shown in Fig. 2.11.

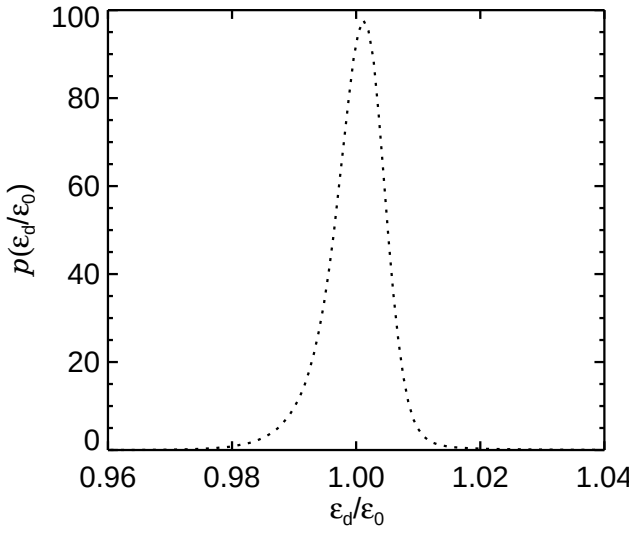

Fig. 2.11 The full dust-to-gas ratio probability distribution function for a short friction time run with $\Omega_0\tau_\mathrm{f} = 2 \times 10^{-7}$ and no gravity. Because the peak is so sharp compared to the intermediate friction time run, only the lower part is shown in Fig. 2.10.

There are two potential sources for the high dust-to-gas ratio contrast that is seen in the intermediate friction time: trapping of dust grains in turbulent vortices or trapping in regions of high pressure by pressure gradient trapping, as mentioned in the introduction. The latter effect can work also in the short friction time approximation, the first can not. According to equation (2.11), the terminal velocity of small dust grains climbing up the local pressure gradient is (we ignore gas velocity and set external gravity to zero)

$$\boldsymbol{w} = \tau_\mathrm{f}[\rho^{-1}(\boldsymbol{\nabla}P - \boldsymbol{J} \times \boldsymbol{B})]\,. \tag{2.35}$$

The evolution of the dust number density of a fluid element is controlled by the continuity equation

$$\frac{\mathrm{D}\ln n}{\mathrm{D}t} = -\boldsymbol{\nabla}\cdot\boldsymbol{w}\,, \tag{2.36}$$

where $\mathrm{D}/\mathrm{D}t \equiv \partial/\partial t + (\boldsymbol{w}\cdot\boldsymbol{\nabla})$ is the advective derivative of the flow. Combining equation (2.36) with equation (2.35) shows that dust should concentrate in regions where $\boldsymbol{\nabla}\cdot[\rho^{-1}(\boldsymbol{\nabla}P - \boldsymbol{J}\times\boldsymbol{B})] \equiv \boldsymbol{\nabla}\cdot\boldsymbol{F} < 0$ and be removed from regions where the divergence is negative. We examine whether this is the case in the two bottom panels of Fig. 2.12. Here the average dust-to-gas ratio (including 1-σ fluctuation intervals) is shown for bins in $\boldsymbol{\nabla}\cdot\boldsymbol{F}$. The left panel is for the short friction time run 64a_ng while the right panel is for the intermediate friction time run 64c_ng. For the intermediate friction time run, there is evidently some correlation between a positive divergence and a low dust-to-gas ratio and vice versa, but the correlation is not very strong.

Vortex trapping is another potential source of the dust-to-gas ratio contrast (Barge and Sommeria 1995). It can be very powerful when $\Omega_0\tau_\mathrm{f}$ is close to unity. The delayed acceleration of a dust grain entering a turbulent gas eddy causes the Coriolis force to dominate completely over the centrifugal force of the eddy. The effect of vortex trapping can be seen from the

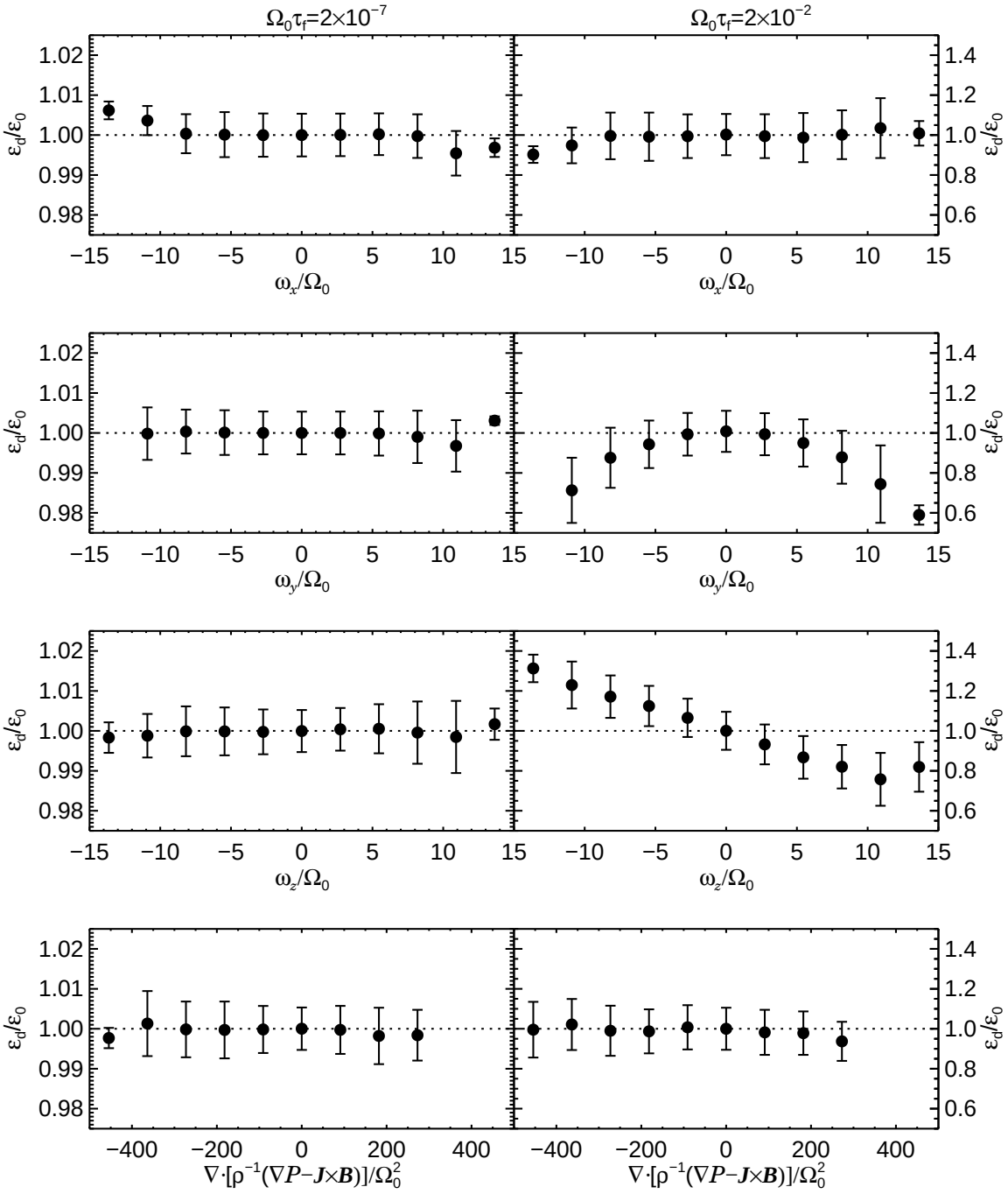

Fig. 2.12 The dust-to-gas ratio $\epsilon_{\rm d}$ in bins of vorticity components (first three rows) and divergence of pressure gradient flux (last row). The large dot shows the average dust-to-gas ratio in the bin, while the bars represent the fluctuation interval. The clearest correlation is between vertical vorticity and dust-to-gas ratio for the intermediate friction time run. This may be due to vortex trapping as explained in the text.

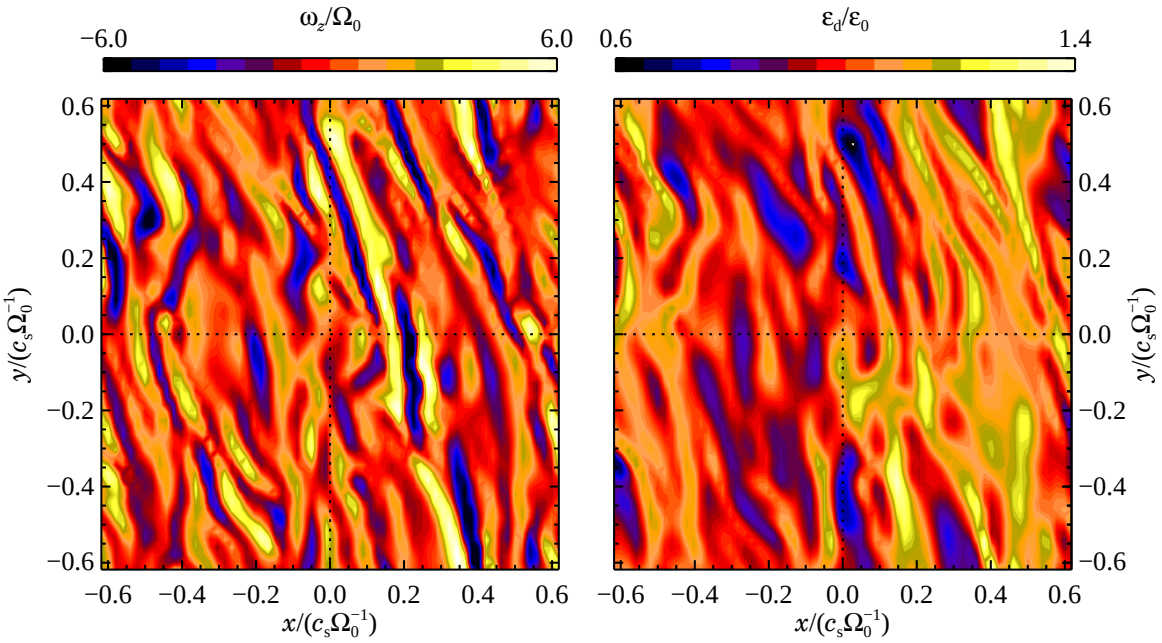

Fig. 2.13 Contour plots of vertical component of vorticity (left panel) and dust-to-gas ratio (right panel) in an arbitrary z-plane for the intermediate friction time run 64c_ng. There is a tendency for positive vorticity (light regions) to correspond to low dust-to-gas ratio (dark regions) and vice versa. This indicates that dust grains are being trapped in turbulent eddies by the vortex trapping mechanism. The dotted lines are reference lines to make comparison between the two plots easier.

vorticity $\boldsymbol{\omega} \equiv \boldsymbol{\nabla} \times \boldsymbol{u}$ of the flow. Cyclonic vortices (with positive ω_z) have an outwards directed Coriolis force relative to the centre of motion and can expel dust grains. Anticyclonic vortices (with negative ω_z) have a Coriolis force that points inwards. Such vortices can trap dust grains. As an illustration of the trapping of dust grains in turbulent features we show in Fig. 2.13 contour plots of ω_z and $\epsilon_{\rm d}$ in an arbitrarily chosen x-y-plane. The vorticity contours show patches of positive and negative vorticity. The correlation between negative vorticity and high dust-to-gas ratio (and vice versa) is clearly seen in many places. However, it is not a perfect 1:1 fit, as can also be expected in a dynamical system that is changing all the time. All concentrations are only surviving as long as a vortex exists. Turbulent eddies have a lifetime comparable to the shear time of the system, i.e. the orbital period.

It is easier to see the correlation between vertical vorticity and dust-to-gas ratio in Fig. 2.12. Here the three top rows show the correlation between dust-to-gas ratio and the three directional components of the vorticity. There is a strong correlation with vertical vorticity component ω_z for the intermediate friction time run. This is exactly as expected in case vortex trapping and expelling is the source of the number density contrast. A vertical vorticity can however also be caused by a non-rotating flow, e.g. if the gas-flow is hyper-Keplerian with a shear velocity that is linear with the radial coordinate $u_y \propto x$. Such a profile can be caused by a radial bump in the gas density. Here dust-trapping would be due to pressure gradient trapping and not due to vortex trapping.

A better test of vortex trapping than vertical vorticity can be devised by taking a closer look at the trapping mechanism (see e.g. Johansen et al. 2004). An anticyclonic vortex is in equilibrium because there is a resulting force on the gas particles pointing towards the centre of rotation. This resulting force is a vector sum of the Coriolis force, the pressure gradient force and the Lorentz force, and it works as a centripetal force that supplies just the right amount of force necessary to orbit the centre of rotation. In the fluid equations, the resulting centripetal force is balanced by the additional advection term that keeps the velocity field unchanged, even though the fluid elements themselves experience an acceleration towards the centre of rotation. Thus for anticyclonic vortices, the advection vector $-(\boldsymbol{u}\cdot\boldsymbol{\nabla})\boldsymbol{u}$ points away from the centre of rotation, while the Coriolis force $\boldsymbol{f}(\boldsymbol{u})$ points towards the centre of rotation, which is exactly in the opposite direction. The occurrence of the Coriolis force pointing in the opposite direction of the advection vector is a sufficient condition for having an anticyclonic vortex and thus vortex trapping. For a cyclonic vortex both the Coriolis force and the advection vector point away from the centre of rotation. Defining the vortex parameter $\Psi \equiv [-(\boldsymbol{u}\cdot\boldsymbol{\nabla})\boldsymbol{u}]\cdot\boldsymbol{f}(\boldsymbol{u})$, we can now recognize cyclones by a positive value of Ψ and anticyclones by a negative value of Ψ. If dust grains are affected by vortex trapping, then there should be an anticorrelation between Ψ and the dust-to-gas ratio at the locations of cyclones and anticyclones. We examine this in Fig. 2.14. It is seen that the anticorrelation between Ψ and dust-to-gas ratio is significant. This allows us to conclude that the large fluctuations in dust-to-gas ratio for the intermediate friction time runs is caused by trapping in turbulent eddies.

Curiously there is also a significant correlation between any non-zero toroidal vorticity component ω_y and a low dust-to-gas ratio for the intermediate friction time run in Fig. 2.12. This may be related to dust grains being expelled from eddies with a rotation axis parallel to the mid-plane (in the absence of gravity; when vertical gravity is included, particles can become suspended in such eddies, see Klahr and Henning 1997; Pasquero et al. 2003). However, there is no similar correlation with the radial component of vorticity ω_x, probably because the shear wipes out any depletions/concentrations on a very short timescale.

A similar search for concentrations of dust grains in MRI turbulence was performed by Hodgson and Brandenburg (1998). They find that for a frozen gas velocity field, intermediate friction time dust grains do indeed concentrate in the turbulent gas structures, but they attribute this effect to dust grains concentrating where the gas velocity field is converging rather than to vortex trapping. For an evolving gas velocity field, they find no concentration of dust. It is not clear why our results differ from these results. However, Hodgson and Brandenburg (1998) focus on concentrations of dust particles in the vertical plane, while in the current work dust concentrations are most pronounced in rotating structures in the horizontal plane.

2.8 Conclusions

The transport properties of dust grains in a turbulent accretion disc is of interest for many aspects of protoplanetary disc modelling and planet formation scenarios. In this chapter we have measured the turbulent diffusion coefficient of dust grains embedded in ideal MHD magnetorotational turbulence directly from numerical simulations. The choice of magnetorotational

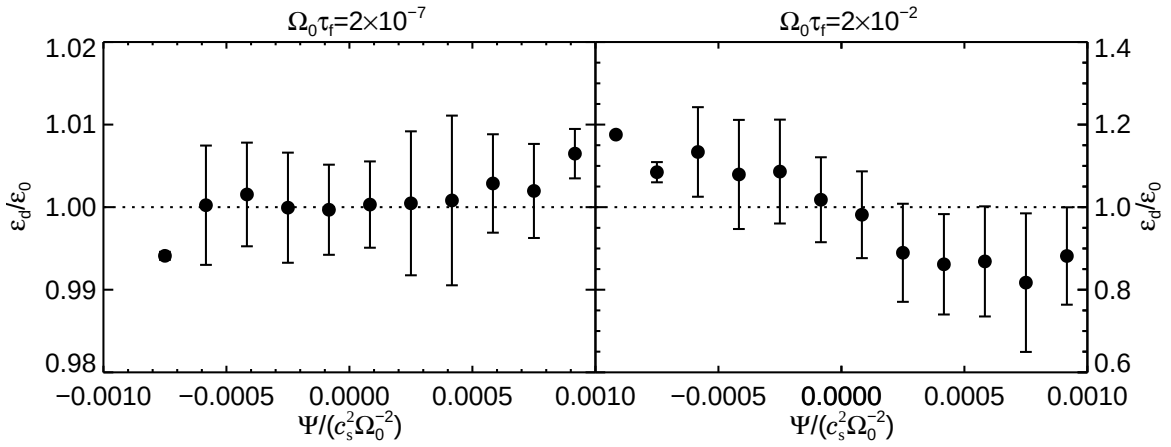

Fig. 2.14 Plot of dust-to-gas ratio in bins of vortex parameter $\Psi \equiv [-(\boldsymbol{u}\cdot\boldsymbol{\nabla})\boldsymbol{u}]\cdot\boldsymbol{f}(\boldsymbol{u})$. Anticyclonic vortices have a negative value of Ψ, whereas for cyclonic vortices Ψ is positive. For the intermediate friction time run, there is a clear anticorrelation between vortex parameter and dust-to-gas ratio. This is an indication that dust is being trapped in anticyclonic vortices.

turbulence was made because there is a growing realization that the magnetorotational instability can work at least in some parts of protoplanetary discs, even where the ionization fraction may be surprisingly low. It is also routinely produced in shearing box simulations, so it is a very accessible form of turbulence. Thus, by the use of MRI, we have a natural source of turbulence, whereas the current only other alternative for similar studies would be the use of driven turbulence in a box. The use of the ideal MHD equations can only be justified as a first approach to calculate the turbulent transport properties of dust grains. Further studies of non-ideal MHD should be made to clarify the transport properties of grains deeply embedded in the disc where the ionization fraction is low and where one is confronted with a "dead zone" around the mid-plane of the disc.

As a numerical solver we have used the Pencil Code. This finite difference code solves the non-conservative form of the dynamical equations. It is special compared to other codes in that it uses sixth order derivatives in space. The numerical scheme of the Pencil Code was stabilized using hyperdiffusivity terms in all the dynamical equations. The effect of hyperdiffusivity is to affect the large scale motion as little as possible, while at the same time quenching unstable modes at the smallest scales of the box. By varying the size of the artificial diffusion coefficient, we have found the direct influence of artificial diffusion on the measured turbulent diffusion coefficient to be negligible, most likely due to the fact that mass diffusion is primarily contributed by the fast and far moving large scales of the turbulence, and these are as mentioned affected only very little by hyperdiffusivity. From this perspective, hyperdiffusivity seems to be a tool that is well suited for measurements of turbulent transport properties.

Since we have only considered dust grains of sizes much less than one meter, the dust grains could be treated as a fluid interacting with the gas through a drag force. For the tiniest dust grains, where the friction time is much shorter than the computational time-step, we have used an algebraic equation to obtain the dust velocity at each time-step. This short friction

time approximation incorporates the tendency of dust grains to move up the local pressure gradient of the gas, an effect which we have referred to as pressure gradient trapping. It can explain such phenomena as the settling of dust grains towards the mid-plane of a stratified disc and the radial drift of dust grains in discs with a radial pressure gradient. In the current work, we have also included the effects of magnetic pressure and tension in the short friction time approximation. For intermediate friction time dust grains, where the friction time is within a few orders of magnitude of the orbital period, we have integrated the dust equation of motion together with the other dynamical equations. Here acceleration effects are allowed, in the sense that dust grains are no longer assumed to instantaneously reach a terminal velocity where the drag force is balanced by the other forces affecting the dust. The fact that the time average of the measured diffusion coefficient was approximately the same for tiny dust grains, using the short friction time approximation, and intermediate size dust grains, with a free evolution of the dust velocity, gives some credit to the validity of the short friction time approximation.

We have chosen to measure the turbulent diffusion coefficient by forcing the dust grains to settle towards a mid-plane by an external force field. This settling was eventually balanced by turbulent diffusion away from the mid-plane. To deduce the value of the turbulent diffusion coefficient, the equilibrium dust density could then be compared with an analytical solution for a parametrized diffusion coefficient. The method works not only for the vertical direction, but also for the radial direction, so that we have been able to measure both the vertical and the radial turbulent diffusion coefficients.

For the short friction time runs, the equilibrium dust number density was excellently fitted with the expected analytical solution. That means that the turbulent transport of small dust grains is well-described as diffusion. For intermediate friction times, the equilibrium dust number density was much more erratic, especially in the radial direction, and did not always give a good fit. We also found that the dust-to-gas ratio probability distribution was much wider than in the short friction time runs. To explore the reason for the large spread in dust-to-gas ratio, we have examined correlations between different parameters of the gas and the dust-to-gas ratio. A strong correlation between vertical vorticity component and dust-to-gas ratio was found. Based on this and an equally strong correlation between the sign of the vortex parameter and the dust-to-gas ratio, we conclude that the spread in dust-to-gas ratio, and thus the fluctuations in the diffusion coefficient, is due to vortex trapping in turbulent eddies (Barge and Sommeria 1995). Some weaker indications that pressure gradient trapping is taking place were also found, but similar to the results of Johansen et al. (2004), the over all dominant trapping mechanism is found to be vortex trapping. The dust-trapping that is seen in the current work happens for relatively well-coupled particles with a friction time on the order of a few percent times the shear time Ω_0^{-1}. One can speculate that for larger particles, dust-trapping mechanisms will be so efficient that the diffusion picture of turbulent transport will no longer be valid, but further investigations into the transport of larger particles will have to examine this. Such an investigation would have to incorporate dust grains as particles moving on top of the gas fluid, since the fluid description of dust grains is no longer valid when the mean free path becomes larger than the scale height of the disc.

In the vertical direction the turbulent diffusion coefficient was measured to be smaller than the total turbulent viscosity and have a Schmidt number of approximately $\mathrm{Sc}_z = 1.5$. The

diffusion coefficient is still considerably larger than the non-magnetic turbulent viscosity alone. The measured radial turbulent diffusion coefficient turned out to be almost twice as large as the vertical diffusion coefficient. It is systematically larger than the total turbulent viscosity, i.e. the sum of the non-magnetic and the magnetic turbulent viscosity, with a Schmidt number of around $\mathrm{Sc}_x = 0.85$. The value of the radial Schmidt number was found to be falling with increasing resolution. Future simulations should try to find convergence for the Schmidt numbers, but this is beyond the scope of the present work.

The anisotropy between the vertical and the radial directions should be taken into account for studies of planetesimal formation which invoke a gravitational instability in the dust sublayer. Here the onset of a gravitational instability in the vertically settled dust layer depends strongly on the effect of vertical diffusion. The amount of anisotropy can be expected to increase if the effect of vertical gravity and stratification is included (S. Fromang, personal communication), since then the buoyancy of the gas would decrease the vertical velocity fluctuations.

We want to stress that even though we find a radial Schmidt number of less than unity, the disc can still be assumed to radially transport dust grains and angular momentum about equally well. This is important for the modelling of radial mixing of dust grains and chemical species, a task which is becoming ever more relevant as more observations of the radial distribution of dust grains and molecules in protoplanetary discs become available. The result is in agreement with Yousef et al. (2003), who find for simulations of forced MHD turbulence a turbulent magnetic Prandtl number of unity. For dust grains, the equality between the radial turbulent diffusion coefficient and the turbulent viscosity is surprising, when considering that most of the angular momentum is transported by magnetic Maxwell stresses, while the dust grains have no coupling with magnetic fields at all. Following the argument of Tennekes and Lumley (1972), both angular momentum transport by Reynolds stresses and radial diffusion depend on the radial velocity fluctuations, so one would expect the non-magnetic α-value and the diffusion coefficient to be similar. The actual cause of the measured mismatch between turbulent diffusion and non-magnetic turbulent viscosity would seem to need more discussion in the future.

Chapter 3

Gravoturbulent formation of planetesimals

From Johansen, Klahr, & Henning (2006): The Astrophysical Journal, vol. 636, p. 1121–1134

3.1 Abstract

We explore the effect of magnetorotational turbulence on the dynamics and concentrations of boulders in local box simulations of a sub-Keplerian protoplanetary disc. The solids are treated as particles each with an independent space coordinate and velocity. We find that the turbulence has two effects on the solids. 1) Meter and decameter bodies are strongly concentrated, locally up to a factor 100 times the average density of solids, whereas decimeter bodies only experience a moderate density increase. The concentrations are located in large scale radial gas density enhancements that arise from a combination of turbulence and shear. 2) For meter-sized boulders, the concentrations cause the average radial drift speed to be reduced by 40%. We find that the densest clumps of solids are gravitationally unstable under physically reasonable values for the gas column density and for the solids-to-gas ratio due to sedimentation. We speculate that planetesimals can form in a solids layer that is not in itself dense enough to undergo gravitational fragmentation, and that fragmentation happens in turbulent density fluctuations in this sublayer.

3.2 Introduction

Planets are believed to form from micrometer-sized dust grains that grow by collisional sticking in protoplanetary gas discs (Safronov 1969, see reviews by Lissauer 1993 and Beckwith et al. 2000). Once the bodies reach a size of around one kilometer, the growth to Moon-sized protoplanets and later real planets is achieved by gravitationally induced collisions (Thommes et al. 2003). Although significant progress has been made in the understanding of the initial conditions of grain growth (Henning et al. 2006), we nevertheless do not yet have a complete picture of how the solids grow 27 orders of magnitude in mass to form kilometer-sized planetesimals.

Growth by coagulation can take place when there is a relative speed between the solids. Various physical effects induce relative speeds at different grain size scales. This allows for a definition of distinct steps in the growth from micrometer dust grains to meter-sized boulders in a turbulent protoplanetary disc. Microscopic dust grains gain their relative speed due to Brownian motion. This process forms relatively compact cluster-cluster aggregates (Dominik and Tielens 1997). The speed of the Brownian motion falls rapidly with increasing grain mass, and so the time-scale for building up larger compact bodies this way becomes prohibitively large, compared to the life-time of a protoplanetary disc.

When Brownian motion is no longer important, the relative speed is dominated by the differential vertical settling in the disc. The vertical component of the gravity of the central star causes the gas to be stratified. Solids do not feel the pressure gradient of the gas and thus continue to fall towards the mid-plane with a velocity given by the balance between vertical gravity and the drag force. Larger solid particles fall faster than smaller grains due to the size-dependent coupling to the gas (actually bodies that are so massive that they are starting to decouple from the gas will rather move on inclined orbits relative to the disc, i.e. perform damped oscillations around the mid-plane). As they fall, they are thus able to sweep up smaller grains in a process that is qualitatively similar to rainfall in the Earth's atmosphere. Upon arrival at the mid-plane, the largest solids can reach sizes of a few centimeters (Safronov 1969). These bodies have grown as compact particle-cluster aggregates with a high porosity.

Turbulent gas motions cause the sedimented solids to diffuse away from the mid-plane (Cuzzi et al. 1993; Dubrulle et al. 1995), where they can meet and collide with a reservoir of microscopic grains. These tiny grains still hover above the mid-plane because their sedimentation time-scale is so long that turbulent diffusion can keep them well-mixed with the gas over a large vertical extent. Turbulence also plays a role for equal-sized macroscopic bodies by inducing a relative collision speed that is much larger than the Brownian motion contribution (Voelk et al. 1980; Weidenschilling 1984).

When estimating the outcome of an interaction between macroscopic bodies, the issues of collision physics must be taken into account. For relative speeds above a certain threshold, the bodies are likely to break up when they collide rather than to stick (Chokshi et al. 1993; Blum and Wurm 2000). This is a problem for macroscopic bodies where the sticking threshold is a few meters per second. Fragmentation caused by high-speed encounters continuously replenish the reservoir of microscopic dust grains. These can then be swept up by the boulders that are lucky enough to avoid critical encounters. However, the sweeping up of smaller solid particles

by a macroscopic body has its limitations when the relative speed exceeds some 10 meter per second (Wurm et al. 2001). At larger relative velocities of up to a hundred meters per second, which are likely to occur due to the high speed of larger bodies, the small particles will erode the boulder.

The time evolution of the size-distribution of solids can be calculated by solving the coagulation equation numerically (e.g. Wetherill 1990; Weidenschilling 1997; Suttner and Yorke 2001). Recently, Dullemond and Dominik (2005) performed numerical simulations of the coagulation for realistic disc environments. Starting with micrometer-sized grains only, they find that a narrow peak of 0.1–10 meter-sized boulders can form in 10^4–10^5 years, when fragmentation is ignored. On the other hand, in a more realistic situation high speed impacts lead to fragmentation. Here Dullemond and Dominik (2005) find that once the size distribution reaches the meter regime, still around 75% of the mass is maintained in microscopic bodies, which are the fragments of larger bodies that have been destroyed in collisions. This picture is given some credit by the fact that microscopic dust grains are observed in protoplanetary discs of millions of years of age, whereas the time-scale for depleting grains of those sizes is only around 1,000 years in the absence of fragmentation.

Besides the problem of getting macroscopic bodies to stick, meter-sized boulders quickly drift radially inward toward the central star due to their aerodynamic friction with the gas in a typical sub-Keplerian disc (Weidenschilling 1977a). The drift time-scale can be as short as 100 years. To avoid evaporation in the inner disc or in the central star, the bodies must grow by least an order of magnitude in size (three orders of magnitude in mass) in a time shorter than this!

A possibility to overcome the growth obstacles was suggested independently by Safronov (1969) and by Goldreich and Ward (1973). The general idea is that boulders sediment towards the mid-plane and form a particle sublayer that undergoes a gravitational instability, forming the planetesimals in a spontaneous event (*gelation*) rather than by continuous growth (*coagulation*). The weakest point in this model is that it requires a laminar disc in order to work. Even a tiny amount of turbulence in the disc will prevent the boulders from an efficient sedimentation towards the mid-plane, and the instability will never occur (Weidenschilling and Cuzzi 1993). Thus disc turbulence had always to be avoided in order to allow for self-gravity assisted planetesimal formation. However, even in a completely laminar disc, the settled solids induce a vertical shear in the gas rotation profile (Weidenschilling 1980; Nakagawa et al. 1986). This can be unstable to a Kelvin-Helmholtz instability. The subsequent Kelvin-Helmholtz turbulence puffs up the solids layer so that the densities needed for a gravitational instability are usually not achieved, unless a solids-to-gas ratio many times higher than the solar composition is adopted (Youdin and Shu 2002).

Nevertheless, solids can reach sizes of around one meter without the help of self-gravity. In this size regime the gradual decoupling from the gas motion enables the bodies to move independently from the gas. This can cause them to be trapped in turbulent features of the gas flow. An important theoretical discovery is that meter-sized boulders are concentrated in gaseous anticyclonic vortices (Barge and Sommeria 1995; Chavanis 2000; Johansen et al. 2004). Inside such vortices the bulk density of solids can locally be enhanced to values sufficient either for enhanced coagulation or even for gravitational fragmentation. Also the radial drift of particles trapped in the vortices is significantly reduced (de la Fuente Marcos

and Barge 2001). Theoretical attention has furthermore been given to the trapping of solids in high pressure regions. Since solids do not feel pressure forces, any pressure-supported gas structure must cause solids to move in the direction of the pressure gradient (Klahr and Lin 2001; Haghighipour and Boss 2003; Klahr and Lin 2005). Recently, Rice et al. (2004) demonstrated that this can lead to large concentrations (a density increase of up to a factor 50) of meter-sized boulders in the high density spiral arms of self-gravitating discs. The same mechanism can drain millimeter-sized solids from the underdense regions around a protoplanet that is not massive enough to open a gap in the gaseous component of the disc (Paardekooper and Mellema 2004).

Giant long-lived vortices may form in protoplanetary disc due to a baroclinic instability (Klahr and Bodenheimer 2003), but the conditions for the baroclinic instability in protoplanetary discs are still not clear (Klahr 2004). Magnetorotational turbulence (MRI) on the other hand is expected to occur in all discs where the ionization fraction is sufficiently high (Gammie 1996; Fromang et al. 2002; Semenov et al. 2004). A search for concentrations of solids in magnetorotational turbulence was done by Hodgson and Brandenburg (1998) who found no apparent concentrations. On the other hand we found evidence in Chapter 2 of this thesis for centimeter-sized solids being trapped in short-lived turbulent eddies present in magnetorotational turbulence. That work was, however, limited by the fluid description of solids, i.e. the friction time must be much shorter than the orbital period, and could not handle solid particles larger than a few centimeters.

In this chapter we expand the work done in Chapter 2 by putting meter-sized solid particles, represented by real particles rather than by a fluid, into magnetorotational turbulence. We show that magnetorotational turbulence (Balbus and Hawley 1991) is not actually an obstacle to the self gravity-aided formation of planetesimals, but rather can be a vital agent to produce locally gravitational unstable regions in the solid component of the disc when the average density in solids would not allow for fragmentation. This process is very similar to the gravoturbulent fragmentation of molecular clouds into protostellar cores (Klessen et al. 2000; Padoan and Nordlund 2004).

3.3 Dynamical equations

For the purpose of treating meter-sized boulders we have adapted the Pencil Code (see also Brandenburg 2003) to include the treatment of solid bodies as particles with a freely evolving (x, y, z)-coordinate on top of the grid. This is necessary because the mean free path of the boulders, with respect to collisions with the gas molecules, is comparable to the scale height of the disc. Thus the solids component can no longer be treated as a fluid, but must be treated as particles each with a freely evolving spatial coordinate $\boldsymbol{x}_i$ and velocity vector $\boldsymbol{v}_i$. In other words, it is no longer possible to define a unique velocity field at a given point in space for the particles, because they keep a memory of their previous motion. Friction only erases this memory for small particles.

3.3.1 Drag force

The particles are coupled to the gas motion by a drag force that is proportional to the velocity difference between the particles and the gas,

$$\boldsymbol{f}_{\rm drag} = -\frac{1}{\tau_{\rm f}}(\boldsymbol{v}_i - \boldsymbol{u})\,. \tag{3.1}$$

Here $\boldsymbol{u}$ is the gas velocity at the location of particle i and $\tau_{\rm f}$ is the friction time. The friction time depends on the solid radius $a_\bullet$ and the solid density $\rho_\bullet$ as

$$\tau_{\rm f} = \frac{a_\bullet^2 \rho_\bullet}{\min(a_\bullet c_{\rm s}, \frac{9}{2}\nu)\rho}\,, \tag{3.2}$$

where ν is the molecular viscosity of the gas, $c_{\rm s}$ is the sound speed and ρ is the gas density. This expression is valid when the particle speed is much lower than the sound speed (Weidenschilling 1977a). Using the kinetic theory expression for viscosity $\nu = c_{\rm s}\lambda/2$, where λ is the mean free path of the gas molecules, the friction time can be divided into two regimes: the Epstein regime is valid when $a_\bullet < 9/4\lambda$. Here the mean free path of the gas molecules is longer than the size of the solid particle, so the gas can not form any flow structure around the object. The friction time is proportional to the solid radius in this regime. In the Stokes regime, where $a_\bullet > 9/4\lambda$, a flow field forms around the object. Now the friction time is proportional to solid radius squared, so the object decouples faster from the gas with increasing size. For an isothermal and unstratified disc, one can treat the friction time $\tau_{\rm f}$ as a constant. The distinction between the Epstein and the Stokes regime is then only important for translating the friction time into a solid radius (see end of this section).

To determine the gas velocity in equation (3.1) at the positions of the particles, we use a three-dimensional first-order interpolation scheme, using the eight grid corner points surrounding a given particle. For multiprocessor runs the particles can move freely between the spatial intervals assigned to each processor using MPI (Message Passing Interface) communication.

3.3.2 Disc model

We consider a protoplanetary disc in the shearing sheet approximation, but for a disc with a radial pressure gradient $\partial \ln P/\partial \ln r = \alpha$ (or $P \propto r^\alpha$). In the shearing sheet approximation this gradient produces a constant additional force that points radially outwards (because the pressure falls outwards). Making the variable transformation $\ln\rho \rightarrow \ln\rho + (1/r_0)\alpha x$, the standard isothermal shearing sheet equation of motion (e.g. Goldreich and Tremaine 1978) gets an extra term,

$$\frac{\partial \boldsymbol{u}}{\partial t} + (\boldsymbol{u}\cdot\boldsymbol{\nabla})\boldsymbol{u} = -2\boldsymbol{\Omega_0}\times\boldsymbol{u} + 3\Omega_0^2\boldsymbol{x} - c_{\rm s}^2\boldsymbol{\nabla}\ln\rho - c_{\rm s}^2\frac{1}{r_0}\alpha\hat{\boldsymbol{x}}\,. \tag{3.3}$$

The terms on the right-hand-side of equation (3.3) are the Coriolis force, the centrifugal force plus the radial gravity expanded to first order, and the two terms representing local and global pressure gradient. The coordinate vector (x, y, z) is measured from the comoving radial position $\boldsymbol{r}_0$ from the central source of gravity, with x pointing radially outwards and

y along the Keplerian flow. At $r = r_0$ the Keplerian frequency is Ω_0. The shearing sheet approximation is valid when all distances are much shorter than r_0. The balance between pressure gradient, centrifugal force and gravity is given for a sub-Keplerian rotation of the disc,

$$u_y^{(0)} = -\frac{3}{2}\Omega_0 x + \frac{c_{\rm s}^2}{2\Omega_0}\frac{1}{r_0}\alpha\,, \tag{3.4}$$

where the first term on the right-hand-side is the purely Keplerian rotation profile, while the second (constant) term is the adjustment due to the global pressure gradient. We now measure all velocities relative to the sub-Keplerian flow using the variable transformation $\boldsymbol{u} \rightarrow \boldsymbol{u} + \boldsymbol{u}_0$. This changes equation (3.3) into

$$\frac{\partial \boldsymbol{u}}{\partial t} + (\boldsymbol{u}\cdot\boldsymbol{\nabla})\boldsymbol{u} + u_y^{(0)}\frac{\partial \boldsymbol{u}}{\partial y} = \boldsymbol{f}(\boldsymbol{u}) - c_{\rm s}^2\boldsymbol{\nabla}\ln\rho\,. \tag{3.5}$$

Here the last term on the left-hand-side represents the advection due to the rotation of the disc relative to the centre of the box (which moves on a purely Keplerian orbit). The function $\boldsymbol{f}$ is defined as

$$\boldsymbol{f}(\boldsymbol{u}) = \begin{pmatrix} 2\Omega_0 u_y \\ -\frac{1}{2}\Omega_0 u_x \\ 0 \end{pmatrix}\,. \tag{3.6}$$

When making the same variable transformation in the equation of motion of the solid particles, there is however no global pressure gradient term to balance the extra Coriolis force imposed by the sub-Keplerian part of the motion, so the result is

$$\frac{\partial \boldsymbol{v}_i}{\partial t} = \boldsymbol{f}(\boldsymbol{v}_i) - \frac{1}{\tau_{\rm f}}(\boldsymbol{v}_i - \boldsymbol{u}) + c_{\rm s}^2\frac{1}{r_0}\alpha\hat{\boldsymbol{x}}\,. \tag{3.7}$$

The modified Coriolis force $\boldsymbol{f}$ appears again because of the presence of $x_i(t)$ in $\boldsymbol{u}_0$. The last term on the right-hand-side reflects the head wind that the solids feel when they moves through the slightly sub-Keplerian gas. The reason that the term appears in the radial component of the equation of motion is that all velocities are measured relative to the rotational velocity of the gas. A solid particle moving at zero velocity with respect to the gas thus experiences an acceleration in the radial direction.

The explicit presence of r_0 in equation (3.7) is non-standard in the shearing sheet. It may seem that the term vanishes for $r_0 \rightarrow \infty$. But this is actually not the case, since the natural timescale of the disc, Ω_0^{-1}, also depends on r_0, so that at large radii there is an immense amount of time at hand to let the tiny global pressure gradient force work. One can quantify this statement by dividing and multiplying by the scale-height H in the last term of equation (3.7) to obtain the result

$$\frac{\partial v_x^{(i)}}{\partial t} = \ldots + c_{\rm s}\Omega_0\frac{H}{r_0}\alpha\,. \tag{3.8}$$

Here $H/r_0 \equiv \xi$ is the ratio of the scale height to the orbital radius, a quantity that is below unity for thin discs. Depending on the temperature profile of a disc, the typical value of ξ is between 0.001 and 0.1. We define the pressure gradient parameter β as $\beta \equiv \alpha\xi$.

For the simulations, we adopt the following dynamical equations for gas velocity $\boldsymbol{u}$, magnetic vector potential $\boldsymbol{A}$, gas density ρ, particle velocities $\boldsymbol{v}_i$ and particle coordinates $\boldsymbol{x}_i$:

$$\begin{aligned}
\frac{\partial \boldsymbol{u}}{\partial t} + (\boldsymbol{u}\cdot\boldsymbol{\nabla})\boldsymbol{u} + u_y^{(0)}\frac{\partial \boldsymbol{u}}{\partial y} &= \boldsymbol{f}(\boldsymbol{u}) - c_{\rm s}^2\boldsymbol{\nabla}\ln\rho \\
&\quad + \frac{1}{\rho}\boldsymbol{J}\times\boldsymbol{B} + \boldsymbol{f}_\nu(\boldsymbol{u},\rho) \qquad (3.9)\\
\frac{\partial \boldsymbol{A}}{\partial t} + u_y^{(0)}\frac{\partial \boldsymbol{A}}{\partial y} &= \boldsymbol{u}\times\boldsymbol{B} \\
&\quad + \frac{3}{2}\Omega_0 A_y\hat{\boldsymbol{x}} + \boldsymbol{f}_\eta(\boldsymbol{A}) \qquad (3.10)\\
\frac{\partial \rho}{\partial t} + \boldsymbol{u}\cdot\boldsymbol{\nabla}\rho + u_y^{(0)}\frac{\partial \rho}{\partial y} &= -\rho\boldsymbol{\nabla}\cdot\boldsymbol{u} + f_{\rm D}(\rho) \qquad (3.11)\\
\frac{\partial \boldsymbol{v}_i}{\partial t} &= \boldsymbol{f}(\boldsymbol{v}_i) + c_{\rm s}\Omega_0\beta\hat{\boldsymbol{x}} \\
&\quad - \frac{1}{\tau_{\rm f}}(\boldsymbol{v}_i - \boldsymbol{u}) \qquad (3.12)\\
\frac{\partial \boldsymbol{x}_i}{\partial t} &= \boldsymbol{v}_i + u_y^{(0)}\hat{\boldsymbol{y}} \qquad (3.13)
\end{aligned}$$

The functions $\boldsymbol{f}_\nu$, $\boldsymbol{f}_\eta$ and $f_{\rm D}$ are hyperdiffusivity terms present to stabilise the finite difference numerical scheme of the Pencil Code. This is explained in more detail in Chapter 2. We shall ignore the effect of the global pressure gradient on the dynamics of the gas, since for $\xi \ll 1$ the increase in density due to the global gradient is much smaller than the average density in the box. Thus we set simply $u_y^{(0)} = -3/2\Omega_{\rm K}x$. We also ignore the contribution from the global density on the Lorentz force term in equation (3.9) and the advection of global density in equation (3.11). Furthermore we do not include vertical gravity in the simulations. This means that we solve exactly the same equations for the gas as in Chapter 2, i.e. without radial pressure stratification. The radial drift of solids then originates exclusively from the dynamical equations of the particles.

We solve the dynamical equations (3.9-3.13) for various values of the friction time and of the box size. The typical resolution is 64^3 for a box size of $1.32H$ on all sides. A similar setup was used in Chapter 2 to calculate the turbulent diffusion coefficient of solids in magnetorotational turbulence. In the present work we expand the model by letting 2,000,000 particles represent the solids. Thus the solids component is typically represented by approximately 8 particles per grid cell. We set the strength of the radial pressure gradient by the parameter $\beta = -0.04$. This would represent e.g. a disc with a global pressure gradient given by $\alpha = -1$ and a scale-height-to-radius ratio of $\xi = 0.04$, which is typical for a solar nebula model (Weidenschilling and Cuzzi 1993). We consider friction times of $\Omega_0\tau_{\rm f} = 0.1, 1, 10$. The translation from friction time into particle size depends on whether the friction force is in the Epstein or in the Stokes regime, but the two drag laws yield quite similar particle sizes in the transition regime. Thus, at the radial location of Jupiter in a typical protoplanetary disc, the friction time corresponds to particles of approximately 0.1, 1 and 10 meters in size.

The simulation parameters are given in Table 3.1. We let the boulders have random initial positions from the beginning and let them start with zero velocity.

Table 3.1. Simulation parameters

Run (1)	N (2)	$L_x \times L_y \times L_z$ (3)	$n_x \times n_y \times n_z$ (4)	n_0 (5)	$\Omega_0 \tau_\mathrm{f}$ (6)	β (7)	Δt (8)
A	2×10^6	$1.32 \times 1.32 \times 1.32$	$64 \times 64 \times 64$	7.6	1.0	-0.04	100
B	2×10^6	$1.32 \times 1.32 \times 1.32$	$64 \times 64 \times 64$	7.6	0.1	-0.04	100
C	2×10^6	$1.32 \times 1.32 \times 1.32$	$64 \times 64 \times 64$	7.6	10.0	-0.04	100
D	2×10^6	$1.32 \times 1.32 \times 1.32$	$64 \times 64 \times 64$	7.6	1.0	0.00	100
E	2×10^6	$1.32 \times 5.28 \times 1.32$	$64 \times 256 \times 64$	1.9	1.0	-0.04	24
F	2×10^6	$1.32 \times 10.56 \times 1.32$	$64 \times 512 \times 64$	1.0	1.0	-0.04	16

Note. — First column: name of run; second column: number of particles; third column: size of the box measured in scale heights; fourth column: grid dimension; fifth column: number of particles per grid cell; sixth column: friction time; seventh column: global pressure gradient parameter; eighth column: number of orbits that the simulation has run.

Table 3.2. Results

Run (1)	$\Omega_0 \tau_\mathrm{f}$ (2)	β (3)	$\max(n)$ (4)	$\overline{v_x}$ (5)	$v_x^{(\mathrm{lam})}$ (6)	$\overline{\sigma}$ (7)	$\overline{\sigma_x}$ (8)	$\overline{\sigma_y}$ (9)	$\overline{\sigma_z}$ (10)
A	1.0	-0.04	81.3	-0.0123	-0.020	0.0222	0.0162	0.0105	0.0077
B	0.1	-0.04	32.6	-0.0034	-0.004	0.0139	0.0064	0.0101	0.0052
C	10.0	-0.04	77.5	-0.0042	-0.004	0.0170	0.0115	0.0094	0.0062
D	1.0	0.00	56.5	-0.0003	0.000	0.0225	0.0165	0.0106	0.0078
F	1.0	-0.04	50.3	-0.0132	-0.020	0.0204	0.0149	0.0093	0.0066
E	1.0	-0.04	50.3	-0.0132	-0.020	0.0194	0.0140	0.0086	0.0061

Note. — First column: name of run; second column: friction time; third column: global pressure gradient parameter; fourth column: maximum particle density in units of the average density; fifth column: radial velocity averaged over space and time; sixth column: predicted radial drift in a non-turbulent disc; seventh to tenth columns: velocity dispersion averaged over space and time. Averages are taken from 5 orbits and beyond. Grid cells with 0 or 1 particles have been excluded for the calculations of velocity dispersions.

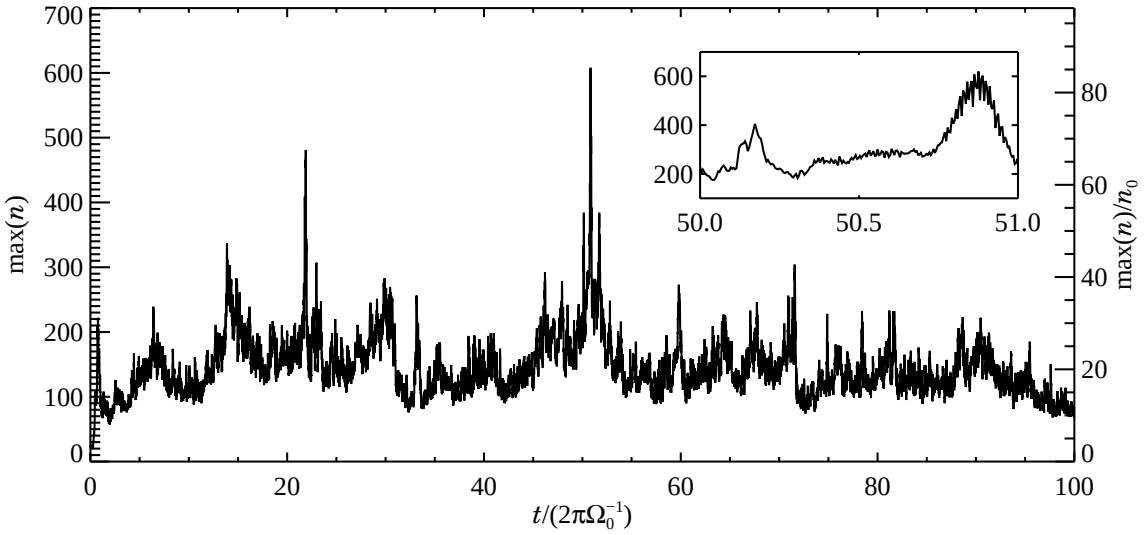

Fig. 3.1 The number of particles in the densest grid cell as a function of time for run A (meter-sized boulders). The maximum density is generally around 20 times the average, but peaks at above 80 times the average particle density. The insert shows a magnification of the time between 50 and 51 orbits.

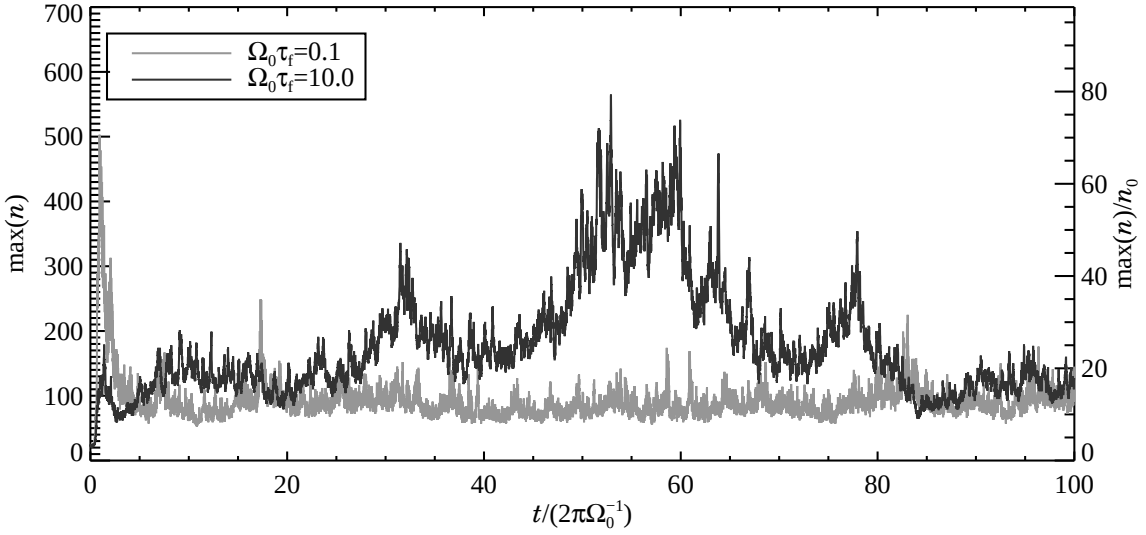

Fig. 3.2 The number of particles in the densest grid cell as a function of time, here for runs B (decimeter-sized boulders) and C (decameter-sized boulders). The first shows only very moderate overdensities, whereas the latter is similar in magnitude to run A (meter-sized boulders), but with broader peaks.

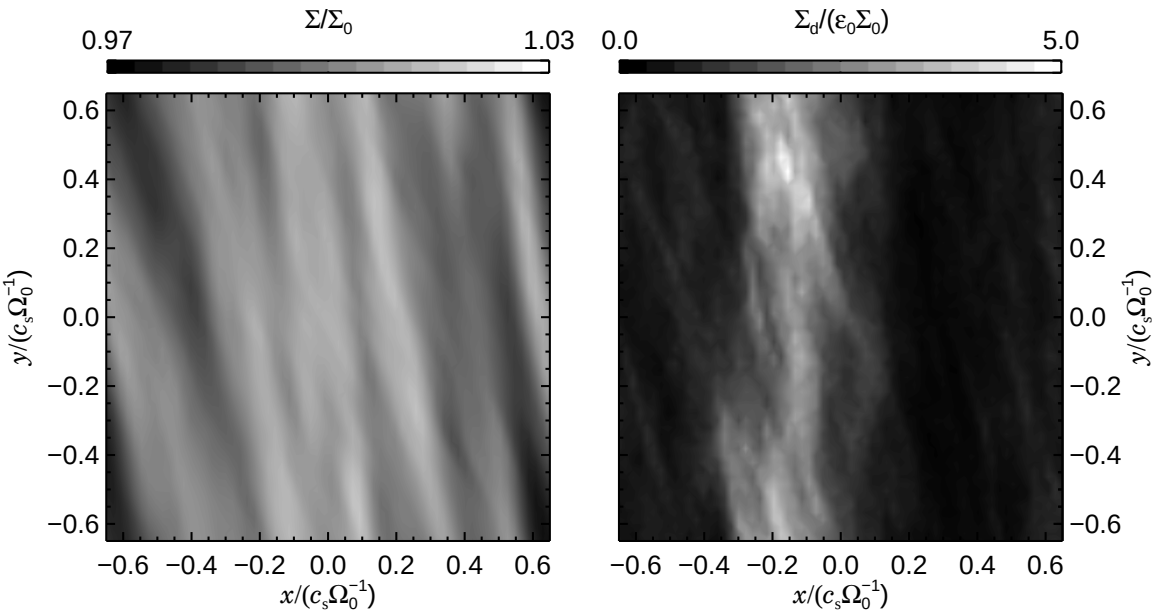

Fig. 3.3 Gas column density Σ (left panel) and solids column density $\Sigma_{\rm d}$ (right panel). The gas column density only varies by a few percent over the box, but still a slightly overdense region is seen near the centre of the box. The solids column density in the same region is up to 5 times the average solids column density.

3.4 Particle concentrations

In Fig. 3.1 we plot the number of particles in the densest grid cell as a function of time for run A (meter-sized boulders, see Table 3.1). The average number of particles per grid cell is 7.6. Evidently there is more than 100 particles in the densest grid cell at most of the times, and at some times the number is even above 600. This is more than 80 times the average number density of solids. In Fig. 3.2 we plot the maximum particle density for runs with $\Omega_0\tau_{\rm f} = 0.1$ (run B, grey curve) and $\Omega_0\tau_{\rm f} = 10$ (run C, black curve). The decimeter-sized boulders are obviously not as strongly concentrated as the meter-sized boulders, whereas the decameter-sized boulders have concentrations that are similar in magnitude to run A. The measured values of the maximum particle density for all the runs can be found in Table 3.2.

To examine whether some structures in the gas density are the source of the high particle densities, we plot in Fig. 3.3 the column densities of gas Σ and of solid particles $\Sigma_{\rm d}$ at a time of 50.9 orbits for run A. The gas column density varies only by a few percent over the box, since the turbulence is highly subsonic, but a region of moderate overdensity is seen around the middle of the box. The column density of solids is very high in about the same region as the gas overdensity, around a factor of five higher than the average column density of solids in the box, so solid particles have moved from the regions that are now underdense into the overdensity structure near the centre of the box.

We explore the radial density structure of the gas and the solids in the box in more detail

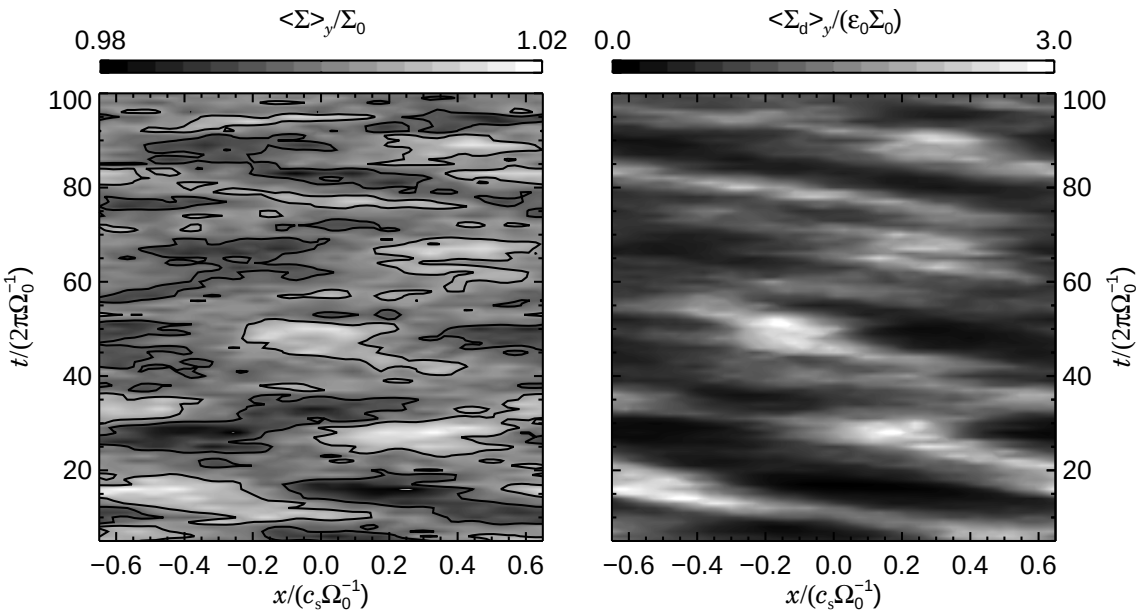

Fig. 3.4 Azimuthally averaged gas and solids column densities as a function of radial position relative to the centre of the box x and time t. Black contour lines are shown at gas density fluctuations of 0.5% from the average value. Large scale density fluctuations are seen to have lifetimes on the order of a few orbits before moving to other radial positions. The solids column density peaks strongly at the locations of the maximal gas column density.

in Fig. 3.4. Here the azimuthally averaged gas and solids column densities are shown as a function of radial position x and time t measured in orbits. Apparently large scale gas density fluctuations live for a few orbits at a constant radial position before decaying and reappearing at another radial position. The fluctuation strength is less than 1% of the average density. The bulk density of solids shows strong peaks at the locations of the gas density maxima. The explanation for this correlation is as follows. Locations of maximal gas density are also local pressure maxima. Such pressure maxima can trap solids (Klahr and Lin 2001; Haghighipour and Boss 2003) as they are locations of Keplerian gas motion. The inner edge of a pressure maximum must move faster than the Keplerian speed because the pressure gradient mimics an additional radial gravity. At the outer edge of a radial pressure enhancement the outwards-directed pressure gradient mimics a decreased gravity, and the gas must move slower than the Keplerian speed. Solid particles do not feel the pressure gradient and are thus forced to move into the pressure bump. In our simulations the radial gas overdensities have a typical lifetime at a given radial position on the order of a few orbits. When the gas overdensity eventually disappears, the particle overdensity is only slowly getting dissolved, and the particles drift and concentrate towards the location of the next gas overdensity. The gas density structure in the azimuthal and vertical directions does not show a similar density increase, and as expected there is also no significant concentration of particles with respect to these two directions. The density fluctuations thus have the form of two-dimensional sheets.

In Fig. 3.5 we plot the maximum density experienced by a 200 particle subset of the 2,000,000 particles during the 100 orbits. The distribution function $\xi(n)$ is defined as the fraction of

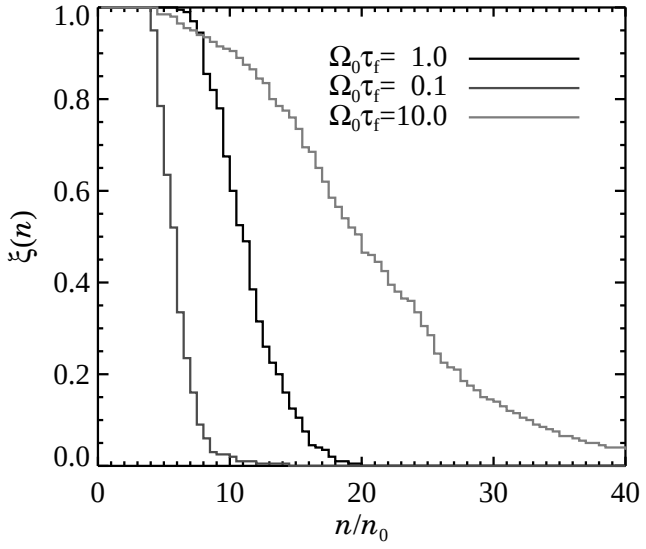

Fig. 3.5 Distribution of maximum particle densities. The curves show the fraction $\xi(n)$ of particles that have been part of a given particle density during the 100 orbits. For $\Omega_0\tau_\mathrm{f} = 0.1$, only concentrations up to 10 are common, whereas for $\Omega_0\tau_\mathrm{f} = 1$, 70% of the particles have experienced at least a 10 times increase in density and 2% even a 20 times increase. For massive boulders with $\Omega_0\tau_\mathrm{f} = 10$, more than 10% were part of a 30 times increase in density.

particles that have been the centre of a number density of at least n over the size of a grid cell. The curves clearly show how large the concentrations are. For decimeter-sized boulders, 95% of them have experienced a 5 times increase in bulk density, whereas only around 2% have been part of a 10 times increase. For meter-sized particles, 70% have been part of a 10 times increase in bulk density, and 1% even took part in a 20 times increase. Particles of decameter-size had more than 10% taking part in a 30 times increase of bulk density. This is very similar to the concentrations that Rice et al. (2004) find in the spiral arms of self-gravitating discs.

In Fig. 3.6 correlations between gas flow and particle density are shown for run D (without global pressure gradient). Here we have taken data at every full orbit, starting at 5 orbits when the turbulence has saturated, and calculated the average particle density in bins of various gas parameters. We also plot the spread in the particle density in each bin. The top two panels show the correlation with two components of the vorticity $\boldsymbol{\omega} = \boldsymbol{\nabla} \times \boldsymbol{u}$. There is some correlation between vertical vorticity component and the particle density, but the spread in each vorticity bin is larger than the average value. The correlation indicates that some trapping of particles is happening in anticyclonic regions, and that regions of cyclonic flow are expelling particles (Barge and Sommeria 1995). Meter-sized particles should be optimally concentrated by vorticity, so the weak correlation between n and ω_z is surprising, considering that for centimeter-sized particles, we found in Chapter 2 an almost linear relation between n and ω_z with very small spread. The explanation may be that the friction time is so high that particle concentrations stay together even after the gas feature which created them has

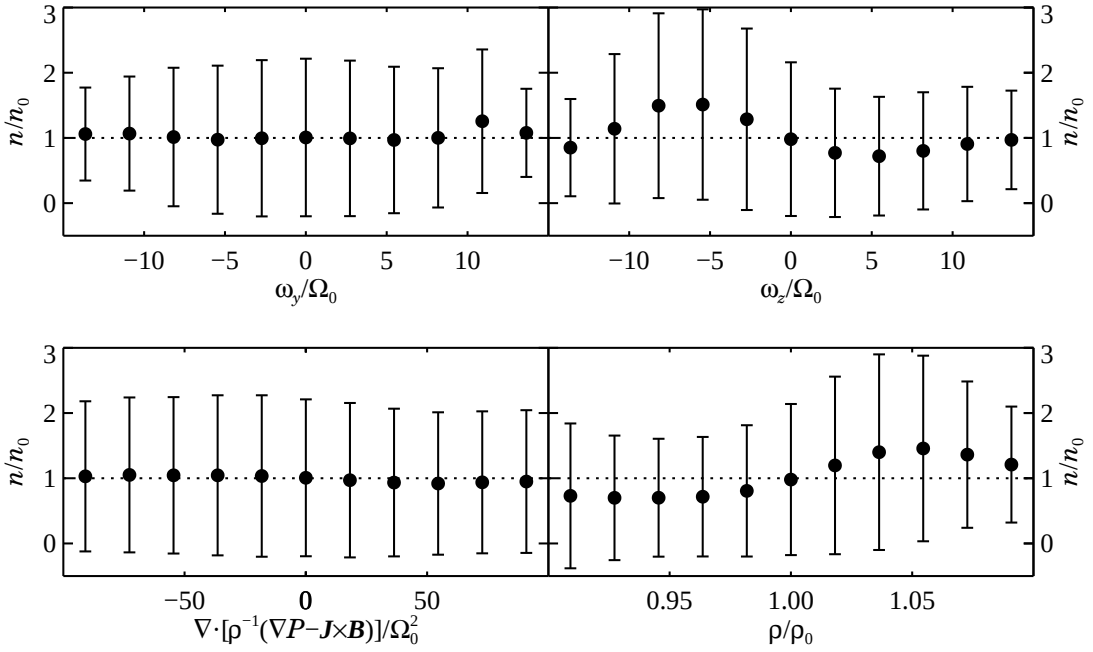

Fig. 3.6 Correlations between particle number density and various gas parameters. The first row considers two components of the vorticity. There is some correlation between n and ω_z, indicating that particles are trapped in regions of anticyclonic flow. In the second row we consider the correlation between particle density and pressure gradient flux (explained in the text) and gas density, respectively. The first correlation is very weak, whereas there is evidently a correlation between gas density and particle density, although the fluctuation bars are significant.

decayed or moved to another location. The limited life-time of the concentrating features weakens the measured correlation with the gas flow.

The lower two panels of Fig. 3.6 show the correlation with divergence of pressure gradient flux and with gas density. In a steady flow, particles accelerate towards an equilibrium velocity where the drag force is in balance with the other forces working on the particles. The equilibrium velocity is

$$\boldsymbol{v} = \tau_{\rm f}\rho^{-1}\left(\boldsymbol{\nabla}P - \boldsymbol{J}\times\boldsymbol{B}\right) \equiv \tau_{\rm f}\boldsymbol{F}\,. \tag{3.14}$$

This is the mechanism for pressure gradient-trapping. Places with a negative value of $\boldsymbol{\nabla}\cdot\boldsymbol{F}$ should produce a high particle density (see Chapter 2). The correlation between $\boldsymbol{\nabla}\cdot\boldsymbol{F}$ and n is existent, but is very weak. The last panel, however, shows that there is a clear correlation between gas density and particle density, as is also evident from Fig. 3.4. All in all, the correlations, even though some of the are quite weak, give the necessary information about the source of the concentrations of solids. The concentrations are primarily due to pressure gradient-trapping in the gas flow. There is also evidence of some vorticity-trapping happening on top of that.

Increases in density of up to two orders of magnitude will make a difference in the coagula-

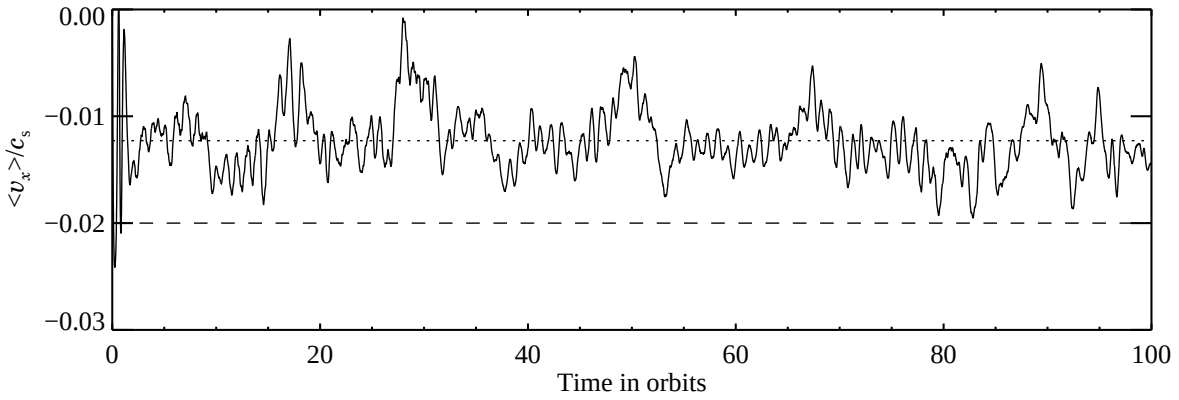

Fig. 3.7 Average radial particle velocity as a function of time for meter-sized boulders. The non-turbulent drift velocity is $v_x^{(\mathrm{lam})} = -0.02\,c_\mathrm{s}$ (indicated with a dashed line), while the average drift velocity in the turbulent case is only around $\overline{v_x} = -0.012\,c_\mathrm{s}$, a reduction by around 40% in speed.

tion process, because at places of larger concentration more collisions (both destructive and constructive) are possible. Also there is a chance of increasing the density to such high values that a gravitational instability can occur in the densest places. We will consider this last point in more detail in Sect. 3.6. In the following section we show that the turbulence not only causes concentrations, but also changes the radial drift velocity of the boulders.

3.5 Drift speed

The global pressure gradient on the gas forces solids to fall radially inwards. If the gas motion in the disc was completely non-turbulent, then the equilibrium radial drift velocity arising from the head wind term present in equation (3.12) would be

$$v_x = \frac{\beta}{\Omega_0\tau_\mathrm{f} + (\Omega_0\tau_\mathrm{f})^{-1}} c_\mathrm{s}\,. \tag{3.15}$$

We derived this expression by solving for $\partial\boldsymbol{v}/\partial t = 0$ in equation (3.12). The highest drift speed occurs for particles with $\Omega_0\tau_\mathrm{f} = 1$ with a laminar drift velocity of $v_x/c_\mathrm{s} = \beta/2$. We have checked by putting particles of different friction times into a non-turbulent disc that the measured drift velocities are in complete agreement with equation (3.15).

The effect of a real turbulent disc on the average drift velocity is seen in Fig. 3.7. Here the average radial velocity of all the particles is shown as a function of time for run A. For reference we overplot the laminar drift velocity ($v_x = -0.02\,c_\mathrm{s}$) from equation (3.15) and the time-averaged drift velocity ($\overline{v_x} = -0.012\,c_\mathrm{s}$). The mean drift velocity is noticeably affected by the turbulence and its absolute value is reduced by 40% compared to the laminar value. The influence that turbulence can have on the mean drift velocity of the particles can be quantified with some simple analytical considerations. Considering the particles for a moment as a fluid

with a number density scalar field n and a velocity vector field $\boldsymbol{w}$, the average radial velocity can be calculated with the expression

$$\langle w_x \rangle = \frac{\int_{x_0}^{x_1} n w_x \mathrm{d}x}{\langle n \rangle L_x} \,. \tag{3.16}$$

Here we have weighted the drift velocity with the number density so that we are effectively measuring the average momentum. We consider now for simplicity particles that have been accelerated by the gas to their terminal velocity (eq. [3.15] including the fluctuation pressure gradient),

$$w_x = \epsilon c_\mathrm{s} \left(\beta + \frac{\partial \ln \rho}{\partial x} \right) , \tag{3.17}$$

where ϵ is defined as $\epsilon = 1/[\Omega_0 \tau_\mathrm{f} + (\Omega_0 \tau_\mathrm{f})^{-1}]$. Inserting now equation (3.17) into equation (3.16), the resulting drift velocity is found to consist of two terms,

$$\langle w_x \rangle = \epsilon \beta c_\mathrm{s} + \frac{\epsilon c_\mathrm{s} \int_{x_0}^{x_1} n \frac{\partial \ln \rho}{\partial x} \mathrm{d}x}{\langle n \rangle L_x} \,. \tag{3.18}$$

The first term on the right-hand-side of equation (3.18) represents the contribution to the average drift velocity from the global pressure gradient (eq.[3.15]). The other term is an extra contribution due to any non-zero correlation between number density n and radial pressure gradient $\partial \ln \rho / \partial x$. This situation is sketched in Fig. 3.8. Here we sketch the global density gradient β (full line) and a sinusoidal density fluctuation $\ln \rho(x)$ (dotted line). Particles concentrate in regions where the gas density fluctuation is positive, because there the divergence of the particle velocity is negative. Due to the total pressure gradient, the newly produced particle clumps drift inwards until the point where the outwards drift towards the fluctuation density maximum balances the inwards drift from the global pressure gradient. This is exactly around the location of the box in Fig. 3.8. Here the correlation between n and $\partial \ln \rho / \partial x$ leads to a positive value of the integral in equation (3.18). A closer inspection of Fig. 3.4 reveals that the overdensities of solids are situated slightly downstream of the gas density fluctuation peaks, which is in good agreement with the prediction in Fig. 3.8. If a significant fraction of the particles end up in such regions, the average drift speed is reduced[1]. For runs B and C, there is no significant reduction of the drift speed (see Table 3.2), but there the predicted drift speed is also ten times lower than for meter-sized objects. Thus the measurement is not as reliable because the random velocity fluctuations of the particles dominate over the radial drift.

Due to the periodic boundary conditions in the y-directions, density structures quickly pass the y-boundaries, by shear advection, and thus possibly have some interference with themselves. To see the effect of the toroidal box size on the radial drift, we have run simulations with a box size of $1.32 \times 5.28 \times 1.32$ (run E) and $1.32 \times 10.56 \times 1.32$ (run F), keeping the resolution constant by adding the appropriate number of grid points in the y-direction. The time evolution of the mean radial drift velocity is shown in Fig. 3.9. It is evidently very similar to Fig. 3.7, so the toroidal size of the box does not influence the radial drift reduction

[1] A more graphic explanation of the speed reduction is to consider a car race over a distance of 100 km. Half of the distance is sand, where the cars can run 50 kilometers per hour, and the other half asphalt, where the cars go 150 kilometers an hour. The average speed of a single car reaching the finish line is less than 100 kilometers per hour, simply because that car spent more time on sandy terrain than on asphalt.

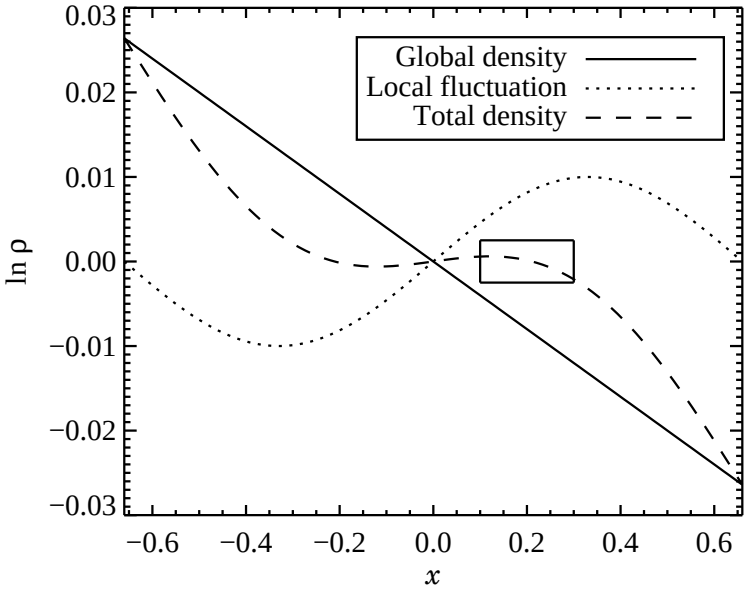

Fig. 3.8 Sketch of how turbulent density fluctuations can cause the average drift velocity to change. The full line shows the global density as a function of radial distance from the centre of the box. On top of this we sketch a large-scale sinusoidal density fluctuation (dotted line) and the total density (dashed line). Solid particles are concentrated in the positive part of the fluctuation. At the same time the concentration drifts towards the location of the box where the total drift speed is zero. If a significant fraction of the particles end up in such regions, then the average drift speed can decrease.

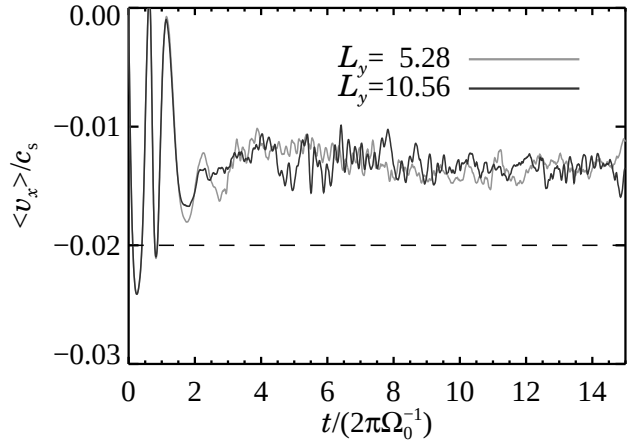

Fig. 3.9 Drift velocity for simulations E and F with larger y-domains. The expected drift velocity in a laminar disc is indicated with a dashed line. The measured drift velocity is approximately the same as for the cube simulations, so the periodic y-boundary is not the reason for the reduced drift speed. Rather it is a side-effect of trapping the particles in radial density enhancements.

noticeably. As seen in Table 3.2, the maximum particle density for runs E and F is quite high at 50 times the average density in the box, but not as high as in run A. However, simulations E and F only ran for 24 and 16 orbits, respectively, because of computational requirements due to the many grid points.

In simulations of the interaction between a planet and a magnetorotationally turbulent disc, Nelson and Papaloizou (2004) find that the average migration velocity of the planets is not changed by the presence of MRI turbulence (whereas the spread in drift velocity causes some planets to even drift outwards). On the other hand, recent simulations by Nelson (2005) indicate that the mean migration of planets can indeed change because of turbulence. The fluctuations in migration speed are however much stronger than the average (so that hundreds of orbits are needed for a reliable estimate of the average). This is a very different kind of drift behaviour than for the boulders in the current work, where the fluctuations in the drift speed are actually much *smaller* than the average. The presence of long-lived attracting regions in the gas may be the reason why boulders react on turbulence in a completely different way than planets do.

Diminishing the radial drift for meter-sized objects by roughly one half may not be saving the boulders from their fate of decaying into the star. One will have to investigate this process by additionally looking at the growth behaviour of the boulders which are sweeping up smaller particles on their way inwards. This sweeping up is determined by the actual drift speed with respect to the local gas motion. Even if the mean drift speed is above the threshold for effective sticking, there will be phases of much lower radial drift, where growth can occur. The overdense regions would also greatly increase the rate of destructive encounters between larger bodies, and thus the reservoir of small bodies would be stronger replenished there. This would not only influence growth of larger bodies, but also possibly have observational consequences.

The present simulations are done in the gentle situation of turbulence in a local box. Global disc simulations have stronger turbulence and larger density fluctuations. One can predict that it would thus also lead to a larger decrease in radial drift speed. This would possibly give the meter-sized boulders enough time to grow to a size safe for radial drift. However, this yet has to be demonstrated in global simulations[2].

3.6 Gravitational instability

We already showed that turbulence can strongly influence the growth of boulders by slowing them down and by concentrating them locally. These results can be incorporated into standard evolution codes for the solid material (e.g. Weidenschilling 1997; Dullemond and Dominik 2005), which try to grow planetesimals from dust grains via coagulation. On the other hand the high local concentration can also lead to a different way of planetesimal formation, i.e. gelation. In the gelation case a cloud of boulders is so dense that gravitational

[2]We have recently become aware of work done by Fromang and Nelson (2005) where the dynamics of boulders in magnetorotational turbulence is considered in global simulations of accretion discs. They found indeed that solids can be trapped inside persistent flow features for even a hundred orbits, i.e. the entire simulation length.

attraction becomes important. While we will not study self-gravity by an N-body approach in this work (as one should), we want at least demonstrate by simple estimations under what conditions the concentration of boulders could clump into planetesimals.

The gravity constant G enters in self-gravity calculations, and thus the equations are no longer scale-free, but depend on the adopted disc model. We characterize a disc model by a column density Σ_0, an average solids-to-gas mass density ratio ϵ_0 (for boulders of the considered size range) and a scale-height-to-radius ratio of ξ. Of course, ϵ_0 will be smaller than the global solids-to-gas ratio ~ 0.02, because only a part of the mass will be present in boulders of the considered size range. We choose for simplicity the value $\epsilon_0 = 0.01$, assuming that 50% of the total mass of solids is in bodies of the considered size, and we shall later discuss in how far this value is reasonable for a protoplanetary disc.

The apparently large number of particles in our numerical simulations is still orders of magnitude away from any real number of boulders in the volume of the protoplanetary disc considered in our simulations. Thus it is necessary and validated to let one superparticle represent an entire swarm of many particles of similar location and velocity in the disc. Superparticle means in this context that one particle has the aerodynamic behaviour of a single boulder, but represents a mass of trillions of such bodies as it mimics an entire swarm of protoplanetesimals. Similar assumptions are common in simulations of giant planet core formation from colliding planetesimals (Kokubo and Ida 2002; Thommes et al. 2003) as well as in cosmological N-body simulations (Sommer-Larsen et al. 2003). We let the simulation box represent the protoplanetary disc in the mid-plane. Each superparticle then contains the mass $m = \epsilon_1 \rho_1 V/N$, where V is the volume of the box, N is the number of superparticles, and ϵ_1 and ρ_1 are the solids-to-gas ratio and the gas density in the mid-plane of the disc. We shall use the isothermal disc expression $\rho_1 = \Sigma_0/(\sqrt{2\pi}H)$ to calculate the mass density in the mid-plane.

To calculate the solids-to-gas ratio in the mid-plane, ϵ_1, one needs to take into account the effect of vertical settling of solid material. Solids move in the direction of higher gas pressure. In the case of vertical stratification, that means that the boulders must sediment towards the mid-plane. An equilibrium is reached when the sedimentation is balanced by the turbulent diffusion, with diffusion coefficient D_t (Schräpler and Henning 2004), away from the mid-plane. This leads to a Gaussian profile of the solids-to-gas ratio (Dubrulle et al. 1995),

$$\epsilon = \epsilon_1 \exp[-z^2/(2H_\epsilon^2)]\,, \tag{3.19}$$

with the solids-to-gas ratio scale height given by the expression $H_\epsilon^2 = D_\mathrm{t}/(\tau_\mathrm{f}\Omega_0^2)$. The solids-to-gas ratio at $z = 0$ is

$$\epsilon_1 = \epsilon_0 \sqrt{\left(\frac{H}{H_\epsilon}\right)^2 + 1}\,, \tag{3.20}$$

where $H = c_\mathrm{s}\Omega_0^{-1}$ is the scale height of the gas. We now proceed by writing the turbulent diffusion coefficient as $D_\mathrm{t} = \delta_\mathrm{t} c_\mathrm{s}^2 \Omega_0^{-1}$, where δ_t is the turbulent diffusion equivalent of α_t of Shakura and Sunyaev (1973). Then the mid-plane solids-to-gas ratio ϵ_1 can be written as

$$\frac{\epsilon_1}{\epsilon_0} = \sqrt{\frac{\Omega_0 \tau_\mathrm{f}}{\delta_\mathrm{t}} + 1} \approx \sqrt{\frac{\Omega_0 \tau_\mathrm{f}}{\delta_\mathrm{t}}}\,, \tag{3.21}$$

where the approximate expression is valid for $\Omega_0\tau_\mathrm{f} \gg \delta_\mathrm{t}$. For $\delta_\mathrm{t} = \alpha_\mathrm{t} = 0.002$ and $\Omega_0\tau_\mathrm{f} = 1$, this gives $\epsilon_1 \approx 22.4\epsilon_0$, so starting from a solids-to-gas ratio of $\epsilon_0 = 0.01$, the mid-plane solids-to-gas ratio can be expected to rise to $\epsilon_1 = 0.22$ due to vertical settling. Such a low solids-to-gas ratio alone will not for any physically reasonable column density cause gravitational fragmentation (Goldreich and Ward 1973) or be subject to vertical stirring by the Kelvin-Helmholtz instability (the Richardson number Ri is around unity, see e.g. Sekiya 1998and stratification with Ri > 0.25 should be stable). Even at such a high solids-to-gas ratio we are still in the gas-dominated regime where the back-reaction from the solids on the gas can be neglected. The turbulent concentrations of solids are assumed to occur in such a vertically settled solids layer. Now the most overdense regions will have a solids-to-gas ratio of unity and beyond. But we have measured that only about 3% of the grid cells have a solids-to-gas ratio of above unity at any given time, and thus it is still reasonable as a first approximation to ignore the back-reaction of the solids on the gas, although a more advanced study should include this effect as well.

To find out if a given overdense clump is gravitationally unstable, we shall compare the different time-scales and length-scales involved in fragmentation by self-gravity in a Jeans-type stability analysis. First we investigate if the clump is gravitationally bound. We consider a clump of radius R, mass M and velocity dispersion σ. The velocity dispersion must include the dispersion due to the background shear. For such a clump with a given mass to be gravitationally unstable, it must have a radius that is smaller than the Jeans radius given by

$$R_\mathrm{J} = \frac{2GM}{\sigma^2}\,. \tag{3.22}$$

If this first criterion is fulfilled, then it is also important that the collapse time-scale of the structure is shorter than the life-time of the overdense clump t_cl. Only then we can be sure that the changing gas flow will not dissolve the concentration before it has had time to contract significantly. The fragmentational collapse happens on the free-fall time-scale

$$t_\mathrm{ff} = \sqrt{\frac{R^3}{GM}}\,. \tag{3.23}$$

The condition for gravitational instability is now that $R < R_\mathrm{J}$ and that at the same time $t_\mathrm{ff} < t_\mathrm{cl}$. We do not have to check separately that the collapse happens faster than a shear time $t_\mathrm{sh} = \Omega_0^{-1}$, since the effect of the background shear is already included in the velocity dispersion.

We now try to find out the smallest value of Σ_0 that gives rise to a gravitational instability. Then we can see whether this is a value that occurs in nature or not. For $\Omega_0\tau_\mathrm{f} = 1$ (run A) the minimum value of the column density turns out to be around $\Sigma_0 = 900\,\mathrm{g\,cm^{-2}}$ (6 times the minimum mass solar nebula value at 5 AU), whereas for $\Omega_0\tau_\mathrm{f} = 10$ (run C), a gravitationally unstable cluster of protoplanetesimals is achieved already at the minimum mass solar nebula value $\Sigma_0 = 150\,\mathrm{g\,cm^{-2}}$.

First run A is considered. Here we can calculate the mass in each superparticle. With $\Sigma_0 = 900\,\mathrm{g\,cm^{-2}}$, $\xi = 0.04$, $r = 5\,\mathrm{AU}$ and $\epsilon_1 = 0.22$, we get $\rho_1 = 1.2 \times 10^{-10}\,\mathrm{g\,cm^{-3}}$ and $m = 8 \times 10^{20}\,\mathrm{g}$. Thus each superparticle represents about 3×10^{14} meter-sized protoplanetesimals. This is five orders of magnitude more mass than in a kilometer-sized planetesimal, but since

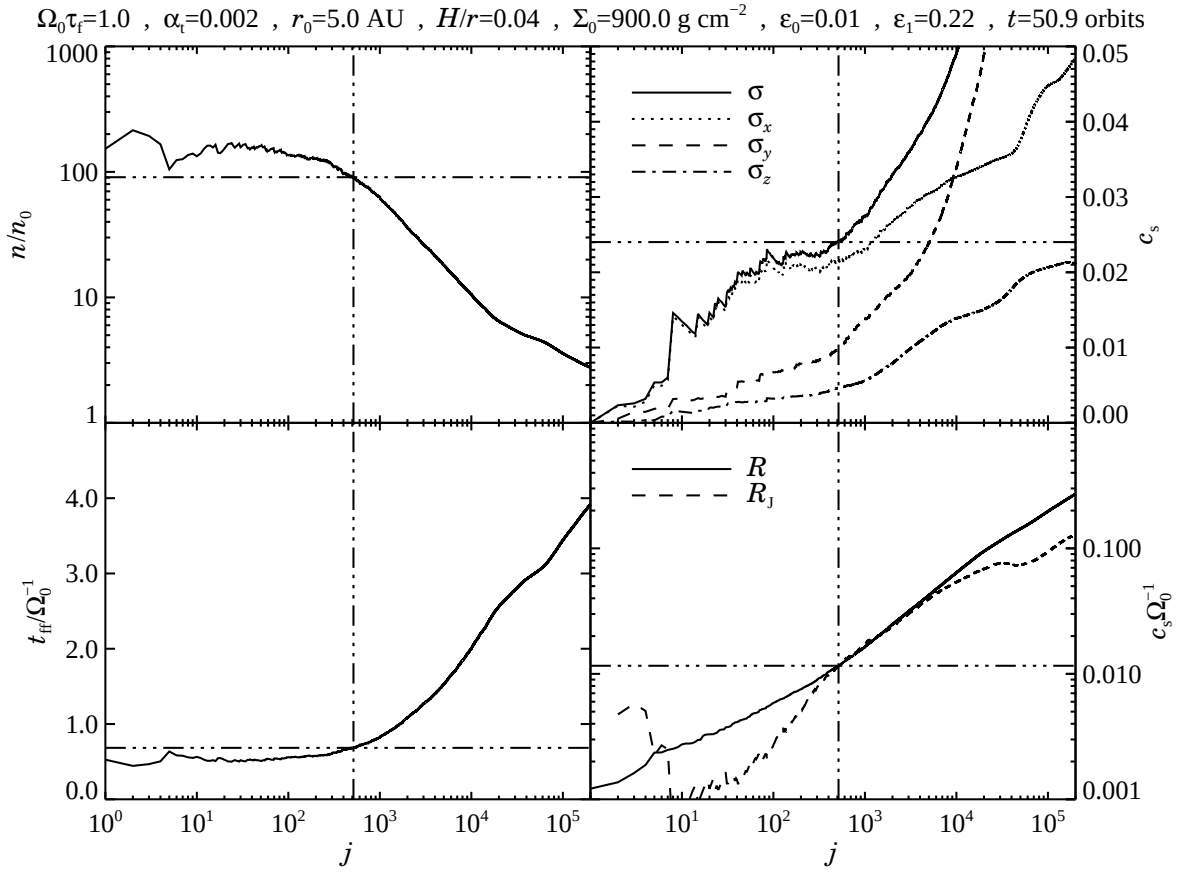

Fig. 3.10 Particle number density n in units of average density n_0, velocity dispersion σ in units of sound speed c_s, free-fall time t_ff relative to the clump life-time t_cl, and clump radius R together with Jeans radius R_J, all as a function of the number of included particles around the densest grid point in the box at a time of 50.9 orbits of run A. The vertical and horizontal dot-dot-dot-dashed lines indicate the regions of gravitational instability for the choice of disc model parameters.

we are interested in identifying gravitationally bound regions with the mass of thousands and thousands of planetesimals, this is not a problem. Actually resolving the mass of even one single planetesimal with meter-sized objects would require on the order of a billion particles, which is way beyond current computational resources.

We examine the region around the densest grid point of run A at a time of $t = 50.9$ orbits in more detail. This time is chosen because there occurs a large concentration of particles, see Fig. 3.1. We consider the j nearest particles to the densest point and calculate for j between 1 and 200,000 the particle number density n, the velocity dispersion σ and its directional components, the free-fall time t_ff, and the radius of the clump together with the Jeans radius R_J. The results are shown in Fig. 3.10. It is reasonable to require at least $j = 100$ for a measurement to be statistically significant (for $j \geq 100$ the relative counting error falls below 10%, see e.g. Casertano and Hut 1985). It is also reasonable to require that the size of the

clump be larger than the size of a grid cell, since any structure in the concentration within a single grid is not well-resolved. The same is true for the velocity dispersion. At $j = 100$ the number density of solids is more than 130 times the average, but the radius of the $j = 100$ clump is only around 0.007, which is smaller than the grid cell radius of $\delta x/2 = 0.01$. At $j \simeq 500$ the clump has the size of a grid cell, and here the number density is more like 100 times the average. This must be multiplied by the enhancement by sedimentation, which is around 20, to give a solids-to-gas ratio increase by a factor of 2000 compared to the original value in the disc. The velocity dispersion is around $\sigma \sim 0.02 \ldots 0.03\, c_{\rm s}$. That includes the velocity dispersion due to the background shear, but this is not a very important effect anyway because the size of the overdense clump is very small. At small scales the velocity dispersion is completely dominated by the radial component, according to Fig. 3.10, whereas the shear only takes over at larger scales.

The free-fall time is a bit below the clump life-time, which is typically one shear time (see insert in Fig. 3.1; note that the time unit is in orbits). For calculating the Jeans radius we have had to adopt a column density as high as $\Sigma_0 = 900\,{\rm g\,cm^{-2}}$ in order to have the clump to be gravitationally unstable. This is mainly due to the high velocity dispersion. The radius of the clump is around one Jeans radius at $j = 1000$, so the clump is gravitationally bound at this scale and would be subject to further contraction by self-gravity. The gravitationally unstable region is around three grid cells in diameter, but even though this is well within the dissipative scales of the turbulence, the effect of the unresolved turbulence on the motion of the particles should be very little, as such small scale turbulence has short life-times and low amplitudes compared to the large scales. Extrapolating the resolved large scale turbulence to the grid-scale with a Kolmogorov law gives lower turbulent velocities than the particle velocity dispersion that we already measure at the grid scale. Thus we conclude that the unresolved turbulence has little or no influence on the particle dynamics. The concentrations and velocity dispersions are exclusively driven by the large resolved scales of the gas motion.

The solid size of the forming object would be roughly 400 km if all the 1000 superparticles end up in just one large body. On the other hand, the outcome of such a collapse may also favour the further fragmentation of the clump. This all depends on how the velocity dispersion behaves with increasing density. In the N-body simulations of Tanga et al. (2004) gas drag works as an efficient way to dissipate the gravitational energy that is released in the contraction of protoplanetesimal clusters. Only such simulations, that include self-gravity and gas drag, could show the further evolution of the overdense boulder clumps that we see in the present work.

For decameter-sized bodies (run C), we plot in Fig. 3.11 the same quantities as in Fig. 3.10 around the densest point at a time of 53 orbits. This time we adopt the minimum mass solar nebula column density of $\Sigma_0 = 150\,{\rm g\,cm^{-2}}$, which gives a mid-plane density of $\rho_1 = 2 \times 10^{-11}\,{\rm g\,cm^{-3}}$. Because of the high friction time, the solids-to-gas ratio in the mid-plane (eq.[3.21]) is now 0.71. The Richardson number is correspondingly lower at around ${\rm Ri} = 0.4$, so it is still stable to Kelvin-Helmholtz instability. The mass of the individual superparticles is here $m = 4 \times 10^{20}\,{\rm g}$. The density is slightly smaller than for meter-sized bodies, at statistically significant counts around 50 times the average, but the velocity dispersion is lower, and also the overdense region is much larger than it was for meter-sized boulders. Thus already a

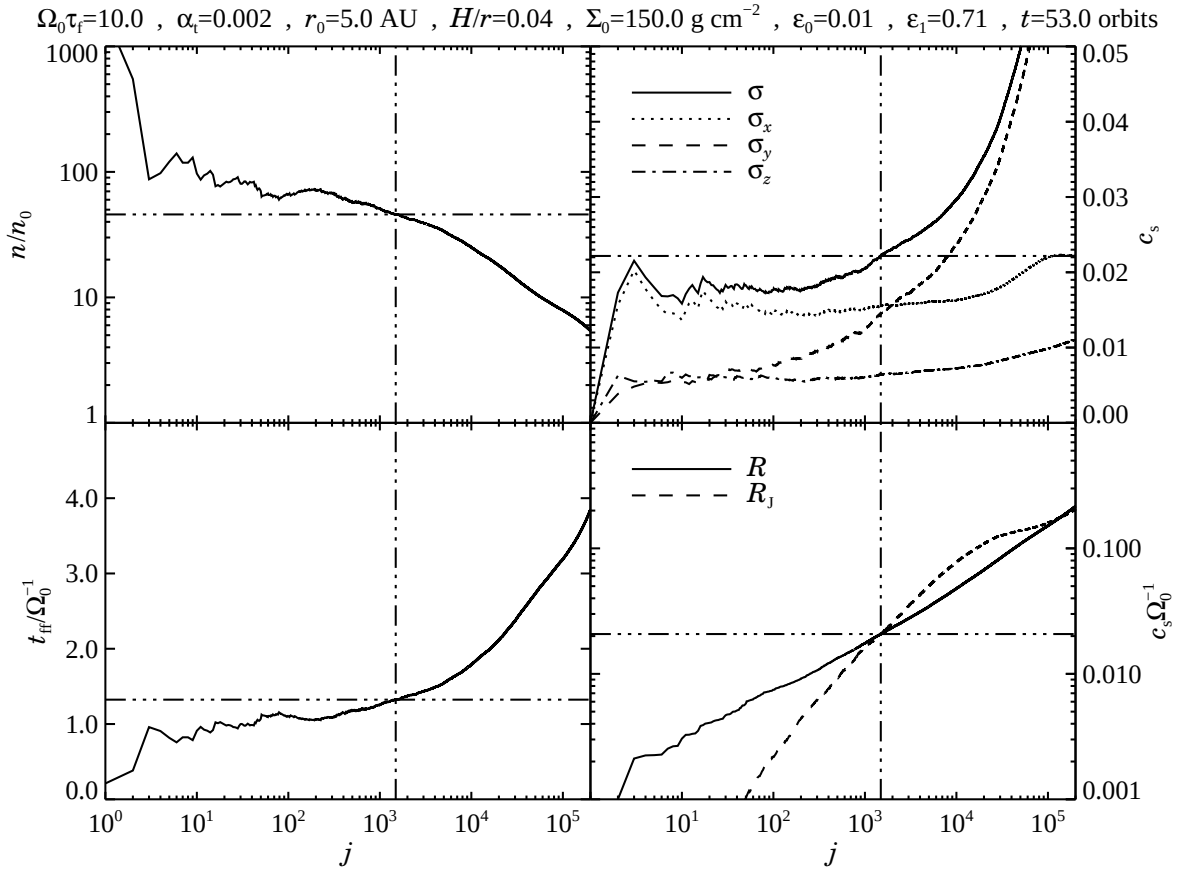

Fig. 3.11 Same as Fig. 3.10, but for run C (decameter-sized bodies) at a time of 53 orbits. Here the minimum mass solar nebula column density is sufficient to have a gravitational instability. This is mainly because the velocity dispersion is smaller than for run A. Also the high density region has a larger extent.

minimum mass solar nebula can produce a gravitational instability. The unstable region is as large as 10 grid cells in diameter, and contains around 10^5 particles. The size of a solid object consisting of this number of superparticles is roughly 1,400 kilometers. Again there is also the possibility that millions of 10-kilometer objects form instead.

The preceding calculations are of course only an estimation of the potential importance of self-gravity. In a real protoplanetary disc there will be a distribution of particle sizes present at any time. If e.g. fragmentation is important, as discussed in the introduction, then the greater part (80%) of the mass may still be present in bodies that are well below one meter in radius (Dullemond and Dominik 2005). With only 20% of the mass in the size range between one and ten meters, the critical column density could be as much as a factor of two higher than stated above. However, this is still in the range of the masses derived for circumstellar discs. So the qualitative picture that the clumps are gravitationally unstable for physically reasonable gas column densities is robust.

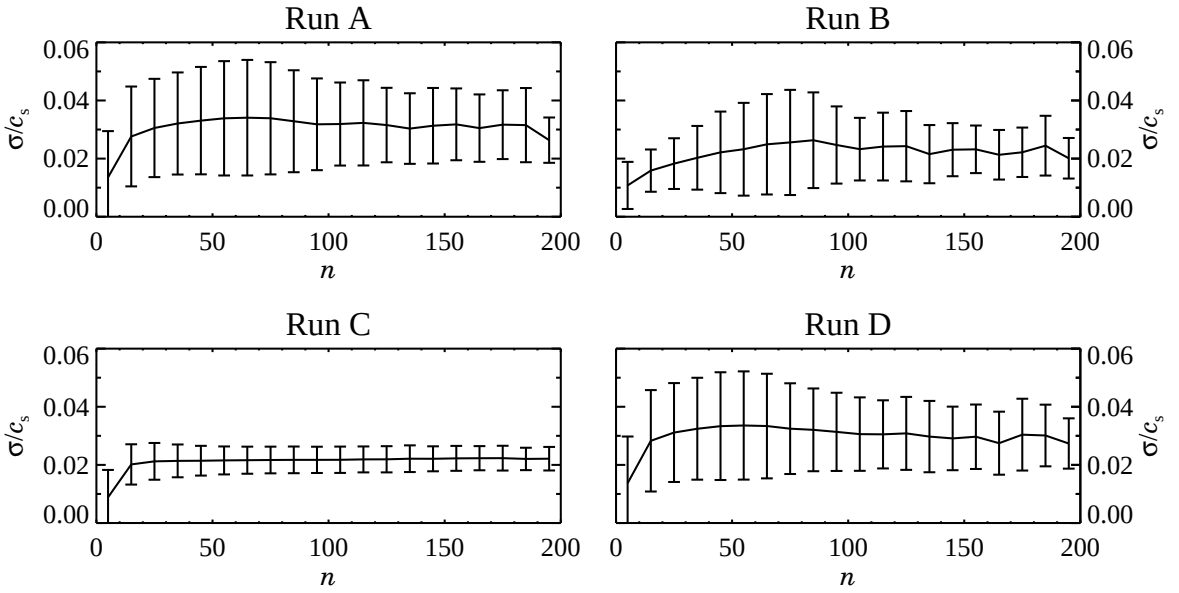

Fig. 3.12 Average velocity dispersion and fluctuation interval as a function of the number of particles in a grid cell. The dispersion rises until there are around 50 particles in a grid cell, and is then constant up to 200 particles, or around 30 times the average bulk density of solids. This corresponds to an isothermal equation of state for the boulders.

To quantify the velocity dispersion in the entire box, we have calculated the average values over all the grid cells. The results are shown in the last four columns of Table 3.2. Grid cells with 0 or 1 particles have been excluded from the average because the velocity dispersion is per definition zero in these underresolved cells. The meter-sized bodies have the highest velocity dispersion, around $\sigma_1 \approx 0.02\, c_\mathrm{s}$, whereas decimeter bodies have $\sigma_{0.1} \approx 0.014\, c_\mathrm{s}$ and decameter bodies have a value of $\sigma_{10} \approx 0.017\, c_\mathrm{s}$. These values are similar to the turbulent velocities of the gas at the largest scales of the box (see Fig. 2.2 in Chapter 2), which again shows that these large scales are the drivers of the particle dynamics. Interestingly run D, which is similar to run A only without the radial pressure gradient, has the same velocity dispersion as run A, so the radial pressure gradient does not add extra velocity dispersion to the boulders. The toroidal component of the velocity dispersion is similar for all the runs because it is dominated by the shear over a grid cell. Run C has a twice as large radial velocity dispersion as run B. This can be explained because the large particles in run C react much slower to the local behaviour of the gas, and thus particles of different velocities and histories are mixed in together.

The behaviour of the velocity dispersion with increasing bulk density of solids is relevant for gravitational instability calculations. The average velocity dispersion, and the fluctuation width, as a function of the number of particles in a grid cell is shown in Fig. 3.12. Again it is evident that the velocity dispersion for $\Omega_0 \tau_\mathrm{f}$ of unity is largest. For all runs the velocity dispersion typically rises until there are around 50 particles in the cell. Then the dispersions stay constant all the way to 200 particles. Thus the equation of state of the particles is isothermal, at least up to 30 times the average bulk density of solids.

3.7 Summary and discussion

We have considered the effect of magnetorotational turbulence on the motion of solid particles with a freely evolving space coordinate. The particle treatment was necessary over the fluid treatment, because the mean free path of the macroscopic boulders is so long that they can no longer be treated as a fluid. The use of magnetorotational turbulence may not be completely justified in the mid-plane of the disc where the ionization fraction due to radiation and cosmic particles is low. But due to its Kolmogorov-like properties, where energy is injected at the unstable large scales and then cascades down to smaller and smaller scales, magnetorotational turbulence can be seen as a sort of "generic disc turbulence".

We find that the turbulence acts on the particles by concentrating meter-sized boulders locally by up to a factor of 100 and by reducing their radial drift by 40%. Both the concentrations and the reduced radial drift happen because the solid particles are temporarily trapped in radial density enhancements. One would not expect such structures to be long-lived in a general turbulent flow, but magnetorotational turbulence in accretion discs is subject to a strong shear that favours elongated toroidal structures. In the presented simulations the typical life-time of the structures is on the order of a few orbits, corresponding to tens or even hundreds of years in the outer parts of a protoplanetary disc. When the density structures eventually dissolve, new structures appear at other locations. We find a strong correlation between a gas column density of a few percent above the average and a several times increase in the column density of solids. We have also seen some evidence for increased solids density in regions of anticyclonicity, but the long friction time of the solid particles makes it difficult to identify the gas flow that caused a given concentration, because the concentration may drift away from the creation site.

The large concentrations naturally occur near the grid scale. In finite resolution computer simulations the dissipative length scale must necessarily be moved from the extremely small dissipative scales of nature to the smallest scales of the simulation box. Thus the turbulence is not well-resolved near the grid scale. On the other hand, the concentrations are driven by the largest scales of the turbulence, because there are the largest velocities and the longest lived features (Voelk et al. 1980). Already the other well-resolved but slightly smaller scales fluctuate too quick and at too low speeds to influence the path of an object that is one meter in size or larger. This argument is given support by the fact that we measure particle velocity dispersions in the grid cells that are comparable to the velocity amplitude of the gas at the largest scales of the simulation. Thus, one should not expect higher resolution to change the concentrations or the velocity dispersions significantly.

Our estimation of the minimum gas column density that would make the densest proto-planetesimal clumps gravitationally unstable is necessarily based on many assumptions. We assumed that half of the mass of the solids in the disc was present in bodies of the considered size, whereas in real discs an even larger part of the solids may be bound in small fragments that result from catastrophic collisions. We also ignored the back-reaction from the solids on the gas. The background state has, both for meter and decameter bodies, a solids-to-gas ratio just below unity (where the back-reaction becomes important). The effect on the magnetorotational instability of drag force from the solids on the gas has to our knowledge never been considered. One can speculate that the drag force will mimic a strong viscosity and thus

disable the source of turbulence where the solids density is high. For the treatment of Kelvin-Helmholtz instability we based it simply on a criterion on the Richardson number Ri. There is some indication that this may be too simplistic and that in protoplanetary discs much higher Richardson numbers are also unstable (Gómez and Ostriker 2005), but one can also speculate that the full inclusion of solid particles in simulations of Kelvin-Helmholtz turbulence would show strong local concentrations like we see here for magnetorotational turbulence. Thus the exact values of six times the minimum solar nebula for meter-sized boulders and just the minimum mass solar nebula for decameter-sized boulders should only be considered as rough estimates. Still, the result that the clumps are gravitationally unstable for reasonable gas column densities is robust enough to warrant further investigations that include treatment of self-gravity between the boulders.

Thus we find that the gravoturbulent formation of planetesimals from the fragmentation of an overdense swarm of meter-sized rocks is possible. Turbulence is in this picture not an obstacle, but rather the ignition spark, as it is responsible for generating the local gravitationally bound overdensities in the vertically sedimented layer of boulders.

Chapter 4

Sedimentation and self-sustained Kelvin-Helmholtz turbulence

From Johansen, Henning, & Klahr (2006): The Astrophysical Journal, vol. 643, p. 1219–1232

4.1 Abstract

We perform numerical simulations of the Kelvin-Helmholtz instability in the mid-plane of a protoplanetary disc. A two-dimensional corotating slice in the azimuthal–vertical plane of the disc is considered where we include the Coriolis force and the radial advection of the Keplerian rotation flow. Solids, treated as individual particles, move under the influence of friction with the gas, while the gas is treated as a compressible fluid. The friction force from the solid particles on the gas leads to a vertical shear in the gas rotation velocity. As the particles settle around the mid-plane due to gravity, the shear increases, and eventually the flow becomes unstable to the Kelvin-Helmholtz instability. The Kelvin-Helmholtz turbulence saturates when the vertical settling of solids is balanced by the turbulent diffusion away from the mid-plane. The azimuthally averaged state of the self-sustained Kelvin-Helmholtz turbulence is found to have a constant Richardson number in the region around the mid-plane where the solids-to-gas ratio is significant. Nevertheless the bulk density of solids has a strong non-axisymmetric component. We identify a powerful clumping mechanism, caused by the dependence of the rotation velocity of the particles on the local solids-to-gas ratio, as the source of the non-axisymmetry. Our simulations confirm recent findings that the critical Richardson number for Kelvin-Helmholtz instability is around unity or larger, rather than the classical value of 1/4.

4.2 Introduction

One of the great unsolved problems of planet formation is how to form planetesimals, the kilometer-sized precursors of real planets (Safronov 1969). At this size solid bodies in a protoplanetary disc can attract each other through gravitational two-body encounters, whereas gravity is insignificant between smaller bodies. Starting from micrometer-sized dust grains, the initial growth is caused by the random Brownian motion of the grains (e.g. Blum and Wurm 2000; Dullemond and Dominik 2005, see Henning et al. (2006) for a review). The vertical component of the gravity from the central object causes the gas in the disc to be stratified with a higher pressure around the mid-plane. Even though the solids do not feel this pressure gradient, the strong frictional coupling with the gas prevents small grains from having any significant vertical motion relative to the gas. However, once the grains have coagulated to form pebbles with sizes of a few centimeters, the solids are no longer completely coupled to the gas motion. They are thus free to fall, or sediment, towards the mid-plane of the disc. The increase in the bulk density of solids opens a promising way of forming planetesimals by increasing the local density around the mid-plane of the disc to values high enough for gravitational fragmentation of the solids layer (Safronov 1969; Goldreich and Ward 1973).

There are however two major unresolved problems with the gravitational fragmentation scenario. Any global turbulence in the disc causes the solid particles to diffuse away from the mid-plane, and thus the density is kept at values that are too low for fragmentation. A turbulent α-value of 10^{-4} is generally enough to prevent efficient sedimentation towards the mid-plane (Weidenschilling and Cuzzi 1993), whereas the α-value due to magnetorotational turbulence (Balbus and Hawley 1991; Brandenburg et al. 1995; Hawley et al. 1995; Armitage 1998) is from a few times 10^{-3} (found in local box simulations with no imposed magnetic field) to 0.1 and higher (in global disc simulations). The presence of a magnetically dead zone around the disc mid-plane (Gammie 1996; Fromang et al. 2002; Semenov et al. 2004) may not mean that there is no turbulence in the mid-plane, as other instabilities may set in and produce significant turbulent motion (Li et al. 2001; Klahr and Bodenheimer 2003). The magnetically active surface layers of the disc can even induce enough turbulent motion in the mid-plane to possibly prevent efficient sedimentation of solids (Fleming and Stone 2003). The presence of a dead zone may actually *in itself* be a source of turbulence. The sudden fall of the accretion rate can lead to a pile up of mass in the dead zone, possibly igniting the magnetorotational instability in bursts (Wünsch et al. 2005) or a Rossby wave instability (Varnière and Tagger 2006).

The second major problem with the gravitational fragmentation scenario is that even in the absence of global disc turbulence, the sedimentation of solids may in itself destabilise the disc. Protoplanetary discs have a radial pressure gradient, because the temperature and the density fall with increasing radial distance from the central object, so the gas rotates at a speed that is slightly below the Keplerian value. The solid particles feel only the gravity and want to rotate purely Keplerian. Close to the equatorial plane of the disc, where the sedimentation of solid particles has increased the solids-to-gas ratio to unity or higher, the gas is forced by the solids to orbit at a higher speed than far away from the mid-plane where the rotation is still sub-Keplerian. Thus there is a vertical dependence of the gas rotation velocity. Such shear flow can be unstable to the Kelvin-Helmholtz instability (KHI), depending on the

stabilising effect of vertical gravity and density stratification. A necessary criterion for the KHI is that the energy required to lift a fluid parcel of gas and solids vertically upwards by an infinitesimal distance is available in the relative vertical motion between infinitesimally close parcels (Chandrasekhar 1961). The turbulent motions resulting from the KHI are strong enough to puff up the particle layer and prevent the formation of an infinitesimally thin particle sheet around the mid-plane of the disc (Weidenschilling 1980; Weidenschilling and Cuzzi 1993).

Modifications to the gravitational fragmentation scenario have been suggested to overcome the problem of Kelvin-Helmholtz turbulence. Sekiya (1998, hereafter referred to as S98) found that if the mid-plane of the disc is in a state of constant Richardson number, as expected for small particles whose settling time is long compared to the growth rate of the KHI, then an increase in the global solids-to-gas ratio can lead to the formation of a high density cusp of solids very close to the mid-plane of the disc, reaching potentially a solids-to-gas ratio of 100 already at a global solids-to-gas ratio that is 10 times the canonical interstellar value of 0.01. The appearance of a superdense cusp of solids in the very mid-plane has been interpreted by Youdin and Shu (2002) as an inability of the gas (or of the KHI) to move more mass than its own away from the mid-plane. As a source of an increased value of the global solids-to-gas ratio, Youdin and Shu (2002) suggest that the solid particles falling radially inwards through the disc pile up in the inner disc. A slowly growing radial self-gravity mode in the bulk density of solids has also been suggested as the source of an increased solids-to-gas ratio at certain radial locations (Youdin 2005a,b). Trapping solid boulders in a turbulent flow is a mechanism for avoiding the problem of self-induced Kelvin-Helmholtz turbulence altogether (Barge and Sommeria 1995; Klahr and Henning 1997; Hodgson and Brandenburg 1998; Chavanis 2000; Johansen et al. 2004). If the solids can undergo a gravitational fragmentation locally, because the boulders are trapped in features of the turbulent gas flow such as vortices or high-pressure regions, then there is no need for an extremely dense layer of solids around the mid-plane. Johansen, Klahr, and Henning (2006b, see also Chapter 3) found that meter-sized boulders are temporarily trapped in regions of slight gas overdensity in magnetorotational turbulence, increasing the solids-to-gas ratio locally by up to two orders of magnitude. They estimate that the solids in such regions should have time to undergo gravitational fragmentation before the high-pressure regions dissolve again. Fromang and Nelson (2005), on the other hand, find that vortices can even form in magnetorotationally turbulent discs, keeping boulders trapped for hundreds of disc rotation periods. The KHI cannot operate inside a vortex because there is no radial pressure gradient, and thus no vertical shear, in the centre of the vortex (Klahr and Bodenheimer 2006).

From a numerical side it has been shown many times that a pure shear flow, i.e. one that is not explicitly supported by any forces, is unstable, both with magnetic fields (Keppens et al. 1999; Keppens and Tóth 1999) and without (Balbus et al. 1996). But the key point here is that the vertical shear formed in a protoplanetary disc is due to the sedimentation of solids, and that the shear is able to regenerate as the solid particles fall down again, thus keeping the flow unstable to KHI. The description of the full non-linear outcome of such a system requires numerical simulations that include solid particles that can move relative to the gas.

Linear stability analysis of solids-induced shear flows in protoplanetary discs have been performed for simplified physical conditions (Sekiya and Ishitsu 2000), but also with Coriolis

forces and Keplerian shear included (Ishitsu and Sekiya 2002, 2003). Recently Gómez and Ostriker (2005, hereafter referred to as GO05) took an approach to include solids into their numerical simulations of the Kelvin-Helmholtz instability by having the solids so extremely well-coupled to the gas that they always move with the instantaneous velocity of the gas. This is indeed a valid description of the dynamics of tiny dust grains. However, the strong coupling to the gas does not allow the solid particles to fall back towards the mid-plane. Thus the saturated state of the Kelvin-Helmholtz turbulence can not be reached this way.

In this chapter we present computer simulations where we have let the solids, represented by particles each with an individual velocity vector and position, move relative to the gas. This allows us to obtain a state of self-sustained Kelvin-Helmholtz turbulence from which we can measure quantities such as the diffusion coefficient and the maximum bulk density of solids. A better knowledge of these important characteristics of Kelvin-Helmholtz turbulence is vital for our understanding of planet formation.

4.3 Dynamical equations

We start by introducing the dynamical equations that we are going to solve for the gas and the particles.

We consider a protoplanetary disc as a plane rotating with the Keplerian frequency Ω_0 at a distance $r = r_0$ from a protostellar object. The plane is oriented so that only the azimuthal and vertical directions (which we name y and z, respectively) of the disc are treated. The absence of the radial x-direction means that the Keplerian shear is ignored. The onset of the KHI is very likely to be affected by the presence of radial shear, since the unstable modes of the KHI are non-axisymmetric and therefore will be sheared out, but we believe the problem of Kelvin-Helmholtz turbulence in protoplanetary discs to be rich enough to allow for such a simplification as a first approach. There is of course the risk that the nature of the instability could change significantly with the inclusion of Keplerian shear (Ishitsu and Sekiya 2003), but on the other hand, the results that we present here regard mostly the dynamics of solid particles in Kelvin-Helmholtz turbulence, and we expect the qualitative results to hold even with the inclusion of the Keplerian shear.

As a dynamical solver we use the Pencil Code, a finite difference code that uses sixth order centred derivatives in space and a third order Runge-Kutta time integration scheme. See Brandenburg (2003) for details on the numerical schemes and test runs.

4.3.1 Gas equations

The three components of the equation of motion of the gas are

$$\begin{aligned}
\frac{\partial u_x}{\partial t} + (\boldsymbol{u}\cdot\boldsymbol{\nabla})u_x &= 2\Omega_0 u_y \\
&\quad -\frac{1}{\gamma}c_{\rm s}\Omega_0\beta - \frac{\epsilon}{\tau_{\rm f}}\left(u_x - w_x\right) , \qquad (4.1)\\
\frac{\partial u_y}{\partial t} + (\boldsymbol{u}\cdot\boldsymbol{\nabla})u_y &= -\frac{1}{2}\Omega_0 u_x \\
&\quad -\frac{1}{\rho}\frac{\partial P}{\partial y} - \frac{\epsilon}{\tau_{\rm f}}\left(u_y - w_y\right) , \qquad (4.2)\\
\frac{\partial u_z}{\partial t} + (\boldsymbol{u}\cdot\boldsymbol{\nabla})u_z &= -\Omega_0^2 z - \frac{1}{\rho}\frac{\partial P}{\partial z} - \frac{\epsilon}{\tau_{\rm f}}\left(u_z - w_z\right) . \qquad (4.3)
\end{aligned}$$

Here $\boldsymbol{u} = (u_x, u_y, u_z)$ denotes the velocity field of the gas measured relative to the Keplerian velocity. We explain now in some detail the terms that are present on the right-hand-side of equations (4.1-4.3). The x- and y-components of the equation of motion contain the Coriolis force due to the rotating disc, to ensure that there is angular momentum conservation. Since velocities are measured relative to the Keplerian shear flow, the advection of the rotation flow by the radial velocity component has been added to the azimuthal component of the Coriolis force, changing the factor -2 to $-1/2$ in equation (4.2). We consider local pressure gradient forces only in the azimuthal and vertical directions, whereas there is a constant global pressure gradient force in the radial direction. The global density is assumed to fall radially outwards as $\partial \ln\rho/\partial \ln r = \alpha$, where α is a constant. Assuming for simplicity that the density decreases isothermally, we can write the radial pressure gradient force as

$$-\frac{1}{\rho}\frac{\partial P}{\partial r} = -\frac{1}{\gamma}c_{\rm s}^2\frac{\partial \ln\rho}{\partial r} . \qquad (4.4)$$

Here $\gamma = 5/3$ is the ratio of specific heats and $c_{\rm s}$ is the constant sound speed. Rewriting this expression and using the isothermal disc expression $H = c_{\rm s}/\Omega_0$, we arrive at the expression

$$-\frac{1}{\rho}\frac{\partial P}{\partial r} = -\frac{1}{\gamma}\frac{H}{r}\frac{\partial \ln\rho}{\partial \ln r}c_{\rm s}\Omega_0 . \qquad (4.5)$$

We then proceed by defining the dimensionless disc parameter $\beta \equiv \frac{H}{r}\frac{\partial \ln\rho}{\partial \ln r}$, where H/r is the scale-height to radius ratio of the disc. This parameter can be assumed to be a constant for a protoplanetary disc. Using equation (4.5) and the definition of β leads to the global pressure gradient term in equation (4.1). We use throughout this work a value of $\beta = -0.1$.

The ratio between the pressure gradient force Δg and two times the solar gravity,

$$\eta = \frac{\Delta g}{2g} = \frac{-\frac{1}{\rho}\frac{\partial P}{\partial r}}{2\Omega_0^2 r} , \qquad (4.6)$$

is often used to parametrize sub-Keplerian discs (Nakagawa et al. 1986). Assuming again an isothermally falling density, equation (4.6) can be written as

$$\eta = -\frac{1}{2}\frac{1}{\gamma}\left(\frac{H}{r}\right)^2\frac{\partial \ln\rho}{\partial \ln r} . \qquad (4.7)$$

The connection between our β and the more widely used η is then

$$\eta = -\frac{1}{2}\frac{1}{\gamma}\frac{H}{r}\beta\,. \tag{4.8}$$

The last term in equations (4.1-4.3) is the friction force that the solid particles exert on the gas. We discuss this in further detail in Sect. 4.3.3 below. Here the velocity field of the solids $\boldsymbol{w} = (w_x, w_y, w_z)$ is a map of the particle velocities onto the grid. To stabilise the finite difference numerical scheme of the Pencil Code, we use a sixth-order momentum-conserving hyperviscosity (e.g. Brandenburg and Sarson 2002; Haugen and Brandenburg 2004; Johansen and Klahr 2005). Hyperviscosity has the advantage over regular second-order viscosity in that it has a huge effect on unstable modes at the smallest scales of the simulation, while leaving the largest scales virtually untouched.

4.3.2 Mass and energy conservation

The conservation of mass, given by the logarithmic density $\ln\rho$, and entropy, s, is expressed in the continuity equation and the heat equation,

$$\frac{\partial \ln\rho}{\partial t} + (\boldsymbol{u}\cdot\boldsymbol{\nabla})\ln\rho = -\boldsymbol{\nabla}\cdot\boldsymbol{u}\,, \tag{4.9}$$

$$\frac{\partial s}{\partial t} + (\boldsymbol{u}\cdot\boldsymbol{\nabla})s = 0\,. \tag{4.10}$$

The advection of the global density gradient due to any radial velocity has been ignored, as well as viscous heating of the gas. We calculate the pressure gradient force in equations (4.1-4.3) by rewriting the vector term as

$$-\rho^{-1}\boldsymbol{\nabla}P = -c_{\rm s}^2(\boldsymbol{\nabla}s/c_{\rm p} + \boldsymbol{\nabla}\ln\rho) \tag{4.11}$$

and using the ideal gas law expression

$$c_{\rm s}^2 = \gamma\frac{P}{\rho} = c_{\rm s0}^2\exp\left[\gamma s/c_{\rm p} + (\gamma{-}1)\ln\frac{\rho}{\rho_0}\right]. \tag{4.12}$$

The two constants $c_{\rm s0}$ and ρ_0 are integration constants from the integration of the first law of thermodynamics. We have chosen the integration constants such that $s = 0$ when $c_{\rm s} = c_{\rm s0}$ and $\rho = \rho_0$. To allow for gravity waves, we must use the perfect gas law, rather than a simple polytropic equation of state. We stabilise the continuity equation and the entropy equation by using a 5th order upwinding scheme (see Dobler et al. 2006) for the advection terms in equations (4.9) and (4.10).

4.3.3 Particle equations

The solids are treated as individual particles moving on the top of the grid. Therefore they have no advection term in their equation of motion, whose components are

$$\frac{\mathrm{d}v_x^{(i)}}{\mathrm{d}t} = 2\Omega_0 v_y^{(i)} - \frac{1}{\tau_\mathrm{f}}\left(v_x^{(i)} - u_x\right), \tag{4.13}$$

$$\frac{\mathrm{d}v_y^{(i)}}{\mathrm{d}t} = -\frac{1}{2}\Omega_0 v_x^{(i)} - \frac{1}{\tau_\mathrm{f}}\left(v_y^{(i)} - u_y\right), \tag{4.14}$$

$$\frac{\mathrm{d}v_z^{(i)}}{\mathrm{d}t} = -\Omega_0^2 z^{(i)} - \frac{1}{\tau_\mathrm{f}}\left(v_z^{(i)} - u_z\right). \tag{4.15}$$

The index i runs in the interval $i = 1 \ldots N$, where N is the number of particles that are considered. The last terms in equations (4.13-4.15) is the friction force. The friction force is assumed to be proportional to the velocity difference between solids and gas with a characteristic braking-down time-scale of τ_f, called the friction time. To conserve the total momentum, the solids must affect the gas by an oppositely directed friction force with friction time τ_f/ϵ, as included in the last terms of equations (4.1-4.3). Here ϵ is the local solids-to-gas mass ratio ρ_d/ρ. The bulk density of solids ρ_d at a grid point is calculated by counting the number of particles within a grid cell volume around the point and multiplying by the mass density $\tilde{\rho}_\mathrm{d}$ that each particle represents. The mass density per particle depends on the number of particles and on the assumed average solids-to-gas ratio ϵ_0 as $\tilde{\rho}_\mathrm{d} = \epsilon_0\rho/N_1$, where N_1 is the number of particles per grid cell. Since the gas is approximately isodense and isothermal, we can assume that the friction time is independent of the local state of the gas at the position of a particle. We also assume that the friction time does not depend on the velocity difference between the particle and the gas. This is valid in the Epstein regime, but also in the Stokes regime when the flow around the solid particles is laminar (Weidenschilling 1977a). For conditions typical for a protoplanetary disc at a radial distance of 5 AU from the central object, a given Stokes number $\Omega_0\tau_\mathrm{f}$ corresponds to the particle radius measured in meters (e.g. Johansen et al. 2004), although this depends somewhat on the adopted disc model. We include the friction force contribution to the computational time-step δt by requiring that the time $(\delta t)_\mathrm{fric} = \tau_\mathrm{f}/(1+\epsilon)$ is resolved at least five times in a time-step. This restriction is strongest for small particles and for large solids-to-gas ratios, whereas the Courant time-step of the gas dominates otherwise.

The particle positions change due to the velocity of the particles as

$$\frac{\mathrm{d}x^{(i)}}{\mathrm{d}t} = 0, \tag{4.16}$$

$$\frac{\mathrm{d}y^{(i)}}{\mathrm{d}t} = v_y^{(i)}, \tag{4.17}$$

$$\frac{\mathrm{d}z^{(i)}}{\mathrm{d}t} = v_z^{(i)}. \tag{4.18}$$

Because the simulations are done in two dimensions, we have not allowed particles to move in the x-direction. The particles are still allowed to have a radial velocity component. This is equivalent to assuming that all radial derivatives are zero, so that no advective transport occurs in this direction.

4.4 Richardson number

Before we discuss the setup of the numerical simulations and the results, we describe in this section some of the analytical results that are already known about the KHI.

The stability of a shear flow can be characterised through the Richardson number Ri, defined as

$$\mathrm{Ri} = \frac{g_z \partial \ln(\rho + \rho_\mathrm{d})/\partial z}{(\partial u_y/\partial z)^2} \,. \tag{4.19}$$

The Richardson number quantifies the fact that vertical gravity g_z and density stratification of gas and solids $\partial \ln(\rho+\rho_\mathrm{d})/\partial z$ are stabilising effects, whereas the shear $\partial u_y/\partial z$ is destabilising. As shown by Chandrasekhar from very simple considerations of the free energy that is present in a stratified shear flow, a flow with $\mathrm{Ri} > 1/4$ is always stable, whereas $\mathrm{Ri} < 1/4$ is necessary, but not sufficient, for an instability (Chandrasekhar 1961 p. 491). These derivations do, however, not include the effect of the Coriolis force, a point that we shall return to later.

For shear flows induced by solids in protoplanetary discs, S98 derived an expression for the vertical density distribution of solids in a protoplanetary disc that is marginally stable to the KHI, i.e. where the gas flow has a constant Richardson number equal to the critical Richardson number for stability $\mathrm{Ri_c}$. For small particle radii the solids-to-gas ratio $\epsilon(z)$ in this state can be written as

$$\epsilon(z) = \begin{cases} \frac{1}{\sqrt{z^2/H_\mathrm{d}^2 + 1/(1+\epsilon_1)^2}} - 1 & \text{for } |z| < z_\mathrm{d} \\ 0 & \text{for } |z| \geq z_\mathrm{d} \end{cases} \,, \tag{4.20}$$

where ϵ_1 is the solids-to-gas ratio in the mid-plane, $z_\mathrm{d} = H_\mathrm{d}\sqrt{1 - 1/(1+\epsilon_1)^2}$, and H_d is the width of the solids layer. The effect of self-gravity between the solids has been ignored. The width of the solids layer can furthermore be written as

$$H_\mathrm{d} = \sqrt{\mathrm{Ri_c}}\frac{|\beta|}{2\gamma} H \,, \tag{4.21}$$

where β is the radial pressure gradient parameter introduced in Sect. 4.3.1, γ is the ratio of specific heats and H is the scale-height of the gas. For $\mathrm{Ri_c} = 1/4$ and $\gamma = 5/3$

$$H_\mathrm{d}/H = \frac{3}{20}|\beta| \,, \tag{4.22}$$

so the width of the marginally stable solids layer is a few percent of a gas scale height.

The expression in equation (4.20) allows for two types of stratification of solids in the marginally stable disc. For $\rho_\mathrm{d} \ll \rho$ the bulk density of solids is constant around the mid-plane, whereas for $\rho_\mathrm{d} \gg \rho$, a cusp of very high density can exist around the mid-plane (S98). Such a cusp can form for two reasons when the solids-to-gas ratio is above unity. Firstly because the gas flow is forced to be Keplerian in such a large region around the mid-plane that the vertical shear is reduced there, stabilising against the KHI, and secondly because it requires a lot of energy to lift up so much solid material from the mid-plane. This effect has been interpreted by Youdin and Shu (2002) as the gas only being able to lift up its own equivalent mass due to KHI.

4.5 Initial condition

The initial condition of the gas is an isothermal, stratified disc with a scale height H. The density depends on the height over the mid-plane z as

$$\rho(z) = \rho_1 \mathrm{e}^{-z^2/(2H^2)}\,, \tag{4.23}$$

where ρ_1 is the density in the mid-plane. The scale height is $H = c_\mathrm{s}/\Omega_0$, where c_s determines the constant initial temperature, to sustain hydrostatic equilibrium in the vertical direction. From the definition of the gas column density Σ, we can calculate the mid-plane density as $\rho_1 = \Sigma/(\sqrt{2\pi}H)$. There is no similar equilibrium to set the density of solids in the disc. Thus we distribute the particles in a Gaussian way around the mid-plane with a scale height H_d, a free parameter, and normalise the distribution so that $\Sigma_\mathrm{d} = \epsilon_0\Sigma$, where ϵ_0 is the global solids-to-gas ratio in the disc.

The constant global pressure gradient force effectively decreases the radial gravity felt by the gas, and thus the orbital speed is no longer Keplerian, but slightly smaller. The sub-Keplerian velocity $u_y^{(0)}$ is given by

$$u_y^{(0)} = \frac{\beta}{2\gamma} c_\mathrm{s}\,. \tag{4.24}$$

This expression is obtained by setting $u_x = \partial u_x/\partial t = \epsilon = 0$ in equation (4.1). The solids, on the other hand, do not feel the global pressure gradient and would thus in the absence of friction move on a Keplerian orbit with $v_y^{(i)} = 0$. The drag force from the gas, however, forces the solids to move at a speed that is below the Keplerian value, at least when the solids-to-gas ratio is low. When the solids-to-gas ratio approaches unity or even larger, the gas is forced by the solids to move with Keplerian speed. The equilibrium gas and solids velocity can be calculated as a function of solids-to-gas ratio (Nakagawa et al. 1986), but we choose to simply start the gas with a sub-Keplerian velocity and the solids with a Keplerian velocity, and then let the velocities approach the equilibrium dynamically (this happens within a few friction times). This way we have checked that the numerical solution indeed approaches the expressions by Nakagawa et al. (1986) for all the velocity components of the gas and the solids, which serves as a control that the friction force from the solid particles on the gas has been correctly implemented in the code.

In the equilibrium state the gas has a positive radial velocity in the mid-plane, but this does not lead to any change of the gas density, since we have ignored the advection of the global density in the continuity equation. The effect of an outwards-moving mid-plane on the global dynamics of a protoplanetary disc is a promising topic of future research.

Periodic boundary conditions are used for all variables in the azimuthal direction. In the vertical direction we impose a condition of zero vertical velocity, whereas the two other velocity components have a zero derivative condition over the boundary. The logarithmic mass density and the entropy have a condition of vanishing third derivatives over the vertical boundary.

We run simulations for three different particle sizes, $\Omega_0\tau_\mathrm{f} = 0.02, 0.1, 1.0$, respectively. When assuming compact spherical particles, these numbers correspond to sizes of centimeters (pebbles), decimeters (rocks), and meters (boulders), respectively. The computation parameters

Table 4.1. Run parameters

Run (1)	$\Omega_0\tau_\mathrm{f}$ (2)	ϵ_0 (3)	$L_y \times L_z$ (4)	$N_y \times N_z$ (5)	N (6)	N_1 (7)	$\Delta t/\Omega_0^{-1}$ (8)
A	0.02	0.01	0.40×0.20	256×128	400,000	12.2	200
B	0.10	0.01	0.40×0.20	256×128	400,000	12.2	200
C	1.00	0.01	0.10×0.05	256×128	400,000	12.2	80
Be2	0.10	0.02	0.40×0.20	256×128	400,000	12.2	100
Be5	0.10	0.05	0.40×0.20	256×128	400,000	12.2	100
Be10	0.10	0.10	0.40×0.20	256×128	400,000	12.2	100
Br512	0.10	0.01	0.40×0.20	512×256	1,600,000	12.2	100

Note. — Col. (1): Name of run. Col. (2): Stokes number. Col. (3): Global solids-to-gas ratio. Col. (4): Size of simulation box. Col. (5): Grid resolution. Col. (6): Number of particles. Col. (7): Number of particles per grid point. Col. (8): Total time of run in units of Ω_0^{-1}

are listed in Table 4.1. The size of the box is set according to the vertical extent of the solids layer in the state of self-sustained Kelvin-Helmholtz turbulence. We make sure that the full width of the solids layer fits at least five times vertically in the box to avoid any effect of the vertical boundaries on the mid-plane. The azimuthal extent of the box is set so that the full width of the solids layer fits at least ten times in this direction. Thus the unstable modes of the Kelvin-Helmholtz turbulence, which have a wavelength that is similar to the width of the solids layer, are very well-resolved.

Since the ratio of particles to grid points is $N_1 \approx 12$, the computation time is strongly dominated by the particles. Each particle needs to "know" the gas velocity field at its own position in space, to calculate the friction forces. For parallel runs we distribute the particles among the different processors so that the position of each particle is within its "host" processor's space interval. As we show in Sect. 4.6, the particles tend to have a strongly non-axisymmetric density distribution in the Kelvin-Helmholtz turbulence. This clumping means that the number of particles on the individual processors varies by a factor of around five, thus slowing the code down by a similar factor compared to a run where the particles were equally distributed over the processors. For this reason we used 32 Opteron processors, each with 2.2 GHz CPU speed and Infiniband interconnections, for around one week for each run.

4.6 Dynamics and density of solids

In this section we focus on the dynamics and the density of the solid particles. The linear growth rate of the Kelvin-Helmholtz instability and the statistical properties of the Kelvin-

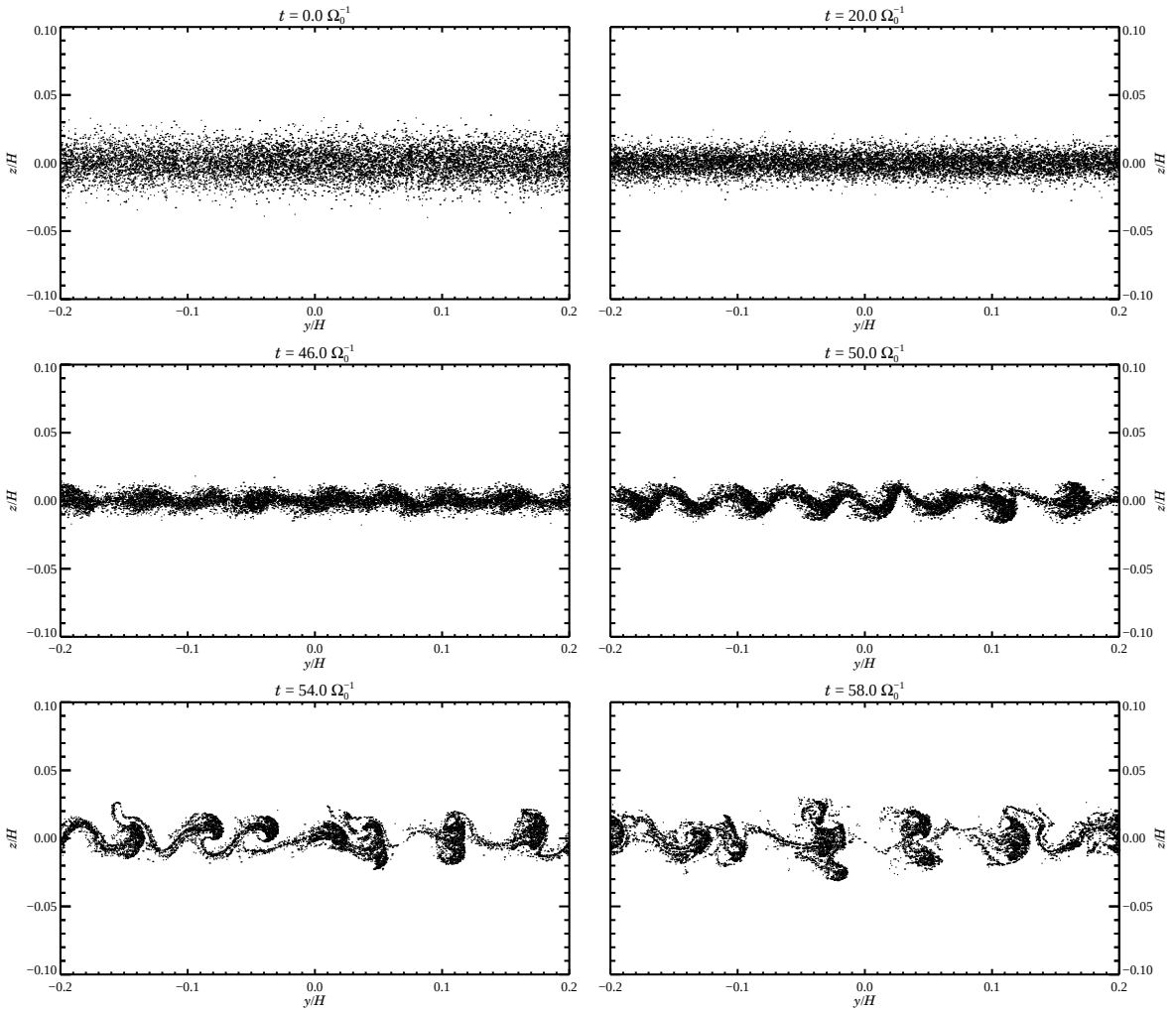

Fig. 4.1 The onset of the Kelvin-Helmholtz instability for cm-sized pebbles with $\Omega_0\tau_\mathrm{f} = 0.02$. The initial Gaussian particle distribution falls towards the mid-plane of the disc on the characteristic time-scale of $t_\mathrm{grav} = 1/(\Omega_0^2\tau_\mathrm{f}) \approx 50\Omega_0^{-1}$. The increased vertical shear in the gas rotation velocity eventually makes the disc unstable to the KHI, forming waves that finally break as the turbulence goes into its non-linear state.

Helmholtz turbulence are treated in the next two sections.

Some representative snapshots of the particle positions for run A ($\Omega_0\tau_\mathrm{f} = 0.02$, or cm-sized pebbles) are shown in Fig. 4.1. The particles, with an initial Gaussian density distribution, settle to the mid-plane due to gravity, on the characteristic time-scale $t_\mathrm{grav} = 1/(\tau_\mathrm{f}\Omega_0^2) \approx 50$. When the width of the layer has decreased to around 0.01 scale heights (the two middle panels of Fig. 4.1), some wave pattern can already be seen in the bulk density of solids. It is the most unstable $u_z(y)$ mode, with a wavelength that is comparable to the vertical width of the layer, that is growing in amplitude. Some shear times later, in the two bottom panels of Fig. 4.1, the growing mode enters the non-linear regime, and impressive patterns of breaking

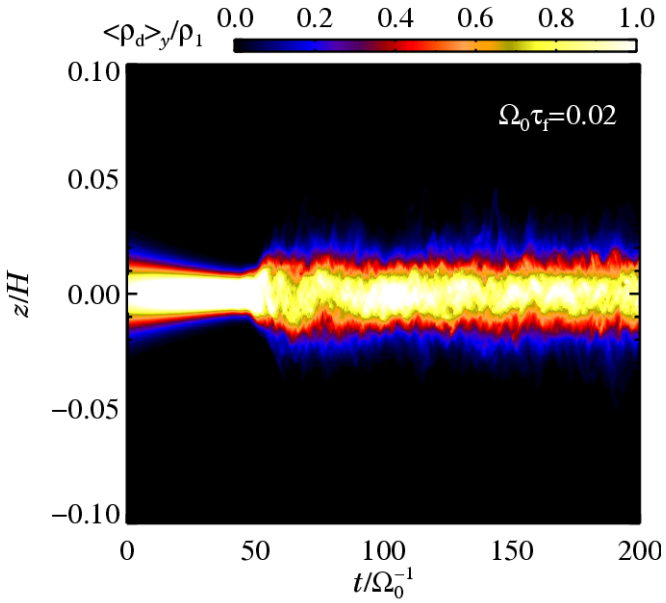

Fig. 4.2 Contour plot of the bulk density of cm-sized pebbles averaged over the azimuthal y-direction, as a function of time t and height over the mid-plane z. After the Kelvin-Helmholtz instability sets in and saturates into turbulence, the width of the solids layer stays approximately constant. The black regions contain no particles at all.

waves appear. The simulation then goes into a state of fully developed Kelvin-Helmholtz turbulence.

4.6.1 Pebbles and rocks

In Figs. 4.2 and 4.3 we show azimuthally averaged density contours as a function of time for particles with friction time $\Omega_0\tau_\mathrm{f} = 0.02$ (run A) and $\Omega_0\tau_\mathrm{f} = 0.1$ (run B, decimeter-sized rocks), respectively. These two particle sizes show very similar behaviour with time. In the beginning the particles move towards the mid-plane unhindered because of the lack of turbulence. The sedimentation happens much faster in run B than in run A because of the different particle sizes. When the KHI eventually sets in, the solids layer is puffed up again and quickly reaches an equilibrium configuration where the vertical distribution of bulk density is practically unchanged with time.

One can already here suspect that the equilibrium bulk density of solids is indeed, as predicted analytically by S98, distributed in such a way that the flow has a constant Richardson number. In Figs. 4.4 and 4.5 we plot the time-averaged bulk density and the Richardson number as a function of vertical height over the mid-plane, again for the two small particle sizes. The solids-to-gas ratio reaches unity in the mid-plane and drops down rapidly away from the mid-plane. For run A the Richardson number is approximately constant, just above unity, in the region around the mid-plane that has a significant bulk density of solids. For run B the value of the Richardson number is also constant, although somewhat smaller than for

the centimeter-sized particles, because the more rapid sedimentation of these larger particles allows the disc to sustain a stronger vertical shear.

4.6.2 Boulders

For bodies with $\Omega_0\tau_\mathrm{f} = 1.0$ (run C, m-sized boulders), the azimuthally averaged bulk density is shown in Fig. 4.6. These meter-sized boulders fall rapidly to the mid-plane, on a time-scale of one shear time, because they are not as coupled to the gas as smaller particles. The scale height of the boulders is very small, less than one percent of the scale height of the gas, because the particles are falling so fast that the disc can sustain a much lower Richardson number than the critical. This is also evident from Fig. 4.8. The Richardson number is well below unity, around 0.1, where significant amounts of solids is present.

A major difference between the large particles and the small particles is the presence of bands in Fig. 4.6. The solid particles are no longer smoothly distributed over z, but rather appear as clumps that oscillate around the mid-plane. The oscillation of a single clump is evident from Fig. 4.7. Here the bulk density contours are plotted at four times separated by one shear time. The clump indicated by the arrow is oscillating around the mid-plane. Such oscillatory behaviour is also be expected from the following considerations. Friction ensures that small particles arrive at the mid-plane with zero residual velocity, whereas larger particles perform damped oscillations around $z = 0$ with a damping time of one friction time. The distinction between the two size regimes can be derived by looking at the differential equation governing vertical settling of particles,

$$\frac{\mathrm{d}v_z(t)}{\mathrm{d}t} = -\Omega_0^2 z - \frac{1}{\tau_\mathrm{f}} v_z \,. \tag{4.25}$$

This second order, linear ordinary differential equation can be solved trivially (e.g. Nakagawa et al. 1986). The result is a split between two types of solutions, depending on the value of $\Omega_0\tau_\mathrm{f}$. For $\Omega_0\tau_\mathrm{f} \leq 0.5$ the solution is a purely exponentially decaying function. On the other hand, for $\Omega_0\tau_\mathrm{f} > 0.5$ the solutions are damped oscillations with a characteristic damping time of around one friction time. For a friction time around unity, the amplitude of the bulk density in a laminar disc would still become virtually zero in just a few friction times. This is not the case in Fig. 4.6 where the scale height of the solids stays approximately constant for at least 80 friction times (the end of the simulation). The KHI is continuously pumping energy into the solids layer at the same rate as the oscillations are damped.

In Fig. 4.9 we plot the root-mean-square value of the z-coordinate of the particles as a function of time for all three runs. The calculated "scale height" of the cm-sized and dm-sized particles are very similar, although the larger particles have a bit lower scale height than the smaller particles. The m-sized particles have a scale height of about one quarter of a percent of that of the gas.

4.6.3 Maximum density and clumping

It is of great relevance for planetesimal formation to find the highest bulk density that is permitted in the saturated Kelvin-Helmholz turbulence. Both coagulation and gravitational

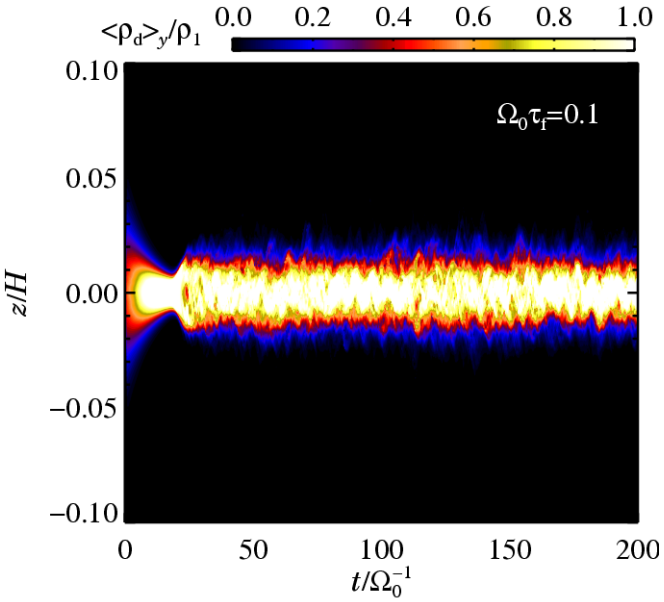

Fig. 4.3 Same as Fig. 4.2, but for dm-sized rocks with $\Omega_0\tau_f = 0.1$. The sedimentation timescale is much faster than in Fig. 4.2, but the width of the solids layer in the self-sustained state of turbulence is approximately the same.

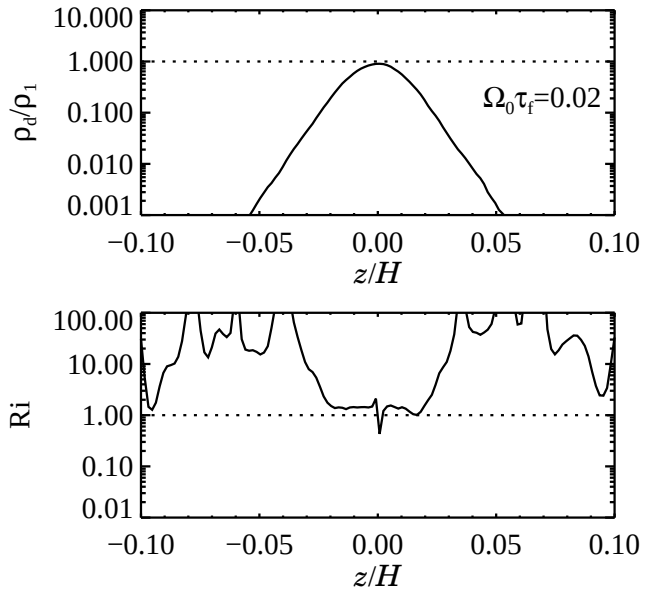

Fig. 4.4 Bulk density and Richardson number of solids with $\Omega_0\tau_f = 0.02$ averaged over the azimuthal direction and over time. The solids-to-gas ratio in the mid-plane is close to unity and falls rapidly outwards. The Richardson number is approximately constant in the mid-plane and has a value around unity.

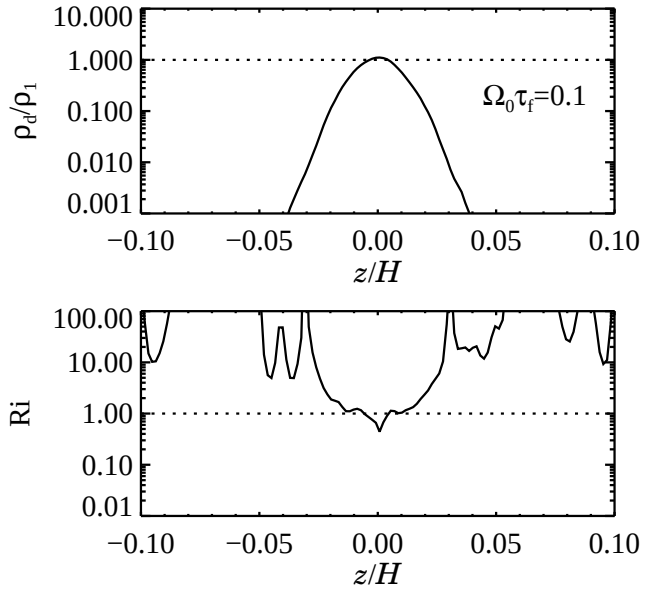

Fig. 4.5 Same as in Fig. 4.4, but for $\Omega_0\tau_f = 0.1$. Although the density in the mid-plane is similar to the value for smaller particles, the solids are more settled and have less pronounced wings away from the mid-plane. The Richardson number is again around unity in the mid-plane.

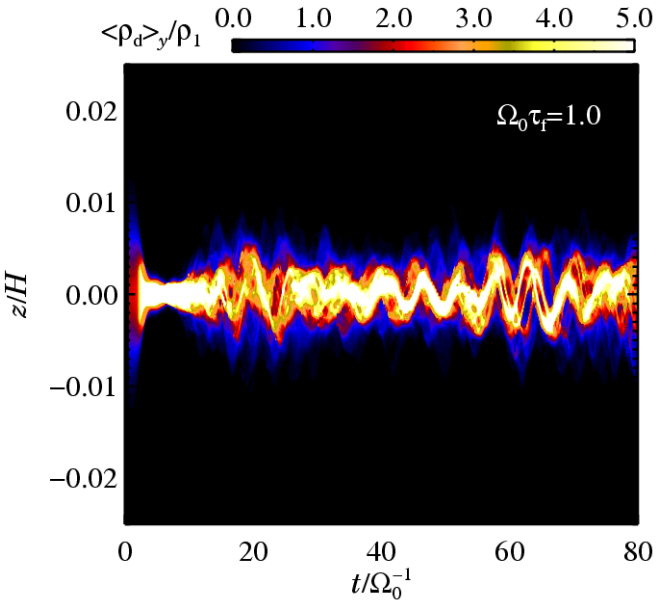

Fig. 4.6 Same as Fig. 4.3, but for m-sized boulders with $\Omega_0\tau_f = 1.0$. The equilibrium scale height of the solids is around 10 times lower than for the smaller particles.

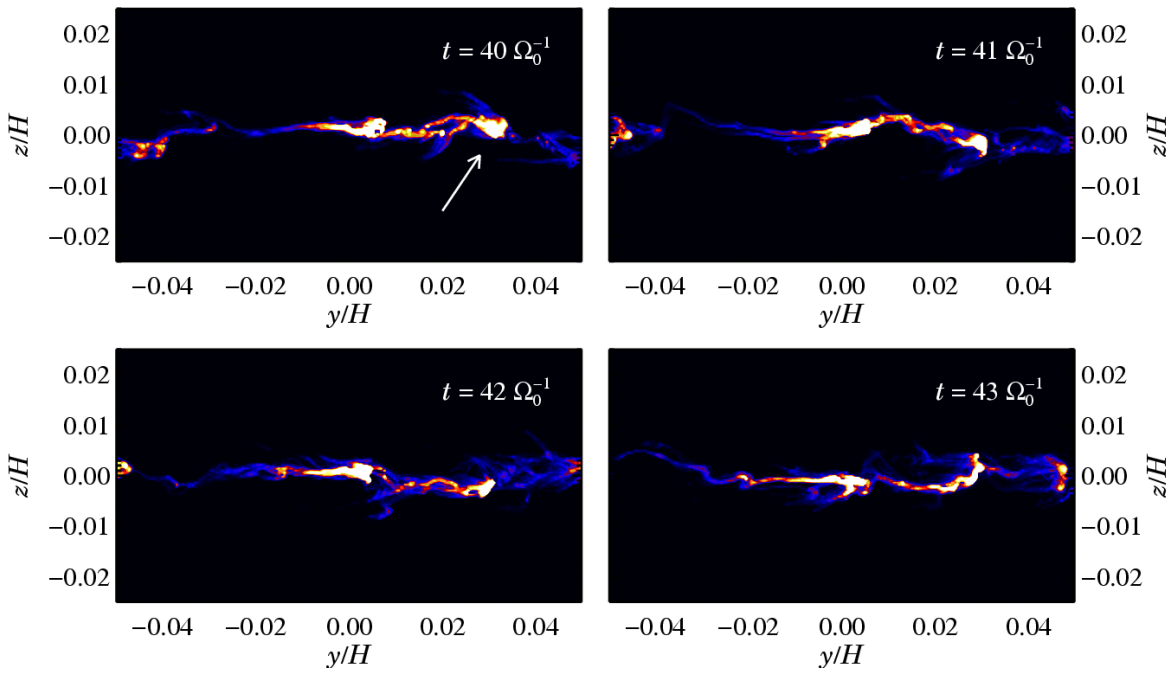

Fig. 4.7 Contour plot of the particle density for $\Omega_0\tau_\mathrm{f} = 1.0$. A clump, indicated by the arrow, oscillates around the mid-plane, a type of motion that is only allowed for particles with $\Omega_0\tau_\mathrm{f} > 0.5$.

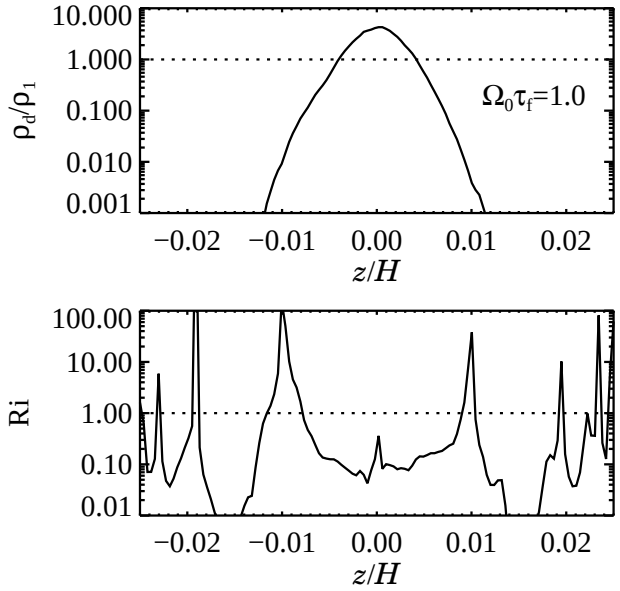

Fig. 4.8 Same as in Fig. 4.4, but for $\Omega_0\tau_\mathrm{f} = 1.0$. The Richardson number around the mid-plane is here way lower than for the smaller particles, around 0.1. This is caused by the extremely rapid settling of m-sized boulders to the mid-plane.

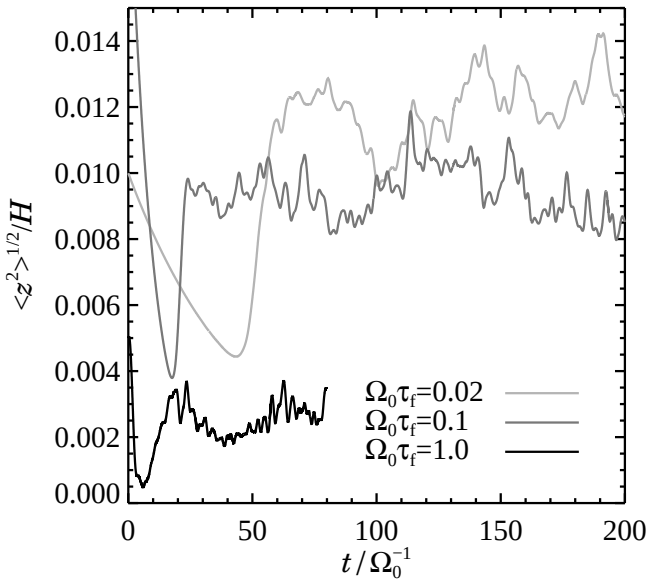

Fig. 4.9 The root-mean-square z-coordinate of the particles for the different runs. For $\Omega_0\tau_f = 0.02$ and $\Omega_0\tau_f = 0.1$, the width of the solids layer is around 1% of a gas scale height, whereas for meter-sized boulders with $\Omega_0\tau_f = 1.0$, the strong sedimentation results in a much lower width, only around 0.25% of a scale height.

fragmentation depend strongly on the mass density of the solids layer. High densities can occur not only when the gas flow or the size of the boulders allow for a high mid-plane density, but also in certain points of the turbulent flow where solid particles tend to accumulate. The latter can only be explored in computer simulations, so we examine the maximum bulk density in any grid point in more detail in this section.

The maximum mass density of solid particles in any grid cell is plotted in Fig. 4.10 as a function of time. Even though the mid-plane solids-to-gas ratio is on the average of the order unity for all particle sizes, the maximum density is much higher at all times, especially for meter-sized particles where the maximum solids-to-gas ratio can be up to one thousand. Decimeter-sized particles have a maximum solids-to-gas ratio of around 20 at all times, whereas the value for centimeter-sized particles is around 10. This is potentially important for building planetesimals. Even if the critical density for gravity-aided planetesimal formation is not reached globally, this is still possible in certain regions of the turbulent flow. Such a gravoturbulent formation of planetesimals was proposed by Johansen et al. (2006b) [see also Chapter 3] to lead to the formation of planetesimals in a magnetorotationally turbulent gas.

In Fig. 4.11 we plot contours of the vertically averaged bulk density as a function of azimuthal coordinate y and time t for decimeter-sized rocks (run B). It is evident that the bulk density has a strong non-axisymmetric component once the Kelvin-Helmholtz turbulence is fully developed. Dense clumps are seen as white stripes, while regions of lower solids-to-gas ratio are grey. A simple way to quantify the amount of non-axisymmetry is to look at the mean deviation of the density from the average density. We define the *azimuthal clumping factor*

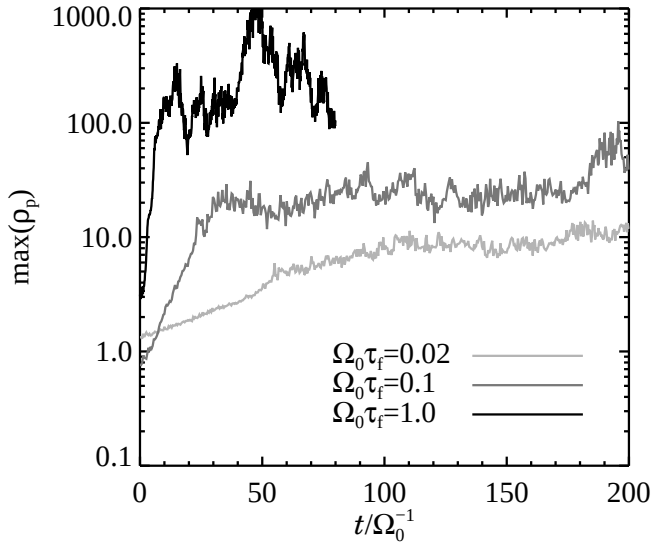

Fig. 4.10 The maximum bulk density of solid particles in any grid cell as a function of time, in units of the gas mid-plane density, as a function of time. The value is much higher than the azimuthally averaged mid-plane densities (presented in previous figures).

c_y as

$$c_y = \frac{\sqrt{\langle [n_y(y) - \langle n_y(y) \rangle]^2 \rangle}}{\langle n_y(y) \rangle} \,. \tag{4.26}$$

Here $n_y(y) \equiv \langle n(y,z) \rangle_z$ is the number density of solids averaged over the vertical direction. Axisymmetry implies $c_y = 0$, whereas higher values of c_y imply stronger and stronger non-axisymmetry. We plot in Fig. 4.12 the azimuthal clumping factor as a function of time for all three values of the friction time. For centimeter and decimeter particles the clumping is of the order unity, or in other words, the average grid point has a density variation from the average that is on the same order as the average, i.e. very strong clumping. For meter-sized particles the azimuthal clumping is even stronger.

The tendency for the solid particles to clump is a consequence of the sub-Keplerian velocity of the gas. Turning again to Fig. 4.11, one sees that brighter regions move at a lower speed (relative to the Keplerian speed) than dark regions do. The speed of a clump is evident from the absolute value of the angle between the tilted time-space wisp and the time-axis. Bright wisps have a higher angle with the time-axis than dark wisps. This instability is very related to the *streaming instability* found by Youdin and Goodman (2005), although in our simulations the clumping happens in the (y,z)-plane and not the (x,z)-plane as in the analysis by Youdin & Goodman. Still the instability is powered in both planes by the dependence of the velocity of the solids on the solids-to-gas ratio, so we consider the instability in the (y,z)-plane a special case of the streaming instability. We refer to Youdin and Goodman (2005) for a linear stability analysis of the coupled flow of gas and solids. In the rest of this section we instead focus on describing the non-linear outcome of the streaming instability with a simple analogy to a hydrodynamical shock.

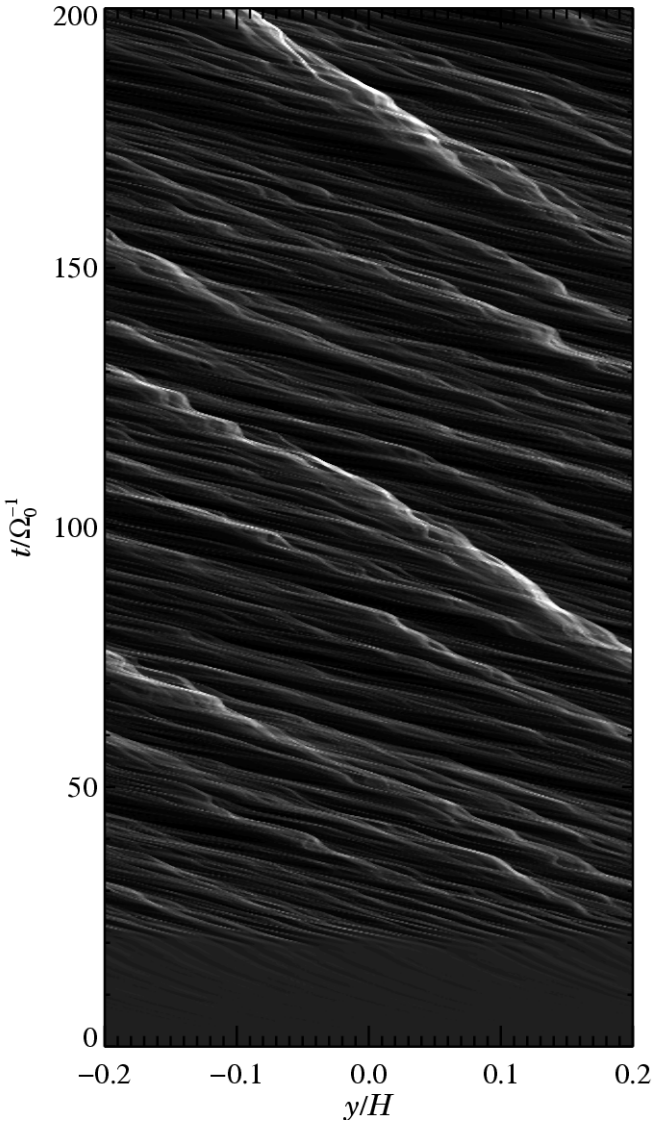

Fig. 4.11 Vertically averaged bulk density of rocks with $\Omega_0\tau_\mathrm{f} = 0.1$ as a function of azimuthal coordinate y and time t. The clumping mechanism is evident from the plot. Regions of high solids-to-gas ratio (light) move slower than regions of low solids-to-gas ratio (grey), seen in the different slopes of the bright and dark wisps on the plot, causing the high density clumps to be continuously fed by low density material. One also sees the rarefaction tail going to the left of the dense clumps and the shock front that is formed against the sub-Keplerian stream.

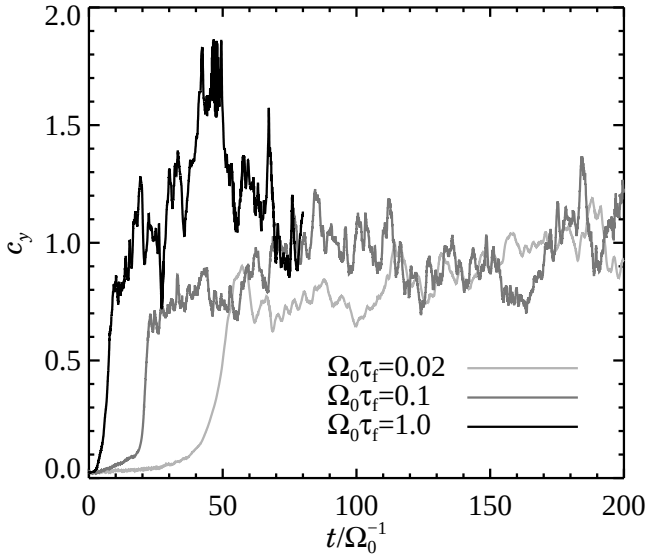

Fig. 4.12 Azimuthal clumping factor c_y versus time for all three particle sizes. A value of around unity corresponds to strong clumping with the average point being 100% away in density from the average density.

Using the derivations given by Nakagawa et al. (1986) for the equilibrium velocities of gas and solids as a function of the solids-to-gas mass ratio ϵ, one can write up the azimuthal velocity component of the solids as

$$w_y = \frac{1+\epsilon}{(1+\epsilon)^2 + (\Omega_0 \tau_\mathrm{f})^2} u_y^{(0)} \,. \tag{4.27}$$

Thus clumps with a high solids-to-gas ratio move slower, relative to the Keplerian speed, than clumps with a low solids-to-gas ratio. The small clumps crash into the big clumps and form larger structures. At the same time, the large clumps steepen up against the direction of the sub-Keplerian flow and develop an escaping tail downstream. This is qualitatively similar to a shock. Considering the continuity equation of the solids-to-gas ratio

$$\frac{\partial \epsilon}{\partial t} = -w_y \frac{\partial \epsilon}{\partial y} - \epsilon \frac{\partial w_y}{\partial y} \,, \tag{4.28}$$

and inserting equation (4.27) in the limit of small Stokes numbers $\Omega_0 \tau_\mathrm{f} \ll 1$, equation (4.28) can be reduced to

$$\frac{\partial \epsilon}{\partial t} = -\frac{u_y^{(0)}}{(1+\epsilon)^2} \frac{\partial \epsilon}{\partial y} \,, \tag{4.29}$$

qualitatively similar to the advection equation of fluid dynamics. The shock behaviour of the clumps arises because the advection velocity $u_y^{(0)}/(1+\epsilon)^2$ depends on the solids-to-gas ratio.

4.6.4 Varying the global solids-to-gas ratio

It is of great interest to investigate the dependence of the density of solids in the mid-plane on the global solids-to-gas ratio in the saturated state of Kelvin-Helmholtz turbulence. Increasing the solids-to-gas ratio beyond the interstellar value should potentially lead to the creation of a very dense mid-plane of solids that the gas is not able to lift up, making the solids layer dense enough to undergo gravitational fragmentation (Sekiya 1998; Youdin and Shu 2002; Youdin and Chiang 2004).

The analytically predicted mid-plane solids-to-gas ratio ϵ_1 is found by applying the normalisation

$$\int_{-\infty}^{\infty} \rho_1 \epsilon(z) \mathrm{d}z = \Sigma_\mathrm{d} \tag{4.30}$$

to the constant Richardson number density of equation (4.20). Here Σ_d is the column density of solids, a free parameter that we set through the global solids-to-gas ratio ϵ_0 as $\Sigma_\mathrm{d} = \epsilon_0 \Sigma$. We have approximated the gas density by the gas density in the mid-plane ρ_1, because for $z \ll H$, the variation in gas density is insignificant compared to the variation in solids density . We proceed by inserting the expression for the solids density in a disc with a constant Richardson number, from equation (4.20), into the integral in equation (4.30). Defining the parameter

$$\chi = \frac{\sqrt{\epsilon_1(2+\epsilon_1)}}{1+\epsilon_1}\,, \tag{4.31}$$

the integration yields

$$-2\chi + \ln\left(\frac{1+\chi}{1-\chi}\right) = \frac{\Sigma_\mathrm{d}}{H_\mathrm{d}\rho_1}\,. \tag{4.32}$$

This is a transcendental equation that we solve numerically for χ as a function of the input parameters H_d, given by equation (4.21), and Σ_d. Once χ is calculated, then the solids-to-gas ratio in the mid-plane ϵ_1 is known from equation (4.31).

In Fig. 4.13 we plot the analytical mid-plane solods-to-gas ratio ϵ_1 as a function of the global solids-to-gas ratio ϵ_0 (dotted line). The non-linear behaviour of ϵ_1 is evident, and already for $\epsilon_0 = 0.1$ does the mid-plane solids-to-gas ratio approach $\epsilon_1 = 100$, which should be enough to have a gravitational instability in the solids layer. We also run numerical simulations with an increased global solids-to-gas ratio (runs Be2, Be5 and Be10, see Table 4.1) to see if a mid-plane solids density cusp develops as predicted. The resulting mid-plane solids-to-gas ratio is indicated with stars in Fig. 4.13. To avoid having a very low time-step, because of the strong friction that the solids exert on the gas when the global solids-to-gas ratio is increased, we have locally increased the friction time in regions of very high solids-to-gas ratio. This approach conserves total momentum because the friction force on the gas and on the solids are made lower at the same time. In the regions where the friction time is increased, the solids-to-gas ratio is so high that gas is dragged along with the particles anyway, so the precise value of the friction time does not matter. As seen in Fig. 4.13 the mid-plane solids-to-gas ratio does indeed increase non-linearly with global solids-to-gas ratio, following a curve that is within a factor of two of the analytical curve. This gives support to the theory that an increased global solids-to-gas ratio, e.g. due to solids that are transported from the outer part of the disc into the inner part, can lead to such a high solids-to-gas ratio in the disc mid-plane that the solids layer fragments to form planetesimals (Youdin and Shu 2002).

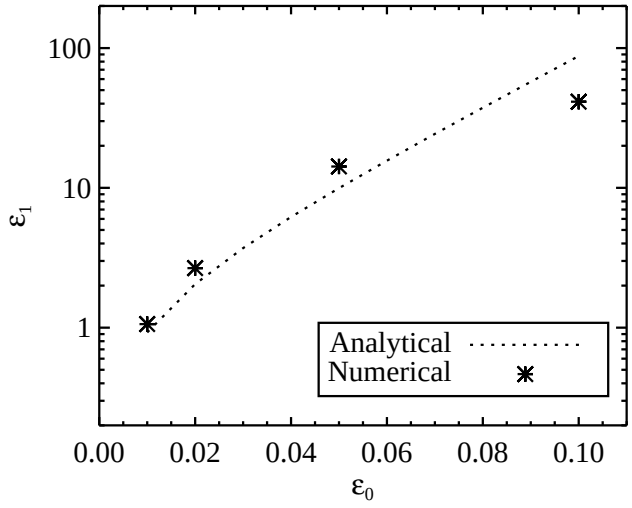

Fig. 4.13 Mid-plane solids-to-gas ratio ϵ_1 as a function of global solids-to-gas ratio ϵ_0. The dotted line shows the analytical value for a solids density with a constant Richardson number of $\mathrm{Ri_c} = 1.0$, while the stars show the result of the numerical simulations for different values of the global solids-to-gas ratio. The results agree nicely, giving support to the idea that a solids-to-gas ratio that is higher than the interstellar value can give rise to high enough mid-plane solids density for a gravitational instability in the solids layer.

4.7 Growth rates

The simulations presented so far all imply a critical Richardson number that is of the order unity, rather than the classically adopted value of 1/4. This confirms the findings of GO05 that shear flows with a Richardson number that is higher than the classical value are actually unstable when the Coriolis force is included in the calculations. To quantify the linear growth of the instability we have run simulations of initial conditions with a constant Richardson number and measured the growth rates of the KHI. Because we are only interested in the linear regime, we have chosen for simplicity to treat solids as a fluid rather than as particles. Thus we solve equations similar to equations (4.13-4.15) for the solids velocity field $\boldsymbol{w}$ including an advection term $(\boldsymbol{w}\cdot\boldsymbol{\nabla})\boldsymbol{w}$. A continuity equation similar to equation (4.9) for the logarithmic solids number density $\ln n$ is solved at the same time.

We consider initial conditions with a constant Richardson number, in the range between 0.1 and 2.0, as given by equation (4.20). The solids-to-gas ratio in the mid-plane ϵ_1 is known from equations (4.31) and (4.32). To avoid any effects of settling of solids, we set the friction time to $\Omega_0\tau_\mathrm{f} = 0.001$. The gravitational settling time is then as high as $1000\Omega_0^{-1}$, and since this is much longer than the duration of the linear growth, the effect on the measured growth rate is insignificant. The vertical velocity of the solids is set to the terminal settling velocity $w_z = -\tau_\mathrm{f}\Omega_0^2 z$. Since the velocity of the solids is not zero, the gas will feel some friction from

the falling solids. The vertical component of the equation of motion of the gas is

$$\frac{\partial u_z}{\partial t} = -\Omega_0^2 z - \frac{1}{\gamma} c_\mathrm{s}^2 \frac{\partial \ln \rho}{\partial z} - \frac{\epsilon}{\tau_\mathrm{f}}(u_z - w_z)\,. \tag{4.33}$$

We insert the terminal velocity expression for the velocity of solids into equation (4.33) and look for equilibrium solutions with $u_z = \partial u_z / \partial t = 0$. The equation is then reduced to

$$0 = -(1+\epsilon)\Omega_0^2 z - \frac{1}{\gamma} c_\mathrm{s}^2 \frac{\partial \ln \rho}{\partial z}\,. \tag{4.34}$$

The drag force exerted by the falling solids on the gas mimics a vertical gravity, and therefore we have combined it with the regular gravity term. In a way it *is* the gravity on the solids that the gas feels, only it is transferred to the gas component through the drag force. One can interpret this as the gas feeling a stronger gravity $\Omega_\mathrm{K}' = \sqrt{1+\epsilon}\Omega_0$ in places of high solids-to-gas ratio, which leads to the creation of a small cusp in the gas density around the mid-plane. Inserting now equation (4.20) into equation (4.34) and applying the boundary condition $\rho(z=0) = \rho_1$ yields

$$\ln \rho(z) = \begin{cases} \ln \rho_1 + \frac{\gamma \Omega_0^2 H_\mathrm{d}^2}{c_\mathrm{s}^2} \left[\frac{1}{1+\epsilon_1} - \sqrt{\frac{z^2}{H_\mathrm{d}^2} + \frac{1}{(1+\epsilon_1)^2}} \right] \\ \qquad\qquad\qquad \text{for } |z| < z_\mathrm{d} \\ \ln \rho_1 + \frac{\gamma \Omega_0^2 H_\mathrm{d}^2}{c_\mathrm{s}^2} \left[-\frac{1}{2}\frac{z^2}{H_\mathrm{d}^2} - \frac{\epsilon_1^2}{2(1+\epsilon_1)^2} \right] \\ \qquad\qquad\qquad \text{for } |z| \geq z_\mathrm{d} \end{cases}\,. \tag{4.35}$$

The cusp around the mid-plane, caused by the extra gravity imposed by the falling solids on the gas, is shown in Fig. 4.14. The variation in density from a normal isothermal disc is only a few parts in ten thousand, so the effect is not big. On the other hand, it is important to have a complete equilibrium solution as the initial condition for the measurement of the linear growth of the instability, as otherwise dynamical effects could dominate over the growth.

We measure the linear growth rate of the KHI by prescribing a solids-to-gas ratio according to equation (4.20) and a gas density according to equation (4.35). We then set the velocity fields of gas and solids according to the expressions derived in Nakagawa et al. (1986). The width of a solids layer with a constant Ri depends on the value of Ri according to equation (4.21), so we have made sure to always resolve the unstable wavelengths by making the box larger with increasing Ri. The fluid simulations are all done with a grid resolution of $N_y \times N_z = 256 \times 128$.

The measured growth rates are shown in Fig. 4.15. At a Richardson number close to zero, the growth rate is similar in magnitude to the rotation frequency Ω_0 of the disc, whereas for larger values of the Richardson number, the growth rate falls rapidly. We find that there is growth out to at least Ri = 2.0, with a growth rate approaching $\omega = 0.01\Omega_0$. There is no evidence for a cut-off in the growth rate at the classical value of the critical Richardson number of 0.25. The range of unstable Richardson numbers is in good agreement with the mid-plane Richardson number in the particle simulations shown in Figs. 4.4 and 4.5. This is another confirmation that the critical Richardson number is around unity or higher when the Coriolis force is included in the calculations. On the other hand, when the Keplerian shear is included, growth rates higher than the shear rate $3/2\Omega_0$ are expected to be required to overcome the shear (Ishitsu and Sekiya 2003), although numerical simulations in 3-D would be required to address these analytical results in detail.

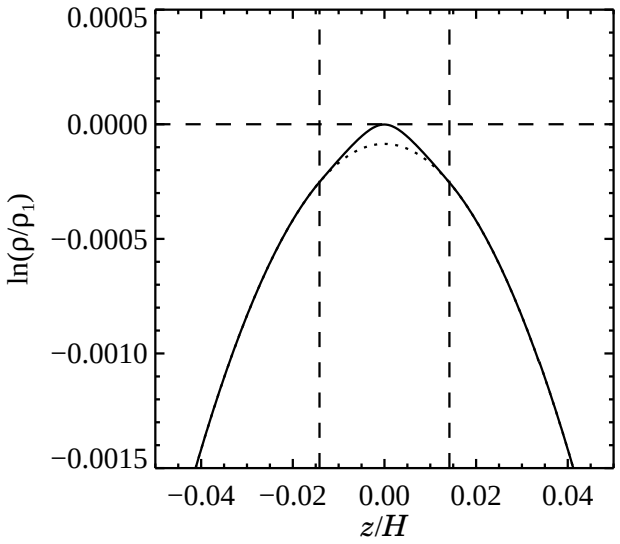

Fig. 4.14 The logarithmic gas density as a function of height over the mid-plane z in the presence of falling solids. The drag force exerted on the gas by the falling solids mimics an extra gravity near the mid-plane, making the gas scale height slightly lower close to the mid-plane. The result is the formation of a cusp, although of a very moderate amplitude of about 1/10000 compared to a disc with no sedimentation of solids (dotted line).

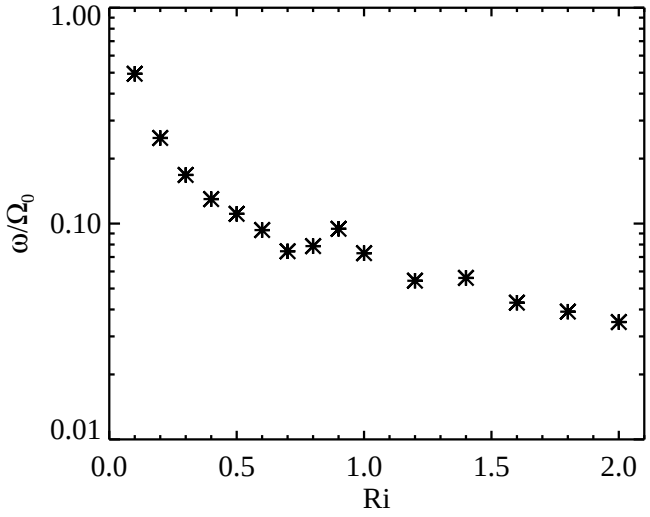

Fig. 4.15 Initial growth rate of the Kelvin-Helmholtz instability as a function of the Richardson number Ri. There is measurable growth out to at least Ri = 2.0, which is way beyond the classical value of the critical Richardson number of $\mathrm{Ri_c} = 0.25$.

Table 4.2. Diffusion coefficients

Run (1)	$\Omega_0\tau_\mathrm{f}$ (2)	$\sqrt{\langle z^2\rangle}/H$ (3)	$\delta_\mathrm{t}/10^{-6}$ (4)
A	0.02	0.0121 ± 0.0010	3.0 ± 0.5
B	0.10	0.0094 ± 0.0008	8.9 ± 1.5
C	1.00	0.0025 ± 0.0004	6.5 ± 2.4
Be2	0.10	0.0081 ± 0.0006	6.5 ± 1.0
Be5	0.10	0.0047 ± 0.0003	2.2 ± 0.3
Be10	0.10	0.0031 ± 0.0002	1.0 ± 0.1
Br512	0.10	0.0086 ± 0.0005	7.5 ± 0.8

Note. — Col. (1): Name of run. Col. (2): Stokes number. Col. (3): Scale height of solids. Col. (4): Diffusion coefficient derived from equation (4.37).

Our measured growth rates are somewhat smaller than in GO05, but we believe that this is due to the different Coriolis force term in the present work. Changing the factor $-1/2$ to a factor -2 in equations (4.2) and (4.14) yields very similar growth rates to GO05. The factor $-1/2$ is a consequence of the advection of the Keplerian rotation velocity when fluid parcels move radially, an effect that was not included in the simulations of GO05.

4.8 Properties of Kelvin-Helmholtz turbulence

4.8.1 Diffusion coefficient

The effect of turbulence on the vertical distribution of solid particles can be quantified as a diffusion process with the turbulent diffusion coefficient D_t (Cuzzi et al. 1993; Dubrulle et al. 1995; Schräpler and Henning 2004). Assuming that D_t is a constant, i.e. independent of the height over the mid-plane, the equilibrium between vertical settling of solids with velocity $w_z = -\tau_\mathrm{f}\Omega_0^2 z$ and turbulent diffusion implies a vertical distribution of the solids-to-gas ratio $\epsilon(z)$ that is Gaussian around the mid-plane (Dubrulle et al. 1995),

$$\epsilon = \epsilon_1 \exp[-z^2/(2H_\epsilon^2)]\,, \tag{4.36}$$

with the solids-to-gas ratio scale height given by the expression $H_\epsilon^2 = D_\mathrm{t}/(\tau_\mathrm{f}\Omega_0^2)$. Writing now $D_\mathrm{t} = \delta_\mathrm{t} H^2 \Omega_0$, we get

$$\delta_\mathrm{t} = \left(\frac{H_\epsilon}{H}\right)^2 \Omega_0\tau_\mathrm{f}\,. \tag{4.37}$$

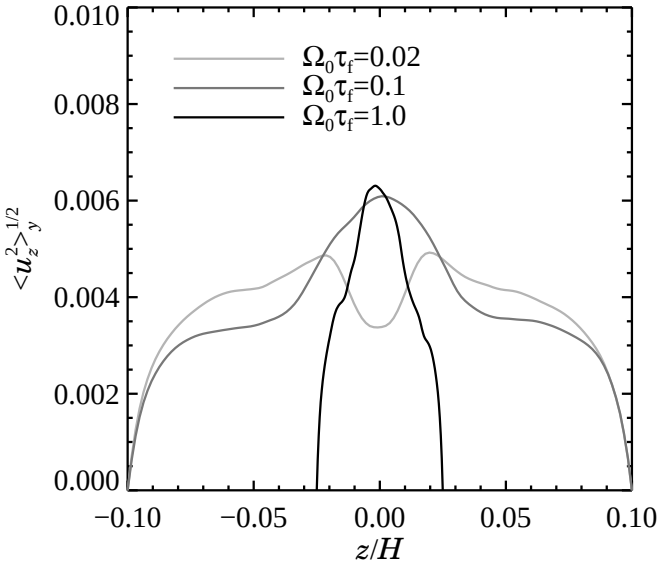

Fig. 4.16 Root-mean-square of the vertical gas velocity as a function of height over the mid-plane. The value is quite independent of Stokes number, but the width of the turbulent region is very small for $\Omega_0\tau_\mathrm{f} = 1$ because of the strong vertical settling of m-sized boulders. The boundary conditions set the vertical speed to zero at the boundaries.

Using equation (4.37), one can translate the scale-height of the solids-to-gas ratio H_ϵ into a turbulent diffusion coefficient δ_t. Such an approach has been used to calculate the turbulent diffusion coefficient of magnetorotational turbulence (Johansen and Klahr 2005). An obvious difference between Kelvin-Helmholtz turbulence and magnetorotational turbulence is that solids play the active role for the first, whereas for the latter the presence of solids does not change the turbulence in any way, because the local solids-to-gas ratio is assumed to be low. Thus, for Kelvin-Helmholtz turbulence we expect the diffusion coefficient to depend on the friction time $\delta_\mathrm{t} = \delta_\mathrm{t}(\tau_\mathrm{f})$.

The calculated turbulent diffusion coefficients for all the simulations are shown in Table 4.2. For the solids-to-gas ratio scale height we have, for simplicity, used the root-mean-square of the z-coordinates of all the particles. The measured coefficients are extremely low, on the order of 10^{-6}. If we assume that the turbulent viscosity α_t is similar to the turbulent diffusion coefficient δ_t, then one sees that Kelvin-Helmholtz turbulence is much weaker than magnetorotational turbulence where α-values from 10^{-3} to unity are found. There is a good agreement between the diffusion coefficients of run B and run Br512 (which has twice the grid and particle resolution). This shows that the solution has converged and that 256×128 is indeed a sufficient resolution to say something meaningful about the Kelvin-Helmholtz turbulence. For the simulations with an increased global solids-to-gas ratio (runs Be2, Be5 and Be10), the scale height of the solids falls with increasing solids-to-gas ratio. This is to be expected from equation (4.20), because of the cusp of high solids density that forms around the mid-plane when $\epsilon_1 \gg 1$. The diffusion coefficient for $\Omega_0\tau_\mathrm{f} = 1.0$ is around 50% lower than for $\Omega_0\tau_\mathrm{f} = 0.1$. Here the strong vertical settling of the solids has decreased the width of the

solids layer significantly, and thus the diffusion coefficient is also much lower.

Turbulent transport coefficients such as α_t and δ_t have an inherent dependence on the width of the turbulent region. Thus the "strength" of the turbulence is better illustrated by the actual turbulent velocity fluctuations. In Fig. 4.16 we plot the root-mean-square of the vertical gas velocity as a function of height over the mid-plane. In the mid-plane, the value is quite independent of the friction time, whereas the width of the turbulent region is much smaller for $\Omega_0\tau_\mathrm{f} = 1$. Thus the turbulence in itself is not weaker, only the turbulent region is smaller, and that means that the transport coefficients are accordingly small.

4.8.2 Comparison with analytical work

It is evident from Table 4.2 that the diffusion coefficient depends on the friction time. In the limit of small Stokes numbers, the constant Richardson number density distribution formulated by S98 predicts that the vertical distribution of solids density should not depend on friction time, and thus, according to equation (4.37), that the diffusion coefficient should be proportional to the friction time. The ratio of the diffusion coefficient of run B to that of run A is $8.9/3.0 \approx 3$, and not $0.1/0.02 = 5$ as would give rise to the same scale height. The factor two difference can be (trivially) attributed to the slight difference in scale heights for the two runs. The squared value is different by almost a factor of two, an indication that vertical settling is not completely negligible for $\Omega_0\tau_\mathrm{f} = 0.1$.

The strength of the Kelvin-Helmholtz turbulence has also been estimated analytically by Cuzzi et al. (1993). They find that the turbulent viscosity ν_t should be approximately (their equation [21])

$$\nu_\mathrm{t} \approx \frac{(\eta v_\mathrm{K})^2}{\Omega_0 \mathrm{Re}^{*2}}\,, \tag{4.38}$$

where v_K is the Keplerian velocity, η is the pressure gradient parameter defined in equation (4.6) and Re^* is the critical Reynolds number at which the flow becomes unstable. This value can be approximated by the Rossby number Ro, the ratio between the advection and Coriolis force terms of the flow. Dobrovolskis et al. (1999) estimate a value of $\mathrm{Ro} \approx 20 \ldots 30$. Using the approximation $\eta \approx c_\mathrm{s}^2/v_\mathrm{K}^2$, equation (4.38) can be written as

$$\nu_\mathrm{t} = D_\mathrm{t} = \frac{\eta}{\mathrm{Ro}^2} c_\mathrm{s}^2 \Omega_0^{-1}\,, \tag{4.39}$$

which appears in its dimensionless form simply as

$$\delta_\mathrm{t} = \frac{\eta}{\mathrm{Ro}^2}\,. \tag{4.40}$$

With $\beta = -0.1$, equation (4.8) gives $\eta = 0.003$. Using $\mathrm{Ro} = 20 \ldots 30$, equation (4.40) gives $\delta_\mathrm{t} \sim 3 \ldots 8 \times 10^{-6}$, quite comparable to the values in Table 4.2. On the other hand, equation (4.38) does not produce a distribution of solids density with a constant Richardson number, and would thus greatly overestimate the diffusion coefficient for even smaller particles. This is also noted by Cuzzi and Weidenschilling (2006) who constrain the validity of equation (4.38) to $\Omega_0\tau_\mathrm{f} > 0.01$. Thus our measured diffusion coefficients are actually in good agreement with both Cuzzi et al. (1993) and with S98.

4.9 Conclusions

The onset of the Kelvin-Helmholtz instability in protoplanetary discs has been known for decades to be the main obstacle for the formation of planetesimals via a gravitational collapse of the particle subdisc. Thus the study of the Kelvin-Helmholtz instability is one of the most intriguing problems of planetesimal formation. It is also a challenging problem to solve, both analytically and numerically, because of the coevolution of the two components gas and solids. Whereas turbulence normally arises from the gas flow alone, in Kelvin-Helmholtz turbulence the solids take the active part as the source of turbulence by piling up around the mid-plane and thus turning the energetically favoured vertical rotation profile into an unstable shear. Planetesimal formation would be deceptively simple could the solids only sediment unhindered, but nature's dislike of thin shear flows precludes this by making the mid-plane turbulent.

In the current work we have shown numerically that when the solid particles are free to move relative to the gas, the Kelvin-Helmholtz turbulence acquires an equilibrium state where the vertical settling of the solids is balanced by the turbulent diffusion away from the mid-plane. For cm-sized pebbles and dm-sized rocks, we find that the solids component forms a layer that has a constant Richardson number. We thus confirm the analytical predictions by Sekiya (1998) for the first time in numerical simulations.

In the saturated turbulence we find the formation of highly overdense regions of solids, not in the mid-plane, but embedded in the turbulent flow. The clumping is very related to the streaming instability found by Youdin and Goodman (2005). Clumps of solids with a bulk density that is equal to or higher than the gas density orbit at the Keplerian velocity, so the clumps overtake sub-Keplerian regions of lower solids density. Thus the dense clumps continue to grow in size and in mass. The final size of a particle clump is given by a balance between this feeding and the loss of material in a rarefaction tail that is formed behind the clump along the sub-Keplerian stream. The gravitational fragmentation of the single clumps into planetesimals is more likely than the whole solids layer fragmenting, because the local solids density in the clumps can be more than an order of magnitude higher than the azimuthally averaged mid-plane density. This process is very much related to the gravoturbulent formation of planetesimals in turbulent magnetohydrodynamical flows (Johansen, Klahr, and Henning 2006b).

A full understanding of the role of Kelvin-Helmholtz turbulence in protoplanetary discs must eventually rely on simulations that include the effect of the Keplerian shear, so future simulations have to be extended into three dimensions. One can to first order expect that growth rates of the KHI larger than the shear rate Ω_0 are required for a mode to grow in amplitude faster than it is being sheared out (Ishitsu and Sekiya 2003), but so far it is an open question in how far the radial shear changes the appearance of the self-sustained state of Kelvin-Helmholz turbulence. Including furthermore the self-gravity between the solid particles, it will become feasible to study the formation of planetesimals in one self-consistent computer simulation and possibly to answer one of the outstanding questions in the planet formation process.

Chapter 5

Turbulent diffusion with an imposed field

From Johansen, Klahr, & Mee (2006): Monthly Notices of the Royal Astronomical Society, vol. 370, p. L71-L75

5.1 Abstract

We study the effect of an imposed vertical magnetic field on the turbulent mass diffusion properties of magnetorotational turbulence in protoplanetary discs. It is well-known that the effective viscosity generated by the turbulence depends strongly on the magnitude of such an external field. In this chapter we show that the turbulent diffusion of the flow also grows, but that the diffusion coefficient does not rise with increasing vertical field as fast as the viscosity does. The vertical Schmidt number, i.e. the ratio between viscosity and vertical diffusion, can be close to 20 for high field magnitudes, whereas the radial Schmidt number is increased from below unity to around 3.5. Our results may have consequences for the interpretation of observations of dust in protoplanetary discs and for chemical evolution modelling of these discs.

5.2 Introduction

Planets form out of micrometer-sized dust grains that are embedded in the gas in protoplanetary discs (see Dominik et al. 2007 for a recent review). The observed infrared radiation from protoplanetary discs comes primarily from micron-sized grains, although observations at longer wavelengths show that some discs have large populations of grains with sizes up to mms and cms (e.g. Rodmann et al. 2006). Turbulent motions in the gas play a big role in the dynamics of chemical species and solids, at least as long as the solids are smaller than a few ten meters. Thus an understanding of how dust particles and chemical species move under the influence of turbulence is vital for our understanding of the physical processes that take place in protoplanetary discs and the observational consequences (Ilgner et al. 2004; Ilgner and Nelson 2006a; Willacy et al. 2006; Dullemond et al. 2006; Semenov et al. 2006).

Turbulence has a number of effects on the embedded dust particles. Larger particles (rocks and boulders) can be trapped in the turbulent flow due to their marginal coupling to the gas (Barge and Sommeria 1995), whereas smaller grains feel the effect of the turbulence as a combination of diffusion and simple advection. Any bulk motion of the gas, e.g. turbulent motion with a turn-over time that is longer than the time-scale that is considered or even a radial accretion flow, leads to an advective transport of the particles rather than diffusion. The turbulent transport acts as diffusion only when the considered time-scale is longer than the eddy turn-over time. The turbulent diffusion coefficient of the grains, $D_\mathrm{t} = \delta c_\mathrm{s}^2 \Omega_0^{-1}$, is often assumed to be equal to the turbulent viscosity of the gas flow $\nu_\mathrm{t} = \alpha c_\mathrm{s}^2 \Omega_0^{-1}$. Here a non-dimensionalisation with sound speed c_s and Keplerian frequency Ω_0 is used (Shakura and Sunyaev 1973). The Schmidt number, a measure of the relative strength of turbulent viscosity and turbulent diffusion, is defined as the ratio $\mathrm{Sc} = \nu_\mathrm{t}/D_\mathrm{t} = \alpha/\delta$. Several recent works have measured the turbulent diffusion coefficient directly from numerical simulations of magnetorotational turbulence (Balbus and Hawley 1991). The simulations by Johansen & Klahr (2005, hereafter JK05, see also Chapter 2 of this thesis) yielded a Schmidt number that is around unity for radial diffusion, whereas Carballido, Stone, & Pringle (2005, hereafter CSP05) found a value as high as 10. The vertical Schmidt number, measured both by JK05, Turner et al. (2006) and by Fromang and Papaloizou (2006), gives more consistently a number between 1 and 3. Here it is worthy of note that Turner et al. (2006) consider stratified discs, and Fromang and Papaloizou (2006) even include the effect of a magnetically dead zone without turbulence around the mid-plane (Gammie 1996; Fleming and Stone 2003).

This chapter addresses the discrepancy between the diffusion properties of turbulence in protoplanetary discs reported in the literature. We show that a vertical imposed magnetic field affects the diffusion coefficient strongly. It is known that a net vertical field component leads to turbulence with a stronger angular momentum transport (Hawley et al. 1995). We perform computer simulations of magnetorotational turbulence for various values of the vertical field and find that turbulent diffusion does not increase as much as the viscosity increases. Thus the ratio between viscous stress and diffusivity, i.e. the Schmidt number, also increases with the magnitude of the external field. As a result we are able to give a possible explanation for the discrepancy in the radial Schmidt numbers found in the literature.

5.3 Sources of an external magnetic field

The properties of any external magnetic field threading protoplanetary discs are not well-known. Close to the central object there is an interaction with the possibly dipolar or maybe quadrupolar magnetic field of the young stellar object. Also the occurrence of jet phenomena indicates that at least for the originating zone of the jet, e.g. a few protostar radii, there should be a large scale vertical magnetic field (e.g. Fendt and Elstner 1999; Vlemmings et al. 2006). However, at larger orbital distances relevant for planet formation, it is not obvious what the global field configuration should look like.

To get some physical insight into the role of an external magnetic field in the dynamics of protoplanetary discs, we do here some rough estimations for two cases, either that the field originates in the central object, or that it comes from the molecular cloud core out of which the disc formed.

5.3.1 Protostar

The dipolar field of the central protostar dominates the gas pressure of the disc until a certain inner disc radius $R_{\rm in}$. This is typically a few times the protostellar radius (Camenzind 1990; Koenigl 1991; Shu et al. 1994). Beyond $R_{\rm in}$ the interaction between the dipole field and the accretion disc is strongly unstable and leads to an opening up of the protostellar dipole field lines (Miller and Stone 1997; Fendt and Elstner 2000; Küker et al. 2003). Even if the protostar could retain its dipolar field at larger orbital radii, the magnetic pressure exerted by the field lines would fall so quickly with orbital radius [$B_z^2(r) \propto r^{-6}$] that it would be completely unimportant at several AU from the protostar where the gas planets are believed to form.

5.3.2 Molecular cloud

In molecular cloud cores the magnetic field, $B_{\rm cloud}$, can be as large as $\sim 100\,\mu$G (Bourke et al. 2001). The gas pressure in the disc can be written as $P = c_{\rm s}^2\rho$, where $c_{\rm s}$ is the sound speed and ρ is the gas density. The mid-plane density of an exponentially stratified disc with scale height H depends on the column density Σ as $\rho = \Sigma/(\sqrt{2\pi}H)$. The scale-height to radius ratio H/r, which also corresponds to the ratio of local sound speed to Keplerian speed $v_{\rm K}$, can be used to rewrite the gas pressure at the mid-plane of the disc as,

$$P = \left(\frac{H}{r}\right)^2 v_{\rm K}^2 \frac{\Sigma(r)}{\sqrt{2\pi}(H/r)r} = \frac{H}{r}\frac{GM_\star}{\sqrt{2\pi}}\frac{\Sigma(r)}{r^2}\,. \tag{5.1}$$

The plasma beta of the external magnetic field is defined as the ratio between gas pressure and magnetic pressure $\beta = P/P_{\rm mag}$. One can write the following scaling for the plasma beta

Table 5.1. Measured turbulent viscosity and diffusion coefficients

Run	$L_x \times L_y \times L_z$	B_0	β	α	Ma_x	Ma_y	Ma_z	δ_x	Sc_x	δ_z	Sc_z
A	1.32×1.32×1.32	0.00	∞	0.0028 ± 0.0004	0.053	0.053	0.041	0.0031	0.90	0.0016	1.75
B	–	0.01	20000	0.0078 ± 0.0015	0.079	0.092	0.064	0.0058	1.34	0.0031	2.52
C	–	0.03	2222	0.0367 ± 0.0142	0.197	0.185	0.140	0.0225	1.63	0.0092	3.99
D	–	0.05	800	0.1811 ± 0.0773	0.416	0.300	0.181	0.0574	3.16	0.0123	14.72
E	–	0.07	408	0.5529 ± 0.0964	0.761	0.421	0.330	0.1984	2.79	0.0300	18.43
A4	1.00×4.00×1.00	0.00	∞	0.0015 ± 0.0002	0.055	0.036	0.031	0.0017	0.88	0.0009	1.71
B4	–	0.01	20000	0.0038 ± 0.0009	0.079	0.057	0.052	0.0038	1.00	0.0024	1.58
C4	–	0.03	2222	0.0414 ± 0.0176	0.206	0.182	0.134	0.0177	2.34	0.0078	5.31
D4	–	0.05	800	0.0793 ± 0.0371	0.279	0.239	0.179	0.0268	2.96	0.0091	8.71
E4	–	0.07	408	0.1242 ± 0.0694	0.366	0.291	0.221	0.0356	3.49	0.0121	10.26

$\beta_{\rm cloud}$ due to the magnetic field from the molecular cloud,

$$\beta_{\rm cloud} = 5.9 \cdot 10^7 \left(\frac{H/r}{0.1}\right) \left(\frac{M_\star}{M_\odot}\right) \left(\frac{B_{\rm cloud}}{\mu{\rm G}}\right)^{-2} \left(\frac{\Sigma}{1\,{\rm g\,cm^{-2}}}\right) \left(\frac{r}{100{\rm AU}}\right)^{-2} . \tag{5.2}$$

Here $\beta_{\rm cloud}$ has a falling trend with r because the low gas density in the outer part of the disc makes the magnetic pressure more important there. For a sufficiently strong cloud field, the plasma beta could be relatively low at a disc radius of several hundred astronomical units.

5.4 Simulations

We simulate a protoplanetary disc in the shearing sheet approximation (e.g. Goldreich and Tremaine 1978; Brandenburg et al. 1995; Hawley et al. 1995). Here a local coordinate frame corotating with the disc with the Keplerian rotation frequency Ω_0 at a distance r_0 from the central source of gravity is considered. The coordinate system is oriented so that x points radially away from the central object, y points in the azimuthal direction parallel to the the Keplerian flow, and z points normal to the disc along the Keplerian rotation vector $\boldsymbol{\Omega}_0$. Numerical calculations are performed using the Pencil Code (a finite difference code that uses sixth order symmetric space derivatives and a third order time-stepping scheme, see Brandenburg 2003).

5.4.1 Gas

Considering the velocity field $\boldsymbol{u}$ relative to the Keplerian flow $u_y^{(0)} = -(3/2)\Omega_0 x$, the equation of motion of the gas is

$$\frac{\partial \boldsymbol{u}}{\partial t} + (\boldsymbol{u}\cdot\boldsymbol{\nabla})\boldsymbol{u} + u_y^{(0)}\frac{\partial \boldsymbol{u}}{\partial y} = \boldsymbol{f}(\boldsymbol{u}) - c_{\rm s}^2 \boldsymbol{\nabla}\ln\rho + \frac{1}{\rho}\boldsymbol{J}\times(\boldsymbol{B}+B_0\hat{\boldsymbol{z}}) + \boldsymbol{f}_\nu\,. \tag{5.3}$$

The left-hand-side of equation (5.3) contains terms for both the advection by the velocity relative to the Keplerian flow and for the advection by the Keplerian flow itself. The terms on the right-hand side are the modified Coriolis force,

$$\boldsymbol{f}(\boldsymbol{u}) = \begin{pmatrix} 2\Omega_0 u_y \\ -\frac{1}{2}\Omega_0 u_x \\ 0 \end{pmatrix} , \tag{5.4}$$

which takes into account that the Keplerian velocity profile is advected with any radial motion, the force due to the isothermal pressure gradient with a constant sound speed c_s, the Lorentz force (including the contribution from an imposed vertical field of strength B_0) and the viscous force $\boldsymbol{f}_\nu$ that is used to stabilise the numerical scheme. The viscosity term is a combination of sixth order hyperviscosity and a localised shock capturing viscosity. The use of hyperviscosity, hyperdiffusion and hyperresistivity is explained in JK05. For the shock viscosity, where extra bulk viscosity is added in regions of flow convergence, we refer to Haugen et al. (2004b) for a detailed description.

The evolution of the mass density is solved for in the continuity equation

$$\frac{\partial \rho}{\partial t} + \boldsymbol{u}\cdot\boldsymbol{\nabla}\rho + u_y^{(0)}\frac{\partial \rho}{\partial y} = -\rho\boldsymbol{\nabla}\cdot\boldsymbol{u} + f_\mathrm{D}\,, \tag{5.5}$$

where f_D is a combination of sixth order hyperdiffusion and shock diffusion. The magnetic field evolves by the induction equation which we write in terms of the magnetic vector potential $\boldsymbol{A}$,

$$\frac{\partial \boldsymbol{A}}{\partial t} + u_y^{(0)}\frac{\partial \boldsymbol{A}}{\partial y} = \frac{3}{2}\Omega_0 A_y \hat{\boldsymbol{x}} + \boldsymbol{u}\times(\boldsymbol{B} + B_0\hat{\boldsymbol{z}}) + \boldsymbol{f}_\eta\,. \tag{5.6}$$

Again we use sixth order hyperresistivity and shock resistivity, through the function $\boldsymbol{f}_\eta$, in regions of strong flow convergence. The value of B_0 sets the strength of an external vertical magnetic field.

5.4.2 Solid particles

The turbulent diffusion coefficient D_t of the flow is measured by letting solid particles settle to the mid-plane of the turbulent disc. The solids layer is represented as individual particles each with a position $\boldsymbol{x}^{(i)}$ and velocity vector $\boldsymbol{v}^{(i)}$ (measured relative to the Keplerian velocity $u_y^{(0)}\hat{\boldsymbol{y}}$). The gas acts on a solid particle through a drag force that is proportional to but in the opposite direction of the difference between the velocity of the particle and the local gas velocity. The solids do not interact mutually and do not have any feedback on the gas. The equation of motion of the solid particles is

$$\frac{\mathrm{d}\boldsymbol{v}^{(i)}}{\mathrm{d}t} = \boldsymbol{f}(\boldsymbol{v}^{(i)}) - \frac{1}{\tau_\mathrm{f}}\left(\boldsymbol{v}^{(i)} - \boldsymbol{u}\right) + \boldsymbol{g}\,, \tag{5.7}$$

where the modified Coriolis force $\boldsymbol{f}$ is defined in equation (5.4), τ_f is the friction time and $\boldsymbol{g}$ is an imposed gravitational field (see below). We assume in the following that τ_f is constant and thus independent of the relative velocity between the grain and the surrounding gas. In protoplanetary discs this is a valid assumption for sufficiently small solids (Weidenschilling

1977a). We use a value of $\Omega_0 \tau_\mathrm{f} = 0.01$ which is small enough that the diffusion coefficient should not differ significantly from that of a passive scalar (which can be seen as a solid particle in the limit of a vanishingly small friction time). This value is also large enough that the computational time-step is set by the Courant criterion for the gas and not by the friction force in the particle equations.

The particles change positions according to the dynamical equation

$$\frac{\mathrm{d}\boldsymbol{x}^{(i)}}{\mathrm{d}t} = \boldsymbol{v}^{(i)} + u_y^{(0)} \hat{\boldsymbol{y}} \,. \tag{5.8}$$

Under the effect of a special gravity field acting on the solid particles only, $\boldsymbol{g}$ in equation (5.7), the particles fall either to the horizontal mid-plane of the disc, in the case of a vertical gravity field $\boldsymbol{g} = g_z(z)\hat{\boldsymbol{z}}$, or to a vertical "mid-plane" in the case of a radial gravity field $\boldsymbol{g} = g_x(x)\hat{\boldsymbol{x}}$. We use a sinusoidal expression $g_i = -g_0 \sin(k_i x_i)$ with a wavelength that is equal to the size of the simulation box. In the equilibrium state, the sedimentation is balanced by the turbulent diffusion away from the mid-plane, and the number density of solids n, for the case of a vertical gravity field, is given by (see JK05)

$$\ln n(z) = \ln n_1 + \frac{\tau_\mathrm{f} g_0}{k_z D_z^{(\mathrm{t})}} \cos(k_z z) \,, \tag{5.9}$$

where n_1 is an integration constant. The equivalent expression for the radial gravity case is found simply by replacing z by x in equation (5.9).

We run simulations with different values of the external magnetic field strength B_0 between 0 and 0.07, corresponding to a β ranging from infinity down to approximately 400. Our computational unit of velocity is the constant sound speed c_s, length is in units of the disc scale-height H, and density is measured in units of mean gas density ρ_0. In these units the turbulent viscosity and the turbulent diffusion coefficient, ν_t and D_t, are numerically equal to the dimensionless coefficients α and δ. The unit of the magnetic field is then $[B] = c_\mathrm{s}\sqrt{\mu_0 \rho_0}$ and is chosen such that $\mu_0 = 1$. For each value of B_0 we run one simulation with a vertical and one simulation with a radial gravitational field on the solid particles. The diffusion coefficients δ_x and δ_z are found by fitting a cosine function to the logarithmic dust density. From the amplitude we then determine the diffusion coefficient using equation (5.9). The run parameters and the results are shown in Table 5.1. Two simulation box sizes are considered, a square box with a side length of 1.32 and an elongated box with $(L_x, L_y, L_z) = (1.0, 4.0, 1.0)$ (similar to the setup of Sano et al. 2004). For the first case we use a resolution of 64^3 grid points and 1,000,000 dust particles. Simulations with 128^3 grid points were done by JK05 and showed only small differences from the 64^3 simulations in the measured Schmidt numbers. Each model is run for twenty local orbits, i.e. $20 \times 2\pi\Omega_0^{-1}$, of the disc. The runs with an elongated box are done with $64 \times 256 \times 64$ grid points and 4,000,000 dust particles.

5.5 Results

For each value of the imposed magnetic field we have measured the α-value from the Reynolds and Maxwell stress tensors (see Table 5.1). The α-value grows approximately exponentially

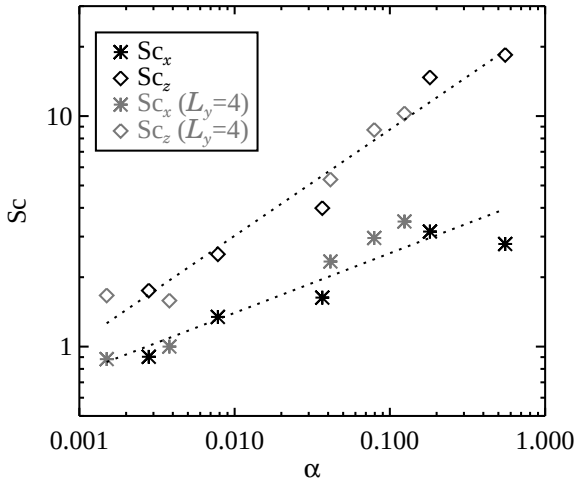

Fig. 5.1 The Schmidt number plotted against the α value and the best power-law fit (dotted lines). The best fit has $\mathrm{Sc}_x = 4.6\alpha^{0.26}$ and $\mathrm{Sc}_z = 25.3\alpha^{0.46}$.

with B_0. An α-value close to unity can be reached already for $B_0 = 0.07$ (corresponding to $\beta \simeq 400$). A similar investigation into the dependence of α on an imposed vertical field was undertaken by Hawley et al. (1995). Comparing with Table 1 in that work, one sees that there is a relatively good agreement between those results and ours. Magnetorotational instability with an imposed vertical field develops into a "channel" solution (Hawley and Balbus 1992; Goodman and Xu 1994; Steinacker and Henning 2001), characterised by the transfer of the most unstable MRI mode to the the largest scale of the simulation box and the subsequent decay of this large scale mode (Sano and Inutsuka 2001). Sufficiently strong vertical fields can even cause stratified discs to break up altogether (Miller and Stone 2000). The creation and destruction of the unstable channel solution gives significant temporal fluctuations in the measured stresses, evident in the standard deviation of the turbulent viscosity in Table 5.1 (see also Fig. 1 of Sano and Inutsuka 2001).

For measuring the turbulent diffusion coefficient we consider the logarithmic number density of the dust particles averaged from 10 to 20 orbits. We have chosen to calculate the diffusion coefficient directly from this average state, rather than calculating it from the instantaneous dust density at a given time t, because large-scale advection flow only works as diffusion when averaged over sufficiently long times. The average dust density was found to be in excellent agreement with the cosine distribution of equation (5.9) with a deviation from a perfect cosine of less than 5% for all simulations. Thus diffusion is a good description of the turbulent transport over long time-scales. This is partly due to the fact that we consider diffusion at the largest scale of the flow, i.e. at a scale that is similar to or larger than the energy injection scale of the MRI. Diffusion over length scales that are smaller than the energy injection scale should be weaker, because dust density concentrations at small length scales are not stretched by the full velocity amplitude of the larger scales, but only by the velocity difference that the larger scales exert over the much narrower dust concentration. The exp(cos) equilibrium state for the dust density, however, has almost all of its power at

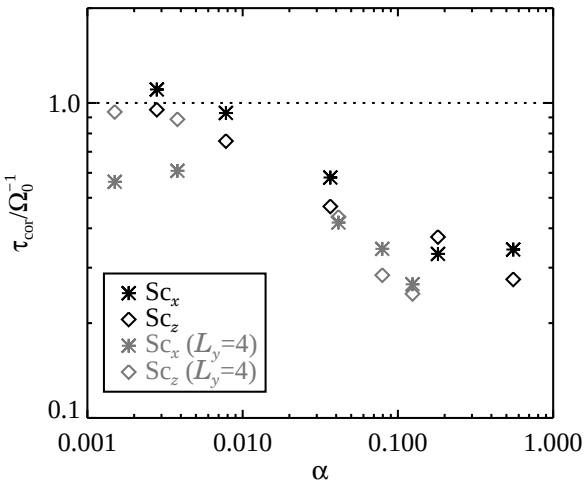

Fig. 5.2 The correlation time of the turbulent mixing coefficients versus the α-value. The correlation times fall significantly with increasing α.

the largest scale of the simulation box, so any scale-dependency of the diffusion coefficient should not have any influence on the equilibrium state (the fact that the logarithmic dust density in the equilibrium state is a cosine supports this).

The measured turbulent diffusion coefficients are written in Table 5.1. It is evident that the turbulent diffusion coefficient does not increase as fast with increasing vertical field as the turbulent viscosity does. In Fig. 5.1 we plot the vertical and radial Schmidt numbers as a function of α. Both Schmidt numbers approximately follow a power law with α. Making a best-fit power law, we find the empirical connections

$$\mathrm{Sc}_x = 4.6\alpha^{0.26}\,, \tag{5.10}$$

$$\mathrm{Sc}_z = 25.3\alpha^{0.46}\,. \tag{5.11}$$

Considering the two box sizes individually (black and grey symbols in Fig. 5.1), the radial Schmidt number is seen to rise slightly faster with increasing α in the case of the elongated box with $L_y = 4$, whereas the vertical Schmidt number follows a trend that is independent of the box size. In ideal MHD simulations with $\beta = 400$, CSP05 find a radial Schmidt number of around 10. Using a similar value for β, we find that the radial Schmidt number rises from unity in the case of no external field to $\sim 3-4$ when $\beta \simeq 400$. This may explain at least part of the discrepancy between the results by CSP05 and JK05. The box size used in CSP05 is $1.0 \times 6.28 \times 1.0$, and is thus comparable to our elongated box. We have tried with $L_y = 6.28$ as well, but found no significant difference in the results.

It is interesting to note that Fromang and Papaloizou (2006) have an α-value of 0.015 and a vertical Schmidt number of 2.8. That fits almost perfectly in Fig. 5.1. Since Fromang and Papaloizou (2006) do not have an imposed vertical field in their simulations, this may mean that the rise in Schmidt number with α is something fundamental and not only an effect of the imposed magnetic field, although further investigations would have to be done to explore this connection in more detail.

5.5.1 Correlation times

One can express the diffusion coefficient caused by the scale k of a turbulent flow as $D_k = u_k \ell_k$. Here u_k is the velocity amplitude of that scale and ℓ_k is the typical length-scale over which a turbulent feature transports before dissolving. The advection length ℓ_k can be approximated by $\ell_k = u_k t_k$, where t_k is the correlation time, or life time, of a turbulent structure. Taking now an average (and weighted) correlation time $\tau_{\rm cor}$ of all the scales, one gets the mixing length expression for the diffusion coefficient in direction i,

$$D_i^{(\rm t)} = \tau_{\rm cor} u_i^2 \,, \tag{5.12}$$

valid for Fickian diffusion (for the validity of Fickian diffusion see Brandenburg et al. 2004b). Here the Mach number, $\sqrt{u_i^2}/c_{\rm s}$, is the root-mean-square velocity fluctuation in real space. The diffusion coefficient should thus scale roughly with Mach number squared. We plot the correlation times, calculated from equation (5.12), of δ_x and δ_z versus the α-value of the flow in Fig. 5.2. The correlation time of the turbulent diffusion coefficients falls steeply with increasing α-value, so even though the Mach number of the flow increases, the time a given turbulent structure has for transporting the dust becomes shorter and shorter. Since the correlation times of radial and vertical diffusion have approximately the same dependence on α, the ratio of the diffusion coefficients can be expressed as $\delta_x/\delta_z = ({\rm Ma}_x/{\rm Ma}_z)^2$. The anisotropy in the diffusion coefficient in favour of the radial direction is then mostly an effect of the anisotropy between the radial and vertical Mach numbers.

5.6 Summary

In this chapter we report that the Schmidt number of magnetorotational turbulence depends strongly on the value of an imposed vertical magnetic field. For large values of the vertical field, the relative strength of the turbulent diffusion falls with respect to the turbulent viscosity. This could explain part of the discrepancy between measurements of the radial turbulent diffusion coefficient in magnetorotational without an imposed field (Johansen and Klahr 2005) and with an imposed field (Carballido et al. 2005). In the tenuous outer regions of protoplanetary discs, field lines from the molecular cloud may be strong enough to give a significant magnetic pressure contribution to the dynamics of the gas flow. Here one should expect that the Schmidt number can be significantly different from unity.

Chapter 6

Linear evolution of the streaming instability

From Youdin & Johansen (2007): The Astrophysical Journal, in press

6.1 Abstract

We present local simulations that verify the linear streaming instability that arises from aerodynamic coupling between solids and gas in protoplanetary discs. This robust instability creates enhancements in the particle density in order to tap the free energy of the relative drift between solids and gas, generated by the radial pressure gradient of the disc. We confirm the analytic growth rates found by Youdin & Goodman (2005) using grid hydrodynamics to simulate the gas and, alternatively, particle and grid representations of the solids. Since the analytic derivation approximates particles as a fluid, this work corroborates the streaming instability when solids are treated as particles. The idealised physical conditions – axisymmetry, uniform particle size, and the neglect of vertical stratification and collisions – provide a rigorous, well-defined test of any numerical algorithm for coupled particle-gas dynamics in protoplanetary discs. We describe a numerical particle-mesh implementation of the drag force, which is crucial for resolving the coupled oscillations. Finally we comment on the balance of energy and angular momentum in two-component discs with frictional coupling. The next chapter details the non-linear evolution of the streaming instability into saturated turbulence with dense particle clumps.

6.2 Introduction

Solid bodies in protoplanetary discs lose angular momentum as they encounter the headwind of the pressure-supported gas disc. The subsequent radial drift is fastest for marginally coupled solids whose aerodynamic stopping times are comparable to the local orbital time (Weidenschilling 1977a). For standard disc models, cm-sized particles at 30 AU and m-sized bodies at 1 AU suffer drift times of only approximately 10 or 100 orbital periods, respectively. Rapid infall imposes severe time-scale constraints on the growth into km-sized solid bodies, or planetesimals, by coagulation. Concerns about the inefficiency of sticking for macroscopic solids (Benz 2000) has also contributed to the concept of a "meter-size barrier" in planet formation (which should not be misinterpreted as implying that growth to meter sizes is easy, see e.g. Blum and Wurm 2000).

The gravitational instability hypothesis (Safronov 1969; Goldreich and Ward 1973) postulates that a sedimented mid-plane layer of small particles (perhaps mm-sized to match chondrules) will fragment directly into gravitationally bound planetesimals, avoiding the problems with sticking efficiency and drift. However, disc turbulence acts to diffuse particles, inhibiting both their vertical settling to the midplane (Weidenschilling and Cuzzi 1993; Dubrulle et al. 1995) and their ability to collapse into bound structures (Youdin 2005a). Even in a completely laminar disc, particle settling generates vertical shear in the orbital motion of the gas. This shear in turn triggers modified Kelvin-Helmholtz instabilities that develop into turbulence, restricting further sedimentation (Goldreich and Ward 1973; Weidenschilling 1980; Cuzzi et al. 1993). This self-induced turbulence may not be able to prevent gravitational collapse if the solids-to-gas ratio is enhanced above Solar abundances (Sekiya 1998; Youdin and Shu 2002; Garaud and Lin 2004; Weidenschilling 2006), possibly due to photoevaporation of the gas-rich surface layers of the stratified disc (Throop and Bally 2005) or to pile-ups of solids in the inner disc from particles that drift in more rapidly from the outer disc (Youdin and Chiang 2004). Significant progress has been made in understanding the turbulence generated by particle settling (Ishitsu and Sekiya 2003; Gómez and Ostriker 2005; Johansen et al. 2006a). However a simulation that incorporates the full 3D nature of these non-axisymmetric instabilities, with radial shear and the independent evolution of solids and gas, has not yet been performed.

This chapter addresses the related streaming instability (Youdin and Goodman 2005 hereafter referred to as YG) where vertical gravity is ignored in order to focus on a simpler manifestation of particle-gas coupling in Keplerian discs. With no vertical shear present, the streaming instability is driven by the relative motion between solids and gas, which is predominantly radial for tightly coupled particles. The ultimate energy source, as with vertical shear instabilities, is the radial gas pressure gradient. Particle feedback on gas dynamics is important not just for establishing the (unstable) equilibrium, but also for generating escalating oscillations. Consequently, streaming instabilities trigger exponential growth of arbitrarily small particle density perturbations, as shown by YG. The single-fluid treatment of Goodman and Pindor (2000) discovered a related boundary layer drag instability in stratified discs that could also concentrate particles. Johansen et al. (2006a) found significant particle clumping in studies of Kelvin-Helmholz instabilities with particle feedback on the gas, which those authors hypothesised was a manifestation of non-linear streaming instabilities. The current study, Chapters 6 and 7 of this thesis, explores the consequences of streaming instabilities, and more generally

the role of particle-gas coupling in protoplanetary discs. This chapter demonstrates that our simulations faithfully reproduce the linear physics of the streaming instability, whether the solids are modelled as a fluid or Lagrangian particles.

The chapter is built up as follows. In §6.3 we present the basic equations of our dynamical system and review the streaming instability. Section 6.4 describes the numerical methods, including the communication of drag forces between particles and a grid in §6.4.2. Our main results, in §6.5, numerically confirm the linear streaming instability. In §6.6 we analyse energy and angular momentum balance in a coupled two-fluid system. We discuss our results in §6.7. The appendices contain an analysis of interpolation and assignment errors in different particle-mesh approaches to calculating drag forces (Appendix A.3), a non-axisymmetric analytical problem used to test drag force assignment over shear-periodic boundaries (Appendix A.4), and a recipe to minimise Poission noise in seeding linear particle density perturbations (Appendix A.5). A companion paper, Johansen & Youdin (2007, hereafter referred to as JY, see also Chapter 7 of this thesis), describes the full non-linear evolution of the streaming instability into turbulence.

6.3 Streaming instability: analytics

6.3.1 Basic equations

We describe the local dynamics of the gas and solid component of a protoplanetary disc in the shearing sheet approximation (e.g. Goldreich and Lynden-Bell 1965; Goldreich and Tremaine 1978). The Cartesian coordinate frame corotates with the Keplerian frequency Ω at an arbitrary orbital distance r from the central gravity source. The coordinate axes are oriented such that x points radially outwards, y points along the rotation direction of the disc, while z points vertically out of the disc, parallel to the Keplerian rotation vector $\boldsymbol{\Omega}$. Our unstratified model omits vertical gravity. We measure all velocities relative to the linearised Keplerian shear flow in the rotating frame $\boldsymbol{V}_0 = V_{y,0}\hat{\boldsymbol{y}} = -(3/2)\Omega x\hat{\boldsymbol{y}}$.

Solids as a fluid

Analytic investigations are greatly simplified by treating solid particles as a continuous fluid of density $\rho_{\rm p}$ and velocity $\boldsymbol{w}$, which evolve according to shearing sheet equations of continuity and motion

$$\frac{\partial\rho_{\rm p}}{\partial t} + \boldsymbol{w}\cdot\boldsymbol{\nabla}\rho_{\rm p} - \frac{3}{2}\Omega x\frac{\partial\rho_{\rm p}}{\partial y} = -\rho_{\rm p}\boldsymbol{\nabla}\cdot\boldsymbol{w}\,, \tag{6.1}$$

$$\frac{\partial\boldsymbol{w}}{\partial t} + (\boldsymbol{w}\cdot\boldsymbol{\nabla})\boldsymbol{w} - \frac{3}{2}\Omega x\frac{\partial\boldsymbol{w}}{\partial y} = 2\Omega w_y\hat{\boldsymbol{x}} - \frac{1}{2}\Omega w_x\hat{\boldsymbol{y}} - \frac{1}{\tau_{\rm f}}\left(\boldsymbol{w}-\boldsymbol{u}\right)\,. \tag{6.2}$$

Transport terms on the left hand side of equations (6.1) and (6.2) include advection by the peculiar velocities, $\boldsymbol{w}$, and by the Kepler shear, $\boldsymbol{V}_0$. The right hand side of the equation of

motion (Eq. [6.2]) contains Coriolis forces (as modified by Kepler shear) and drag acceleration relative to the gas component with velocity $\boldsymbol{u}$. We apply a linear drag force with constant friction time $\tau_{\rm f}$, valid for relatively small particles in the Epstein or Stokes regimes (Adachi et al. 1976; Weidenschilling 1977a). Epstein's Law, $\tau_{\rm f}^{\rm (Ep)} = \rho_\bullet R/(\rho_{\rm g} c_{\rm s})$ holds for particles of size $R \lesssim \lambda_{\rm g}$, where $\lambda_{\rm g} \approx (r/{\rm AU})^{2.75}\,{\rm cm}$ is the mean free path of the gas molecules, $c_{\rm s}$ is the gas sound speed, and $\rho_\bullet$ is the internal density of rock/ice. Stokes' Law, $\tau_{\rm f}^{\rm (St)} = \tau_{\rm f}^{\rm (Ep)} R/\lambda_{\rm g}$ applies in the relatively narrow range $\lambda_{\rm g} \lesssim R \lesssim \lambda_{\rm g} v_{\rm K}/c_{\rm s}$, where $v_{\rm K} \equiv \Omega r$ is the local Keplerian speed. Yet larger particles, $R \gtrsim \lambda_{\rm g} v_{\rm K}/c_{\rm s}$, trigger turbulent wakes with non-linear drag accelerations, which can not be modelled with a constant friction time. Note that Stokes' Law is independent of gas density (since $\lambda_{\rm g} \propto 1/\rho_{\rm g}$). The dependence of Epstein's law on gas density fluctuations is neglected in our calculations as it is a small correction for low Mach number flow.

The solid component does not feel a pressure gradient, neither from the gas, because the mass per solid particle is so high, nor from interparticle collisions, because the number density is so low. Drag effects dominate collisional effects, since the collision time, $t_{\rm coll} = \rho_\bullet R/(\rho_{\rm p} c_{\rm p})$, is long with $t_{\rm coll}/\tau_{\rm f} \approx (\rho_{\rm g}/\rho_{\rm p})(c_{\rm s}/c_{\rm p}) \gg 1$, even when the particle density is large, since the rms speed of particles, $c_{\rm p}$, is much smaller than the gas sound speed.

For numerical work, we also use a Lagrangian description of particle motion, see §6.4.1.

Gas evolution

The equations of continuity and motion for the gas read

$$\frac{\partial \rho_{\rm g}}{\partial t} + \boldsymbol{u}\cdot\boldsymbol{\nabla}\rho_{\rm g} - \frac{3}{2}\Omega x \frac{\partial \rho_{\rm g}}{\partial y} = -\rho_{\rm g}\boldsymbol{\nabla}\cdot\boldsymbol{u}\,, \tag{6.3}$$

$$\begin{aligned}\frac{\partial \boldsymbol{u}}{\partial t} + (\boldsymbol{u}\cdot\boldsymbol{\nabla})\boldsymbol{u} - \frac{3}{2}\Omega x \frac{\partial \boldsymbol{u}}{\partial y} &= 2\Omega u_y \hat{\boldsymbol{x}} \\ &\quad -\frac{1}{2}\Omega u_x \hat{\boldsymbol{y}} - c_{\rm s}^2 \boldsymbol{\nabla}\ln\rho_{\rm g} \\ &\quad +2\eta\Omega^2 r\hat{\boldsymbol{x}} - \frac{\epsilon}{\tau_{\rm f}}(\boldsymbol{u}-\boldsymbol{w})\,.\end{aligned} \tag{6.4}$$

Equation (6.3) reduces to $\boldsymbol{\nabla}\cdot\boldsymbol{u} = 0$ for an incompressible gas, as was considered in YG. The momentum equation (6.4) contains advection and Coriolis forces as equation (6.2). The main distinction between the two components is that gas is effected by pressure gradients. We include both local pressure gradients from isothermal gas density fluctuations and a constant acceleration by a global radial pressure gradient, $\partial P/\partial r$, expressed using the dimensionless measure of sub-Keplerian rotation

$$\eta \equiv -\frac{\partial P/\partial r}{2\rho_{\rm g}\Omega^2 r} \sim \frac{c_{\rm s}^2}{v_{\rm K}^2}\,. \tag{6.5}$$

The feedback of the linear drag force scales with the density ratio of particles to gas,

$$\epsilon \equiv \rho_{\rm p}/\rho_{\rm g}\,, \tag{6.6}$$

which ensures that total momentum is conserved.

6.3.2 Equilibrium state

Equilibrium solutions to the mutually coupled equations (6.2) and (6.4) were obtained by Nakagawa et al. (1986 hereafter referred to as NSH) for local and linear dynamics. The in-plane deviations from Keplerian rotation are

$$u_x = \frac{2\epsilon\tau_\mathrm{s}}{(1+\epsilon)^2+\tau_\mathrm{s}^2}\eta v_\mathrm{K}\,, \tag{6.7}$$

$$u_y = -\left[1+\frac{\epsilon\tau_\mathrm{s}^2}{(1+\epsilon)^2+\tau_\mathrm{s}^2}\right]\frac{\eta v_\mathrm{K}}{1+\epsilon}\,, \tag{6.8}$$

$$w_x = -\frac{2\tau_\mathrm{s}}{(1+\epsilon)^2+\tau_\mathrm{s}^2}\eta v_\mathrm{K}\,, \tag{6.9}$$

$$w_y = -\left[1-\frac{\tau_\mathrm{s}^2}{(1+\epsilon)^2+\tau_\mathrm{s}^2}\right]\frac{\eta v_\mathrm{K}}{1+\epsilon}\,. \tag{6.10}$$

The dimensionless stopping time, $\tau_\mathrm{s} \equiv \Omega\tau_\mathrm{f}$, is a convenient measure of coupling strength, since marginal coupling, $\tau_\mathrm{s} = 1$, famously maximises the radial drift speed of an isolated particle. Velocities scale with the sub-Keplerian velocity, ηv_K, where $v_\mathrm{K} \equiv \Omega r$. The azimuthal velocities are factored into the centre-of-mass motion,

$$V_y^{(\mathrm{com})} \equiv \frac{\rho_\mathrm{g}u_y+\rho_\mathrm{p}w_y}{\rho_\mathrm{p}+\rho_\mathrm{g}} = -\frac{\eta v_\mathrm{K}}{1+\epsilon}\,, \tag{6.11}$$

and order τ_s^2 drift motions (see YG for details).

Vertical gradients in the solids-to-gas ratio ϵ give gradients in $V_y^{(\mathrm{com})} \approx u_y \approx w_y$ (for $\tau_\mathrm{s} \ll 1$) that trigger the settling-induced Kelvin-Helmholz instabilities discussed in the introduction. As in YG, we also neglect vertical gravity in the present work in order to allow for a laminar equilibrium state. With vertical gravity, any initial condition must be time-dependent (due to vertical settling) and/or turbulent (to halt the settling). Furthermore, in stratified discs, drift speeds (and even directions) vary with height above the midplane, since τ_s rises with decreasing gas density and since the radial gas pressure gradient can reverse away from the mid-plane (Takeuchi and Lin 2002). This is particularly relevant for small grains that remain above the midplane for many orbital times. The severity of the unstratified approximation is justified by the insights gained from an initially simple, well-defined problem that rapidly turns complex.

6.3.3 Streaming instability

The streaming motion of solid particles through gas presents a source of free energy that is driven by pressure gradients and mediated by drag and Coriolis forces. YG showed, by linearly perturbing equations (6.2) and (6.4) about the equilibrium state given by equations (6.7-6.10), that this streaming robustly triggers instability in protoplanetary discs. The instability provides a novel mechanism to generate growing particle density perturbations in a moderately dense mid-plane layer of macroscopic particles, while smaller particles ($\tau_\mathrm{s} \ll 1$) with poor drag feedback ($\epsilon \ll 1$) will give rise to only very low, sub-dynamical growth rates.

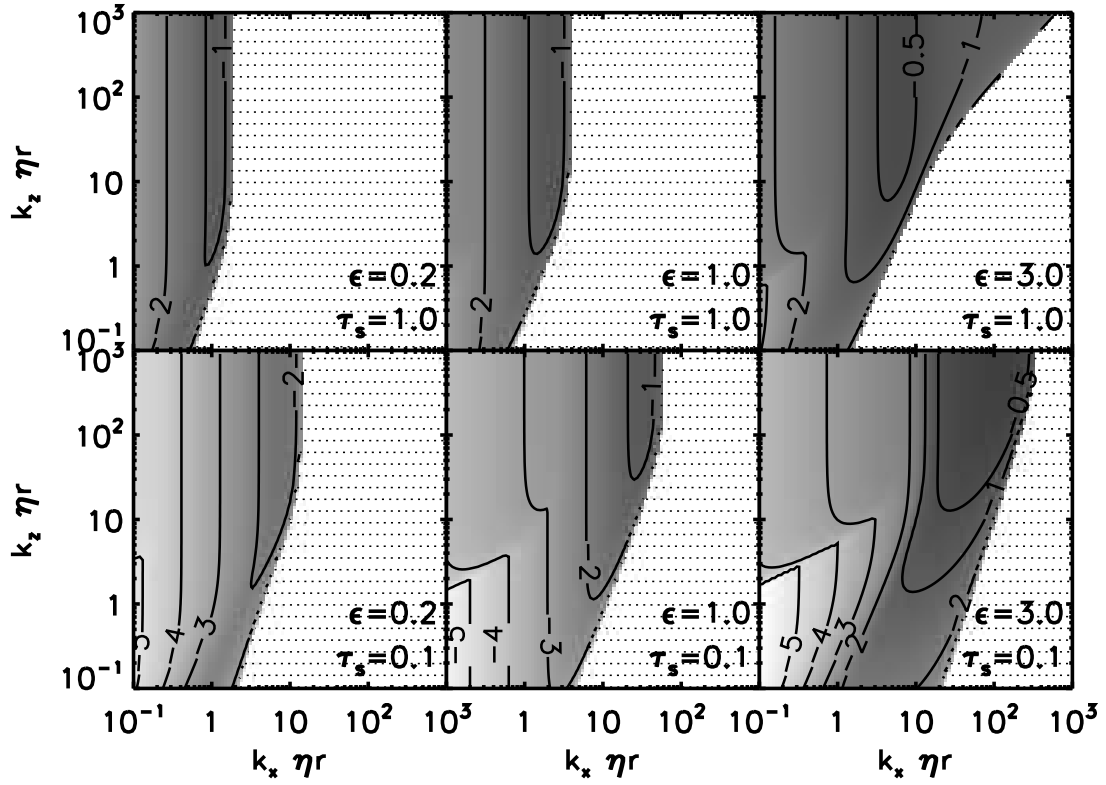

Fig. 6.1 Linear growth rate s of the streaming instability vs. radial and vertical wavenumbers for a friction time of $\tau_s = 1.0$ (upper row) and $\tau_s = 0.1$ (lower row). Three values of the solids-to-gas density ratio, $\epsilon = 0.2, 1.0, 3.0$, are considered along the columns. Contours label $\log_{10}(s/\Omega)$, darker shading corresponds to faster growth rates, while the dotted regions contain only damped modes.

The YG analysis and the linear test simulations in this chapter are "2.5-D", i.e. all three components of velocity fluctuations are considered,[1] but perturbations are axisymmetric and characterised by the radial and vertical wavenumbers, k_x and k_z. The growth rates for several choices of τ_s and ϵ (which henceforth indicates the *average* value of ρ_p/ρ_g in the background state, unless otherwise noted) are shown in Fig. 6.1 as a function of the dimensionless wavenumbers $K_x \equiv k_x \eta r$ and $K_z = k_z \eta r$.

Since particles only affect gas dynamics via drag feedback, growth rates increase for larger ϵ, while the relevant length scales shrink, most likely because the response time-scale of the gas speeds up as τ_f/ϵ. Fig. 6.2 shows these trends, along with the particularly sharp increase of s across $\epsilon = 1$ for tightly coupled particles with $\tau_s = 0.1$. The crucial physical distinction for marginal coupling (for which the same sharp increase is not present) may be that for $\tau_s \approx 1$, azimuthal drift (of order τ_s^2) is no longer negligible compared to radial drift (of order τ_s). For a more technical difference, note the grey curves in Fig. 6.2, which show that the phase speed of waves changes sign near $\epsilon \approx 1$. YG noted that the phase speed tends to track the

[1] And all three components are necessary for axisymmetric instability (YG).

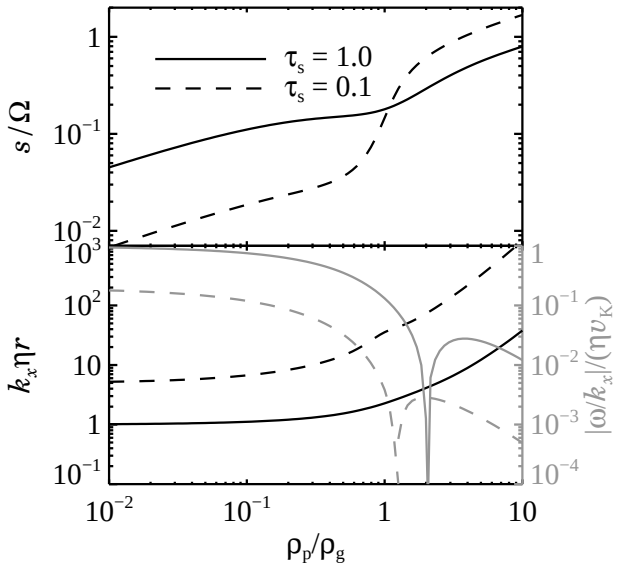

Fig. 6.2 Peak growth rate, s, of the streaming instability and fastest growing radial wavenumber, k_x, versus the solids-to-gas density ratio $\epsilon = \rho_\mathrm{p}/\rho_\mathrm{g}$ for a friction time of $\tau_\mathrm{s} = 1.0$ (solid line) and $\tau_\mathrm{s} = 0.1$ (dashed line). Growth becomes faster and occurs at smaller scales for increasing ϵ, with a particularly sharp increase in s across $\epsilon = 1$ for tightly coupled particles with $\tau_\mathrm{s} = 0.1$. Gray curves in lower plot (associated with grey axis on right) show the radial phase speed of waves. The sharp dips near $\epsilon \approx 1$–2 indicate a sign change for the wave speed: inward when gas dominates and outward when particles dominate.

component with the fastest radial drift – solids for $\epsilon < 1$ and gas for $\epsilon > 1$. Curiously at $\tau_\mathrm{s} = 1$ the transition is delayed to $\epsilon \simeq 2$. As τ_s decreases the switch in phase speeds gets closer to $\epsilon = 1$, coinciding with the rise in growth rates across $\epsilon = 1$ becoming steeper and of larger amplitude (see also Fig. 3 of YG for the $\tau_\mathrm{s} = 0.01$ case).

The trend with τ_s is complicated as well. In the gas-dominated regime ($\epsilon < 1$) growth rates show the expected rise toward the $\tau_\mathrm{s} \approx 1$ "sweetspot": streaming motions are large yet particles still respond effectively to the gas. The situation reverses when particles dominate ($\epsilon > 1$), with growth rates that are actually faster for tighter coupling, but at smaller length scales.

Returning for a moment to Fig. 6.1, it is also evident that growth does not peak at a single pair of wavenumbers. The fastest growing K_x can be determined, with only damped modes for sufficiently large K_x, but growth remains flat for large K_z (indeed the curves of Fig. 6.2 are calculated in the limit $K_z/K_x \gg 1$). A physical explanation for the difference between large or small K_z/K_x follows. The (near) incompressibility of the gas imposes a ratio $|u_z/u_x| \simeq |K_x/K_z|$. With $K_z \gg K_x$, velocity vectors are nearly parallel to the $x - y$ plane with negligible vertical velocities (just enough to maintain gas incompressibility). Since the balance of Coriolis forces is maintained in thin vertical sheets, instability persists to large K_z. On the other hand, large K_x/K_z shrinks u_x and destroys the necessary balance of Coriolis forces.

The linear growth regime is surprisingly complex, considering the simplicity of the physical system. Toy models to explain the mechanism have unfortunately fallen short of capturing the essence of the instability. For instance, one might suspect that, since streaming instabilities involve particle density enhancements, they arise because radial drift slows in overdense regions [see equation (6.9)] leading to local traffic jams. This effect, while relevant, does not explain linear growth of infinitesimal perturbations. To see this, consider the axisymmetric evolution of particle density that follows from the equilibrium drift speed [equation (6.9)] and continuity [equation (6.1)], which we express for simplicity in terms of a *variable* (only for now) $\epsilon = \rho_{\rm p}(x,t)/\rho_{\rm g,0} = \epsilon_0 + \epsilon'(x,t)$ as

$$\frac{\partial \epsilon'}{\partial t} = -\frac{\partial(\epsilon w_x)}{\partial x} = 2\eta v_{\rm K}\tau_{\rm s}\frac{\partial}{\partial x}\left[\frac{\epsilon}{(1+\epsilon)^2+\tau_{\rm s}^2}\right]. \tag{6.12}$$

Linearising about $\epsilon' \ll \epsilon_0$ clearly gives stable wave propagation at the drift speed. Non-linear perturbations in equation (6.12) will steepen a particle density wave, with no amplitude growth (readily shown by the method of characteristics, see Shu 1992). Even if the traffic jam concept fails to explain the linear growth of the streaming instability, it may be used to explain the non-linear clumping seen in JY (see also §6.6.1 in this chapter).

We find in JY that non-linear states also show remarkable diversity with friction time and solids-to-gas ratio. We must, however, first ensure that the numerical algorithms can capture and confirm the linear growth phase.

Eigenvectors and vertical standing waves

To test the growth rates of Fig. 6.1 computationally, the eigenvectors, i.e. relative amplitudes and phases of the density and velocity perturbations, must be carefully seeded for a specific choice of parameters $\tau_{\rm s}, \epsilon, K_x, K_z$. The perturbation in each dynamical variable f can be written in terms of its complex amplitude $\tilde{f}$ (a component of the full eigenvector) as $f(x,z) = \Re\{\tilde{f}\exp[{\rm i}(k_x x + k_z z - \omega t)]\}$, where $\omega \equiv \omega_\Re + {\rm i}s$ is the complex eigenvalue containing the wave frequency $\omega_\Re$ and the growth rate s. We choose to eliminate the superfluous vertical phase speed by superposing pairs of modes with vertical wavenumbers k_z and $-k_z$, respectively. Under a vertical parity transformation the vertical velocity amplitudes are odd, while all others are even. The superposition yields

$$\begin{aligned} f_{\rm e}(x,z) &= [\Re(\tilde{f})\cos(k_x x - \omega_\Re t) - \\ &\quad \Im(\tilde{f})\sin(k_x x - \omega_\Re t)]\cos(k_z z)\exp(st), \end{aligned} \tag{6.13}$$

$$\begin{aligned} f_{\rm o}(x,z) &= -[\Re(\tilde{f})\sin(k_x x - \omega_\Re t) + \\ &\quad \Im(\tilde{f})\cos(k_x x - \omega_\Re t)]\sin(k_z z)\exp(st), \end{aligned} \tag{6.14}$$

for even (e) and odd (o) dynamical variables, respectively, which are now clearly standing waves in z.

Table 6.1 lists eigenvalues and eigenvectors for the cases we will test numerically in §6.5. The calculation is similar to that of YG except gas compressibility was added so that a gas density perturbation can be included in the numerical calculations. The effect of the gas compressibility is otherwise negligible for $\eta v_{\rm K}/c_{\rm s} \sim c_{\rm s}/v_{\rm K} \ll 1$ (the reason it was neglected in

Table 6.1. Test mode eigensystems

	$\tilde{u}_x$	$\tilde{u}_y$	$\tilde{u}_z$	$\tilde{\rho}_\mathrm{g}$
linA: $\tau_\mathrm{s}=0.1, \epsilon=3.0$	-0.1691398	$+0.1336704$	$+0.1691389$	$+0.0000224$
$(K_x=30, K_z=30)$	$+0.0361553\mathrm{i}$	$+0.0591695\mathrm{i}$	$-0.0361555\mathrm{i}$	$+0.0000212\mathrm{i}$
linB: $\tau_\mathrm{s}=0.1, \epsilon=0.2$	-0.0174121	$+0.2767976$	$+0.0174130$	-0.0000067
$(K_x=6, K_z=6)$	$-0.2770347\mathrm{i}$	$-0.0187568\mathrm{i}$	$+0.2770423\mathrm{i}$	$-0.0000691\mathrm{i}$
	$\tilde{w}_x$	$\tilde{w}_y$	$\tilde{w}_z$	ω
linA: $\tau_\mathrm{s}=0.1, \epsilon=3.0$	-0.1398623	$+0.1305628$	$+0.1639549$	-0.3480127
$(K_x=30, K_z=30)$	$+0.0372951\mathrm{i}$	$+0.0640574\mathrm{i}$	$-0.0233277\mathrm{i}$	$+0.4190204\mathrm{i}$
linB: $\tau_\mathrm{s}=0.1, \epsilon=0.2$	$+0.0462916$	$+0.2739304$	$+0.0083263$	$+0.4998786$
$(K_x=6, K_z=6)$	$-0.2743072\mathrm{i}$	$+0.0039293\mathrm{i}$	$+0.2768866\mathrm{i}$	$+0.0154764\mathrm{i}$

Note. — Frequency ω is normalised to Ω, velocities are normalised to ηv_K, and densities to the average value for particles or gas respectively. All eigenvalue coefficients are relative to the particle density perturbation, which should be set to $\tilde{\rho}_\mathrm{p} \ll 1$ for the evolution of the mode to be linear. We used $\tilde{\rho}_\mathrm{p} = 10^{-6}$ to normalise the eigenvector. The (tiny) effect of compressibility is included in the coefficients with $\eta v_\mathrm{K}/c_\mathrm{s} = 0.05$. The growth rate s is the imaginary part of ω.

YG), affecting eigenvalues and eigenvectors in the 5th digit for our choice of $\eta v_\mathrm{K}/c_\mathrm{s} = 0.05$. We also checked that the sound waves introduced by gas compression are rapidly damped. Note that Table 6.1 shows the gas density (and thus pressure) perturbations are out of phase (by $\sim 90^\circ$ and $\sim 180^\circ$ for A and B, respectively) with the particle density perturbation. Thus solids are not merely collecting in pressure maxima, as occurs in gas density structures that are steady in time.

6.4 Numerical methods

As a numerical solver we use the Pencil Code. This is a modular finite difference code that uses 6th order symmetric spatial derivatives and a 3rd order Runge-Kutta time integration (see Brandenburg 2003 for details). A module already exists for solving the equation of motion of a dust fluid that interacts with the main gas fluid through drag force (Johansen et al. 2004; Johansen and Klahr 2005). The basic dynamical equations in the (here unstratified) shearing sheet are equations (6.3) and (6.4) for the gas and equations (6.1) and (6.2) for the solids. This equation set is stabilised by adding small diffusive terms to the equation of motion and by upwinding the advection term in the continuity equations (for details, see Johansen and Klahr 2005; Dobler et al. 2006). Treating particles as a fluid facilitates analytic calculations and is significantly cheaper for numerical simulations, but is not always the desired approach.

6.4.1 Solids as particles

Using Lagrangian particles provides a more realistic description of the dynamics of the solids, and there are two main reasons to justify the additional effort.[2] First, particles at a given position need not have a single well-defined velocity as the fluid approximation assumes, i.e. trajectories can cross. This concern is particularly valid for marginal and looser coupling. Second, and more seriously, the fluid treatment cannot capture large density gradients, especially since the "sound speed" of the pressureless fluid is zero. Stabilisation of steep density gradients would require a large artificial viscosity that compromises the dynamics. Thus a Lagrangian treatment of the solids is necessary for the non-linear simulations of JY which generate large particles overdensities. Since the analysis of YG describes solids as a fluid, we must demonstrate that the instability does not depend crucially on this assumption.

When treating solids as numerical particles, or rather as *superparticles* since each numerical particle effectively represents a huge number of individual solids, each particle i has a position $\boldsymbol{x}^{(i)}$ and a velocity $\boldsymbol{v}^{(i)}$ relative to the Keplerian shear. Particle motions are governed by Hill's equations (Wisdom and Tremaine 1988)

$$\begin{aligned}\frac{\mathrm{d}\boldsymbol{v}^{(i)}}{\mathrm{d}t} &= 2\Omega v_y^{(i)}\hat{\boldsymbol{x}} - \frac{1}{2}\Omega v_x^{(i)}\hat{\boldsymbol{y}} \\ &\qquad -\frac{1}{\tau_\mathrm{f}}\left[\boldsymbol{v}^{(i)} - \overline{\boldsymbol{u}(\boldsymbol{x}^{(i)})}\right], \qquad (6.15)\\ \frac{\mathrm{d}\boldsymbol{x}^{(i)}}{\mathrm{d}t} &= \boldsymbol{v}^{(i)} - \frac{3}{2}\Omega x^{(i)}\hat{\boldsymbol{y}}, \qquad (6.16)\end{aligned}$$

here including drag force and expressed in a form to appear as the Lagrangian equivalent to equation (6.2). For axisymmetric simulations in the radial-vertical plane, the evolution of $v_y^{(i)}(t)$ is included but the azimuthal component of equation (6.16) is irrelevant, effectively replaced by $\mathrm{d}y^{(i)}/\mathrm{d}t = 0$ since that dimension that is not present. The interpolation of gas velocities at the particle positions, $\overline{\boldsymbol{u}(\boldsymbol{x}^{(i)})}$, is addressed in the next section.

6.4.2 Drag force calculation

The computation of drag forces between Lagrangian particles and an Eulerian grid requires some care to avoid spurious accelerations and to ensure momentum conservation. Small errors in the gas velocity are dangerously amplified by the subtraction of highly correlated particle velocities. Our drag force algorithm involves three steps:

1. Interpolating gas velocities at particle positions
2. Calculating the drag force on particles
3. Assigning the back-reaction force to the gas from particles in nearby cells

[2] See Garaud et al. (2004) for a thorough analysis of the validity of fluid descriptions of particle motion subject to gas drag

For the first step, interpolation, we begin with gas velocities, $\boldsymbol{u}^{(\boldsymbol{j})}$, defined on a uniform grid where the index $\boldsymbol{j}$ labels the cells centred on positions $\boldsymbol{x}^{(\boldsymbol{j})}$. We interpolate to the particle positions, $\boldsymbol{x}^{(i)}$, using a weight function, W_I, as

$$\overline{\boldsymbol{u}(\boldsymbol{x}^{(i)})} = \sum_{\boldsymbol{j}} W_\mathrm{I}(\boldsymbol{x}^{(i)} - \boldsymbol{x}^{(\boldsymbol{j})})\boldsymbol{u}^{(\boldsymbol{j})} \,. \tag{6.17}$$

The weight function is normalised as $\sum_{\boldsymbol{j}} W_\mathrm{I}(\boldsymbol{x}^{(i)} - \boldsymbol{x}^{(\boldsymbol{j})}) = 1$ for any $\boldsymbol{x}^{(i)}$, and has non-zero contributions only from the cells in the immediate vicinity of $\boldsymbol{x}^{(\boldsymbol{j})}$.

The second step, calculating the drag acceleration on particle i,

$$\boldsymbol{f}_\mathrm{p}^{(i)} = -\frac{\boldsymbol{v}^{(i)} - \overline{\boldsymbol{u}(\boldsymbol{x}^{(i)})}}{\tau_\mathrm{f}} \,, \tag{6.18}$$

is trivial once the relevant quantities are defined, but this is the step that amplifies interpolation errors in $\overline{\boldsymbol{u}(\boldsymbol{x}^{(i)})}$, because of strong coupling to particle velocities, a problem that worsens for smaller τ_f. We note that other choices of the drag law (e.g. non-linear in the velocity or including gas density fluctuations in Epstein drag) would be simple to implement by interpolating the relevant grid-based quantities as in equation (6.17).

Finally, we calculate the back-reaction drag force, $\boldsymbol{f}_\mathrm{g}^{(\boldsymbol{j})}$, on the gas in cell $\boldsymbol{j}$. Assigning particle velocities to a mesh risks violating momentum conservation. Instead we follow the suggestion of Jim Stone (personal communication) and use Newton's third law to directly assign the force on the particles back to the gas,

$$\boldsymbol{f}_\mathrm{g}^{(\boldsymbol{j})} = -\frac{m_\mathrm{p}}{\rho_\mathrm{g}^{(\boldsymbol{j})} V_\mathrm{cell}} \sum_i W_A(\boldsymbol{x}^{(i)} - \boldsymbol{x}^{(\boldsymbol{j})})\boldsymbol{f}_\mathrm{p}^{(i)} \,, \tag{6.19}$$

where m_p is the mass of a particle (if not uniform it would be inside the sum), and V_cell is the volume of a grid cell. The assignment function W_A obeys the same conditions as W_I, so that only particles in a given cell or its nearby neighbours contribute to the sum. Global momentum conservation follows trivially from summation of equation (6.19),

$$V_\mathrm{cell} \sum_{\boldsymbol{j}} \rho_\mathrm{g}^{(\boldsymbol{j})} f_\mathrm{g}^{(\boldsymbol{j})} + m_\mathrm{p} \sum_i f_p^{(i)} = 0 \,, \tag{6.20}$$

with no reference to the drag law, the interpolation function, or any properties of the assignment function except normalisation. Thus unlike particle-mesh calculations with interacting particles (e.g. by self-gravity), we are flexible to choose W_I and W_A independently, without violating momentum conservation. Nevertheless, choosing $W_\mathrm{A} = W_\mathrm{I}$ is safest since drag forces from gas to particles – and vice-versa – are smoothed symmetrically.

We opted for second order interpolation and assignment methods, either quadratic spline or quadratic polynomial, which use three grid cells in each dimension, for a total of 9 (27) for 2-D (3-D) simulations, respectively. This gave considerable improvement over lower order bilinear interpolation (but at a computational cost – the drag force calculations dominate the wall time in our simulations with high order interpolation and assignment). The details and errors associated with the interpolation schemes are described in Appendix A.3. The quadratic spline assignment/interpolation method is often referred to as the Triangular Shaped Cloud scheme (TSC, see Hockney and Eastwood 1981).

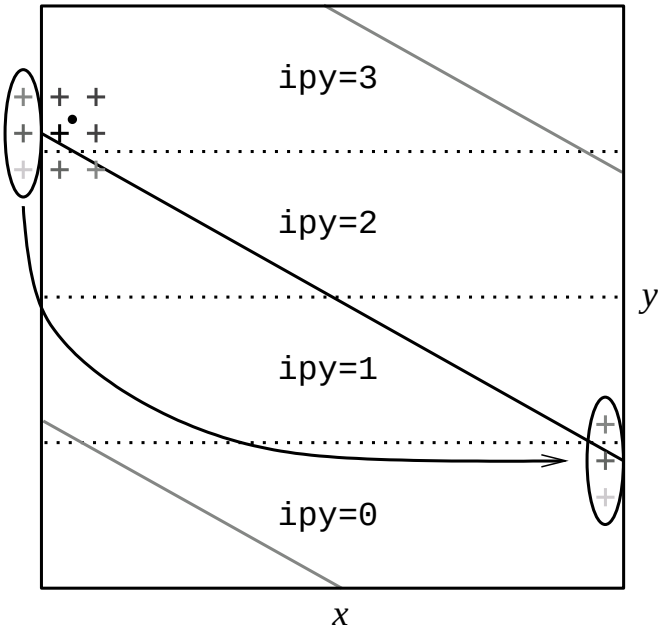

Fig. 6.3 A sketch of the shear-periodic radial (x) boundary condition for the assignment of drag forces from a particle to the gas. The dot represents a particle near the boundary and crosses indicate the (centres of) gas cells that receive a drag acceleration with the second order TSC assignment scheme (grayscale of crosses indicates rough weight of drag force received by gas in each cell). We illustrate an example with 4 processors in the y-direction (labelled `ipy`). The periodic direction is indicated by solid diagonal lines. The drag force assigned to ghost cells across the boundary (circled on left) is shifted in Fourier space and then added as an acceleration on the physical grid cells at the outer boundary. Note that in practice (a) the drag force from an individual particle influences more than three grid cells across the boundary, since displacements are not integer multiples of the grid spacing and (b) drag forces from all particles on a ghost zone are added before Fourier shifting.

Boundary conditions for the drag force

Our implementation of periodic boundary conditions, and use of higher (than zeroth, as in Johansen et al. 2006a) order assignment schemes, causes particles near grid edges to exert drag forces on mesh points across the boundaries. In non-axisymmetric simulations (such as the 3-D simulations that we present in JY) the radial direction is shear-periodic so that two connected points at the inner and outer radial boundary are $\Delta y(t) = \mathrm{mod}[(3/2)\Omega L_x t, L_y]$ apart in the azimuthal direction. Techniques for implementing radial boundary conditions in the shearing box are well-known (Hawley et al. 1995). Fluid variables in zones on one radial boundary are copied to ghost zones adjacent to the opposite boundary and shifted azimuthally. Then differences across boundaries are performed, i.e. "copy, shift, and difference."

The implementation of shear periodic boundary conditions for drag forces on the gas is a subtly different "assign, shift, and add" procedure, as sketched in Fig. 6.3. First we assign the (appropriate fraction of) drag accelerations from particles in boundary zones to gas in the

ghost zones. Then we shift the accelerations on the radial ghost zones in the y-direction, the inner by $-\Delta y(t)$, and the outer by $+\Delta y(t)$. Finally these shifted accelerations are added (or folded) to the first real zone on the opposite side of the mesh. We interpolate (since the ghost zones do not slide by integer numbers of grid cells) by applying the azimuthal shift in Fourier space. Fourier interpolation has the advantage over high order polynomial interpolation that the function and all its derivatives are continuous. A numerical test of the radial boundary condition with shearing waves is described in Appendix A.4.

6.5 Numerical tests of linear growth

We now present measurements of linear growth rates of the streaming instability from numerical simulations. These results confirm the capabilities of our code and verify the authenticity of this fundamental instability, not yet explicitly established for a particle-based treatment of solids. Our efforts in reproducing growth rates to a satisfactory accuracy were useful in developing our numerical implementation of drag forces. We hope that others who simulate coupled particle-gas discs will conduct similar dynamical tests of the simplest (identified) aerodynamic drag instability.

We choose two different test problems: an eigenvector for $\tau_{\rm s} = 0.1$, $\epsilon = 3.0$, $K_x = K_z = 30$ (run linA), which grows rapidly with $s/\Omega = 0.41902$, and an eigenvector for $\tau_{\rm s} = 0.1$, $\epsilon = 0.2$, $K_x = K_z = 6$ (run linB) that grows more slowly with $s/\Omega = 0.01548$ and hence is more numerically demanding. The total initial velocities are the sum of the equilibrium drift solutions of equations (6.7-6.10), and the vertically standing wave of equations (6.13-6.14) with eigenvectors from Table 6.1. The initial amplitude of the particle density was set to 10^{-6} in all cases to ensure linearity.

6.5.1 Growth for solids as a fluid

The measured growth rate when particles are treated as a fluid is shown with a solid black line in Figs. 6.4 and 6.5 (the top and bottom plots are identical for the two-fluid case). The eight panels show the growth rate of the velocity and density of the gas (top row) and of the solids (bottom row) as a function of the number of grid points per wavelength. We have varied the resolution between 3 and 64 grid points per wavelength for the fluid treatment of solids and between 8 and 64 grid points per wavelength for the particle treatment. The growth rates are obtained by spatially Fourier transforming the 8 dynamical variables at 10 fixed times over $\Delta t = 0.2\Omega^{-1}$ and measuring the amplitude growth of the relevant Fourier mode. There is generally an excellent agreement between the measured growth rates when the solids are treated as a fluid and the analytical values down to 4 grid points per wavelength, except for the gas density which shows some variation from the analytical value for crude resolutions. This disagreement is not surprising since small errors in the cancellation of $\partial u_x/\partial x$ and $\partial u_z/\partial z$ for the nearly incompressible gas give spurious growth to the gas density according to the linearised continuity equation $\partial \ln \rho'_{\rm g}/\partial t = -\boldsymbol{\nabla} \cdot \boldsymbol{u}'$. While the gas density perturbations are too small to affect the drag force, they also cause the pressure perturbations which are significant. Fortuitously, the errors in the gas density (for crude resolutions) do not affect

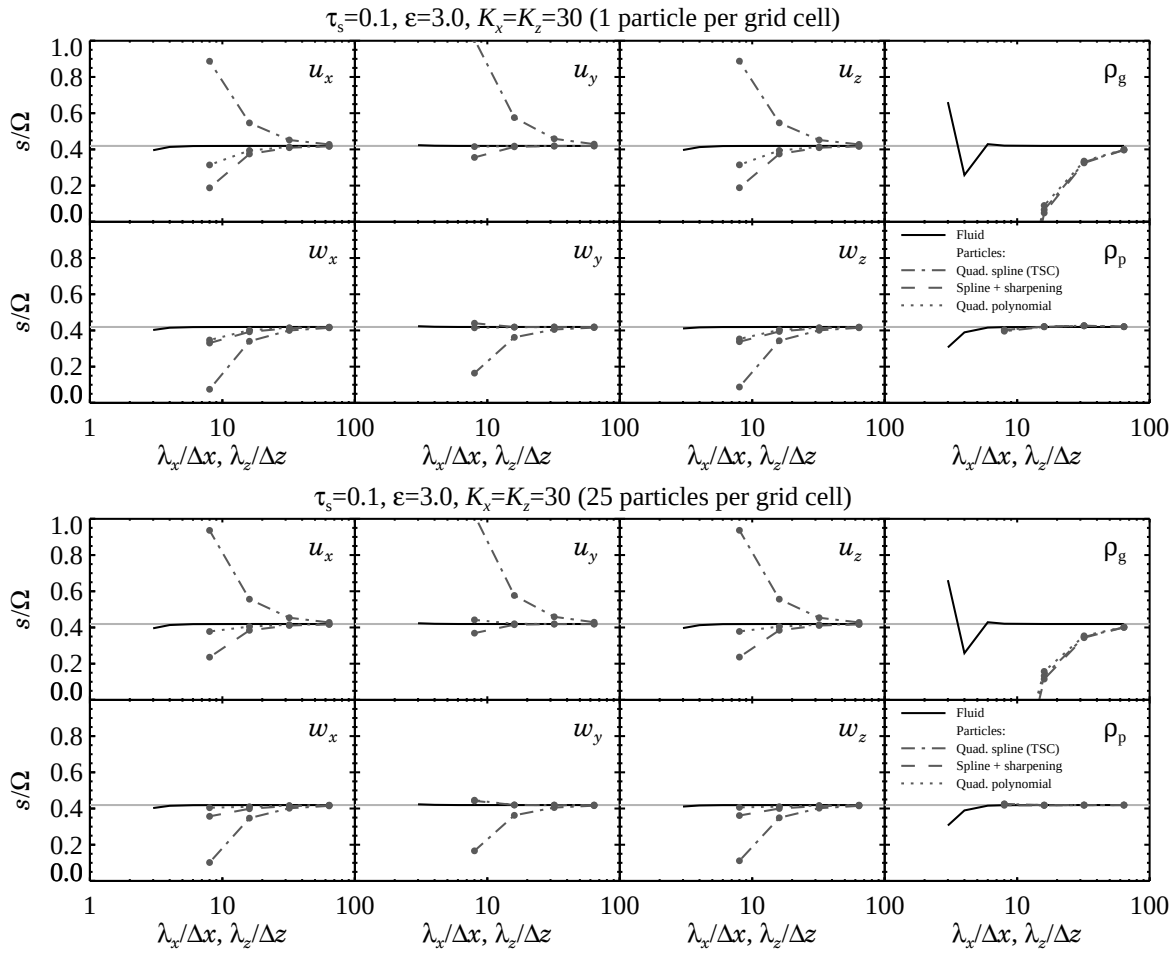

Fig. 6.4 Measured growth rate of a seeded mode with $K_x = K_z = 30$ and $\tau_\mathrm{s} = 0.1$, $\epsilon = 3.0$ as a function of the number of grid-points per wavelength, shown for 1 and 25 particles per grid cell in the top and bottom plots, respectively. The behaviour of each dynamical variable is shown separately. The analytical growth rate, $s = 0.41903\Omega$, is indicated with a grey line. The fluid treatment (solid black line) gives excellent agreement with the analytical growth rate down to 4 grid points per wavelength, whereas 16 grid points is needed for the regular TSC scheme (dash-dotted line). Applying Fourier sharpening to the initial condition gives some improvement (dashed line). Replacing spline interpolation with polynomial interpolation (dotted line) gives better growth rates, but polynomial interpolation has the disadvantage of being discontinuous over cell interfaces. Increasing the number of particles per grid cell from 1 to 25 has minimal influence on the linear growth.

the other dynamical variables. It may help that spurious sound waves damp rapidly (in a stopping time).

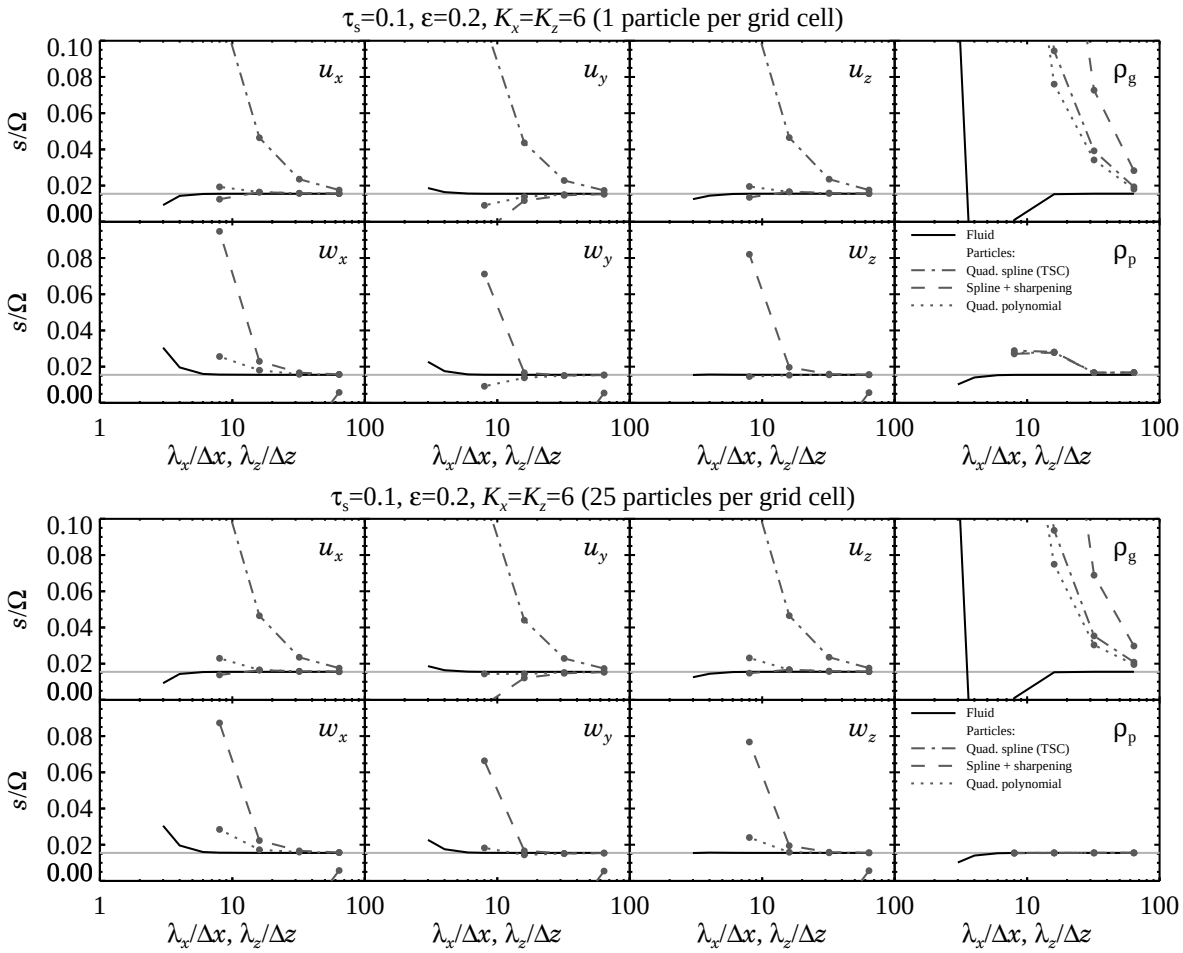

Fig. 6.5 Similar to Fig. 6.4 but for a mode with $K_x = K_z = 6$ and $\tau_\mathrm{s} = 0.1$, $\epsilon = 0.2$ that has an analytical growth rate of $s = 0.01548\Omega$. The agreement with the analytical growth shows a comparable resolution dependance to Fig. 6.4, but here the increase to 25 particles per grid cell shows better agreement for ρ_p.

6.5.2 Growth for solids as particles

Reproducing analytic growth rates using a particle representation of the solids is significantly more difficult than in the two-fluid case. Poisson fluctuations from undersampling and truncation errors in the drag force calculation cause numerical discrepancies. Section 6.4.2 and Appendix A.3 describe the algorithms for computing drag forces and the errors associated with interpolation and assignment.

Cold start initialisation

To avoid shot noise in seeding linear particle density perturbations we use a “cold start” algorithm (described in detail in Appendix A.5) for the initial particle positions. First we

place all particles on a uniform grid. Then we apply a small, spatially periodic shift to their positions. This seeds the desired mode with minimal noise leaked to other wavelengths. We experimented with different numbers of particles: 25 particles per grid cell to match the non-linear runs of JY, and 1 particle per grid cell as a test.

With the cold start to eliminate noise and the TSC assignment scheme to smoothly distribute a particle's influence over the nearest three grid cells per dimension, communicating initial density perturbations of infinitesimal amplitude with only a few particles is trivial. Fig. 6.6 demonstrates the algorithm effectiveness with the near perfect replication of a 1-D particle density perturbation of amplitude 10^{-6} with only 32 grid cells and one particle per cell. This is nothing more (or less) than the miracle of continuous numbers. The use of many particles per grid cell is still necessary to get good statistics in non-linear simulations.

Results

The growth rates with solids as particles are shown (together with the two-fluid results) in Figs. 6.4 and 6.5 as a function of spatial resolution. The top and bottom plots in each figure are for 1 and 25 particles per grid cell, respectively. Particle number makes little difference for the agreement with linear theory, although additional particles give some improvement, notably for the growth rate of $\rho_{\rm p}$ in Fig. 6.5.

While all runs use the TSC scheme to assign drag forces to the gas, three different techniques were tested for the interpolation of gas velocities to particle positions: (1) quadratic spline interpolation, (2) quadratic spline interpolation with an initial Fourier sharpening of the gas velocity field, and (3) quadratic polynomial interpolation. Errors in gas velocity interpolation are the most dangerous since they are amplified in the force calculation by subtracting a particle velocity that is highly correlated with the gas flow.

The first technique, quadratic spline interpolation, uses the same weight function as TSC assignment and gives smooth interpolates with a reduced fluctuation amplitude. The dash-dotted lines in Figs. 6.4 and 6.5 show that this technique accurately reproduces the growth of $\rho_{\rm p}$. The results for the other variables are poor for resolutions of less than 16 grid points per wave length. This is a result of spurious drag forces generated because interpolation reduces gas fluctuation amplitudes.[3]

The second interpolation technique (shown with dashed lines in Figs. 6.4 and 6.5) still uses quadratic splines, but sharpens the initial gas velocities to correct the drag force. The amplitude of the Fourier modes $\tilde{\boldsymbol{u}}$ are increased by the precise amount, $[1 - \Delta^2(k_x^2 + k_z^2)/8]^{-1}$, that interpolation reduces them (see Appendix A.3). The sharpened TSC scheme gives much better growth rates, but still not as good as the two-fluid results. In a non-linear simulation with an evolving power spectrum, one could sharpen $\boldsymbol{u}$ with a pair of Fourier transforms at each time-step, but this was deemed too computationally costly. By getting improved results with only the initial condition sharpened, we show that growth rate discrepancies with

[3]This is why, for unsharpened spline interpolation, growth rates are too large for $\boldsymbol{u}$ (gas is accelerated toward the unsmoothed amplitude by particles) and too small for $\boldsymbol{w}$ (particles are decelerated by the lowered gas amplitudes).

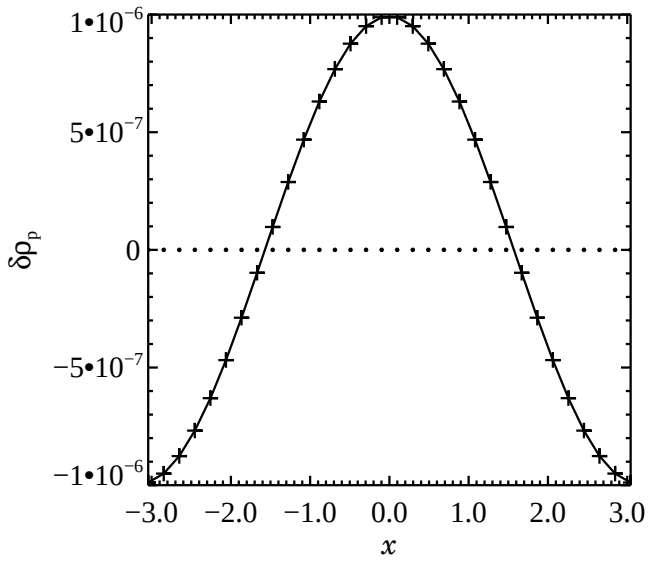

Fig. 6.6 A sinusoidal particle density perturbation of amplitude 10^{-6} as generated by the shifting algorithm of Appendix A.5 with 32 particles – only one per grid cell! The crosses (connected by the solid line) plot the TSC assignment of particle (over)density to the grid cells. Dots indicate the positions of the particles, but the shift is imperceptibly small.

spline interpolation are largely due to differences between numerical (discretised) and analytic eigenvectors that should not compromise the non-linear simulations.

The third approach (shown with dotted lines in Figs. 6.4 and 6.5) opts for precise quadratic polynomial interpolation instead of smoother splines. The resulting growth rates are comparable, or slightly better than, the sharpened splines. Despite the simplicity and good results obtained with this technique, we did not use it in the non-linear runs. Discontinuities in the interpolates at cell boundaries would add noise by leaking power to the grid scale. Since the errors of TSC are well-behaved (spatially smooth across a grid cell, declining with increasing resolution, and leaving particle density growth unaffected even at low resolution), we used spline interpolation in the non-linear runs. We also prefer the symmetry of using the same weight functions for interpolation (quadratic spline) and assignment (TSC).

Overall, numerical growth rates with solids treated as particles agree well with linear theory down to 16 grid points per wavelength, although the particle density grows at the correct rate even at 8 grid points per wavelength. Anomalies, particularly in the gas density, suggest that sound waves are being triggered due to interpolation errors, but these spurious motions damp and do not impede the expected growth of particle density perturbations.

6.6 Energy and angular momentum balance

This section provides brief overviews of energy and angular momentum in coupled particle-gas discs in order to provide a point of reference to more familiar dynamical systems, and because it will help us interpret the non-linear results of JY. We denote $\mathcal{L} \equiv \rho_{\rm g} u_y + \rho_{\rm p} w_y$ as the total angular momentum density of solids and gas, ignoring the radius factor that is constant in the local approximation. The azimuthal components of equations (6.2) and (6.4) give

$$\left(\frac{\partial}{\partial t} - \frac{3}{2} \Omega x \frac{\partial}{\partial y} \right) \mathcal{L} + \boldsymbol{\nabla} \cdot \boldsymbol{\mathcal{F}} = -\frac{\Omega}{2} \mathcal{F}_{\rho,x} - \frac{\partial P}{\partial y} \,. \tag{6.21}$$

The terms on the left hand side relate local changes in $\mathcal{L}$ to the transport of $\mathcal{L}$ by the Keplerian flow and to the angular momentum flux $\boldsymbol{\mathcal{F}}_{\mathcal{L}} \equiv \rho_{\rm g} u_y \boldsymbol{u} + \rho_{\rm p} w_y \boldsymbol{w}$. We do not call this flux a Reynolds stress because the velocities $\boldsymbol{u}$ and $\boldsymbol{w}$ have not been decomposed into fluctuations about their mean. The NSH equilibrium of equations (6.7-6.10) transports angular momentum radially inwards,

$$\mathcal{F}_{\mathcal{L},x} \equiv \rho_{\rm g} u_x u_y + \rho_{\rm p} w_x w_y \tag{6.22}$$

$$= -2 \tau_{\rm s}^3 \rho_{\rm p} \left[\frac{\eta v_{\rm K}}{(1+\epsilon)^2 + \tau_{\rm s}^2} \right]^2 \,, \tag{6.23}$$

a consequence of the slower rotation of the outgoing gas relative to the faster rotation of the incoming particles. This differs from the usual outward transport of angular momentum in accretion discs (Lynden-Bell and Pringle 1974), because the driving agent is not orbital shear, but the radial pressure gradient.

The terms on the right hand side of equation (6.21) represent sources or sinks of angular momentum: the radial mass flux, $\mathcal{F}_{\rho,x} \equiv \rho_{\rm g} u_x + \rho_{\rm p} w_x$, and azimuthal pressure gradients, where P is promoted to denote the total gas pressure (background and perturbations) in this section. Equation (6.21) proves that axisymmetric equilibrium solutions cannot transport mass radially in the local model, a condition obeyed by equations (6.7) and (6.9). Note that equation (6.21) does not explicitly include drag forces, which transfer momentum between gas and solids, but (of course) do not dissipate $\mathcal{L}$.

The evolution of kinetic energy density $\mathcal{E} \equiv (\rho_{\rm g} |\boldsymbol{u}|^2 + \rho_{\rm p} |\boldsymbol{w}|^2)/2$ is found by summing the dot products of $\rho_{\rm g} \boldsymbol{u}$ with equation (6.4) and $\rho_{\rm p} \boldsymbol{w}$ with equation (6.2) to give

$$\left(\frac{\partial}{\partial t} - \frac{3}{2} x \Omega \frac{\partial}{\partial y} \right) \mathcal{E} + \boldsymbol{\nabla} \cdot \boldsymbol{\mathcal{F}}_{\mathcal{E}} = \dot{\mathcal{E}}_{\rm drag} - \boldsymbol{u} \cdot \boldsymbol{\nabla} P + \frac{3}{2} \Omega \mathcal{F}_{\mathcal{L},x} \,, \tag{6.24}$$

where the energy flux, $\boldsymbol{\mathcal{F}}_{\mathcal{E}} \equiv \rho_{\rm g} |\boldsymbol{u}|^2 \boldsymbol{u} + \rho_{\rm p} |\boldsymbol{w}|^2 \boldsymbol{w}$, transports energy radially inward (outward) when gas (particles) dominate the mass, respectively.[4] The sources and sinks on the right hand side include the energy lost to drag dissipation,

$$\dot{\mathcal{E}}_{\rm drag} \equiv -\rho_{\rm p} |\boldsymbol{w} - \boldsymbol{u}|^2 / \tau_{\rm f} \tag{6.25}$$

$$= -\frac{4(1+\epsilon)^2 \tau_{\rm s} + \tau_{\rm s}^3}{[(1+\epsilon)^2 + \tau_{\rm s}^2]^2} (\eta v_{\rm K})^2 \rho_{\rm p} \Omega \,, \tag{6.26}$$

[4] Actually this result only holds in the centre of mass reference frame, i.e. with $V_y^{(\rm com)}$ subtracted.

where the second equality applies to the NSH equilibrium. A simple estimate of the effective temperature produced when the dissipated kinetic energy is released as thermal heat gives

$$T_{\rm drag} < \left[\Sigma_{\rm p}\Omega(\eta v_{\rm K})^2/\sigma_{\rm SB}\right]^{1/4} \sim 30(r/{\rm AU})^{-3/4}\,{\rm K} \tag{6.27}$$

as an upper limit for the case of marginal coupling and $\epsilon \ll 1$, where $\Sigma_{\rm p} \simeq \rho_{\rm p} H_{\rm p}$ is the surface density of the solid component and $H_{\rm p}$ is the scale height of the sublayer of solids. The above temperature limit is significantly colder than even passively irradiated discs (Chiang and Goldreich 1997), a comforting fact for SED modellers.

The $\dot{\mathcal{E}}_{\rm work} \equiv -\boldsymbol{u}\cdot\boldsymbol{\nabla}P$ term represents energy gained from the work done by the total pressure forces. The equilibrium value of

$$\dot{\mathcal{E}}_{\rm work} = -u_x(\partial P/\partial r) = \frac{4\tau_{\rm s}}{(1+\epsilon)^2+\tau_{\rm s}^2}(\eta v_{\rm K})^2\rho_{\rm p}\Omega \tag{6.28}$$

shows that $|\dot{\mathcal{E}}_{\rm work}| > |\dot{\mathcal{E}}_{\rm drag}|$, i.e. more energy is put into the system by pressure work than removed by drag. The final term,

$$\dot{\mathcal{E}}_{\mathcal{L}} \equiv (3/2)\Omega\mathcal{F}_{\mathcal{L},x} = -\frac{3\tau_{\rm s}^3}{\left[(1+\epsilon)^2+\tau_{\rm s}^2\right]^2}(\eta v_{\rm K})^2\rho_{\rm p}\Omega\,, \tag{6.29}$$

is well known in studies of viscous or collisional discs as the heat generated by the outward transport of angular momentum (Shu and Stewart 1985; Lithwick and Chiang 2007). However, in our case angular momentum transport is reversed according to equation (6.23) and provides a sink of kinetic energy. The phenomenon of "backwards" angular momentum transport, and the dynamical cooling it provides, has been famously offered as an explanation for the sharp edges of planetary rings (Borderies et al. 1982).

Equations (6.26), (6.28), and (6.29) verify that the heating and cooling terms sum up to zero in the equilibrium state: $\dot{\mathcal{E}}_{\rm drag} + \dot{\mathcal{E}}_{\rm work} + \dot{\mathcal{E}}_{\mathcal{L}} = 0$. The work done by pressure forces balances dissipation by drag forces and losses from the backwards transport of angular momentum.

6.6.1 Clumping and dissipation

In this subsection we will show that particle clumping reduces energy dissipation by drag forces, at least in a laminar state. Particles effectively "draft" off each other like birds flying in formation or bicycle riders in a peloton. This drafting does not rely on overlapping turbulent wakes, but instead depends on slowing relative gas motions by the collective inertia of particles. It is tempting to argue that the lowered dissipation rate explains the tendency of particles to clump. As usual, the story is more complicated, but the evolution of $\dot{\mathcal{E}}_{\rm drag}$ turns out to be a useful diagnostic for the non-linear simulations of JY.

First we demonstrate that dissipation is reduced by clumping. Consider the equilibrium drag dissipation of equation (6.26), for simplicity in the tight coupling limit ($\tau_{\rm s} \ll 1$), which we now express per unit surface area instead of volume as

$$\Lambda_{\rm diss} \equiv \dot{\mathcal{E}}_{\rm diss} H_{\rm p} \approx -\frac{4\tau_{\rm s}}{(1+\epsilon)^2}(\eta v_{\rm K})^2\Sigma_{\rm p}\Omega\,. \tag{6.30}$$

Now imagine concentrating the particles into a volume smaller by a factor $n > 1$ via vertical setting or clumping. Compared to the uniform solids-to-gas ratio ϵ the new value is $n\epsilon$ in clumps and 0 in voids. The new height-averaged dissipation rate is

$$\Lambda^*_{\rm diss} = -\frac{4\tau_{\rm s}}{(1+n\epsilon)^2}(\eta v_{\rm K})^2 \Sigma_{\rm p} \Omega \,. \tag{6.31}$$

The fractional change in dissipation (for $\tau_{\rm s} \ll 1$),

$$f_\Lambda \equiv \frac{\Lambda^*_{\rm diss}}{\Lambda_{\rm diss}} = \left(\frac{1+\epsilon}{1+n\epsilon}\right)^2 < 1 \,, \tag{6.32}$$

shows that clumping decreases the net dissipation of well-coupled particles and that the effect becomes stronger with increasing ϵ.

Unfortunately there is no reason to expect in general that the dissipation rate decreases, especially since the system is not closed, but driven by pressure gradients. Examples of driven systems in which mechanical dissipation increases with the spontaneous transition from laminar to turbulent flow include drag on a rigid body (e.g. an aircraft wing) and Rayleigh convection with fixed temperature on the endplates (Jeremy Goodman, personal communication). Indeed the non-linear simulations of JY find that $|\dot{\mathcal{E}}_{\rm drag}|$ could increase or decrease in the non-linear state. Obviously drag dissipation is affected not just by clumping (as in the toy laminar calculation here) but by the turbulent velocities that tend to increase dissipation. Nevertheless JY demonstrate that runs with the largest (and longest lived) overdensities show a decrease in $|\dot{\mathcal{E}}_{\rm drag}|$, lending credence to the hypothesis that drafting can augment particles' ability to clump.

6.7 Discussion

This chapter begins our numerical exploration of the streaming instability, which uses aerodynamic particle-gas coupling to tap the radial pressure gradient in protoplanetary discs. Growing oscillations arise in an idealised model for protoplanetary discs that assumes a local, unstratified, and non-self-gravitating shearing box with gas and uniformly-sized, non-colliding solids. Studying a relatively simple system isolates the surprisingly rich consequences of mutual drag coupling in discs. Also, the well-defined growth rates of seeded eigenvectors make the streaming instability an ideal test of numerical implementations of particle-gas dynamics, as suggested in YG. We encourage those who study manifestations of particle-gas dynamics in discs to consider the linear streaming instability as a test problem if the feedback of solids on gas dynamics is relevant.

This work is largely successful in reproducing the analytic growth rates of YG. The two-fluid simulations, which treat solids as a pressureless fluid, give excellent results with minimal computational effort. Particle-fluid simulations also converge to the analytic results, but higher spatial resolution is required. Treating the solids as particles has several advantages – it is more realistic, it can validate the often-used fluid approximation for solids, and it allows the development of non-linear density enhancements without spurious shocks. Refinements of the particle-fluid algorithm used in Johansen et al. (2006a) are described, notably the use of higher

order interpolation and assignment schemes to minimise errors in the drag force computation. These errors become more drastic as the stopping time decreases and errors grow relative to the diminishing difference between gas and particle velocities. Smaller stopping times also give shorter length scales, thereby imposing stricter Courant criteria. These restrictions actually dominate the obvious concern that tighter coupling stiffens the equations of motion. Detailed modelling of the smallest particles in protoplanetary discs, especially in the inner regions with high gas densities, will require further algorithm development and increased computational power. In the meantime, studies of moderate coupling can establish the relevant physical phenomena and provide a baseline for extrapolation to more extreme parameters.

Having developed a particle-mesh scheme that can be trusted to simulate coupled particle-gas dynamics with feedback, we proceed to explore the non-linear evolution of streaming instabilities in the next chapter with particular attention to the growth and saturation of particle overdensities.

Chapter 7

Non-linear evolution of the streaming instability

From Johansen & Youdin (2007): The Astrophysical Journal, in press

7.1 Abstract

We present simulations of the non-linear evolution of streaming instabilities in protoplanetary discs. The two components of the disc, gas treated with grid hydrodynamics and solids treated as superparticles, are mutually coupled by drag forces. We find that the initially laminar equilibrium flow spontaneously develops into turbulence in our unstratified local model. Marginally coupled solids (that couple to the gas on a Keplerian time-scale) trigger an upward cascade to large particle clumps with peak overdensities above 100. The clumps evolve dynamically by losing material downstream to the radial drift flow while receiving recycled material from upstream. Smaller, more tightly coupled solids produce weaker turbulence with more transient overdensities on smaller length scales. The net inward radial drift is decreased for marginally coupled particles, whereas the tightly coupled particles migrate faster in the saturated turbulent state. The turbulent diffusion of solid particles, measured by their random walk, depends strongly on their stopping time and on the solids-to-gas ratio of the background state, but diffusion is generally modest, particularly for tightly coupled solids. Angular momentum transport is too weak and of the wrong sign to influence stellar accretion. Self-gravity and collisions will be needed to determine the relevance of particle overdensities for planetesimal formation.

7.2 Introduction

This chapter extends our preparatory numerical investigations of the streaming instability (Youdin and Johansen 2007, hereafter YJ, see also Chapter 6 of this thesis) into the non-linear regime. The linear streaming instability was first described by Youdin and Goodman (2005, hereafter YG) who found that the radial and azimuthal drift of solids through gas in a protoplanetary disc triggers growing oscillations that concentrate particles. YJ details the numerical techniques used to study the evolution of solids and gas in a local patch of a protoplanetary disc and demonstrates that our code successfully reproduces the linear growth rates derived by YG. This chapter describes the non-linear evolution of the streaming instability to a fully turbulent state and studies the consequences for particle concentration and transport.

The starward drift of solids, caused by the sub-Keplerian headwind encountered by the particles, is not just a trigger for streaming instabilities, but also a source of theoretical difficulties. Growing planetesimals by coagulation faces severe time-scale constraints due to the loss off solids (ultimately to the star or sublimation in the inner disc). The restriction is most acute for 10 cm "rocks" through 1 m "boulders" with drift times of only a few hundred orbits (Weidenschilling 1977a) in most of the planet-forming region of standard minimum mass nebula models (Weidenschilling 1977b; Hayashi 1981). The drift of mm-sized solids in a few times 10^5 years at 30 AU is at best marginally consistent with the observed mm-excess from the outer parts T-Tauri discs with ages of a few Myr (Wilner et al. 2000; Rodmann et al. 2006). This mismatch between theory and observations may indicate that simple drift time estimates are missing important dynamical effects. We refer to generally to Brauer et al. (2007) for an extensive treatment of theoretical ways to main such a population of pebbles, but reiterate here a few main points from that and other papers on the subject.

Several mechanisms could impede the radial influx of solids. The increased inertia of solids in a dense midplane sublayer decreases drift speeds as the local gas mass fraction squared (Nakagawa et al. 1986; Youdin and Chiang 2004). Since such high densities may trigger rapid gravitational collapse of solids (Youdin and Shu 2002), sedimentation alone is not a satisfactory explanation of the long lifetimes of pebbles in the discs, even if the turbulence is weak enough to allow the formation of an extremely thin mid-plane layer. Turbulent diffusion in accretion discs will maintain a small fraction of particles in the outer disc (Stepinski and Valageas 1996; Takeuchi and Lin 2002), but this scenario requires a particle reservoir that exceeds by far the observed amount of mm-sized solids and thus implies disc masses that are orders of magnitude larger than minimum mass models. Giant anticyclonic vortices (Barge and Sommeria 1995; de la Fuente Marcos and Barge 2001) stall migration by trapping marginally coupled solids. However the formation and stability of vortices in discs is not clear (Goodman et al. 1987; Klahr and Bodenheimer 2003; Johansen et al. 2004; Barranco and Marcus 2005; Fromang and Nelson 2005). Any local pressure maximum – not only vortices – can trap boulders (Klahr and Lin 2001; Haghighipour and Boss 2003), e.g. spiral arms of massive self-gravitating discs (Rice et al. 2004) or even transient pressure enhancements in magnetorotational turbulence (Johansen et al. 2006b). The present work will show that streaming turbulence modestly slows the average radial drift of marginally coupled solids. An ultimate solution of the drift problem may require rapid (faster than drift) planetesimal formation (by gravitational collapse and/or coagulation) *and* fragmentation to maintain

observed populations of small solids (Dullemond and Dominik 2005).

The dynamical particle trapping mechanisms mentioned above increase particle densities, with an efficiency that depends on (often uncertain) structure lifetimes. Local particle overdensities can seed gravitational collapse of solids and affect the rates of (and balance between) coagulation and collisional fragmentation. Optically thick clumps could even influence radiative transfer if the disc itself is optically thin, and thereby alter observational estimates of disc mass and particle size (see Draine 2006 for a general discussion of the role of optical depth, but not clumping *per se*). Radial drift inherently augments the surface density of solids in the inner disc as particles pile up from larger orbital radii, as long as particles are smaller than the gas mean free path so that Epstein drag applies (Youdin and Shu 2002; Youdin and Chiang 2004). In simulations and experiments of forced Kolmogorov turbulence, particles concentrate in low vorticity regions at the viscous dissipation scale (Fessler et al. 1994; Padoan et al. 2006). Efficient collection requires small particles that couple to the rapid turnover time at the dissipation scale. Cuzzi et al. (2001) apply this passive turbulent concentration to the size-sorting of chondrules (abundant, partially-molten, mm-sized inclusions found in primitive meteorites) in the inner solar nebula.

Johansen et al. (2006a) discovered active turbulent concentration (active meaning that the drag feedback on gas was included) of larger particles (from cm-sized pebbles to m-sized boulders) in simulations of Kelvin-Helmholz midplane turbulence. Dense clumps of solids plough through the gas at near the Keplerian speed, scooping up more isolated particles that move with the sub-Keplerian headwind. Since this particle concentration mechanism relies on two-way drag forces, it was (and still is) considered a non-linear manifestation of streaming instabilities. The current work further explores active concentration, isolating the role of drag feedback by ignoring vertical stratification. We consider different geometries, both axisymmetric in the radial-vertical plane and fully 3-D, than Johansen et al. (2006a), who considered the azimuthal-vertical plane, and we use the higher order interpolation scheme for drag forces described in YJ. We will thus show that the "pure" streaming instability also produces strongly non-linear particle overdensities.

Turbulent diffusion controls the extent to which particles sediment in the mid-plane (Dubrulle et al. 1995) and whether (or how fast) self-gravity can collect solids into rings and bound clumps (Youdin 2005a,b). Diffusion is the most fundamental parameter governing whether planetesimals can form by gravitational instability (as originally proposed by Safronov 1969; Goldreich and Ward 1973), because the oft-mentioned critical density for gravitational collapse is irrelevant when drag forces are included to transfer angular momentum from the solids to the gas (Ward 1976, 2000). Passive diffusion of particles in magnetorotational turbulence has been found to be quite strong (Johansen and Klahr 2005; Turner et al. 2006; Fromang and Papaloizou 2006), although the Schmidt number (the ratio between the turbulent viscosity of the gas and the particle diffusion) increases in the presence of a net vertical magnetic field (Carballido et al. 2005; Johansen et al. 2006c). In the present work we measure the active particle diffusion in streaming turbulence, by considering the random walk of the particles away from a reference point, and find it to be relatively weak, especially for smaller particles.

The chapter is built up as follows. In §7.3 we briefly reiterate the physical model of the protoplanetary disc and our numerical method for solving the dynamical equations of gas and solids. In §7.4 we present the non-linear simulations and the topography of the turbulent

state, before analysing in §7.5 the statistics and causes of particle clumping in more detail. Then §7.6 addresses the transport and diffusion of particles and angular momentum in the saturated streaming turbulence. We summarise our results in §7.7.

7.3 Numerical method

The dynamical equations and the numerical method are presented in detail in YJ, but we briefly recapitulate the main points in this section. As a numerical solver we use the Pencil Code. This is a finite difference code that uses 6th order symmetric spatial derivatives and a 3rd order Runge-Kutta time integration (see Brandenburg 2003 for details).

We model a local patch in a protoplanetary disc with the shearing sheet approximation (e.g. Goldreich and Tremaine 1978). A Cartesian coordinate frame that corotates with the Kepler frequency Ω at a distance r from the central star is oriented with x, y and z axes pointing radially outwards, along the orbital direction, and vertically out of the disc (parallel to the Keplerian angular momentum vector), respectively. We solve the equations of motion for deviations from Keplerian rotation in an unstratified model, i.e. vertical gravity is ignored. The gas (and not the solids) is subject to pressure forces, including the global radial pressure gradient, constant in the local approximation and measured by the dimensionless parameter

$$\eta \equiv -\frac{\partial P/\partial r}{2\rho_{\rm g}\Omega^2 r} \approx \left(\frac{c_{\rm s}}{v_{\rm K}}\right)^2 , \tag{7.1}$$

where $v_{\rm K} = \Omega r$ is the Keplerian orbital speed, while P, $\rho_{\rm g}$, and $c_{\rm s}$ are the pressure, density and sound speed of our isothermal gas. All our simulations use $\eta = 0.005$ and $c_{\rm s}/v_{\rm K} = H/r = 0.1$, where H is the gas scale-height. Our results can be applied to different values of η if velocities are scaled by $\eta v_{\rm K}$, the pressure-supported velocity, and lengths are scales by ηr, the radial distance between points where Keplerian and pressure-supported velocities are equal.[1]

The solids are treated alternatively as a pressureless fluid or as superparticles that each contain the mass of many actual solid bodies. Solids and gas mutually interact by frictional drag forces that are linear in the relative velocity. This models small particles with a friction (or stopping) time $\tau_{\rm f}$ that is independent of the relative speed between gas and particles (i.e. no turbulent wakes form). The translation from friction time to the radius of a particle depends only on gas properties and the material density of the solids. As a rule of thumb the radius of a compact icy particle in meters is roughly equal to the dimensionless stopping time

$$\tau_{\rm s} \equiv \Omega\tau_{\rm f} \tag{7.2}$$

at Jupiter's location ($r \approx 5\,{\rm AU}$) in standard minimum mass nebula models (Hayashi 1981).

When solids are treated as numerical particles, we calculate the drag acceleration by interpolating the gas velocity at the positions of the particles using a second-order spline fit to the 9 (27) nearest grid points that surround a given particle for 2-D (3-D) grids. To conserve momentum we assign the drag force on each single particle back to the gas using a Triangular

[1] The value of $H/(\eta r)$ ($= 20$ in our simulations) changes with this scaling, but should not affect the results as long as Mach numbers remain low ($H/r \ll 1$) so that gas compressibility is insignificant.

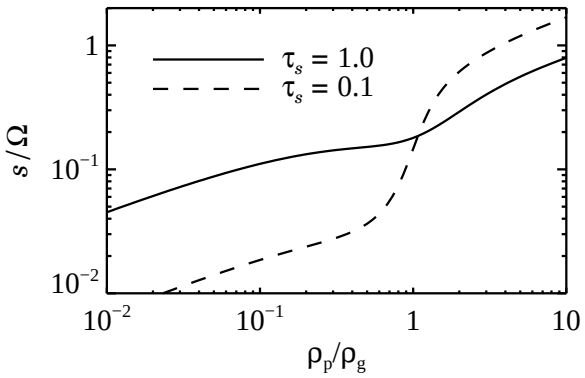

Fig. 7.1 Peak growth rate s of the streaming instability versus the solids-to-gas ratio ϵ for friction times of $\tau_s = 1.0$ (solid line) and $\tau_s = 0.1$ (dashed line). The steep rise in growth rate when $\tau_s = 0.1$ particles cross $\rho_p/\rho_g = 1$ explains the cavitation in the non-linear run AB (see Fig. 7.5).

Shaped Cloud (TSC) scheme (Hockney and Eastwood 1981). This smoothing of the particles' influence helps overcome shot noise, and should not be seen as an SPH (smoothed particle hydrodynamics) approach since our particles carry no hydrodynamic properties. We showed in YJ that 1 particle per grid point is enough to resolve the linear growth of the streaming instability, but to better handle Poisson fluctuations for a wider range of densities, we generally use 25 particles per grid point in the non-linear simulations.

An equilibrium solution to the coupled equations of motion of the gas and the solids was found by Nakagawa et al. (1986 hereafter referred to as NSH) where drag balances the radial pressure gradient and Coriolis forces. YG found that this equilibrium triggered a linear drag instability. The peak growth rate of this streaming instability is shown in Fig. 7.1 as a function of the solids-to-gas ratio ϵ for τ_s of 0.1 and 1.0. See Figs. 1 and 2 of YJ (and the accompanying text) for the dependence of growth rates on wavenumber.

7.4 Non-Linear evolution to turbulence

With confidence from YJ that the code solves correctly for the linear growth of the streaming instability, we turn our focus to the non-linear evolution into turbulence. We generically refer to the non-linear states of our runs as "turbulent," because they contain stochastic fluctuations that diffuse material and momentum. Some cases (the gas-dominated AA and BA runs, see below) appear more wave-like with peaks in the spatial and temporal Fourier spectra (as we will see in Fig. 7.12). However, even these runs exhibit diffusion and stochastic fluctuations on a range of scales, so we also label them as turbulent. This section describes the simulation parameters and main results for marginal vs. tighter coupling. More detailed analyses of the turbulent state follow in later sections.

Table 7.1. Run Parameters

Run (1)	τ_s (2)	ϵ (3)	$L_x \times L_y \times L_z$ (4)	$N_x \times N_y \times N_z$ (5)	N_p (6)	Δt (7)
AA	0.1	0.2	$4.0 \times 4.0 \times 4.0$	$256 \times 1 \times 256$	—	2000.0
AB	0.1	1.0	$2.0 \times 2.0 \times 2.0$	$256 \times 1 \times 256$	1.6×10^6	50.0
AC	0.1	3.0	$2.0 \times 2.0 \times 2.0$	$256 \times 1 \times 256$	1.6×10^6	50.0
BA	1.0	0.2	$40.0 \times 40.0 \times 40.0$	$256 \times 1 \times 256$	1.6×10^6	500.0
BB	1.0	1.0	$20.0 \times 20.0 \times 20.0$	$256 \times 1 \times 256$	1.6×10^6	250.0
BC	1.0	3.0	$20.0 \times 20.0 \times 20.0$	$256 \times 1 \times 256$	1.6×10^6	250.0
AB-3D	0.1	1.0	$2.0 \times 2.0 \times 2.0$	$128 \times 128 \times 128$	2.0×10^7	35.0
BA-3D	1.0	0.2	$40.0 \times 40.0 \times 40.0$	$128 \times 128 \times 128$	2.0×10^7	300.0

Note. — Col. (1): Name of run. Col. (2): Friction time. Col. (3): Solids-to-gas ratio. Col. (4): Box size in units of ηr. Col. (5): Grid resolution. Col. (6): Number of particles. Col. (7): Total run time in units of Ω^{-1}.

7.4.1 Run parameters and initialisation

The parameters of the different non-linear simulations are listed in Table 7.1. We consider two particle sizes, represented as friction times: tightly coupled solids with $\tau_s = 0.1$ (those runs are labelled A*, where * represents a solids-to-gas ratio label) and larger, more loosely coupled particles with $\tau_s = 1.0$ (labelled B*). Three values of the solids-to-gas mass ratio, $\epsilon = 0.2, 1.0, 3.0$ (labelled *A, *B, *C, respectively) are considered for each friction time. For instance model AB uses $\tau_s = 0.1$ and $\epsilon = 1.0$. The chosen particle abundances are well above the Solar composition of $\epsilon \sim 0.01$, but can very well be achieved in a sedimented mid-plane layer of solids, depending on turbulent diffusion and various particle enrichment or gas depletion mechanisms.

The size of the simulation box was chosen in all cases such that the most unstable radial wavelengths are resolved with at least 8 grid points. Two of the runs (labelled AB-3D, BA-3D) were fully 3-D, all others were 2.5-D simulations of the radial-vertical plane with all three velocity components, consistent with the linear analysis of YG. Fully periodic boundary conditions were used for the 2.5-D runs, while the 3-D simulations impose a shear-periodic boundary condition in the radial direction (see §6.4.2). Particles are initially placed randomly throughout the simulation box. This "warm start" gives a white noise power spectrum with scale-independent Fourier amplitudes of $\tilde{\rho}_p(\boldsymbol{k})/\langle\rho_p\rangle \sim 1/\sqrt{N_p}$ in the particle density. The noise serves as a seed for streaming instabilities. The velocities of gas and solids are initially set to the equilibrium values of NSH.

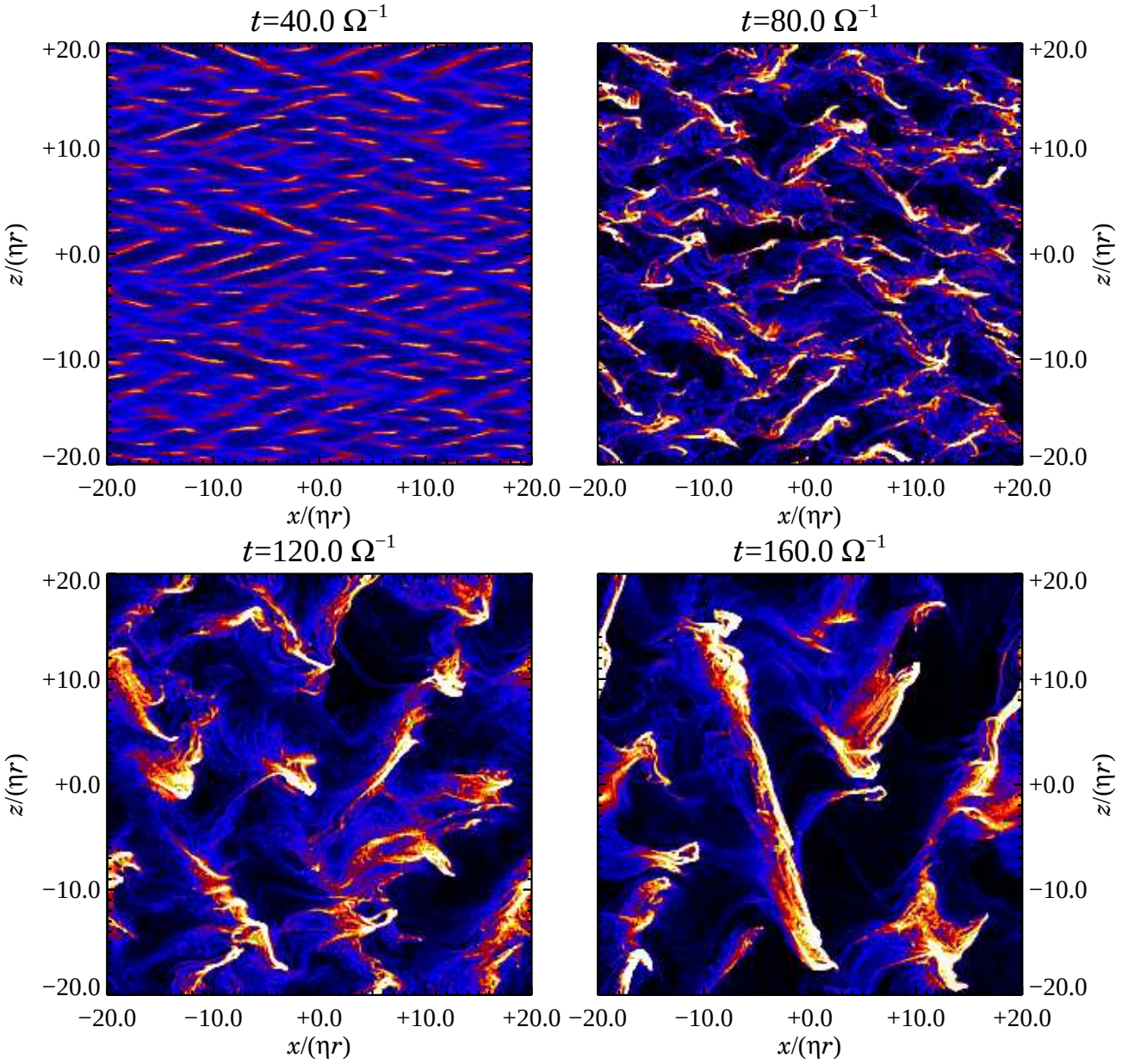

Fig. 7.2 Particle density snapshots for run BA with friction time $\tau_s = 1.0$ and a solids-to-gas ratio of $\epsilon = 0.2$. Particle densities increase from black (zero density) to bright yellow/white (solids-to-gas of unity or higher). The evident linear wavelength in the first frame results from the streaming instability feeding off the drift of the particles through the gas. Subsequent frames document a surprising consequence of the self-consistently generated turbulence: the non-linear cascade of dense particle clumps into larger filaments.

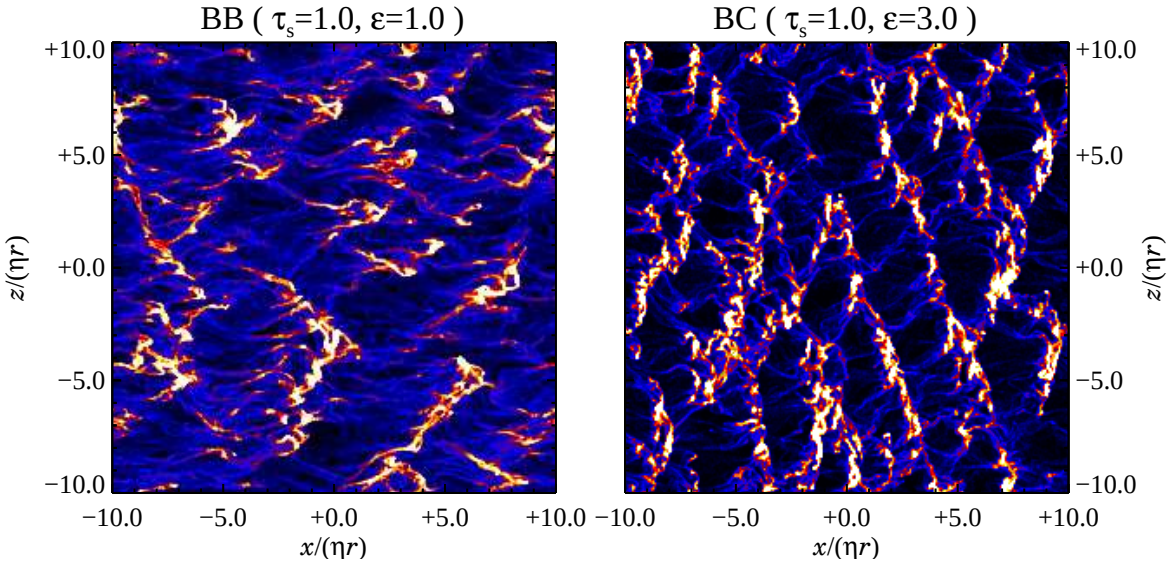

Fig. 7.3 The saturated state of runs BB and BC (both at a time of $t = 100\Omega^{-1}$). The range of the solids-to-gas ratio is from 0-5 in the left plot and from 0-15 in the right plot, giving both the same relative scale for particle overdensities as Fig. 7.2. The tendency for dense clumps to lean against the radial drift flow is evident.

7.4.2 Marginally coupled boulders

Many drag force phenomena are most prominent for marginally coupled, $\tau_s = 1$, particles, corresponding to approximately meter-sized boulders at $r \approx 5$ AU in the solar nebula. Streaming instabilities are no exception, with fast linear growth[2] and significant particle clumping in this regime. Fig. 7.2 shows four snapshots of the evolution of the streaming instability into turbulence for run BA ($\tau_s = 1.0$ $\epsilon = 0.2$). The initial growth is dominated by the fastest linear modes (first frame of Fig. 7.2), consistent with the maximum analytic growth rate, $s \approx 0.1\Omega$ for $k_x \eta r \approx 1$ (see Fig. 7.1 and also Figs. 1 & 2 of YJ).

A non-linearly fluctuating, i.e. turbulent, state is reached after some 80 local shear times (second frame of Fig. 7.2). Solids become concentrated in a few massive clumps surrounded by an ocean of lower density material. Radial drift speeds are lower in such dense regions (we discuss the reduced radial drift further in §7.6.1). Solid particles are eventually lost downstream from the clumps into the voids, where the radial drift is faster, until they fall into another dense particle clump. Over a time-scale of more than 100 shear times (third and fourth frame of Fig. 7.2) this leads to an upward cascade of the density structure into extended filaments (actually rolls and sheets if we extend into the symmetric azimuthal dimension). The filaments are predominantly aligned in the vertical direction, which maximises their ability to intercept particles, but are slightly tilted radially in alternating directions. Strong bulk motions are exhibited by the filaments along their long axis. This helps them stay upwind (motions are in

[2]Somewhat paradoxically, tight coupling gives faster growth in the particle-dominated regime, but on smaller scales.

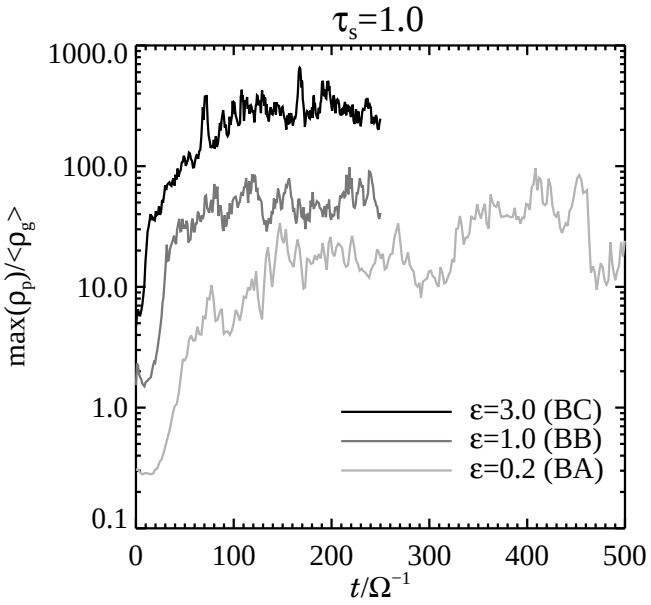

Fig. 7.4 Maximum bulk density of solids, in units of the average gas density in the box, as a function of time for the three marginally coupled runs. The maximum density is generally around two orders of magnitude higher than the mean bulk density of the solids. The particle density has been assigned to the mesh using the TSC scheme.

the $+z, +x$ or $-z, +x$ directions), and leads to their disruption in several orbital times when alternately aligned filaments collide.[3] The bulk motion also leads to efficient mixing of particles, especially in the vertical direction (see §7.6.3). The extended filaments are closely related to the long-lived vertically-oscillating clumps seen in 2-D simulations of the Kelvin-Helmholtz instability with $\tau_{\rm s} = 1.0$ particles (see Fig. 8 of Johansen et al. 2006a).

The $\tau_{\rm s} = 1.0$ runs with larger ϵ values (BB and BC) evolve similarly to run BA, but with a less pronounced cascade to larger scales (the saturated states of those two runs are shown in Fig. 7.3). Fig. 7.4 shows the evolution of maximum particle density (assigned with the TSC scheme to the grid) versus time for all three runs. The non-linear state is characterised by density peaks 100 times (or more) above the average particle density. Run BA has a longer run time, not only because the gas-dominated case is more astrophysically interesting, but also because it took longer to reach a saturated state. Fig. 7.4 shows signs of secular growth in densities over the entire $\Delta t = 500\Omega^{-1}$. Even longer runs would better characterise long term fluctuations in the saturated state, but such computational resources would probably be better spent on a more realistic model with vertical gravity.

Table 7.2 lists turbulent Mach numbers of the gas flow (after subtracting the mean flow, see §7.5.1). The anisotropic turbulence of run BA, with stronger fluctuations in the vertical direction, is clear. Turbulence is more isotropic in the other marginally coupled runs.

[3]The behaviour described is best seen in a movie of run AB which can be downloaded from `http://www.mpia.de/homes/johansen/research\_en.php`.

Table 7.2. Flow Properties

Run (1)	$\tau_{\rm s}$ (2)	ϵ (3)	Ma_x (4)	Ma_y (5)	Ma_z (6)	$\overline{v_x}$ (7)	$\overline{v_x}^{(\rm NSH)}$ (8)
AA	0.1	0.2	5.7×10^{-4}	1.1×10^{-3}	3.4×10^{-3}	-0.138	-0.138
AB	0.1	1.0	1.2×10^{-2}	6.1×10^{-3}	8.5×10^{-3}	-0.108	-0.050
AC	0.1	3.0	8.7×10^{-3}	4.5×10^{-3}	6.4×10^{-3}	-0.035	-0.012
BA	1.0	0.2	1.2×10^{-2}	1.8×10^{-2}	4.0×10^{-2}	-0.520	-0.820
BB	1.0	1.0	9.3×10^{-3}	1.1×10^{-2}	9.2×10^{-3}	-0.341	-0.400
BC	1.0	3.0	8.9×10^{-3}	1.3×10^{-2}	1.1×10^{-2}	-0.118	-0.118
AB-3D	0.1	1.0	5.3×10^{-3}	3.4×10^{-3}	2.7×10^{-3}	-0.064	-0.050
BA-3D	1.0	0.2	1.2×10^{-2}	1.7×10^{-2}	3.3×10^{-2}	-0.545	-0.820

Note. — Col. (1): Name of run. Col. (2): Friction time. Col. (3): Solids-to-gas ratio. Col. (4)-(6): Turbulent Mach number of the gas. Col. (7): Mean radial particle velocity in units of $\eta v_{\rm K}$. Col. (8): Mean radial particle velocity in NSH state.

7.4.3 Tightly coupled rocks

Simulations with shorter friction times are more costly because the shorter unstable length-scales (Figs. 1 & 2 of YJ) impose more stringent Courant criteria. The effort was nevertheless rewarded with a qualitatively very different behaviour for the $\tau_s = 0.1$ runs. These particles correspond to solid rocks of approximately 10 cm size at $r = 5$ AU in the solar nebula.

$\tau_s = 0.1$, $\epsilon = 1.0$: Cavitation

Fig. 7.5 shows four snapshots of the particle density for run AB (friction time $\tau_{\rm s} = 0.1$, solids-to-gas ratio $\epsilon = 1.0$). The first frame displays the initial Poisson noise. In contrast to run BA (see the first frame of Fig. 7.2), we do not see the smooth growth of linear waves over ten or more of orbital times (an expectation which follows from the peak growth rate $s \approx 0.15\Omega$). Instead a few voids with dense inner rims appear by $t = 6\Omega^{-1}$ (second frame). The cavities expand rapidly (third frame), leading to a fully turbulent state after only two orbits, i.e. $t \approx 12\Omega^{-1}$ (fourth frame).

The effect of Poisson fluctuations on the linear growth properties in Fig. 7.1 largely explains the surprisingly rapid and non-uniform growth. The $\epsilon = 1.0$ state lies amid a steep rise in growth rates from the gas-dominated to particle-dominated regimes. Specifically the growth time for $\epsilon = 1.0$, $t_{\rm grow} \equiv 1/s = 6.8\Omega^{-1}$, is halved for a modest increase in the solids-to-gas ratio to $\epsilon = 1.25$. This enhanced growth applies in locally overdense regions. Poisson fluctuations from assigning $N_{\rm p} = 1.6\times10^6$ particles to $N_{\rm b} = 256^2$ bins generate density fluctuations with a

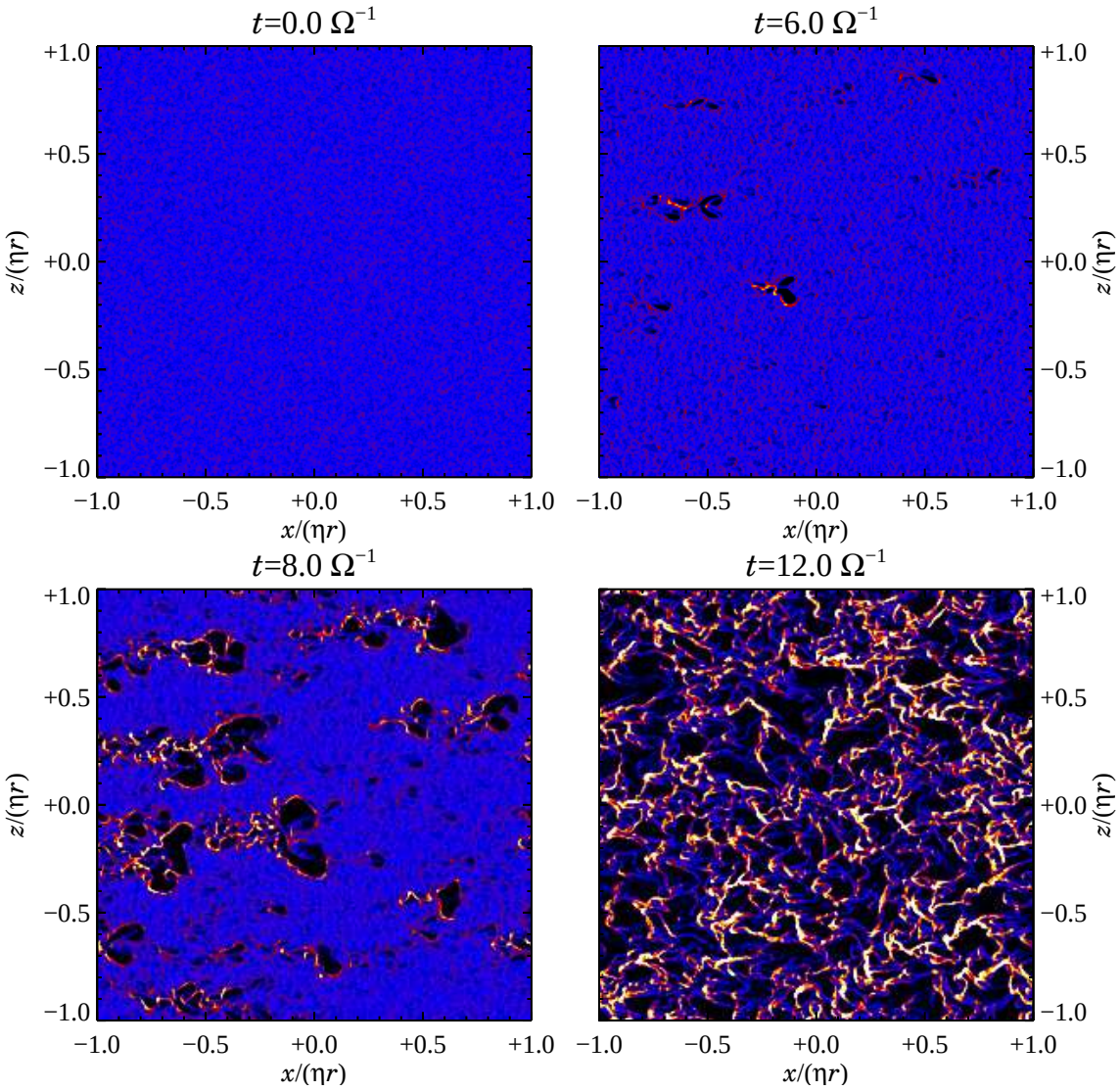

Fig. 7.5 The onset of streaming turbulence for run AB ($\tau_s = 0.1$, $\epsilon = 1.0$). The plots show colour coded particle density (black is zero particle density, bright is a solids-to-gas ratio of 5 or higher). The first frame shows only the initial Poisson noise. After around one orbital period small voids form. The inner edges of the cavities are loaded with particles that can fall rapidly through the voids in the absence of any collective drag force effects there. The voids rapidly expand, and a self-sustained turbulent state sets in after around 2 orbits. This atypical onset of turbulence is caused by an increased growth rate of the streaming instability in slightly overdense grid cells (see Fig. 7.1).

standard deviation of $\delta_p \simeq \sqrt{N_b/N_p} \approx 0.2$. The TSC assignment smooths these fluctuations somewhat, but random overdensities 25% or greater still exist in over 1000 cells (1.6% of the total). Since a region with $\epsilon \approx 1.25$ is already non-linear after two e-foldings (consistent with the observed $t \approx 6\Omega^{-1}$), enhanced growth in overdense regions plausibly explains the growth of cavities.

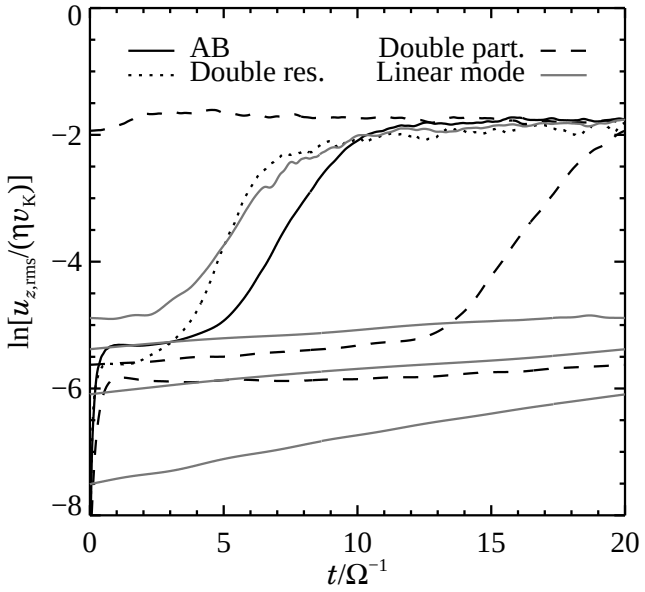

Fig. 7.6 Growth of the streaming instability, as measured by the amplitude of vertical velocity fluctuations, for different numerical approaches to run AB. Only a seeded linear mode (grey line) grows with the expected growth rate of $s \approx 0.1\Omega$ (some curves have been wrapped around several times to allow simulations to run further). Fast growing cavities occur both at double resolution (dotted line) and with twice as many particles per grid cell (dashed line). Since cavities are triggered by Poisson density fluctuations, explosive growth is delayed with twice as many particles. The saturated state is the same for all cases.

We confirm this physical explanation for the cavities by running five variations to AB: (1) doubling the spatial resolution, (2) doubling the number of particles per grid cell, (3) seeding a linear mode (an eigenvector) with the "cold start" algorithm used for the linear tests in YJ, (4) the same linear mode, but the particle density distribution is seeded randomly (and thus dominated by Poisson fluctuations), and (5) quadratic polynomial instead of spline interpolation (see Appendix A of YJ). The growth of the root-mean-square of the vertical gas velocity for the first three variations is shown in Fig. 7.6 along with the original run BA. Variation (1) [and also (4) and (5), not shown] give essentially the same behaviour run BA, which eliminates obvious numerical effects (grid resolution and interpolation scheme) as the source of cavities.[4] Doubling the particle number, variation (2), delays the onset of cavitation, as expected with lower amplitude Poisson fluctuations. Variation (3) suppresses all Poission noise, and the "cold" linear mode grows at the analytic rate, $s \approx 0.1\Omega$, until non-linear effects finally dominate after $t = 60\Omega^{-1}$. Perhaps most importantly, all approaches lead to the same saturated state, despite markedly different routes to turbulence. This speaks to the robustness, not just of transient cavitation, but of all the non-linear results.

We also investigated the velocity structure at the onset of cavitation. Quadrupolar structures (most prominent in the vertical velocity) appear as isolated modes of the streaming instability.

[4]Variation (5) is interesting because the Poisson density fluctuations dominate the carefully seeded velocities.

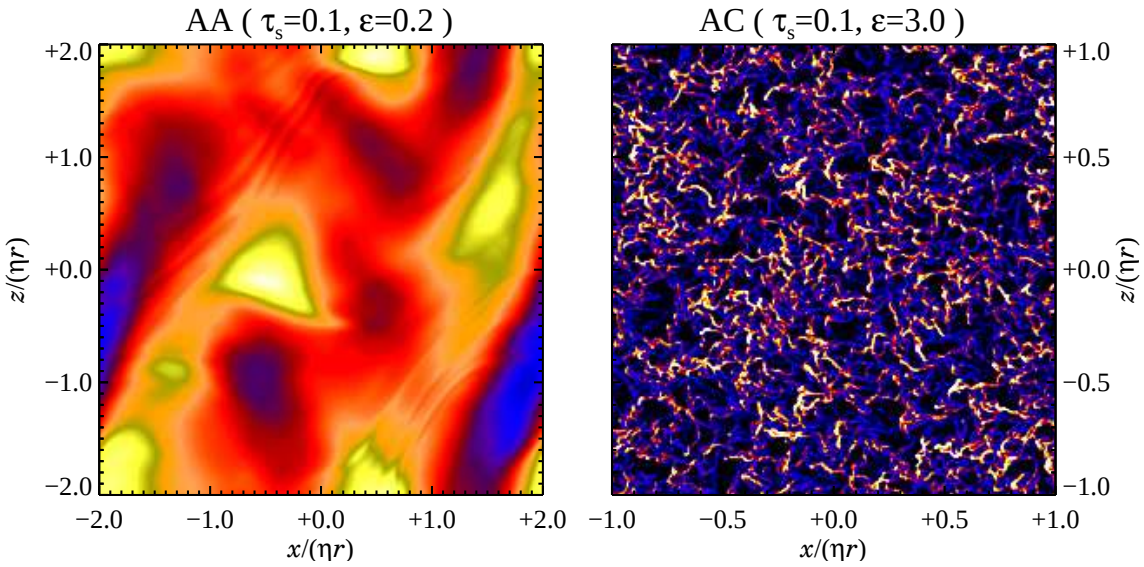

Fig. 7.7 The saturated states of run AA (at $t = 1000\Omega^{-1}$) and run AC (at $t = 50\Omega^{-1}$). The range in solids-to-gas ratio is 0.15-0.25 in the left plot and 0-15 in the right plot. Run AA (calculated with the two fluid code, see §7.4.3 for explanation) is dominated by oscillatory motion of slightly overdense clumps. The turbulent state of run AC is very much like run AB, but at smaller scales. Also the non-linear state of run AC develops simultaneously throughout the grid, unlike the cavitation of run AB.

The length scale of the quadrupolar distortions did not vary upon doubling the grid resolution (with a fixed number of particles per grid cell).

Fortunately, our Poisson noise hypothesis does not predict cavitation where it should not occur. Run AC ($\tau_s = 0.1$, $\epsilon = 3.0$) has a fast linear growth rate with a relatively weak dependence on the local value of ϵ (see Fig. 7.1). Accordingly non-linear fluctuations appear uniformly throughout the grid in run AC, instead of cavitating first in a few spots. The saturated state of run AC (shown in the right panel of Fig. 7.7) is similar to run AB, but with smaller scale fluctuations. Like run AB, the marginally coupled run BB has equal densities of particles and gas, but with $\tau_s = 1.0$ the rise in growth rates across $\epsilon = 1$ was much smoother (see Fig. 7.1).[5] Since the effect of Poisson fluctuations is weak (an overdensity of 25% only cuts the growth time by 12% for $\tau_s = 1.0$ instead of halving it for $\tau_s = 0.1$) run BB displays orderly growth of the dominant linear modes.

$\tau_s = 0.1$, $\epsilon = 0.2$: weak overdensities

Fig. 7.8 plots the maximum particle density versus time for the three tightly coupled simulations. The streaming instability produces particle overdensities of 20 or more in runs AB and AC. However the gas-dominated case AA has a qualitatively different behaviour. Growth saturates (see left panel of Fig. 7.7) in a few growth times, $t_{\rm grow} = 1/s \approx 42\Omega^{-1}$, as expected.

[5] Fig. 3 of YG confirms this trend, showing that the transition is yet sharper for $\tau_s = 0.01$ "pebbles."

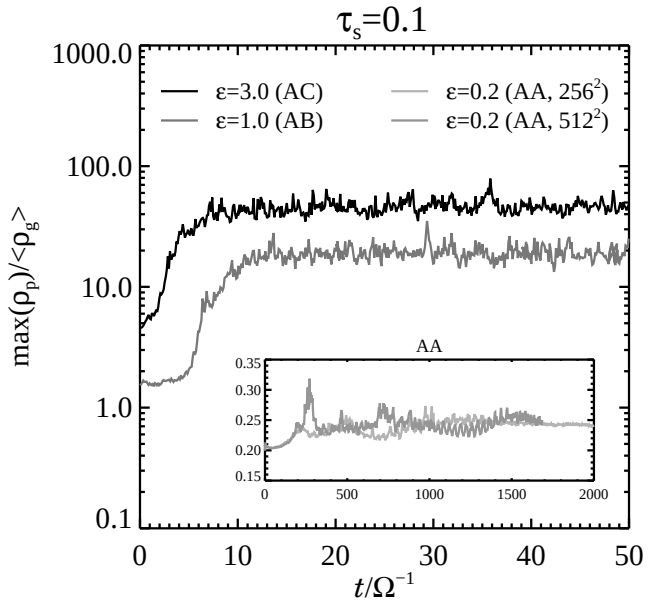

Fig. 7.8 Maximum bulk density of solids for the three tightly coupled runs (AB, AC and in the insert AA at two different resolutions). The maximum density is around an order of magnitude higher than the average for the $\epsilon = 1.0, 3.0$ runs, whereas the turbulent state of the $\epsilon = 0.2$ run only experiences very mild relative overdensities of around 20% at both 256^2 and 512^2 mesh resolution.

However the particle overdensities are very mild, only 20% on average (see inset of Fig. 7.8). To test for convergence we ran the simulation at both 256^2 and 512^2 grid points, but the qualitative evolution of maximum bulk density of solids is unchanged (after a small initial peak in the 512^2 run).

We emphasise that run AA was performed with the two-fluid code, not the particle-fluid approach used in the other simulations. This choice was necessitated by computational cost of long growth times with short wavelengths that restrict the code to small time steps. It is tempting to suspect that the weak overdensities in AA are a consequence of the two-fluid approach. However the limitation of the pressureless fluid model of solids is that density gradients steepen and shock, causing numerical instabilities, *not* that they are stably smoothed. To confirm this we ran two-fluid simulations of case AB and obtained the expected (from the particle-fluid run) growth of particle density until the code crashed after the growth of non-linear overdensities. By contrast AA simply never generates large density fluctuations, apparently since drag feedback on the gas is too weak in the small particle, gas-dominated regime.

7.4.4 3-D simulations

We have also performed full 3-D simulations of the streaming instability with 128^3 grid points and $N_\mathrm{p} = 2 \times 10^7$ particles. The linear analysis of YG assumed axisymmetry, partly for sim-

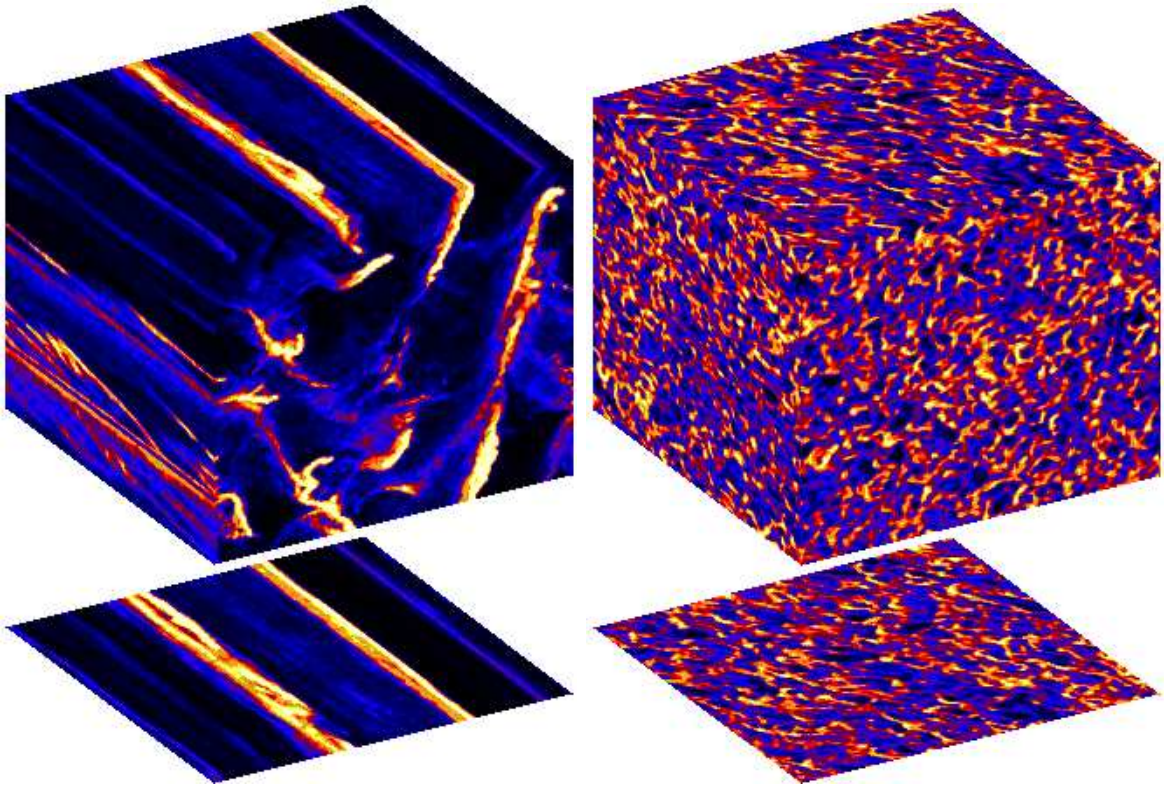

Fig. 7.9 Saturated streaming turbulence for run BA-3D ($\epsilon = 0.2$, $\tau_s = 1.0$, left) and run AB-3D ($\epsilon = 1.0$, $\tau_s = 0.1$, right). The boxes are oriented with the radial x-axis to the right and slightly up, the azimuthal y-axis to the left and up, and the vertical z-axis directly up. The contours show the particle density at the sides of the simulation box after the streaming turbulence has saturated. The axisymmetry of the marginally coupled particles witnesses the smearing effect of Keplerian shear on the relatively long-lived clumps. The tightly coupled particles drive rapid fluctuations that develop fully non-axisymmetric density patterns.

plicity, but also because modes that grow slowly (with $s < \Omega$) will be sheared into rings in any event. Computer simulations are needed to determine whether the saturated state remains azimuthally symmetric in 3-D and how the presence of the azimuthal direction affects turbulent properties. Note that even axisymmetric linear instabilities can give rise to non-axisymmetric parasitic instabilities (e.g. Kelvin-Helmholtz instabilities that feed off the channel flow of the magnetorotational instability, see Goodman and Xu 1994).

Fig. 7.9 shows the particle density for runs BA-3D and AB-3D in a saturated state. The marginally coupled case (BA-3D) maintains a high degree of axisymmetry. The radial-vertical plane shows the cascade into sheets similar to the 2.5-D case (as seen in Fig. 7.2). The quantitative analysis of turbulent properties (see Tables 7.2 and 7.3) confirms that BA-3D is very similar to the 2.5-D case. The ability to maintain azimuthal symmetry suggests (as we will confirm in §7.5.3) that particles reside in clumps for longer than an orbital time, so that clumps become azimuthally elongated by radial shear. Notice that the clump lifetime is not so long that structures appear perfectly axisymmetric.

Table 7.3. Turbulent transport

Run (1)	τ_s (2)	ϵ (3)	D_x (4)	D_z (5)	$\mathcal{F}^{(\mathrm{turb})}_{\mathcal{L},x}$ (6)	$\mathcal{F}^{(\mathrm{NSH})}_{\mathcal{L},x}$ (7)
AA	0.1	0.2	$(1.4 \pm 6.2) \times 10^{-7}$	$(6.0 \pm 262) \times 10^{-7}$	-2.2×10^{-8}	-4.8×10^{-7}
AB	0.1	1.0	$(4.4 \pm 0.4) \times 10^{-5}$	$(2.9 \pm 0.5) \times 10^{-5}$	-6.1×10^{-5}	-3.1×10^{-7}
AC	0.1	3.0	$(2.0 \pm 0.2) \times 10^{-5}$	$(1.8 \pm 0.2) \times 10^{-5}$	-6.0×10^{-5}	-5.8×10^{-8}
BA	1.0	0.2	$(2.2 \pm 0.6) \times 10^{-3}$	$(1.5 \pm 0.8) \times 10^{-2}$	6.7×10^{-5}	-1.7×10^{-4}
BB	1.0	1.0	$(7.6 \pm 0.7) \times 10^{-4}$	$(1.7 \pm 0.4) \times 10^{-4}$	-4.0×10^{-5}	-2.0×10^{-4}
BC	1.0	3.0	$(2.8 \pm 0.2) \times 10^{-4}$	$(6.2 \pm 0.9) \times 10^{-4}$	-1.5×10^{-4}	-5.2×10^{-5}
AB-3D	0.1	1.0	$(1.6 \pm 0.2) \times 10^{-5}$	$(2.7 \pm 0.1) \times 10^{-6}$	-1.5×10^{-5}	-3.1×10^{-7}
BA-3D	1.0	0.2	$(2.0 \pm 0.3) \times 10^{-3}$	$(8.2 \pm 2.5) \times 10^{-3}$	6.0×10^{-5}	-1.7×10^{-4}

Note. — Col. (1): Name of run. Col. (2): Friction time. Col. (3): Solids-to-gas ratio. Col. (4)-(5): Turbulent diffusion coefficient in units of $c_\mathrm{s}^2 \Omega^{-1}$ (interval indicates one standard deviation in each direction). Col. (6): Radial flux of azimuthal momentum relative to NSH state. Col. (7): Radial flux of azimuthal momentum in NSH state. All quantities are normalised with standard combinations of Ω, c_s and ρ_g.

The tightly coupled case (AB-3D) on the other hand evolves completely non-axisymmetrically. Indeed the correlation time of the clumps is short enough that they are not significantly elongated by Keplerian shear. Similar to the 2.5-D case, cavities (now fully 3-D and non-axisymmetric) developed out of the initial Poisson noise in run AB-3D. The saturated state appears to have less pronounced clumps than run AB (the fourth panel of Fig. 7.5). Tables 7.2 and 7.3 show that the 3-D turbulence indeed has lower velocities (Mach numbers) and weaker diffusion, particularly in the vertical direction. It is to be expected that turbulent properties in the 3-D runs change more for the case that is non-axisymmetric (AB-3D) than the case that remains axisymmetric (BA-3D) and was already capturing the relevant physics.

The peak particle densities for the two 3-D runs are shown in Fig. 7.10. Compared to the density evolution of the 2.5-D runs (Figs. 7.4 and 7.8) it is evident that BA-3D agrees well with BA, whereas AB-3D achieves a somewhat lower maximum density than AB does. We will focus most of our analysis on the 2.5-D runs because we could conduct a more systematic study of parameter space at higher spatial resolution. The 3-D runs presented here support this choice by giving qualitatively (and for BA, fairly quantitatively) similar results to the 2.5-D runs.

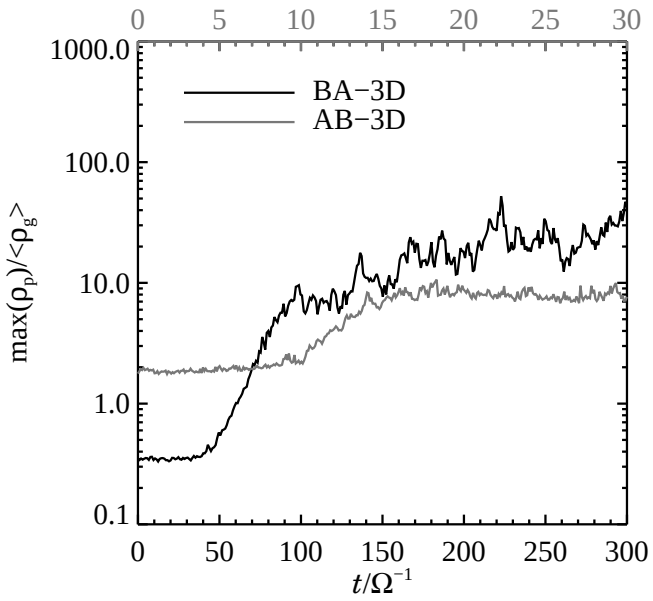

Fig. 7.10 Evolution of the maximum bulk density of solids in the two 3-D simulations (notice the different time axes). The density of AB-3D is somewhat lower than in the 2.5-D case (Fig. 7.8), whereas the marginally coupled BA-3D shows good agreement with run BA in Fig. 7.4.

7.5 Particle concentration

The ability of drag forces to concentrate particles via the non-linear evolution of the streaming instability is now analysed in detail. This fundamentally important process could alter the collisional evolution of the size spectrum of particles, leading to an enhanced growth of the average particle radius, or even trigger gravitational instabilities in the solid component of protoplanetary discs.

7.5.1 Gas does not clump

We emphasise that gas densities remain nearly constant, despite non-linear particle overdensities in streaming turbulence. Gas overdensities are $\lesssim 1\%$ in all runs. This validates our use of a constant stopping time, τ_f (which would otherwise vary with gas density in the Epstein regime). We note that the linear analysis of YG assumed a perfectly incompressible gas. YJ confirmed that the linear growth is indeed unaffected by gas compressibility, which we now see also remains weak in the non-linear regime.

The gas fluctuations are consistent with the small Mach numbers in Table 7.2, which are below (but near) the scale set by the pressure supported velocity, ηv_K, with $\eta v_\mathrm{K}/c_\mathrm{s} = 0.05$ in our simulations. Curiously, the range in *radial* Mach numbers is remarkably narrow for all the 2.5-D simulations, from 8.7×10^{-3} to 1.2×10^{-2} (with the weakly turbulent, two-fluid

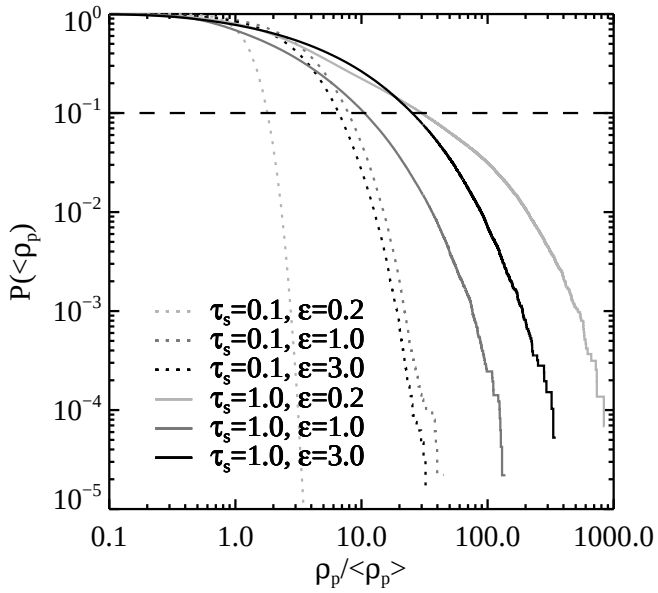

run AA excluded).

7.5.2 Particle density distribution

To get a clear picture of both typical and maximum particle overdensities, Fig. 7.11 plots the cumulative distributions of particle density during the saturated phase of the simulations. The distributions measure the fraction of particles with ambient densities above a given value, and are averaged over many snapshots to ensure adequate sampling. Particle densities relative to the gas are readily obtained by multiplying the x-axis values by $\epsilon = \langle\rho_\mathrm{p}\rangle/\langle\rho_\mathrm{g}\rangle$. Run BA ($\tau_s = 1.0$, $\epsilon = 0.2$) has the largest particle overdensities, of nearly 1000, meaning ρ_p reaches nearly 200 times the gas density. However since run BC ($\tau_s = 1.0$, $\epsilon = 3.0$) starts with a particle density 15 times larger, it experiences larger peak values of $\rho_\mathrm{p}/\langle\rho_\mathrm{g}\rangle \approx 900$. Curiously run BB ($\tau_s = 1.0$, $\epsilon = 1.0$) is not an intermediate case but has smaller overdensities relative to both particles and gas.

Particle concentration is more modest during the tightly coupled runs. Case AB and AC have very similar particle overdensities, with an average $\delta_\mathrm{p} \approx 2$–$3$ and a peak $\delta_\mathrm{p} \approx 30$. For case AA ($\tau_s = 0.1$, $\epsilon = 0.2$) the overdensities are negligible. It is remarkable (if a bit mysterious) that the $\epsilon = 0.2$ runs give both the strongest (BA) and weakest (AA) particle overdensities, depending on stopping time!

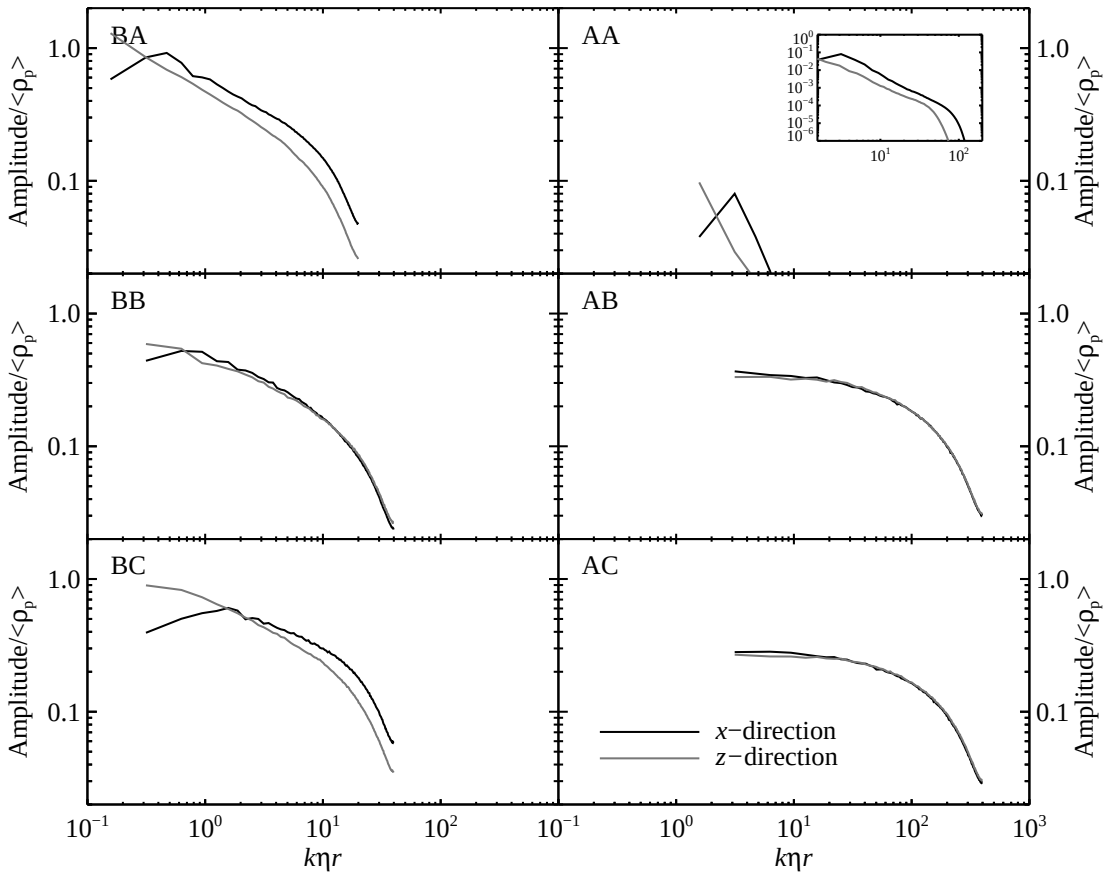

Fig. 7.12 Power spectra of the bulk particle density, along the x-direction (black line) and the z-direction (grey line). The Fourier amplitudes are shown normalised with the mean density of particles in each simulation. Runs BA, BB and BC show clear peaks at large scales in agreement with the scale of the clumps seen in Figs. 7.2 and 7.3, whereas the power in the tightly coupled runs AB and AC is largely isotropic and monotonically decreasing with decreasing wave length. Run AA is extremely top heavy with power almost exclusively at the few largest scales of the box (see insert).

Fourier spectra of the particle density are shown in Fig. 7.12. The absolute value of the Fourier amplitudes, normalised by the mean bulk density of particles, has been averaged over many snapshots during the saturated turbulent state of the simulations. Runs BA, BB and BC show clear peaks at large scales in agreement with the scale of the clumps seen in Figs. 7.2 and 7.3, whereas the power in the tightly coupled runs AB and AC is largely isotropic and monotonically decreasing with decreasing wave length. Run AA is extremely dominated by the very largest scales of the box.

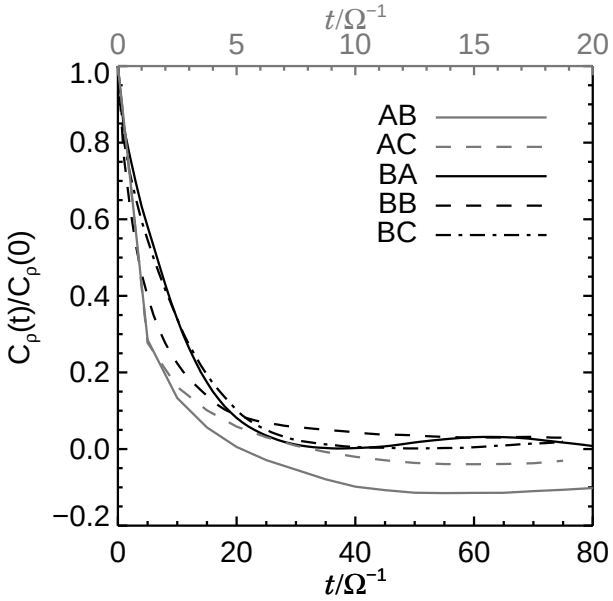

Fig. 7.13 Time correlation functions for particle density indicate how long particles reside in dense clumps. Runs BA and BC have long correlation times of $\sim 7\Omega^{-1}$, while BB has a slightly shorter value of $3.5\Omega^{-1}$. These $\tau_s = 1.0$ runs use black lines and the lower black time axis. The tightly coupled runs, AB and AC (grey lines and the upper grey compressed time axis), have very short correlation times $< 1\Omega^{-1}$.

7.5.3 Correlation times

The residence time of particles in dense clumps affects the cosmogonical processes, e.g. gravitational collapse or chondrule formation, that might occur therein. For this purpose, we measure the time correlation function of the ambient density, $\rho_{\rm p}^{(i)}$, experienced by particle i,

$$C_\rho(t) = \langle \rho_p^{(i)}(t')\rho_p^{(i)}(t'+t)\rangle - \langle \rho_{\rm p}^{(i)}\rangle^2 \,, \tag{7.3}$$

from snapshots of the particle positions taken every $\Delta t = \Omega^{-1}$ apart. The brackets indicate an average over time[6] and the particles tracked (10% of the total was more than sufficient for convergence). Subtraction of the mean squared $\rho_{\rm p}^{(i)}$ ensures that positive (negative) values of $C_\rho(t)$ correspond to correlation (anticorrelation), respectively.

Fig. 7.13 plots the time correlation function for the saturated state of the 2.5-D simulations. A characteristic correlation time, $t_{\rm corr}$, is obtained when C_ρ drops to half its peak value.[7] Runs BA and BC have the longest $t_{\rm corr} \approx (6\text{–}7)\Omega^{-1}$. Run BA is the best sampled and shows a secondary peak past $t = 60\Omega^{-1}$ indicating either periodicity or (more likely) secular changes

[6]Since averaging is restricted to intervals t apart, the largest t considered is never more than half the (non-linearly saturated) duration of the simulation.

[7]We considered defining correlation functions and times only for particles initially residing in overdense regions, but equation (7.3) is a quadratic measure that already favours such regions. The simpler, more standard definition is sufficient for our purposes.

from the ongoing cascade and small clump numbers. Run BB enjoys a shorter $t_{\rm corr} \approx 3.5\Omega^{-1}$, but C_ρ does not quite drop to zero, an indication that a fraction of particles remain in dense regions.

The runs with tighter coupling of $\tau_s = 0.1$ (AB and AC) had quite short $t_{\rm corr} \approx 0.7\Omega^{-1}$ (note the compressed time axis in Fig. 7.13 for these runs). The short correlation times are consistent with the less pronounced clumping and lack of upward cascade when compared to the marginally coupled runs. For run AC, C_ρ is significantly negative for $t > 20\Omega^{-1}$, indicating that particles avoid dense clumps after leaving them.

It is clear from movies of the simulations that many clumps persist longer than $t_{\rm corr}$, particularly in the marginally coupled $\tau_s = 1.0$ runs. The particles that make up a clump continuously leak out downstream to the radial drift flow and are replaced with new particles drifting in from upstream. The mismatch between clump lifetime and density correlation time is evidence that the clumps are a dynamical, collective phenomenon in the solid component, rather than a persisting density enhancement. That situation might change with the inclusion of the self-gravity of the solid particles, as this could cause the clumps as a whole to collapse under their own weight, fragmenting perhaps into gravitationally bound objects. We plan to include the self-gravity of the particles in a future research project.

7.5.4 Energetics of clumping

The growth of particle clumps shields solids from the full brunt of drag forces, akin to the drafting practised in bicycle pelotons. In YJ §5.1 we show that the rate of energy dissipation by drag forces,

$$\dot{\mathcal{E}}_{\rm drag} = -\rho_{\rm p}|\boldsymbol{v}_{\rm g} - \boldsymbol{v}_{\rm p}|^2/\tau_{\rm f}\,, \tag{7.4}$$

is diminished (brought closer to zero) by particle clumping in the laminar state (at least for tight or marginal coupling). To determine the relevance of this process for the saturated turbulent state, Fig. 7.14 plots the time evolution of the energy dissipation rate for the marginally coupled runs (black time axis) and two of the tightly coupled runs (grey time axis). For the tightly coupled runs (AB and AC) the dissipation actually becomes stronger (more negative) in the saturated state, a consequence of increased relative velocities in the turbulent state. Since these runs also have significant overdensities, the lowering of $|\dot{\mathcal{E}}_{\rm drag}|$ is apparently not a necessary condition for clumping. The short clump lifetimes (see Fig. 7.13) is consistent with the inability to reduce dissipation by drafting for $\tau_{\rm s} = 0.1$.

By contrast, all marginally coupled runs (BA, BB and BC) show diminished dissipation in the non-linear state, more consistent with the analytic expectations from clumps in a laminar flow. The longer correlation times and the upward cascade into large clumps exhibiting bulk motion (particularly in AB, see §7.4.2) foster the reduction of $|\dot{\mathcal{E}}_{\rm drag}|$. The resulting particle overdensities are significantly larger for these $\tau_{\rm s} = 1.0$ runs (see Fig. 7.11). Thus diminishing drag dissipation is not required to generate particle overdensities, but this drafting mechanism can augment the growth of dense clumps.

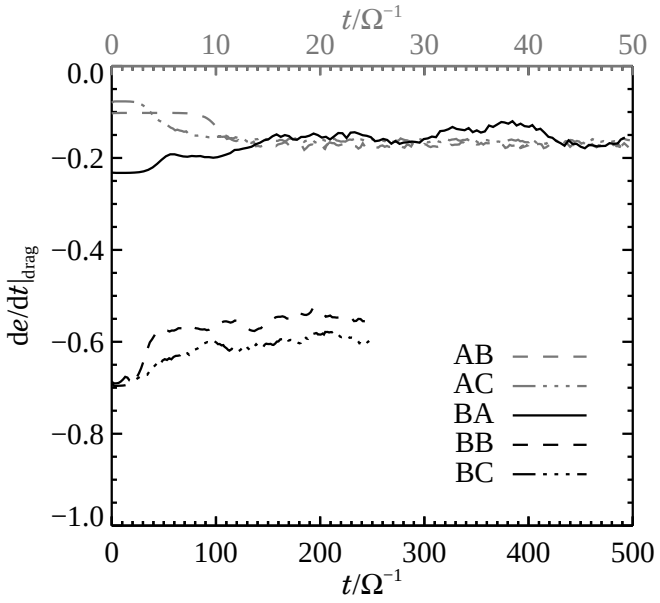

Fig. 7.14 The energy dissipation rate [normalised to $\langle\rho_{\rm g}\rangle(\eta v_{\rm K})^2\Omega$] from drag forces between solids and gas. Marginally coupled runs BA, BB and BC (black curves) reduce the dissipation rate in the turbulent state, by shielding particles in dense, long-lived particle clumps. Tightly coupled runs AB and AC (grey curves, which follow the top grey time axis) show increased dissipation, since particle clumps are too short-lived to allow such shielding.

7.6 Transport

In this section we quantify the effect of the streaming turbulence on the radial drift of particles, radial momentum transport and on the diffusive mixing of solids.

7.6.1 Radial drift

We initially expected that streaming turbulence would reduce the radial migration of particles, due to the pronounced particle clumping. The laminar drift of particles slows as [see YJ equation (7c)]

$$w_x^{\rm (NSH)} = -\frac{2\tau_{\rm s}}{(1+\rho_{\rm p}/\rho_{\rm g})^2+\tau_{\rm s}^2}\eta v_{\rm K} \tag{7.5}$$

$$\rightarrow -\left(\frac{\rho_{\rm p}}{\rho_{\rm g}}\right)^2 2\eta v_{\rm K}\tau_{\rm s} \ \text{ for } \ \frac{\rho_{\rm p}}{\rho_{\rm g}} \gg 1, \tau_{\rm s} \tag{7.6}$$

with increasing particle inertia. The results of the simulations are more complicated since turbulent velocity fluctuations produce drift speeds that deviate from local equilibrium.

Table 7.2 lists average radial drift velocities in the turbulent state, along with the laminar equilibrium values from NSH. Radial drift decreases by about 40% during run BA, as is also

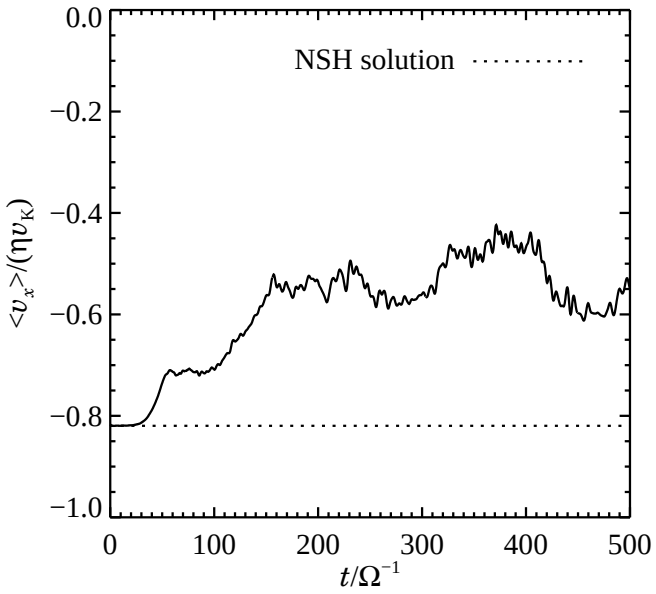

Fig. 7.15 Evolution of the radial drift speed of solids during run BA, averaged over all 1,600,000 particles. Streaming turbulence slows the influx of solids by 40% below the laminar drift speed (dotted line) on average, with significant temporal fluctuations that correlate with peaks in the maximum bulk density of particles (Fig. 7.4).

shown in Fig. 7.15. For the other $\tau_s = 1.0$ runs, BB displays a modest 15% reduction while BC is unchanged despite significant overdensities. The tightly coupled runs show marked increases in drift speeds of 200% for AB and 300% for AC. Note that BA has the fastest laminar drift (due to marginal coupling and low solids-to-gas ratio), while AC (followed by AB) have the slowest laminar drift (because of tight coupling and large particle inertia). While the same ordering of drift speeds holds in the turbulent state, the range of speeds for different parameter choices shrinks (i.e. the fastest slow down and the slowest speed up). We examine this trend in detail below.

Fig. 7.16 shows (with black histograms) the distribution of drift velocities, averaged over time in the turbulent state, for six different runs. For comparison, the location of the equilibrium drift velocity is indicated with a short vertical line (labelled NSH). The full grey lines plot the average ambient particle density for particles in a given velocity bin, and should be compared to the dash-dotted grey lines that show the laminar relation between particle density and drift velocity (from the inversion of eq. [7.5]). The laminar drift velocities have a finite range from 0 for infinite particle densities to the single-particle case, $w_x^{(\min)} = -\eta v_K$ for $\tau_s = 1.0$ and $w_x^{(\min)} \simeq -0.2\eta v_K$ for $\tau_s = 0.1$. The actual velocity range extends beyond these limits in the turbulent state.

First consider the marginally coupled runs (left column of Fig. 7.16). The velocity distribution is non-Gaussian with a clear negative skewness (velocities drop sharply at the right side of the Gaussian, with a more gradual decline toward negative velocities). The grey lines show the expected trend of slower inward drift for higher ambient densities. For particles moving

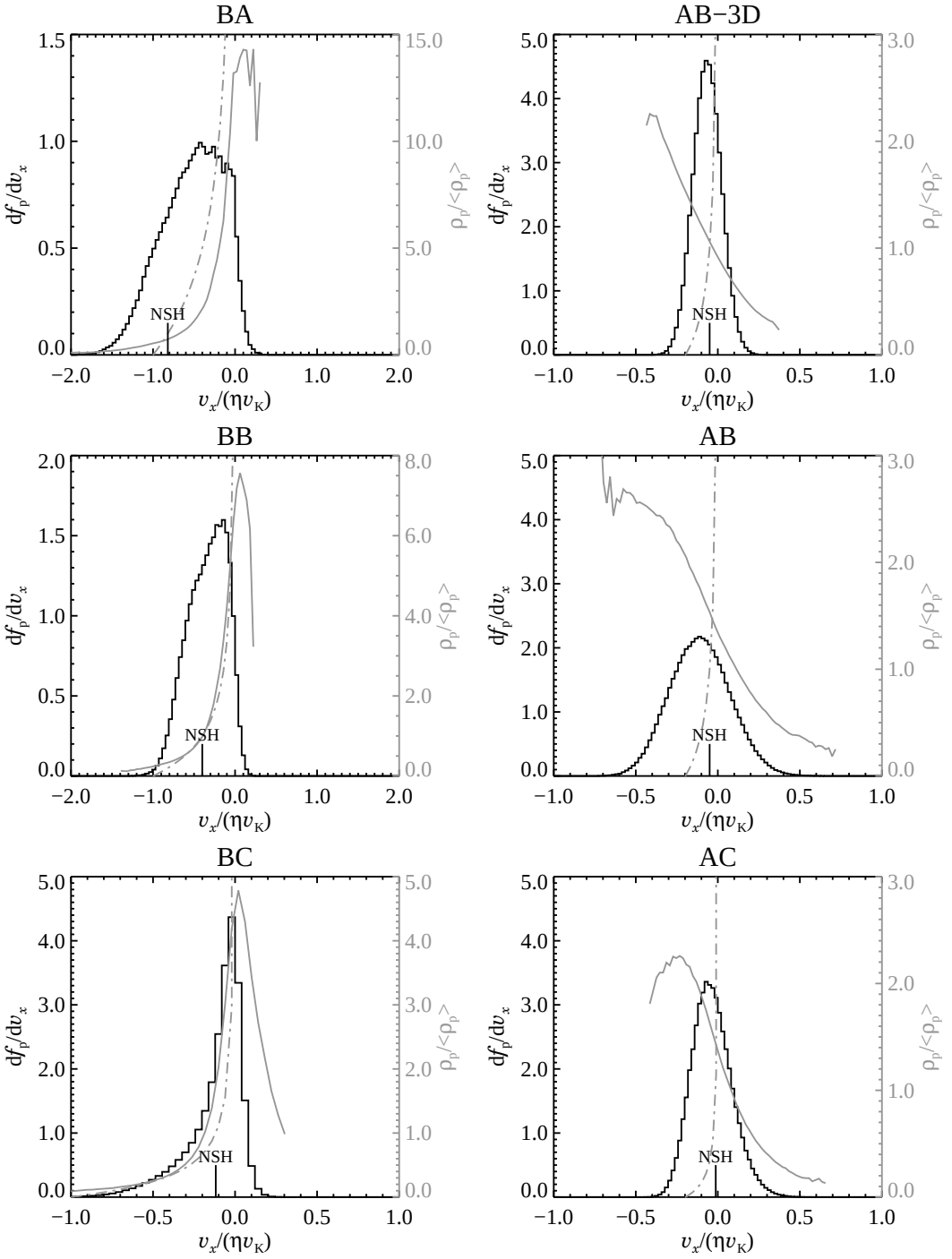

Fig. 7.16 Histograms of the fraction of particles with a given radial drift velocity v_x in the turbulent state (black curves). The short vertical lines (labelled NSH) indicate analytical drift velocities in the initial state with no turbulence or clumping. Marginally coupled (B*) runs show a slowing of the net drift speed, whereas tightly coupled runs (A*) produce faster infall. The grey lines (following the right y-axes) show the average particle density in each velocity bin. For reference the grey dash-dotted lines plot the laminar particle density vs. drift velocity relation. The B* runs display the expected decrease in drift speeds with increasing density, whereas the A* runs (surprisingly) follow the opposite trend.

radially outward with $v_x > 0$, the average particle density drops with increasing speed. This is reasonable behaviour since low density particle clumps can more readily be fed angular momentum and pushed outward by gas fluctuations.[8] The extended tails of fast-drifting material at low densities are responsible for the modest (or non-existent for BC) reduction of drift velocities, despite the slowing, or even reversal, of motion in overdense regions.

Now consider the tightly coupled runs in the right column of Fig. 7.16. The velocity distributions are nearly Gaussian and extend well beyond the range of laminar drift velocities, indicating that turbulent fluctuations dominate. The peaks are shifted leftward, which produces the higher turbulent drift speeds of Table 7.2. The grey curves plot the astounding fact that overdense regions drift in faster, a reversal of the laminar trend. This is seen in the movie of AB where dense clumps snake their way inwards while underdense diffuse material races out (the snake patterns are visible in Fig. 7.5 as well).

Effective drag on clumps

The tendency for faster migration of dense clumps for $\tau_s = 0.1$ can be understood as a consequence of an effective, macroscopic drag force acting on the clumps. The gas inside the clump is tied to the clump, but exterior gas passes freely around the surface, exerting an effective drag. If the effective friction time of the clump is closer to unity than the original τ_s, then the dense clump will behave more like a marginally coupled solid and drift inward faster. This collective drag effect is similar to the plate drag model of Ekman layers on the surface of particle subdiscs (Goldreich and Ward 1973; Goodman and Pindor 2000).

We estimate the friction time $\tau_f^{(\mathrm{eff})}$ of a clump of radius R_{clump} as the time required to encounter its own mass, M_{clump}, in gas.[9] That gives for 3-D clumps (2-D clumps give the same final scaling)

$$\tau_f^{(\mathrm{eff})} \sim \frac{M_{\mathrm{clump}}}{\rho_g R_{\mathrm{clump}}^2 \Delta v} \sim \frac{\rho_p}{\rho_g} \frac{R_{\mathrm{clump}}}{\Delta v}\,, \tag{7.7}$$

where ρ_p is the bulk particle density inside the clump and Δv is the speed of the clump relative to the gas. Multiplying each side by Ω yields

$$\Omega \tau_f^{(\mathrm{eff})} \sim \frac{\rho_p}{\rho_g} \frac{R_{\mathrm{clump}}}{\eta r} \frac{\eta v_K}{\Delta v}\,. \tag{7.8}$$

If we dare test this heuristic hypothesis, reading the size of the clumpy plateaus from Figs. 7.5 and 7.7 and the bulk density and speed of the dense clumps relative to the gas from Fig. 7.16, we find for run AB the values $\rho_p/\langle\rho_g\rangle \approx 2.5$, $R_{\mathrm{clump}}/(\eta r) \approx 0.1$, $\Delta v \approx \eta v_K$ (the velocity difference between high density material and low density material in Fig. 7.16), corresponding to an effective friction time of $\Omega\tau_f^{(\mathrm{eff})} \approx 0.25$ Run AC has $\rho_p/\langle\rho_g\rangle \approx 6$, $R_{\mathrm{clump}}/(\eta r) \approx 0.05$, $\Delta v \approx \eta v_K$, yielding a very similar value of $\tau_f^{(\mathrm{eff})} \approx 0.3$. Thus our crude estimates show that the clumps couple aerodynamically to the gas more loosely than the individual particles do, explaining at least qualitatively the faster drift of dense clumps and the increase in drag dissipation, two surprising features of the $\tau_s = 0.1$ runs.

[8] In the absence of fluctuations and with an outwardly decreasing pressure, particles only drift inwards.

[9] This is the valid criterion for high Reynolds number, turbulent drag.

7.6.2 Momentum flux

The radial flux of orbital momentum, $\mathcal{F}_{\mathcal{L},x} = \rho_{\rm g} u_x u_y + \rho_{\rm p} w_x w_y$, and its contribution to disc heating are discussed in YJ §5. For laminar flow the drag equilibrium between solids and gas gives (equation 18b of YJ)

$$\mathcal{F}^{(\rm NSH)}_{\mathcal{L},x} = -2\tau_{\rm s}^3 \rho_{\rm p} \left[\frac{\eta v_{\rm K}}{(1+\epsilon)^2 + \tau_{\rm s}^2} \right]^2 . \tag{7.9}$$

The *inward* transport of angular momentum follows from the the slower rotation of the outgoing gas and the faster rotation of the incoming particles. The values for $\mathcal{F}_{\mathcal{L},x}$ in the saturated turbulent flow are given in Table 7.3 and are decomposed as $\mathcal{F}_{\mathcal{L},x} = \mathcal{F}^{(\rm NSH)}_{\mathcal{L},x} + \mathcal{F}^{(\rm turb)}_{\mathcal{L},x}$, i.e. the laminar value and changes caused by turbulence. If the turbulence were driven by orbital shear, which releases free energy via outward angular momentum transport, $\mathcal{F}^{(\rm turb)}_{\mathcal{L},x}$ would be positive. Instead, most runs have $\mathcal{F}^{(\rm turb)}_{\mathcal{L},x} < 0$, which is physically allowed since work done by the global pressure gradient powers streaming turbulence. Only run BA (and BA-3D) has $\mathcal{F}^{(\rm turb)}_{\mathcal{L},x} > 0$, but the net angular momentum flux is still inward. Thus in all our simulations, angular momentum transport acts to take kinetic energy out of the motion, at the rate $\dot{\mathcal{E}}_{\mathcal{L}} = (3/2)\Omega \mathcal{F}_{\mathcal{L},x} < 0$ (see YJ §5). As in any shearing box simulation with (shear) periodic boundary conditions, momentum fluxes are divergence-free constants, which prohibits secular evolution. Global simulations are needed to fully investigate the role of "backwards" angular momentum transport from streaming turbulence on disc evolution.

7.6.3 Turbulent diffusion

The turbulent mixing of particles is usually modelled as a diffusive process in which particle motions are described by a random walk for large length-scales and over long time-scales. We provide here best fits to the diffusion coefficients in the radial and vertical directions. Since the motion of particles is very complex, and furthermore the particles are not passive contaminants but the cause of turbulence, we also test the validity of the diffusion approximation.

We track the deviation of particle positions, $x_i(t)$ and $z_i(t)$, from their positions at an initial time t_0 when turbulence has already developed. Here we are not concerned with the net radial drift of particles, but the spreading of the distribution $x_i(t) - x_i(t_0)$ (and similarly for vertical motions, although no systematic motion over long time-scales is expected in this direction). Particles are allowed to move greater distances than the box size by deconvoluting any particles that were transferred over the periodic boundaries by the code. For pure diffusion, the distribution tends to a Gaussian with a variance, σ^2, that grows linearly with time.[10] An example of how the particles spread out with time is shown in Fig. 7.17 for radial mixing in the BA simulation. The diffusion coefficients, D_x and D_z, are extracted as

$$D_{x,z} \equiv \frac{1}{2} \frac{\partial \sigma^2_{x,z}}{\partial t} . \tag{7.10}$$

[10]Since particles are allowed to cross the periodic boundaries, at late times different portions of the distribution will overlap. This just means that only turbulent scales up to a certain length scale are considered, something that should not significantly affect the integrity of the measurements.

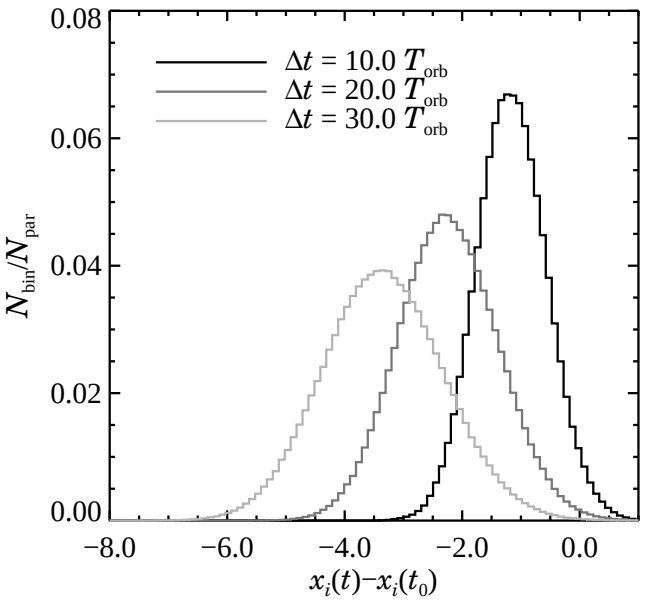

Fig. 7.17 The histograms plot the radial distance that particles in run BA have travelled since the reference time of $t_0 = 20T_{\rm orb}$. The curve moves inward due to the radial drift, while spreading as a random walk with a Gaussian width σ that increases as the square root of time. The Gaussians are slightly platykurtic, or flat-tailed, due to a population of solid particles that experience decreased diffusion in the massive particle clumps seen in Fig. 7.2.

The best fit diffusion coefficients are listed in Table 7.3, using the standard normalisation by $c_{\rm s}^2\Omega^{-1}$. The dimensionless diffusion coefficients lie in the interval $10^{-7}\ldots10^{-2}$, ranging from extremely small up to values that are comparable to the diffusion caused by magnetorotational turbulence (Carballido et al. 2005; Johansen and Klahr 2005). For the smaller $\tau_s = 0.1$ particles the diffusion is quite weak, $< 5 \times 10^{-5}$. This is because more tightly coupled particles trigger weaker turbulence with smaller length scales, a result consistent with smaller linear growth rates and wavelengths for lower τ_s (see YG). Run BA ($\tau_s = 1.0, \epsilon = 0.2$) exhibits anomalously large diffusion, especially in the vertical direction, $D_z \approx 0.01$. This is due to the significant bulk motion of elongated clumps (discussed in §7.4.2).

The upper limit for the diffusion appears to be set by the characteristic length and velocity scales, ηr and $\eta v_{\rm K}$, to be $D \lesssim \eta^2 v_{\rm K} r \approx \eta c_{\rm s}^2/\Omega$, i.e. $D \lesssim \eta = 5 \times 10^{-3}$ when non-dimensionalised. Indeed even the extreme D_z in run BA only violates this order of magnitude criterion by a factor of three. As a consistency check on the diffusion coefficients, $D_{x,z} \approx \delta w_{x,z}^2 t_{\rm corr}$ is obeyed within a factor of a few, for random velocities, $\delta\boldsymbol{w}$, from Table 7.2 (for the gas, but particle values are not more than $\sim 10\%$ different) and the correlation times, $t_{\rm corr}$, from Fig. 7.13.

It will be interesting to compare these results to stratified disc models with self-consistent vertical settling, where the relevant parameters are τ_s and the solids-to-gas *surface* density ratio (instead of ϵ).

Validity of the diffusion approximation

We performed several tests of the diffusion approximation. The time variation of the diffusion coefficients should be small, and especially should lack an overall deviation from $\partial\sigma^2/\partial t \propto$ constant. This was true for most runs, as indicated by the error bars on the diffusion coefficients in Table 7.3. The two exceptions were again run BA, which exhibited large fluctuations due to the interactions between a few large particle clumps, and the two-fluid run AA. This run was seeded with tracer particles, following the velocity field of the solid fluid, in order to be able to use the random walk approach to measure diffusion. The tracer particles exhibited extremely small diffusion with a huge fluctuation interval, an effect of the weak non-linear state of run AA where periodic bulk motion of a few clumps dominates over random motion (see Fig. 7.7). Particles spread out and gather again in a way that is distinctly not a random walk, but over longer time-scales the particle distribution still spread out as a Gaussian. The enormous error interval indicates that the turbulent transport is not like diffusion on short time-scales.

We also tested Gaussianity by measuring the skewness and kurtosis of the particle displacement distributions. Most runs were fairly Gaussian, except for a modest skewness, $\sim 10\%$, in the radial (and not vertical) distributions, which is readily explained by the interaction of the radial drift flow with clumps. The BA run exhibited a kurtosis of -0.5, i.e. slightly platykurtic or small-tailed (see Fig. 7.17), consistent with transport influenced by bulk motions, and not just a random walk. Modelling turbulent transport as diffusion is under all circumstances only an approximation. Still, the turbulent diffusion coefficient is a good measure of the time-scale on which solid particles are mixed by the turbulent motion.

7.7 Summary

In this chapter we have shown that solid particles can trigger turbulence in gaseous protoplanetary discs via the streaming instability and thereby cause their own clumping. We have ignored a number of complicating effects. Most critical is perhaps the lack of vertical gravity, but we believe it was instructive to see how the streaming instability evolves in a pure model that has exact linear solutions first. We plan to include both vertical gravity and the self-gravity of the solids in a future research project. A distribution of particle sizes and physical collisions between particles have also been ignored, even though coagulation, fragmentation, and collisional cooling are likely relevant in dense particle clumps. As the complex behaviour of our simple model system shows, significant progress on basic physical processes can be made before the "kitchen sink" approach is required.

The most striking consequence of streaming turbulence is the growth of overdense particle clumps without self-gravity. This effect was previously seen in the non-linear simulations of particle settling and Kelvin-Helmholtz turbulence by Johansen et al. (2006a). In both that work and this one, clumping can be a self-propagating phenomenon. The increased inertia in dense clumps decreases their drift speeds, creating local "traffic jams." We saw this behaviour for marginally coupled solids, which developed the largest relative overdensities, above 100, with an upward cascade to long-lived, vertically elongated filaments. Marginally coupled

solids have the highest radial drift speed and are known to exhibit the most pronounced drag-related phenomena, so it is not surprising that marginal coupling also gives rise to the most dramatic streaming turbulence. While clumping may not in itself explain how to keep large amounts of marginally coupled particles at large orbital distances (Wilner et al. 2000), it does provide a rigorous prediction that the spatial distribution of such solids will not be smooth, but will vary on scales of around one gas scale-height.

A qualitatively different clumping behaviour was seen for smaller, more tightly coupled solids. Overdensities were lower, in the tens, and clumps were smaller scale and short-lived. To extend the analogy, these runs appeared more like a game of bumper cars than a full-scale traffic jam. The biggest surprise was the complete reversal of the laminar relation between drift speed and particle density. Dense clumps actually fell in faster than particles in voids for the tightly coupled solids. Our heuristic explanation is that robust clumps can withstand turbulent boundary layer flows that sap their angular momentum, as in an Ekman layer flow. A similar explanation has been applied to the surfaces of particle sub-discs as the plate drag *ansatz* (Goldreich and Ward 1973; Goodman and Pindor 2000; Weidenschilling 2003). The run with the tightest coupling and lowest initial solids-to-gas density ratio, and consequently the lowest linear growth rate, developed very meek non-linear density fluctuations. Thus non-linear clumping appears to require either marginal coupling or a moderately large background solids-to-gas ratio of around unity or higher. Further studies of the streaming instability for smaller particles, such as chondrules, would be interesting, but are computationally costly (see §7.4.3).

It is hardly surprising that the solids-to-gas density ratio strongly affects the non-linear state since the streaming instability relies on particle feedback to influence gas dynamics. However, the sharp transition across particle-gas equality is remarkable, especially for tight coupling – the weak streaming instabilities in the gas-dominated regime become explosive once the solids-to-gas ratio reaches unity. Youdin and Shu (2002) argued that this threshold also sets a limit to the quantity of solids that can be stirred by the Kelvin-Helmholz instability. Vigorous turbulence (if stronger than particles themselves can stir) could prevent the accumulations of such high midplane particle densities. There is little doubt, however, that dramatic events occur whenever particle densities reach that of the gas.

Planetesimal formation models generally involve either high particle densities, in a gravitational collapse scenario, or efficient coagulation to particle sizes for which radial drift is no longer a problem. Both scenarios involve conditions – high particle densities and/or marginal drag force coupling – where streaming instabilities can abet further growth towards planetesimals by generating overdense clumps in the particle component.

Chapter 8

Summary and outlook

In my thesis work I have performed computer simulations of the motion of gas and solids in protoplanetary discs in order to understand the early stages of planet formation. The important step from meter-sized boulders to kilometer-sized planetesimals is an unsolved problem of planet formation, because boulders have poor sticking properties (Benz 2000) and spiral into the inner part of the nebula in as little as a few 100 years (Weidenschilling 1977a).

Turbulence has largely been considered as a source of mass diffusion (and thus a nuisance) in models of planet formation (as in the classical paper by Weidenschilling and Cuzzi 1993, but see also Cuzzi et al. 2001 for an interesting way to concentrate small solids at the dissipation length scale of the turbulence). As shown in many of the chapters in this thesis, turbulence (both arising from magnetorotational, Kelvin-Helmholtz and streaming instabilities) does indeed diffuse solid particles and prevent sedimentation. But another aspect of all the different types of turbulence is their ability to concentrate solids. Two different factors are important for these concentrations. Solid particles are concentrated by magnetorotational turbulence (Chapter 3) because of the subtle effect that gas high pressures enter an equilibrium with Coriolis forces, forming high density structures that are perfect solutions to the non-linear equations of motion and continuity and whose lifetimes are thus not necessarily set by the usual mixing theory, nor by shear or Coriolis forces. Since local gas pressure gradients are crucial for maintaining these structures, solid particles will have to end up there as they drift radially through the disc. The high pressure regions are definitely something that needs further exploration in the future: can they be made stronger or weaker by including additional physics such as heating (by viscosity and irradiation) and radiative transport, stratification and dead zones?

Another concentration effect is based on drag force interaction and thus relies on some degree of sedimentation to raise the solids-to-gas bulk density ratio above the canonical interstellar value of 0.01. The relative drift of solids and gas in pressure-supported discs is linearly unstable to the powerful streaming instability (Youdin and Goodman 2005; Chapters 4, 6 and 7 in this thesis), causing turbulence and the appearance of clumps of significant particle overdensities. The next step in 3-D models of the streaming instability is to consider vertical gravity and magnetorotational turbulence to see if the clumps still exist under such conditions.

Preliminary results, that are not included in this thesis, indicate that the streaming instability can operate even in magnetorotationally turbulent discs (Johansen, Oishi, Mac Low, Klahr, Henning, & Youdin, in preparation) because the already overdense high pressure regions turn off the sub-Keplerian gas head wind locally and are loaded with boulders drifting in at the full sub-Keplerian speed from further out.

The measurements of the diffusion properties of magnetorotational turbulence can be very useful for modelling protoplanetary discs (e.g. Dullemond and Dominik 2004) and for understanding the presence of crystalline silicates in the outers parts of these discs (van Boekel et al. 2004) and in solar system comets (Gail 2001). Although there is doubt as to whether the magnerotational instability can operate everywhere in the disc, it is the only known linear Keplerian shear instability (Balbus and Hawley 1998) and is thus very likely responsible for the observed accretion onto young stars (Gullbring et al. 1998). Thus it is one of the fortunate instances where 3-D protoplanetary disc turbulence simulations are directly useful for understanding observations (considering a more advanced disc model with active surface layers and a magnetically dead mid-plane Fromang and Papaloizou 2006 found twice as high vertical Schmidt numbers as reported in Chapter 2 of this thesis). The fact that the Schmidt number depends on the imposed magnetic field (Chapter 5) may also yield a possibility to determine the magnetic field environment if in the future the Schmidt number can somehow be extracted from observations of protoplanetary discs, e.g. by measuring directly the scale height of different size dust grains.

The simulations without any global turbulence may in a way be considered to be numerical experiments more than reality – maybe driven by the same sentiments that drove Viktor Safronov and others to blindly believe that discs are turbulent without even knowing the specific path to turbulence. Circumstellar discs *must* be turbulent (as also indicated by observed accretion of matter onto young stars). Still the instabilities that were derived for analytical models of discs with no global turbulence – the Kelvin-Helmholtz and streaming instabilities – teach us a lot about the coupled motion of gas and solids and will surely be important in understanding planetesimal formation in globally turbulent media as well, and also in magnetically inactive zones of the disc where significant random motion and accretion can occur due to the influence from the magnetically active surface layers (Fleming and Stone 2003).

I hope in the future to work on more advanced models of the turbulence where a part of the disc around the mid-plane is not ionised enough for magnetorotational instability. Gammie (1996) already found that accretion in such a setup has no equilibrium solution (i.e. $\dot{M}$ can not obtain a constant value throughout the disc), leading to pileup of mass in the dead zone and periodic outbursts due to the violent onset of gravitational instabilities or magnetorotational instability in the heated gas (Wünsch et al. 2005). Such time-dependent behaviour of dead zone may have important consequences for planet formation, e.g. by trapping migrating boulders during outbursts in temporarily denser or hotter regions, but it will require a global rather than a local treatment of the protoplanetary disc.

In a paper on the possible effects of turbulence on planet formation, Safronov (1958) ends with this wonderful quote:

> "Being only an astronomer the author should like to know the opinions of special-

ists on turbulence about these questions."

We are in a way still in the situation today that planet formation models depends hugely on whether discs are turbulent or not and on what kind of turbulence operates. I think one can learn a lot from Viktor Safronov's general attitude to planet formation: we need to know more about the stellar environment, about turbulence, about sticking physics. All these open questions will hopefully keep planet formation a truly interdisciplinary and vibrant topic for the next many, many years.

Appendix A

Appendices

A.1 Hyperdiffusivity

In this appendix we discuss the use of hyperdiffusivity and present the hyperversions of viscosity, mass diffusion and resistivity that we are applying in this work.

Because the Pencil Code is a finite-difference code, artificial diffusivity terms are needed in all dynamical equations to stabilise the numerical scheme. For this purpose, we use sixth order hyperdiffusivity terms which affect mainly high wave numbers, the smallest scales in the simulation, and preserve the energy at low wave numbers. Hyperviscosity and magnetic hyperdiffusivity have been used extensively to study the properties of forced magnetohydrodynamical turbulence (e.g. Brandenburg and Sarson 2002 and references therein). The prospect is to affect large scales as little as possible by dissipation, thus widening the inertial range beyond what can be achieved with a regular viscosity operator.

Possible side effects of using hyperviscosity and magnetic hyperdiffusivity is to increase the bottleneck effect (a physical effect in turbulence where energy piles up around the dissipative scale, see e.g. Biskamp and Müller 2000) and to cause the dynamo-generated magnetic field in helical flows to saturate at a higher level than what is seen when using a regular viscosity operator (Brandenburg and Sarson 2002). Nevertheless, for forced non-magnetic turbulence Haugen and Brandenburg (2004) show that the shape of the inertial range for runs with hyperviscosity is very similar to the shape for higher resolution runs without hyperviscosity.

For the current work we define a momentum-conserving hyperviscosity function $\boldsymbol{f}_\nu$ as

$$\boldsymbol{f}_\nu(\boldsymbol{u},\rho) = (-1)^{m-1}\rho^{-1}\boldsymbol{\nabla}\cdot(\nu_m\rho\boldsymbol{S}^{(2m-1)})\,. \tag{A.1}$$

Here $\boldsymbol{S}^{(l)}$ is a simplified lth order rate-of-strain tensor defined as

$$S_{ij}^{(l)} = \frac{\partial^l u_i}{\partial x_j^l}\,. \tag{A.2}$$

We refer to Haugen and Brandenburg (2004) for a more strict rate-of-strain tensor that is constructed to be symmetric and to have positive definite energy dissipation, but note that

the form proposed in equation (A.2) is computationally much simpler. For computational simplicity we shall also consider the dynamical viscosity $\mu_m \equiv \nu_m \rho$ to be constant. Then the hyperviscosity function takes the appearance

$$\boldsymbol{f}_\nu(\boldsymbol{u}, \rho) = (-1)^{m-1} \frac{\mu_m}{\rho} \nabla^{2m} \boldsymbol{u}\,, \tag{A.3}$$

where $\nabla^{2m} \equiv \nabla_x^{2m} + \nabla_y^{2m} + \nabla_z^{2m}$ is a high order differential operator that reduces to a Laplacian for $m = 1$. For the purpose of stabilising the numerical scheme we adopt a sixth order hyperviscosity by setting $m = 3$ in equation (A.3). The hyperviscosity function $\boldsymbol{f}_\nu$ then appears as

$$\boldsymbol{f}_\nu(\boldsymbol{u}, \rho) = \frac{\mu_3}{\rho} \nabla^6 \boldsymbol{u}\,. \tag{A.4}$$

For the artificial mass diffusion term we define the hyperdiffusion function f_D as

$$f_\mathrm{D}(\rho) = (-1)^{m-1} D_m \nabla^{2m} \rho\,, \tag{A.5}$$

where D_m is a constant diffusion coefficient. Using f_D as a diffusion term in the continuity equation conserves mass density. Again we adopt a hyperdiffusivity version with $m = 3$, leading to the expression

$$f_\mathrm{D}(\rho) = D_3 \nabla^6 \rho\,. \tag{A.6}$$

The hyperresistivity function $\boldsymbol{f}_\eta$ is defined as

$$\boldsymbol{f}_\eta(\boldsymbol{A}) = (-1)^{m-1} \eta_m \nabla^{2m} \boldsymbol{A}\,, \tag{A.7}$$

where η_m is the magnetic diffusivity. As for viscosity and diffusion we use a hyperresistivity scheme with $m = 3$ in equation (A.7). Then the resistivity function $\boldsymbol{f}_\eta$ comes out as

$$\boldsymbol{f}_\eta(\boldsymbol{A}) = \eta_3 \nabla^6 \boldsymbol{A}\,. \tag{A.8}$$

Using this function as a resistivity term in the induction equation conserves all components of the magnetic field $\boldsymbol{B}$.

A.2 Radial diffusion equilibrium

In this appendix we derive the equilibrium dust density when the dust is exposed to a radial gravity. We define a sinusoidal gravity field similar to what was done in the z-direction as

$$g_x = -g_0 \sin(k_x x)\,, \tag{A.9}$$

where $k_x = 2\pi/L_x$ is the radial wave number of the field. In the horizontal plane the Coriolis force connects the radial and toroidal motions, so that any velocity in one direction results in an acceleration in the other direction. If not for the damping effect of friction, dust grains starting with any non-zero velocity would be forced to move in epicyclic motion. Fortunately the drag force from the gas permits an equilibrium solution to the dust equation of motion

equation (2.5). We solve for $\boldsymbol{u} = w_z = 0$, $w_x = w_x(x)$ and $w_y = w_y(x)$ and get the two component equations of the equation of motion

$$0 = -w_x\frac{\partial w_x}{\partial x} + 2\Omega_{\rm K} w_y - \frac{1}{\tau_{\rm f}} w_x - g_0 \sin(k_x x)\,, \tag{A.10}$$

$$0 = -w_x\frac{\partial w_y}{\partial x} - \frac{1}{2}\Omega_{\rm K} w_x - \frac{1}{\tau_{\rm f}} w_y\,. \tag{A.11}$$

Again the advection is ignored. This leads to an algebraic linear system of equations in w_x and w_y,

$$0 = 2\Omega_{\rm K} w_y - \frac{1}{\tau_{\rm f}} w_x - g_0 \sin(k_x x)\,, \tag{A.12}$$

$$0 = -\frac{1}{2}\Omega_{\rm K} w_x - \frac{1}{\tau_{\rm f}} w_y\,, \tag{A.13}$$

that has the solution

$$\left\{ \begin{array}{rcl} w_x &=& -\frac{\tau_{\rm f} g_0}{1+\Omega_{\rm K}^2\tau_{\rm f}^2}\sin(k_x x) \approx -\tau_{\rm f} g_0 \sin(k_x x) \\ w_y &=& \frac{\Omega_{\rm K}\tau_{\rm f}^2 g_0}{2(1+\Omega_{\rm K}^2\tau_{\rm f}^2)}\sin(k_x x) \approx \frac{1}{2}\Omega_{\rm K}\tau_{\rm f}^2 g_0 \sin(k_x x) \end{array} \right. . \tag{A.14}$$

Here the approximate expressions are valid to first order in $\Omega_{\rm K}\tau_{\rm f}$. The ratio between toroidal and radial velocity is $|w_y/w_x| = \frac{1}{2}\Omega_{\rm K}\tau_{\rm f}$, so the toroidally imposed velocity becomes unimportant with sufficiently short friction time. For this form of velocity field, the equilibrium continuity equation takes the form

$$0 = -\frac{\partial}{\partial x}\left[w_x(x) n(x,y) - D_x^{(\rm t)}\frac{\partial n(x,y)}{\partial x}\right] - \frac{\partial}{\partial y}\left[\{w_y(x) + u_y^{(0)}(x)\} n(x,y) - D_y^{(\rm t)}\frac{\partial n(x,y)}{\partial y}\right]. \tag{A.15}$$

By considering solutions to equation (A.15) of the form $n(x,y) = n(x)$, the y-derivative term of equation (A.15) vanishes entirely. Then the equilibrium solution to the continuity equation, when assuming that the total flux of number density radially through the box is zero, is simply

$$\ln n = \ln n_1 + \frac{\tau_{\rm f} g_0}{k_x D_x^{(\rm t)}}\cos(k_x x)\,, \tag{A.16}$$

formally identical to the vertical case.

A.3 Weight functions and interpolation/assignment errors

The choice of weight functions for interpolation, $W_{\rm I}$, and assignment, $W_{\rm A}$, involves trading computational cost against performance. We will consider only 1-D weight functions which are combined multiplicatively to form multidimensional weights, $W(\boldsymbol{x} - \boldsymbol{x_j}) = W(x - x_\ell)W(y - y_m)W(z - z_n)$, for the cell centred at $\boldsymbol{x_j} = x_\ell\hat{\boldsymbol{x}} + y_m\hat{\boldsymbol{y}} + z_m\hat{\boldsymbol{z}}$. This assumes a rectilinear domain of influence, which is simpler (if less physical) than circular/spherical clouds.

The interpolation function in the non-linear simulations uses quadratic splines (QS),

$$W_{\rm I}^{(\rm QS)}(\delta x_\ell) = \left\{ \begin{array}{ll} \frac{3}{4} - \frac{\delta x_\ell^2}{\Delta^2} & \text{if } |\delta x_\ell| < \Delta/2 \\ \frac{1}{2}\left(\frac{3}{2} - \frac{|\delta x_\ell|}{\Delta}\right)^2 & \text{if } \Delta/2 < |\delta x_\ell| < 3\Delta/2 \\ 0 & \text{if } |\delta x_\ell| > 3\Delta/2 \end{array} \right. , \tag{A.17}$$

where $\delta x_\ell \equiv x - x_\ell$ measures the distance from a cell centre and W_I extends over three cells of width Δ. The interpolation errors are calculated by considering a periodic function (of arbitrary phase) sampled at the grid points. The QS interpolated values at arbitrary x in cell ℓ are

$$\overline{\cos(kx+\phi)}_\mathrm{I}^{(\mathrm{QS})} \simeq \cos(kx+\phi)\left[1-\frac{(\Delta k)^2}{8}\right] + \sin(kx+\phi)\left[\frac{(\Delta k)^3}{24}\delta x_\ell(1-4\delta x_\ell^2)\right] + \mathcal{O}(\Delta k)^4\,. \quad \text{(A.18)}$$

The amplitude of a periodic signal is reduced by $1-(\Delta k)^2/8$. For an arbitrary distribution, this smoothing can be simply corrected for in Fourier space. This sharpening is included, but only for the initial amplitudes of $\boldsymbol{u}$, in some linear tests (§6.5.2), but was too costly for the non-linear runs in JY. There is also a noise, i.e. an error that depends on position relative to cell centre δx_ℓ, of amplitude $(k\Delta)^3/(72\sqrt{3})$.

We also considered quadratic polynomial interpolation (QP), which performs a best fit through the three nearest grid points, resulting in a weight function

$$W_\mathrm{I}^{(\mathrm{QP})}(\delta x_\ell) = \begin{cases} 1-\frac{\delta x_\ell^2}{\Delta^2}, & \text{if } |\delta x_\ell| < \Delta/2 \\ \frac{1}{2}\left(1-\frac{|\delta x_\ell|}{\Delta}\right)\left(2-\frac{|\delta x_\ell|}{\Delta}\right), & \text{if } \Delta/2 < |\delta x_\ell| < 3\Delta/2 \\ 0, & \text{if } |\delta x_\ell| > 3\Delta/2 \end{cases}. \quad \text{(A.19)}$$

The QP interpolated values of a periodic signal read

$$\overline{\cos(kx+\phi)}_\mathrm{I}^{(\mathrm{QP})} \simeq \cos(kx+\phi) + \sin(kx+\phi)\left[\frac{(\Delta k)^3}{6}\delta x_\ell(1-\delta x_\ell^2)\right] + \mathcal{O}(\Delta k)^4\,. \quad \text{(A.20)}$$

The amplitude is preserved to second order, an improvement over quadratic spline interpolation. The noise, however, has an amplitude of $(\Delta k)^3/16$, a factor of 15 larger than with quadratic spline. Also troubling is the discontinuity of $(\Delta k)^3/8$ at the cell boundaries.

The assignment function used in all the non-linear simulations of JY is the Triangular Shaped Cloud (TSC) scheme, as opposed to the lower order NGP (Nearest Grid Point, which was used in Johansen et al. 2006a) or CIC (Cloud In Cell) schemes (Hockney and Eastwood 1981). The TSC assignment weight function is identical to the quadratic spline interpolation weight function, $W_\mathrm{A}^{(\mathrm{TSC})} \equiv W_\mathrm{I}^{(\mathrm{QS})}$. Assignment errors depend partly on sampling, i.e. the number of particles that make a non-zero contribution to a sum like equation (6.19). A higher order method like TSC samples more particles at a given grid point and gives a smoother distribution than lower order methods. The fractional amplitude reduction of a mode perfectly sampled by TSC is identical to the result for quadratic spline interpolation, $1-(\Delta k)^2/8$. This is the same order, but larger than for CIC $[1-(\Delta k)^2/12]$ or NGP $[1-(\Delta k)^2/24]$ assignment, although especially the NGP scheme would require an enormous particle number to achieve good sampling of linear perturbations. In principle Fourier sharpening could be applied in the force assignment step, but it is less important to consider, since the errors are not magnified by a subsequent subtraction.

A.4 Numerical test of particle assignment over shearing boundaries

This Appendix studies the behaviour of a linear, non-axisymmetric wave of gas and particles in order to test drag force assignment across the shear-periodic radial boundary. Solutions from the full simulation of the Pencil Code are compared to the following semi-analytic problem. We use local, linearised equations of continuity and motion to describe the evolution of gas and particle density $\rho'_{\rm g}(x,y,t)$, $\rho'_{\rm p}(x,y,t)$ relative to a constant density background state $\rho_{\rm g,0}$, $\rho_{\rm p,0}$, and gas and particle velocities $\boldsymbol{u}'(x,y,t)$, $\boldsymbol{w}'(x,y,t)$ relative to the Keplerian shear flow $\boldsymbol{V}_0=-(3/2)\Omega x\hat{\boldsymbol{y}}$. We assume a shearing wave solution, $q'(x,y,t)=\hat{q}(t)\exp[{\rm i}(k_x(t)x+k_y y)]$, for each perturbation variable, with (see e.g. Goldreich and Lynden-Bell 1965; Brandenburg et al. 2004a)

$$k_x(t)=k_x(0)+(3/2)\Omega t k_y\,. \tag{A.21}$$

The wave amplitudes then evolve as coupled ordinary differential equations in time[1],

$$\begin{aligned}
{\rm d}\hat{\rho}_{\rm g}/{\rm d}t &= -\rho_{\rm g,0}[{\rm i}k_x(t)\hat{w}_x+{\rm i}k_y\hat{w}_y]\,, &\text{(A.22)}\\
{\rm d}\hat{u}_x/{\rm d}t &= 2\Omega\hat{u}_y-\epsilon_0(\hat{u}_x-\hat{w}_x)/\tau_{\rm f}-{\rm i}k_x(t)c_{\rm s}^2\hat{\rho}_{\rm g}/\rho_{\rm g,0}\,, &\text{(A.23)}\\
{\rm d}\hat{u}_y/{\rm d}t &= -\Omega\hat{u}_x/2-\epsilon_0(\hat{u}_y-\hat{w}_y)/\tau_{\rm f}-{\rm i}k_y c_{\rm s}^2\hat{\rho}_{\rm g}/\rho_{\rm g,0}\,, &\text{(A.24)}\\
{\rm d}\hat{\rho}_{\rm p}/{\rm d}t &= -\rho_{\rm p,0}[{\rm i}k_x(t)\hat{w}_x+{\rm i}k_y\hat{w}_y]\,, &\text{(A.25)}\\
{\rm d}\hat{w}_x/{\rm d}t &= 2\Omega\hat{w}_y-(\hat{w}_x-\hat{u}_x)/\tau_{\rm f}\,, &\text{(A.26)}\\
{\rm d}\hat{w}_y/{\rm d}t &= -\Omega\hat{w}_x/2-(\hat{w}_y-\hat{u}_y)/\tau_{\rm f}\,. &\text{(A.27)}
\end{aligned}$$

where $\epsilon_0\equiv\rho_{\rm p,0}/\rho_{\rm g,0}$. We solve this system of ordinary differential equations numerically for $\Omega=\rho_{\rm g,0}=\rho_{\rm p,0}=\tau_{\rm f}=c_{\rm s}=k_y=1$ using a third-order Runge-Kutta time integration method to follow the temporal evolution of a non-axisymmetric wave with the initial condition $k_x=-1,\hat{u}_x=\hat{\rho}_{\rm g}=\hat{w}_x=\hat{w}_y=\hat{\rho}_{\rm p}=0,\hat{u}_y=10^{-3}$. The semi-analytic solution is then compared to the evolution obtained with the full solver of the Pencil Code using 64^2 grid points with 1 particle per grid point to cover a box of size $L_x=L_z=2\pi$. Fig. A.1 shows the evolution of the absolute value of the particle amplitudes $\hat{\rho}_{\rm p}$ (dash-dotted line), $\hat{w}_x$ (dotted line) and $\hat{w}_y$ (dashed line) in comparison with the analytical solution (grey lines). There is an excellent agreement for $t\lesssim 5.0$. At later times, the wave becomes so tightly wound that damping of the wave amplitude by the TSC scheme becomes significant. Most importantly this non-axisymmetric test problem never shows any spurious features near the radial boundary (or anywhere else), validating our implementation of drag force assignment over the boundaries.

A.5 Cold start: algorithm for seeding density perturbations

Seeding low amplitude (we use $\delta_{\rm p}=10^{-6}$) density perturbations with particles is non-trivial. The desired density distribution cannot be seeded by random numbers for a reasonable number of particles, $N_{\rm p}$. The white Poisson noise has a constant Fourier amplitude of $\sim 1/\sqrt{N_{\rm p}}$ at all scales, i.e., we would need a total number of particles $N_{\rm p}\gg 10^{12}$ to resolve $\delta_{\rm p}=10^{-6}$!

[1]Note that for this test problem no global pressure gradient, and thus no drift motions, are included.

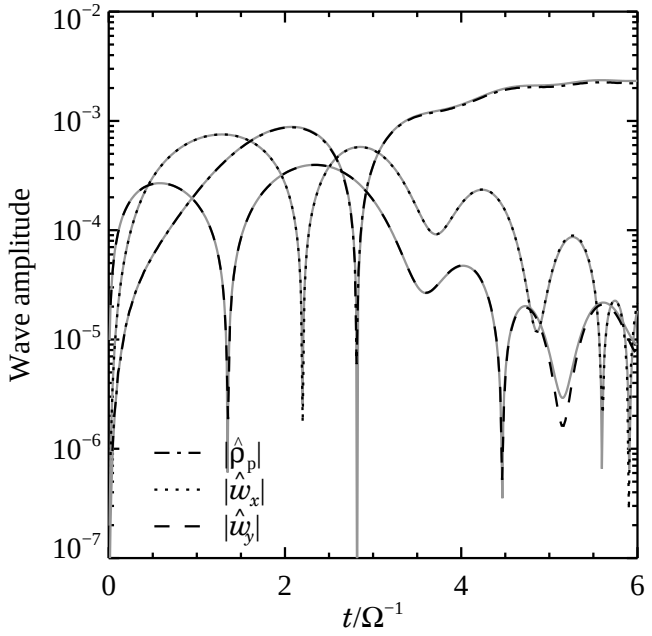

Fig. A.1 The temporal evolution of a leading shear wave of gas and solid particles. The plot shows a comparison between the semi-analytic solution to the linearised equation system (grey lines) and the solution obtained with the full solver of the Pencil Code for the amplitude of the particle density $\hat{\rho}_\mathrm{p}$ (black dash-dotted line) and of the particle velocity components $\hat{w}_x$ (black dotted line) and $\hat{w}_y$ (black dashed line). There is excellent agreement between the numerical and the analytical solutions up until $t \simeq 5\Omega^{-1}$ where damping of the amplitude of the tightly wound wave by the Triangular Shaped Cloud scheme becomes significant.

Instead we borrow a tactic from cosmological simulations (e.g. Trac and Pen 2006) to concentrate power in a desired mode. We first assign particles to a uniform grid with positions, $\boldsymbol{x}_i$, labelled by a particle index $i = 1, 2, ..., N_\mathrm{p}$. This grid is defined relative to the gas grid with an integer number of particles in each gas cell. We introduce linear perturbations to the density by applying periodic shifts to the particle positions. To approximate a density distribution

$$\rho_\mathrm{p}(\boldsymbol{x}) = \langle \rho_\mathrm{p} \rangle [1 + A \cos(\boldsymbol{k}_0 \cdot \boldsymbol{x})] \tag{A.28}$$

with $A \ll 1$, the desired shift from the uniform grid is

$$\boldsymbol{\xi}_i = -\frac{\boldsymbol{k}_0}{k_0^2} A \sin(\boldsymbol{k}_0 \cdot \boldsymbol{x}_i)\,. \tag{A.29}$$

The resulting density distribution,

$$\rho_\mathrm{p}(\boldsymbol{x}) = \sum_i \delta(\boldsymbol{x} - \boldsymbol{x}_i - \boldsymbol{\xi}_i)\,, \tag{A.30}$$

has a Fourier transform

$$\tilde{\rho}_{\rm p}(\boldsymbol{k}) = V_{\rm cell}^{-1} \sum_i \exp\left\{{\rm i}\boldsymbol{k}\cdot[\boldsymbol{x}_i+\boldsymbol{\xi}_i]\right\} \tag{A.31}$$

$$\approx \frac{N_{\rm p}}{V_{\rm cell}}\left[\delta_{\boldsymbol{k},0} + A(\delta_{\boldsymbol{k},\boldsymbol{k}_0}+\delta_{\boldsymbol{k},-\boldsymbol{k}_0})/2\right] + \tilde{\rho}_{\rm p}^{(2)}(\boldsymbol{k}) + \mathcal{O}(A^3)\,, \tag{A.32}$$

where $V_{\rm cell}$ is the volume of a grid cell. The final step shows that we reproduce the desired plane wave to lowest order by performing an expansion about $\boldsymbol{\xi}_i \ll \boldsymbol{x}_i$ and using summation relations for periodic functions (we ignore the sub-gridscale aliases of $\boldsymbol{k}_0$). The standing wave solutions described in Sect. 6.3.3 are produced by summing two plane-wave displacements of $\pm k_z$. The quadratic error term

$$\tilde{\rho}_{\rm p}^{(2)}(\boldsymbol{k}) = \frac{N_{\rm p}}{V}\frac{A^2}{2}(\delta_{\boldsymbol{k},2\boldsymbol{k}_0}+\delta_{\boldsymbol{k},-2\boldsymbol{k}_0}) \tag{A.33}$$

is small for $A \ll 1$, but is eliminated by a further displacement

$$\boldsymbol{\xi}_i^{(2)} = \frac{\boldsymbol{k}_0}{2k_0^2}A^2\sin(2\boldsymbol{k}_0\cdot\boldsymbol{x}_i)\,. \tag{A.34}$$

Thus equation (A.30) has the desired Fourier properties even with only one particle per grid cell. However, the binned density distribution is actually what is relevant for influencing gas dynamics. When the TSC assignment scheme (described in Appendix B) is applied to the "cold start" positions, we cleanly get the desired density distribution assigned on the mesh, even for arbitrarily small shift amplitudes.

Bibliography

I. Adachi, C. Hayashi, and K. Nakazawa. The gas drag effect on the elliptical motion of a solid body in the primordial solar nebula. *Progress of Theoretical Physics*, 56:1756–1771, 1976.

Y. Alibert, O. Mousis, C. Mordasini, and W. Benz. New Jupiter and Saturn Formation Models Meet Observations. ApJ, 626:L57–L60, 2005.

Y. Amelin, A. N. Krot, I. D. Hutcheon, and A. A. Ulyanov. Lead Isotopic Ages of Chondrules and Calcium-Aluminum-Rich Inclusions. *Science*, 297:1678–1683, 2002.

R. Arlt and G. Rüdiger. Global accretion disk simulations of magneto-rotational instability. A&A, 374:1035–1048, 2001.

P. J. Armitage. Turbulence and Angular Momentum Transport in Global Accretion Disk Simulation. ApJ, 501:L189+, 1998.

J. Baker, M. Bizzarro, N. Wittig, J. Connelly, and H. Haack. Early planetesimal melting from an age of 4.5662Gyr for differentiated meteorites. Nature, 436:1127–1131, 2005.

S. A. Balbus and J. F. Hawley. A powerful local shear instability in weakly magnetized disks. I - Linear analysis. II - Nonlinear evolution. ApJ, 376:214–233, 1991.

S. A. Balbus and J. F. Hawley. Instability, turbulence, and enhanced transport in accretion disks. *Reviews of Modern Physics*, 70:1–53, 1998.

S. A. Balbus, J. F. Hawley, and J. M. Stone. Nonlinear Stability, Hydrodynamical Turbulence, and Transport in Disks. ApJ, 467:76–+, 1996.

P. Barge and J. Sommeria. Did planet formation begin inside persistent gaseous vortices? A&A, 295:L1–L4, 1995.

J. A. Barranco and P. S. Marcus. Three-dimensional Vortices in Stratified Protoplanetary Disks. ApJ, 623:1157–1170, 2005.

S. V. W. Beckwith, A. I. Sargent, R. S. Chini, and R. Guesten. A survey for circumstellar disks around young stellar objects. AJ, 99:924–945, 1990.

S. V. W. Beckwith, T. Henning, and Y. Nakagawa. Dust Properties and Assembly of Large Particles in Protoplanetary Disks. *Protostars and Planets IV*, pages 533–+, 2000.

W. Benz. Low Velocity Collisions and the Growth of Planetesimals. *Space Science Reviews*, 92:279–294, 2000.

C. Bertout, G. Basri, and J. Bouvier. Accretion disks around T Tauri stars. ApJ, 330:350–373, 1988.

D. Biskamp and W.-C. Müller. Scaling properties of three-dimensional isotropic magnetohydrodynamic turbulence. *Physics of Plasmas*, 7:4889–4900, 2000.

J. Blum and G. Wurm. Experiments on Sticking, Restructuring, and Fragmentation of Preplanetary Dust Aggregates. *Icarus*, 143:138–146, 2000.

D. Bockelée-Morvan, D. Gautier, F. Hersant, J.-M. Huré, and F. Robert. Turbulent radial mixing in the solar nebula as the source of crystalline silicates in comets. A&A, 384: 1107–1118, 2002.

A. C. Boley, T. W. Hartquist, R. H. Durisen, and S. Michael. The Internal Energy for Molecular Hydrogen in Gravitationally Unstable Protoplanetary Disks. ApJ, 656:L89–L92, 2007.

N. Borderies, P. Goldreich, and S. Tremaine. Sharp edges of planetary rings. Nature, 299: 209–211, 1982.

A. P. Boss. Giant planet formation by gravitational instability. *Science*, 276:1836–1839, 1997.

A. P. Boss. Evolution of the Solar Nebula. V. Disk Instabilities with Varied Thermodynamics. ApJ, 576:462–472, 2002.

A. P. Boss. Rapid Formation of Outer Giant Planets by Disk Instability. ApJ, 599:577–581, 2003.

T. L. Bourke, P. C. Myers, G. Robinson, and A. R. Hyland. New OH Zeeman Measurements of Magnetic Field Strengths in Molecular Clouds. ApJ, 554:916–932, 2001.

A. Brandenburg. *Computational aspects of astrophysical MHD and turbulence*, pages 269–+. Advances in Nonlinear Dynamics, 2003.

A. Brandenburg and G. R. Sarson. Effect of Hyperdiffusivity on Turbulent Dynamos with Helicity. *Physical Review Letters*, 88(5):055003–+, 2002.

A. Brandenburg, A. Nordlund, R. F. Stein, and U. Torkelsson. Dynamo-generated Turbulence and Large-Scale Magnetic Fields in a Keplerian Shear Flow. ApJ, 446:741–+, 1995.

A. Brandenburg, B. Dintrans, and N. E. L. Haugen. Shearing and embedding box simulations of the magnetorotational instability. In R. Rosner, G. Rüdiger, and A. Bonanno, editors, *AIP Conf. Proc. 733: MHD Couette Flows: Experiments and Models*, pages 122–136, 2004a.

A. Brandenburg, P. J. Käpylä, and A. Mohammed. Non-Fickian diffusion and tau approximation from numerical turbulence. *Physics of Fluids*, 16:1020–1027, 2004b.

F. Brauer, C. Dullemond, A. Johansen, Th. Henning, H. Klahr, and A. Natta. Survival of the mm-cm size grain population observed in protoplanetary disks. *Submitted to A&A*, 2007.

K. Cai, R. H. Durisen, S. Michael, A. C. Boley, A. C. Mejía, M. K. Pickett, and P. D'Alessio. The Effects of Metallicity and Grain Size on Gravitational Instabilities in Protoplanetary Disks. ApJ, 636:L149–L152, 2006.

M. Camenzind. Magnetized Disk-Winds and the Origin of Bipolar Outflows. In G. Klare, editor, *Reviews in Modern Astronomy*, pages 234–265, 1990.

A. G. W. Cameron. Physics of the primitive solar accretion disk. *Moon and Planets*, 18:5–40, 1978.

A. Carballido, J. M. Stone, and J. E. Pringle. Diffusion coefficient of a passive contaminant in a local MHD model of a turbulent accretion disc. MNRAS, 358:1055–1060, 2005.

S. Casertano and P. Hut. Core radius and density measurements in N-body experiments Connections with theoretical and observational definitions. ApJ, 298:80–94, 1985.

S. Chandrasekhar. *Hydrodynamic and hydromagnetic stability*. International Series of Monographs on Physics, Oxford: Clarendon, 1961, 1961.

P. H. Chavanis. Trapping of dust by coherent vortices in the solar nebula. A&A, 356:1089–1111, 2000.

E. I. Chiang and P. Goldreich. Spectral Energy Distributions of T Tauri Stars with Passive Circumstellar Disks. ApJ, 490:368–+, 1997.

A. Chokshi, A. G. G. M. Tielens, and D. Hollenbach. Dust coagulation. ApJ, 407:806–819, 1993.

J. N. Cuzzi and S. J. Weidenschilling. *Particle-Gas Dynamics and Primary Accretion*, pages 353–381. Meteorites and the Early Solar System II, 2006.

J. N. Cuzzi, A. R. Dobrovolskis, and J. M. Champney. Particle-gas dynamics in the midplane of a protoplanetary nebula. *Icarus*, 106:102–+, 1993.

J. N. Cuzzi, R. C. Hogan, J. M. Paque, and A. R. Dobrovolskis. Size-selective Concentration of Chondrules and Other Small Particles in Protoplanetary Nebula Turbulence. ApJ, 546: 496–508, 2001.

C. de la Fuente Marcos and P. Barge. The effect of long-lived vortical circulation on the dynamics of dust particles in the mid-plane of a protoplanetary disc. MNRAS, 323:601–614, 2001.

W. Dobler, M. Stix, and A. Brandenburg. Magnetic Field Generation in Fully Convective Rotating Spheres. ApJ, 638:336–347, 2006.

A. R. Dobrovolskis, J. S. Dacles-Mariani, and J. N. Cuzzi. Production and damping of turbulence by particles in the solar nebula. J. Geophys. Res., 104:30805–+, 1999.

C. Dominik and A. G. G. M. Tielens. The Physics of Dust Coagulation and the Structure of Dust Aggregates in Space. ApJ, 480:647–+, 1997.

C. Dominik, J. Blum, J. N. Cuzzi, and G. Wurm. Growth of Dust as the Initial Step Toward Planet Formation. In B. Reipurth, D. Jewitt, and K. Keil, editors, *Protostars and Planets V*, pages 783–800, 2007.

B. T. Draine. On the Submillimeter Opacity of Protoplanetary Disks. ApJ, 636:1114–1120, 2006.

B. Dubrulle, G. Morfill, and M. Sterzik. The dust subdisk in the protoplanetary nebula. *Icarus*, 114:237–246, 1995.

B. Dubrulle, L. Marié, C. Normand, D. Richard, F. Hersant, and J.-P. Zahn. An hydrodynamic shear instability in stratified disks. A&A, 429:1–13, 2005.

C. P. Dullemond. The 2-D structure of dusty disks around Herbig Ae/Be stars. I. Models with grey opacities. A&A, 395:853–862, 2002.

C. P. Dullemond and C. Dominik. The effect of dust settling on the appearance of protoplanetary disks. A&A, 421:1075–1086, 2004.

C. P. Dullemond and C. Dominik. Dust coagulation in protoplanetary disks: A rapid depletion of small grains. A&A, 434:971–986, 2005.

C. P. Dullemond, D. Apai, and S. Walch. Crystalline Silicates as a Probe of Disk Formation History. ApJ, 640:L67–L70, 2006.

C. Fendt and D. Elstner. Long-term evolution of a dipolar-type magnetosphere interacting with an accretion disk. A&A, 349:L61–L64, 1999.

C. Fendt and D. Elstner. Long-term evolution of a dipole type magnetosphere interacting with an accretion disk. II. Transition into a quasi-stationary spherically radial outflow. A&A, 363:208–222, 2000.

J. R. Fessler, J. D. Kulick, and J. K. Eaton. Preferential concentration of heavy particles in a turbulent channel flow. *Physics of Fluids*, 6:3742–3749, 1994.

T. Fleming and J. M. Stone. Local Magnetohydrodynamic Models of Layered Accretion Disks. ApJ, 585:908–920, 2003.

S. Fromang and R. P. Nelson. On the accumulation of solid bodies in global turbulent protoplanetary disc models. MNRAS, 364:L81–L85, 2005.

S. Fromang and J. Papaloizou. Dust settling in local simulations of turbulent protoplanetary disks. A&A, 452:751–762, 2006.

S. Fromang, C. Terquem, and S. A. Balbus. The ionization fraction in α models of protoplanetary discs. MNRAS, 329:18–28, 2002.

H.-P. Gail. Radial mixing in protoplanetary accretion disks. I. Stationary disc models with annealing and carbon combustion. A&A, 378:192–213, 2001.

C. F. Gammie. Layered Accretion in T Tauri Disks. ApJ, 457:355–+, 1996.

C. F. Gammie. Nonlinear outcome of gravitational instability in cooling, gaseous disks. ApJ, 553:174–183, 2001.

P. Garaud and D. N. C. Lin. On the Evolution and Stability of a Protoplanetary Disk Dust Layer. ApJ, 608:1050–1075, 2004.

P. Garaud, L. Barrière-Fouchet, and D. N. C. Lin. Individual and Average Behavior of Particles in a Protoplanetary Nebula. ApJ, 603:292–306, 2004.

P. Goldreich and D. Lynden-Bell. II. Spiral arms as sheared gravitational instabilities. MNRAS, 130:125–+, 1965.

P. Goldreich and S. Tremaine. The excitation and evolution of density waves. ApJ, 222: 850–858, 1978.

P. Goldreich and S. Tremaine. Disk-satellite interactions. ApJ, 241:425–441, 1980.

P. Goldreich and W. R. Ward. The Formation of Planetesimals. ApJ, 183:1051–1062, 1973.

G. C. Gómez and E. C. Ostriker. The Effect of the Coriolis Force on Kelvin-Helmholtz-driven Mixing in Protoplanetary Disks. ApJ, 630:1093–1106, 2005.

J. Goodman and B. Pindor. Secular Instability and Planetesimal Formation in the Dust Layer. *Icarus*, 148:537–549, 2000.

J. Goodman and G. Xu. Parasitic instabilities in magnetized, differentially rotating disks. ApJ, 432:213–223, 1994.

J. Goodman, R. Narayan, and P. Goldreich. The stability of accretion tori. II - Non-linear evolution to discrete planets. MNRAS, 225:695–711, 1987.

E. Gullbring, L. Hartmann, C. Briceno, and N. Calvet. Disk Accretion Rates for T Tauri Stars. ApJ, 492:323–+, 1998.

N. Haghighipour and A. P. Boss. On Gas Drag-Induced Rapid Migration of Solids in a Nonuniform Solar Nebula. ApJ, 598:1301–1311, 2003.

M. S. Hanner. The Silicate Material in Comets. *Space Science Reviews*, 90:99–108, 1999.

N. E. Haugen and A. Brandenburg. Inertial range scaling in numerical turbulence with hyperviscosity. Phys. Rev. E, 70(2):026405–+, 2004.

N. E. Haugen, A. Brandenburg, and W. Dobler. Simulations of nonhelical hydromagnetic turbulence. Phys. Rev. E, 70(1):016308–+, 2004a.

N. E. L. Haugen, A. Brandenburg, and A. J. Mee. Mach number dependence of the onset of dynamo action. MNRAS, 353:947–952, 2004b.

J. F. Hawley and S. A. Balbus. A Powerful Local Shear Instability in Weakly Magnetized Disks. II. Nonlinear Evolution. ApJ, 376:223–+, 1991.

J. F. Hawley and S. A. Balbus. A powerful local shear instability in weakly magnetized disks. III - Long-term evolution in a shearing sheet. ApJ, 400:595–609, 1992.

J. F. Hawley, C. F. Gammie, and S. A. Balbus. Local Three-dimensional Magnetohydrodynamic Simulations of Accretion Disks. ApJ, 440:742–+, 1995.

C. Hayashi. Structure of the Solar Nebula, Growth and Decay of Magnetic Fields and Effects of Magnetic and Turbulent Viscosities on the Nebula. *Progress of Theoretical Physics Supplement*, 70:35–53, 1981.

T. Henning, C. P. Dullemond, S. Wolf, and C. Dominik. *Dust coagulation in protoplanetary disks*, pages 112–128. Planet Formation, 2006.

R. W. Hockney and J. W. Eastwood. *Computer Simulation Using Particles*. Computer Simulation Using Particles, New York: McGraw-Hill, 1981, 1981.

L. S. Hodgson and A. Brandenburg. Turbulence effects in planetesimal formation. A&A, 330: 1169–1174, 1998.

O. Hubickyj, P. Bodenheimer, and J. J. Lissauer. Accretion of the gaseous envelope of Jupiter around a 5 10 Earth-mass core. *Icarus*, 179:415–431, 2005.

I. J. Iben. Stellar Evolution. VI. Evolution from the Main Sequence to the Red-Giant Branch for Stars of Mass 1 $M_{\odot}$, 1.25 $M_{\odot}$, and 1.5 $M_{\odot}$. ApJ, 147:624–+, 1967.

M. Ilgner and R. P. Nelson. On the ionisation fraction in protoplanetary disks. II. The effect of turbulent mixing on gas-phase chemistry. A&A, 445:223–232, 2006a.

M. Ilgner and R. P. Nelson. On the ionisation fraction in protoplanetary disks. III. The effect of X-ray flares on gas-phase chemistry. A&A, 455:731–740, 2006b.

M. Ilgner, T. Henning, A. J. Markwick, and T. J. Millar. Transport processes and chemical evolution in steady accretion disk flows. A&A, 415:643–659, 2004.

N. Ishitsu and M. Sekiya. Shear instabilities in the dust layer of the solar nebula III. Effects of the Coriolis force. *Earth, Planets, and Space*, 54:917–926, 2002.

N. Ishitsu and M. Sekiya. The effects of the tidal force on shear instabilities in the dust layer of the solar nebula. *Icarus*, 165:181–194, 2003.

A. Johansen and H. Klahr. Dust Diffusion in Protoplanetary Disks by Magnetorotational Turbulence. ApJ, 634:1353–1371, 2005.

A. Johansen, A. C. Andersen, and A. Brandenburg. Simulations of dust-trapping vortices in protoplanetary discs. A&A, 417:361–374, 2004.

A. Johansen, T. Henning, and H. Klahr. Dust Sedimentation and Self-sustained Kelvin-Helmholtz Turbulence in Protoplanetary Disk Midplanes. ApJ, 643:1219–1232, 2006a.

A. Johansen, H. Klahr, and T. Henning. Gravoturbulent Formation of Planetesimals. ApJ, 636:1121–1134, 2006b.

A. Johansen, H. Klahr, and A. J. Mee. Turbulent diffusion in protoplanetary discs: the effect of an imposed magnetic field. MNRAS, 370:L71–L75, 2006c.

R. Keppens and G. Tóth. Nonlinear dynamics of Kelvin-Helmholtz unstable magnetized jets: Three-dimensional effects. *Physics of Plasmas*, 6:1461–1469, 1999.

R. Keppens, G. Tóth, R. H. J. Westermann, and J. P. Goedbloed. Growth and saturation of the Kelvin-Helmholtz instability with parallel and antiparallel magnetic fields. *Journal of Plasma Physics*, 61:1–19, 1999.

H. Klahr. The Global Baroclinic Instability in Accretion Disks. II. Local Linear Analysis. ApJ, 606:1070–1082, 2004.

H. Klahr and P. Bodenheimer. Formation of Giant Planets by Concurrent Accretion of Solids and Gas inside an Anticyclonic Vortex. ApJ, 639:432–440, 2006.

H. Klahr and W. Brandner. *Planet Formation*. Planet Formation, 2006.

H. Klahr and D. N. C. Lin. Dust Distribution in Gas Disks. II. Self-induced Ring Formation through a Clumping Instability. ApJ, 632:1113–1121, 2005.

H. H. Klahr and P. Bodenheimer. Turbulence in Accretion Disks: Vorticity Generation and Angular Momentum Transport via the Global Baroclinic Instability. ApJ, 582:869–892, 2003.

H. H. Klahr and T. Henning. Particle-Trapping Eddies in Protoplanetary Accretion Disks. *Icarus*, 128:213–229, 1997.

H. H. Klahr and D. N. C. Lin. Dust Distribution in Gas Disks: A Model for the Ring around HR 4796A. ApJ, 554:1095–1109, 2001.

R. S. Klessen, F. Heitsch, and M.-M. Mac Low. Gravitational Collapse in Turbulent Molecular Clouds. I. Gasdynamical Turbulence. ApJ, 535:887–906, 2000.

A. Koenigl. Disk accretion onto magnetic T Tauri stars. ApJ, 370:L39–L43, 1991.

E. Kokubo and S. Ida. Formation of Protoplanet Systems and Diversity of Planetary Systems. ApJ, 581:666–680, 2002.

M. Küker, T. Henning, and G. Rüdiger. Magnetic Star-Disk Coupling in Classical T Tauri Systems. ApJ, 589:397–409, 2003.

T. Kusaka, T. Nakano, and C. Hayashi. Growth of Solid Particles in the Primordial Solar Nebula. *Progress of Theoretical Physics*, 44:1580–1595, 1970.

H. Li, J. M. Finn, R. V. E. Lovelace, and S. A. Colgate. Rossby Wave Instability of Thin Accretion Disks. II. Detailed Linear Theory. ApJ, 533:1023–1034, 2000.

H. Li, S. A. Colgate, B. Wendroff, and R. Liska. Rossby Wave Instability of Thin Accretion Disks. III. Nonlinear Simulations. ApJ, 551:874–896, 2001.

D. N. C. Lin and J. Papaloizou. On the structure and evolution of the primordial solar nebula. MNRAS, 191:37–48, 1980.

J. J. Lissauer. Planet formation. ARA&A, 31:129–174, 1993.

Y. Lithwick and E. Chiang. Collisional Particle Disks. ApJ, 656:524–533, 2007.

D. Lynden-Bell and J. E. Pringle. The evolution of viscous discs and the origin of the nebular variables. MNRAS, 168:603–637, 1974.

L. Mayer, G. Lufkin, T. Quinn, and J. Wadsley. Fragmentation of gravitationally unstable gaseous protoplanetary disks with radiative transfer. *ArXiv Astrophysics e-prints*, 2006.

E. E. Mendoza. Infrared Excesses in T Tauri Stars and Related Objects. ApJ, 151:977–+, 1968.

K. A. Miller and J. M. Stone. Magnetohydrodynamic Simulations of Stellar Magnetosphere–Accretion Disk Interaction. ApJ, 489:890–+, 1997.

K. A. Miller and J. M. Stone. The Formation and Structure of a Strongly Magnetized Corona above a Weakly Magnetized Accretion Disk. ApJ, 534:398–419, 2000.

H. Mizuno. Formation of the Giant Planets. *Progress of Theoretical Physics*, 64:544–557, 1980.

Y. Nakagawa, M. Sekiya, and C. Hayashi. Settling and growth of dust particles in a laminar phase of a low-mass solar nebula. *Icarus*, 67:375–390, 1986.

R. P. Nelson. On the orbital evolution of low mass protoplanets in turbulent, magnetised disks. A&A, 443:1067–1085, 2005.

R. P. Nelson and J. C. B. Papaloizou. The interaction of giant planets with a disc with MHD turbulence - IV. Migration rates of embedded protoplanets. MNRAS, 350:849–864, 2004.

O. R. Norton. *The Cambridge Encyclopedia of Meteorites*. The Cambridge Encyclopedia of Meteorites, by O. Richard Norton, pp. 374. ISBN 0521621437. Cambridge, UK: Cambridge University Press, March 2002., 2002.

S.-J. Paardekooper and G. Mellema. Planets opening dust gaps in gas disks. A&A, 425: L9–L12, 2004.

S.-J. Paardekooper and G. Mellema. Halting type I planet migration in non-isothermal disks. A&A, 459:L17–L20, 2006.

P. Padoan and Å. Nordlund. The "Mysterious" Origin of Brown Dwarfs. ApJ, 617:559–564, 2004.

P. Padoan, L. Cambrésy, M. Juvela, A. Kritsuk, W. D. Langer, and M. L. Norman. Can We Trust the Dust? Evidence of Dust Segregation in Molecular Clouds. ApJ, 649:807–815, 2006.

C. Pasquero, A. Provenzale, and E. A. Spiegel. Suspension and Fall of Heavy Particles in Random Two-Dimensional Flow. *Physical Review Letters*, 91(5):054502–+, 2003.

C. Patterson. Age of meteorites and the earth. Geochim. Cosmochim. Acta, 10:230–237, 1956.

J. B. Pollack, O. Hubickyj, P. Bodenheimer, J. J. Lissauer, M. Podolak, and Y. Greenzweig. Formation of the Giant Planets by Concurrent Accretion of Solids and Gas. *Icarus*, 124: 62–85, 1996.

J. E. Pringle. Accretion discs in astrophysics. ARA&A, 19:137–162, 1981.

M. W. Reeks. On probability density function equations for particle dispersion in a uniform shear flow. *Journal of Fluid Mechanics*, 522:263–302, 2005.

W. K. M. Rice, P. J. Armitage, M. R. Bate, and I. A. Bonnell. The effect of cooling on the global stability of self-gravitating protoplanetary discs. MNRAS, 339:1025–1030, 2003.

W. K. M. Rice, G. Lodato, J. E. Pringle, P. J. Armitage, and I. A. Bonnell. Accelerated planetesimal growth in self-gravitating protoplanetary discs. MNRAS, 355:543–552, 2004.

W. K. M. Rice, G. Lodato, and P. J. Armitage. Investigating fragmentation conditions in self-gravitating accretion discs. MNRAS, 364:L56–L60, 2005.

J. Rodmann, T. Henning, C. J. Chandler, L. G. Mundy, and D. J. Wilner. Large dust particles in disks around T Tauri stars. A&A, 446:211–221, 2006.

D. Ryu and J. Goodman. Convective instability in differentially rotating disks. ApJ, 388: 438–450, 1992.

V. S. Safronov. On the Turbulence in the Protoplanetary Cloud. In J. M. Burgers and R. N. Thomas, editors, *IAU Symp. 8: Cosmical Gas Dynamics*, pages 1023–+, 1958.

V. S. Safronov. *Evoliutsiia doplanetnogo oblaka.* 1969., 1969.

T. Sano and S.-i. Inutsuka. Saturation and Thermalization of the Magnetorotational Instability: Recurrent Channel Flows and Reconnections. ApJ, 561:L179–L182, 2001.

T. Sano, S. M. Miyama, T. Umebayashi, and T. Nakano. Magnetorotational Instability in Protoplanetary Disks. II. Ionization State and Unstable Regions. ApJ, 543:486–501, 2000.

T. Sano, S.-i. Inutsuka, N. J. Turner, and J. M. Stone. Angular Momentum Transport by Magnetohydrodynamic Turbulence in Accretion Disks: Gas Pressure Dependence of the Saturation Level of the Magnetorotational Instability. ApJ, 605:321–339, 2004.

N. C. Santos, G. Israelian, and M. Mayor. The metal-rich nature of stars with planets. A&A, 373:1019–1031, 2001.

R. Schräpler and T. Henning. Dust Diffusion, Sedimentation, and Gravitational Instabilities in Protoplanetary Disks. ApJ, 614:960–978, 2004.

M. Sekiya. Quasi-Equilibrium Density Distributions of Small Dust Aggregations in the Solar Nebula. *Icarus*, 133:298–309, 1998.

M. Sekiya and N. Ishitsu. Shear instabilities in the dust layer of the solar nebula I. The linear analysis of a non-gravitating one-fluid model without the Coriolis and the solar tidal forces. *Earth, Planets, and Space*, 52:517–526, 2000.

D. Semenov, D. Wiebe, and T. Henning. Reduction of chemical networks. II. Analysis of the fractional ionisation in protoplanetary discs. A&A, 417:93–106, 2004.

D. Semenov, D. Wiebe, and T. Henning. Gas-Phase CO in Protoplanetary Disks: A Challenge for Turbulent Mixing. ApJ, 647:L57–L60, 2006.

N. I. Shakura and R. A. Sunyaev. Black holes in binary systems. Observational appearance. A&A, 24:337–355, 1973.

D. Shalybkov and G. Rüdiger. Stability of density-stratified viscous Taylor-Couette flows. A&A, 438:411–417, 2005.

F. Shu, J. Najita, E. Ostriker, F. Wilkin, S. Ruden, and S. Lizano. Magnetocentrifugally driven flows from young stars and disks. 1: A generalized model. ApJ, 429:781–796, 1994.

F. H. Shu. *Physics of Astrophysics, Vol. II.* Physics of Astrophysics, Vol. II, by Frank H. Shu. Published by University Science Books, ISBN 0-935702-65-2, 476pp, 1992., 1992.

F. H. Shu and G. R. Stewart. The collisional dynamics of particulate disks. *Icarus*, 62: 360–383, 1985.

A. Sicilia-Aguilar, L. Hartmann, N. Calvet, S. T. Megeath, J. Muzerolle, L. Allen, P. D'Alessio, B. Merín, J. Stauffer, E. Young, and C. Lada. Disk Evolution in Cep OB2: Results from the Spitzer Space Telescope. ApJ, 638:897–919, 2006.

J. Sommer-Larsen, M. Götz, and L. Portinari. Galaxy Formation: Cold Dark Matter, Feedback, and the Hubble Sequence. ApJ, 596:47–66, 2003.

A. Steinacker and T. Henning. Global Three-dimensional Magnetohydrodynamic Simulations of Accretion Disks and the Surrounding Magnetosphere. ApJ, 554:514–527, 2001.

T. F. Stepinski and P. Valageas. Global evolution of solid matter in turbulent protoplanetary disks. I. Aerodynamics of solid particles. A&A, 309:301–312, 1996.

G. R. Stewart and G. W. Wetherill. Evolution of planetesimal velocities. *Icarus*, 74:542–553, 1988.

G. Suttner and H. W. Yorke. Early Dust Evolution in Protostellar Accretion Disks. ApJ, 551:461–477, 2001.

T. Takeuchi and D. N. C. Lin. Radial Flow of Dust Particles in Accretion Disks. ApJ, 581: 1344–1355, 2002.

P. Tanga, S. J. Weidenschilling, P. Michel, and D. C. Richardson. Gravitational instability and clustering in a disk of planetesimals. A&A, 427:1105–1115, 2004.

H. Tennekes and J. L. Lumley. *First Course in Turbulence.* First Course in Turbulence, Cambridge: MIT Press, 1972, 1972.

L. Testi, A. Natta, D. S. Shepherd, and D. J. Wilner. Large grains in the disk of CQ Tau. A&A, 403:323–328, 2003.

E. W. Thommes, M. J. Duncan, and H. F. Levison. Oligarchic growth of giant planets. *Icarus*, 161:431–455, 2003.

H. B. Throop and J. Bally. Can Photoevaporation Trigger Planetesimal Formation? ApJ, 623:L149–L152, 2005.

A. Toomre. On the gravitational stability of a disk of stars. ApJ, 139:1217–1238, 1964.

H. Trac and U.-L. Pen. Out-of-core hydrodynamic simulations for cosmological applications. *New Astronomy*, 11:273–286, 2006.

M. Trieloff, E. K. Jessberger, I. Herrwerth, J. Hopp, C. Fiéni, M. Ghélis, M. Bourot-Denise, and P. Pellas. Structure and thermal history of the H-chondrite parent asteroid revealed by thermochronometry. Nature, 422:502–506, 2003.

N. J. Turner, K. Willacy, G. Bryden, and H. W. Yorke. Turbulent Mixing in the Outer Solar Nebula. ApJ, 639:1218–1226, 2006.

N. J. Turner, T. Sano, and N. Dziourkevitch. Turbulent Mixing and the Dead Zone in Protostellar Disks. ApJ, 659:729–737, 2007.

R. van Boekel, M. Min, C. Leinert, L. B. F. M. Waters, A. Richichi, O. Chesneau, C. Dominik, W. Jaffe, A. Dutrey, U. Graser, T. Henning, J. de Jong, R. Köhler, A. de Koter, B. Lopez, F. Malbet, S. Morel, F. Paresce, G. Perrin, T. Preibisch, F. Przygodda, M. Schöller, and M. Wittkowski. The building blocks of planets within the 'terrestrial' region of protoplanetary disks. Nature, 432:479–482, 2004.

P. Varnière and M. Tagger. Reviving Dead Zones in accretion disks by Rossby vortices at their boundaries. A&A, 446:L13–L16, 2006.

W. H. T. Vlemmings, P. J. Diamond, and H. Imai. A magnetically collimated jet from an evolved star. Nature, 440:58–60, 2006.

H. J. Voelk, F. C. Jones, G. E. Morfill, and S. Roeser. Collisions between grains in a turbulent gas. A&A, 85:316–325, 1980.

W. R. Ward. The formation of the solar system. In *Frontiers of Astrophysics,* ed. E.H. Avrett, pages 1–40, 1976.

W. R. Ward. Protoplanet Migration by Nebula Tides. *Icarus*, 126:261–281, 1997.

W. R. Ward. *On Planetesimal Formation: The Role of Collective Particle Behavior*, pages 75–84. Origin of the earth and moon, edited by R.M. Canup and K. Righter and 69 collaborating authors. Tucson: University of Arizona Press., p.75-84, 2000.

S. J. Weidenschilling. Aerodynamics of solid bodies in the solar nebula. MNRAS, 180:57–70, 1977a.

S. J. Weidenschilling. The distribution of mass in the planetary system and solar nebula. Ap&SS, 51:153–158, 1977b.

S. J. Weidenschilling. Dust to planetesimals - Settling and coagulation in the solar nebula. *Icarus*, 44:172–189, 1980.

S. J. Weidenschilling. Evolution of grains in a turbulent solar nebula. *Icarus*, 60:553–567, 1984.

S. J. Weidenschilling. Can gravitational instability form planetesimals? *Icarus*, 116:433–435, 1995.

S. J. Weidenschilling. The Origin of Comets in the Solar Nebula: A Unified Model. *Icarus*, 127:290–306, 1997.

S. J. Weidenschilling. Radial drift of particles in the solar nebula: implications for planetesimal formation. *Icarus*, 165:438–442, 2003.

S. J. Weidenschilling. Models of particle layers in the midplane of the solar nebula. *Icarus*, 181:572–586, 2006.

S. J. Weidenschilling and J. N. Cuzzi. Formation of planetesimals in the solar nebula. In E. H. Levy and J. I. Lunine, editors, *Protostars and Planets III*, pages 1031–1060, 1993.

G. W. Wetherill. Comparison of analytical and physical modeling of planetesimal accumulation. *Icarus*, 88:336–354, 1990.

F. L. Whipple. On certain aerodynamic processes for asteroids and comets. In A. Elvius, editor, *From Plasma to Planet*, pages 211–+, 1972.

K. Willacy, W. Langer, M. Allen, and G. Bryden. Turbulence-driven Diffusion in Protoplanetary Disks: Chemical Effects in the Outer Regions. ApJ, 644:1202–1213, 2006.

D. J. Wilner, P. T. P. Ho, J. H. Kastner, and L. F. Rodríguez. VLA Imaging of the Disk Surrounding the Nearby Young Star TW Hydrae. ApJ, 534:L101–L104, 2000.

J. Wisdom and S. Tremaine. Local simulations of planetary rings. AJ, 95:925–940, 1988.

R. Wünsch, H. Klahr, and M. Różyczka. Two-dimensional models of layered protoplanetary discs - I. The ring instability. MNRAS, 362:361–368, 2005.

G. Wurm, J. Blum, and J. E. Colwell. NOTE: A New Mechanism Relevant to the Formation of Planetesimals in the Solar Nebula. *Icarus*, 151:318–321, 2001.

A. Youdin and A Johansen. Protoplanetary Disk Turbulence Driven by the Streaming Instability: Linear Evolution and Numerical Methods. *Accepted for publication in ApJ*, 2007.

A. N. Youdin. Planetesimal Formation without Thresholds. II: Gravitational Instability of Solids in Turbulent Protoplanetary Disks. *ArXiv Astrophysics e-prints*, 2005a.

A. N. Youdin. Planetesimal Formation without Thresholds. I: Dissipative Gravitational Instabilities and Particle Stirring by Turbulence. *ArXiv Astrophysics e-prints*, 2005b.

A. N. Youdin and E. I. Chiang. Particle Pileups and Planetesimal Formation. ApJ, 601: 1109–1119, 2004.

A. N. Youdin and J. Goodman. Streaming Instabilities in Protoplanetary Disks. ApJ, 620: 459–469, 2005.

A. N. Youdin and F. H. Shu. Planetesimal Formation by Gravitational Instability. ApJ, 580: 494–505, 2002.

T. A. Yousef, A. Brandenburg, and G. Rüdiger. Turbulent magnetic Prandtl number and magnetic diffusivity quenching from simulations. A&A, 411:321–327, 2003.